Understanding seismic body waves retrieved from noise correlations : Toward a passive deep Earth imaging

Lei Li

Communauté UNIVERSITÉ Grenoble Alpes

THÈSE

Pour obtenir le grade de

DOCTEUR DE LA COMMUNAUTÉ UNIVERSITÉ GRENOBLE ALPES

Spécialité : Terre Solide (CETSOL)

Arrêté ministériel : 25 mai 2016

Présentée par

Lei LI

Thèse dirigée par **Michel CAMPILLO**, Professeur , UGA
préparée au sein du **Laboratoire Institut des Sciences de la Terre**
dans **l'École Doctorale Terre, Univers, Environnement**

Reconstruction des ondes de volume par corrélation du bruit ambiant : vers l'imagerie passive de la Terre profonde

Understanding seismic body waves retrieved from noise correlations: Toward a passive deep Earth imaging

Thèse soutenue publiquement le **3 octobre 2018**,
devant le jury composé de :

Monsieur MICHEL CAMPILLO
PROFESSEUR, UNIVERSITE GRENOBLE ALPES, Directeur de thèse
Monsieur FABRICE ARDHUIN
DIRECTEUR DE RECHERCHE, IFREMER CENTRE DE BRETAGNE, Examinateur
Madame ANNE PAUL
DIRECTRICE DE RECHERCHE, CNRS DELEGATION ALPES, Président
Monsieur PIERRE BOUÉ
MAÎTRE DE CONFÉRENCES, UNIVERSITE GRENOBLE ALPES, Invitée
Monsieur NIKOLAI SHAPIRO
DIRECTEUR DE RECHERCHE, CNRS DELEGATION PARIS-VILLEJUIF, Examinateur
Monsieur LUDOVIC MARGERIN
CHARGE DE RECHERCHE, CNRS DELEGATION MIDI-PYRENEES, Rapporteur
Monsieur XIAOFEI CHEN
PROFESSEUR, UNIV SUD SCIENCES & TECH-SHENZHEN-CHINE, Rapporteur

SUMMARY

This work aims toward an improved understanding of the seismic signals derived from the inter-receiver correlation functions of seismic noise, which is valuable and critical for a reliable noise-based deep Earth imaging. The thesis consists of seven chapters. Chapter 1 introduces background knowledge on seismic noise, from its classifications to various origins. Chapter 2 provides a literature overview on the history and development of the emerging noise correlation method, and reviews various techniques for the pre-processing of seismic noise data and post-processing of noise correlation functions. Statistics-based noise processing methods and a modified scheme for computing correlation function are developed in this chapter. Chapter 3 proposes several Radon-based techniques to analyze the slownesses of correlated wavefields and to unveil the origin of noise-derived seismic signals. Chapter 4 shows that body waves penetrating into deep Earth can be extracted from noise correlations at teleseismic distances, with noise records from two regional seismic networks. Chapter 5 applies the techniques proposed in chapter 3 to the double-array noise correlations computed in chapter 4, and accordingly reveals the origin of an early spurious phase observed in chapter 4. Chapter 6 discusses several situations that bring ambiguities into the noise-derived seismic signals and can potentially bias the noise-based imaging of subsurface structure. The last chapter provides a summarization over the contributions of this thesis and an outlook of several ongoing and prospected works.

Keywords: ambient noise; body wave; noise correlation; quasi-stationary phase

RÉSUMÉ

Ce travail vise à améliorer la compréhension des signaux sismiques dérivés des fonctions de corrélation inter-récepteur du bruit sismique, ce qui est critique pour une imagerie fiable de la Terre profonde basée sur le bruit. La thèse comprend sept chapitres. Le chapitre 1 introduit les connaissances de base sur le bruit sismique, de la terminologie à ses origines diverses. Le chapitre 2 fournit une vue d'ensemble de la littérature sur l'historique et le développement de la méthode récente de corrélation de bruit, et passe en revue diverses techniques pour le prétraitement des données de bruit sismique et le post-traitement des fonctions de corrélation de bruit. Des méthodes de traitement du bruit basées sur les statistiques et un schéma modifié pour calculer la fonction de corrélation sont développés dans ce chapitre. Le chapitre 3 propose plusieurs techniques basées sur la transformée de Radon pour mesurer les lenteurs des champs d'ondes corrélés et analyser en termes de phases sismiques les signaux dérivés du bruit. Le chapitre 4 montre que les ondes de volume sondant la Terre profonde peuvent être extraites des corrélations de bruit à des distances télésismiques, avec des enregistrements de bruit provenant de deux réseaux sismiques régionaux. Le chapitre 5 applique les techniques proposées au chapitre 3 aux corrélations de bruit entre deux réseaux calculées au chapitre 4, et permet de comprendre l'origine de la phase précoce non-physique observée dans les données. Le chapitre 6 discute des conditions dans lesquelles apparaissent des phases sans correspondance dans la réponse physique de la Terre qui peuvent fausser les analyses des structures profondes basées sur le bruit.. Le dernier chapitre fournit un résumé sur les contributions de cette thèse et une perspective de plusieurs travaux soit en cours soit envisagés pour le futur.

Mots-clés : bruit ambiant; corrélation de bruit; ondes de volume; phase quasi-stationnaire

Table of Contents

1. WINDS, OCEAN WAVES AND SEISMIC NOISE 1

1.1. GLOBAL WINDS 3

1.1.1. Driving Forces 3

1.1.2. Global Patterns 4

1.2. OCEAN WAVES 6

1.2.1. Types of Ocean Waves 6

1.2.2. Global Patterns 7

1.2.3. Ocean Wave Spectra 9

1.3. SEISMIC NOISE 10

1.3.1. Noise Spectrum 12

1.3.2. Microtremor 14

1.3.2.1. Origins 14

1.3.2.2. Spatiotemporal Variability 15

1.3.2.3. Applications 16

1.3.3. Microseism 16

1.3.3.1. Primary Microseism 17

1.3.3.2. Secondary Microseism 18

1.3.3.3. Effects of Bathymetric Modulation 21

1.3.3.4. Early History of Microseism Studies 23

1.3.3.5. Significance of Microseism Observations 27

1.3.4. Seismic Hum 30

1.3.4.1. Discovery 30

1.3.4.2. Open Questions on Origins 31

1.3.4.3. Implications 33

1.3.5. Persistent Localized Noise Sources 34

1.3.6. Composition of Seismic Noise 35

1.4. SUMMARY 38

2. CORRELATION COMPUTATION AND SIGNAL CONSTRUCTION 39

2.1. A LITERATURE REVIEW 39

2.1.1. History and Current Status 39

2.1.2. Applications *42*
2.1.2.1. Surface Waves 43
2.1.2.2. Body Waves 47
2.1.2.3. Scattering and Coda Waves 48
2.1.2.4. Monitoring 49
2.1.2.5. Noise Source Location 51
2.1.2.6. High-Order Correlations 53
2.1.2.7. More Applications 54
2.2. SCHEMATIC OF SEISMIC INTERFEROMETRY 55
2.2.1. Typical Model Geometry *55*
2.2.2. Signal Retrieval *56*
2.2.3. Source Averaging *59*
2.2.4. Noise Source Classification *62*
2.3. PROCESSING OF NOISE DATA 65
2.3.1. General Processing Flow *65*
2.3.2. Segment-Based Noise Data Processing *68*
2.3.3. Descriptive Statistics of Seismograms *70*
2.3.3.1. Lower-Order Statistics: Mean and Variance 70
2.3.3.2. Higher-Order Statistics: Skewness and Kurtosis 71
2.3.3.3. Statistics of Continuous Seismogram 72
2.3.4. Selection Filters for Noise Data Processing *74*
2.3.4.1. Variance-Based Selection Filter 74
2.3.4.2. Kurtosis-Based Selection Filter 75
2.3.5. Separation Filters for Noise Data Processing *77*
2.3.5.1. Mean and Median Filters 78
2.3.5.2. Hampel Filter 78
2.4. COMPUTATION OF CORRELATION FUNCTIONS 78
2.4.1. Conventional Scheme *79*
2.4.2. Modified Scheme *80*
2.4.3. Numerical Comparisons *82*
2.5. PROCESSING OF CORRELATION FUNCTIONS 83
2.6. SUMMARY 85
3. RADON-BASED TECHNIQUES IN DOUBLE-ARRAY INTERFEROMETRY 87
3.1. DOUBLE-ARRAY INTERFEROMETRY 87

3.2. Radon-Based Applications 88
3.2.1. Classic Radon Transform 88
3.2.2. Double-Beam Method 90
3.2.3. Vespagram 90
3.2.4. Slowness Analysis 90
3.2.5. Noise Source Imaging 91
3.3. Summary 94

4. BODY WAVES IN DOUBLE-ARRAY NOISE CORRELATIONS 95

4.1. Seismic Networks and Noise Data 95
4.2. Double-Array Noise Correlations 97
4.2.1. Broadband Waveform Sections 97
4.2.2. Broadband Vespagrams 99
4.3. Spectral Analysis of Reconstructed Seismic Phases 100
4.4. Correlations in Secondary Microseism Frequency Band 102
4.4.1. Filtered Waveform Sections 102
4.4.2. Filtered Vespagrams 103
4.5. Summary 104

5. SEISMIC INTERFEROMETRY OF QUASI-STATIONARY PHASE 105

5.1. Observation of Coherent Spurious Arrival 105
5.1.1. A Quick Review 105
5.1.2. Daily Noise Correlations 107
5.2. Origin of Spurious Phase 109
5.2.1. Double-Array Slowness Analysis 109
5.2.2. Tracking Paths of Interferometric Waves 110
5.2.3. Noise Source Imaging 113
5.2.4. Quasi-Stationary Phase Interferometry 114
5.3. Temporal Variations of Spurious Phase 116
5.3.1. Daily Variations of Spurious Phase 117
5.3.2. Classification of Daily Noise Correlations 118
5.4. Comparisons with Seismological Observations 119
5.4.1. Comparisons with Global Large Earthquakes 120
5.4.2. Comparisons with Seismicity in New Zealand 121

5.4.3. Comparisons with Microseisms in New Zealand *122*
5.5. COMPARISONS WITH HINDCAST DATA 124
5.5.1. Hindcast Data Surrounding Source Region *124*
5.5.2. Oceanic Microseism Events *128*
5.5.2.1. Event around 2008-05-01 128
5.5.2.2. Event around 2008-05-23 133
5.5.2.3. Event around 2008-07-31 136
5.5.3. Correlating with Global Wave Heights *139*
5.5.4. Correlating with Global Microseism Sources *141*
5.6. SUMMARY AND DISCUSSIONS 143
6. AMBIGUITIES IN NOISE-DERIVED BODY WAVES 146
6.1. EFFECTS OF NOISE SOURCE DISTRIBUTION 146
6.1.1. Near-Simultaneous P Arrivals *146*
6.1.2. Comparisons with Hindcast Data *147*
6.1.2.1. Global Microseism Excitation 147
6.1.2.2. Global Correlation Map 147
6.1.3. Interpretations *148*
6.1.3.1. Origins of Regular P Arrival 148
6.1.3.2. Origins of Biased P Arrival 149
6.2. EFFECTS OF MULTIPATH INTERFERENCE 150
6.2.1. Multipath due to Conversion *150*
6.2.2. Multipath due to Reflection *151*
6.2.2.1. General Case 151
6.2.2.2. Specific Case of PcP 152
6.2.3. Implications in Noise-Based Imaging *153*
6.3. SUMMARY AND DISCUSSIONS 155
7. CONTRIBUTIONS OF THESIS AND PERSPECTIVES FOR FUTURE WORKS 157
7.1. CONTRIBUTIONS OF THESIS 157
7.1.1. Contributions to Noise-Based Techniques *157*
7.1.2. Contributions to Noise-Based Theory and Observations *157*
7.2. ONGOING AND FUTURE WORKS 158
7.2.1. Noise-Based Deep Earth Imaging *158*
7.2.2. Compiling Catalogue of Global Microseism Events *159*

7.2.3. Exploring Microseism Datasets with Machine Learning 160

7.2.4. Global Ambient Noise Correlation Wavefield..... 160

7.2.5. Global Coda Correlation Wavefield 164

REFERENCES 171

List of Figures

Figure 1.1. Pulsatory oscillations with a period of about 6 sec recorded by a seismograph in 1898. 1
Figure 1.2. Excitation of ambient noise by coupling of atmosphere, hydrosphere and lithosphere. 2
Figure 1.3. Global maps of annual average surface net solar radiation and sea surface temperature 3
Figure 1.4. Global maps of monthly average atmospheric pressure at sea level. 4
Figure 1.5. Idealized depiction of global wind patterns. 5
Figure 1.6. Global map of annual mean 10-meter wind speed. 5
Figure 1.7. Global maps of monthly average 10-meter wind speed 6
Figure 1.8. Idealized spectrum and causes of ocean waves. 7
Figure 1.9. Global maps of monthly average significant wave height. 8
Figure 1.10. Global maps of mean significant wave height in the northern and austral winters. 9
Figure 1.11. Cartoon of water surface fluctuations and examples of 1D and 2D ocean wave spectra. 10
Figure 1.12. Examples of vertical-component continuous seismograms and spectrograms in the frequency bands of microtremor, microseism and seismic hum. 11
Figure 1.13. New low and high noise models proposed by (Peterson 1993). 13
Figure 1.14. Diurnal and seasonal variations in the power of seismic noise. 15
Figure 1.15. Schematic of the generation mechanisms for the secondary and primary microseisms. 17
Figure 1.16. Global maps of monthly average PSD of oceanic secondary microseism excitation. 21
Figure 1.17. Global maps of mean microseism excitation in the northern and austral winter half years. 21
Figure 1.18. Global continent topography and ocean bathymetry. 22
Figure 1.19. Bathymetric amplification factors for microseism Rayleigh, P and S waves. 23
Figure 1.20. Vertical acceleration spectrum from Black Forest Observatory and ocean wave height spectrum from the shelf off Florida. 30
Figure 1.21. Schematic of seismic hum excitation by the interaction of ocean infragravity waves with ocean bottom and plot of the effective pressure and shear traction inferred from cross-spectra between pairs of 618 global broadband stations. 32
Figure 1.22. Typical power spectrum and causitive forces of microseisms and seismic hum. 35
Figure 1.23. Schematic of ocean wave-wave interaction generating secondary microseisms. 36
Figure 1.24. Backprojection of microseismic body waves to locate noise source and frequency-slowness analysis of Z, R and T components of continuous seismograms at 0.15 Hz. 37
Figure 1.25. A summary over the relationships between winds, ocean waves and microseisms. 38
Figure 2.1. Body wave reflections and Rayleigh waves in the correlation functions of seismic noise recorded by the LAPNET array deployed in Finland. 43

Figure 2.2. Noise-derived phase velocity and azimuthal anisotropy of Rayleigh waves in western United States, in comparisons with the results obtained from earthquake data. 45
Figure 2.3. Noise-derived attenuations across the United States. 46
Figure 2.4. Noise-based monitoring of seismic velocity in Moon and Earth. 50
Figure 2.5. Grid-search imaging to locate noise sources for the presence of spurious surface waves in the noise correlations between a station in Europe and a network in the United States, and between a station in the United States and a network in Europe. 52
Figure 2.6. Geometry of typical configurations in seismic interferometry. 55
Figure 2.7. Signal recovery from the interferometry of coherent waves emanating from an effective source and propagate following the effective paths. 57
Figure 2.8. Interferometry of coherent waves emanating from an ineffective noise source. 58
Figure 2.9. Construction of the causal and acausal signals via source averaging for uniform and non-uniform source distributions. 59
Figure 2.10. Classification of noise sources and decomposition of ambient wavefields. 62
Figure 2.11. Examples of various types of recordings in seismograms. 63
Figure 2.12. Simplified classification of noise sources and decomposition of ambient wavefields. 64
Figure 2.13. Workflow of noise data processing. 69
Figure 2.14. Descriptive statistics of a raw seismogram. 72
Figure 2.15. Descriptive statistics of spectral-whitened seismogram. 73
Figure 2.16. Descriptive statistics of whitened and clipped seismogram. 73
Figure 2.17. An example of stationary noise with the amplitude histogram. 75
Figure 2.18. Examples of seismic noise with different types of amplitude histograms. 76
Figure 2.19. Kurtosis-based selection filter. 77
Figure 2.20. Schematic of the conventional scheme for computing correlation functions. 79
Figure 2.21. Schematic of the new scheme for calculating unattenuated correlation functions. 81
Figure 2.22. Numerical comparisons between the conventional scheme and the modified scheme. 82
Figure 2.23. General workflow of noise correlation applications 86
Figure 3.1. Ray representation of double-array interferometry 87
Figure 3.2. A cartoon depicting the Radon transform. 88
Figure 3.3. Synthetic example of Radon transform in wavefield decomposition and signal extraction. 89
Figure 3.4. Theoretical curves of traveltimes and ray parameters for typical seismic body phases. 91
Figure 3.5. Global stacks of vertical components of earthquake seismogram of 3 to 10 sec periods. 92
Figure 3.6. Global stacks of earthquake seismogram with theoretical traveltime curves. 93
Figure 4.1. Geometry of the LAPNET array in Finland and the FNET array in Japan. 95
Figure 4.2. Histogram of the inter-station distances between all FNET-LAPNET station pairs. 96
Figure 4.3. Broadband acausal and causal noise correlations between all FNET-LAPNET station pairs. 98

Figure 4.4. Broadband acausal and causal FNET-LAPNET noise correlations stacked in 0.1° bins. 99
Figure 4.5. Acausal and causal vespagrams of the annual FNET-LAPNET noise correlations. 100
Figure 4.6. Double-beamed waveforms and spectral magnitudes of the noise-derived body waves. 101
Figure 4.7. Sections of the FNET-LAPNET noise correlations filtered from 5 to 10 sec. 102
Figure 4.8. Vespagrams of the FNET-LAPNET noise correlations filtered from 5 to 10 sec. 103
Figure 5.1. Broadband and filtered acausal noise correlations between all FNET and LAPNET station pairs, aligned and windowed around the spurious phase. 106
Figure 5.2. Broadband and filtered acausal noise correlations on 2008-05-01, aligned and windowed around the spurious phase.....107
Figure 5.3. Waveform section of the acausal noise correlations on 2008-05-01. 108
Figure 5.4. Vespagram of the acausal noise correlations on 2008-05-01.....108
Figure 5.5. Double-array slowness analysis for the spurious phase. 110
Figure 5.6. Global stacks of vertical components of earthquake seismograms at 6 sec period. 112
Figure 5.7. Theoretical curves of ray parameter and traveltime with respect to distance. 113
Figure 5.8. Maps of the probability of noise source distribution. 114
Figure 5.9. Ray paths of P and PKP waves and their time delays for different noise sources. 115
Figure 5.10. Synthetic experiments of P-PKP interferometry of quasi-stationary phase. 116
Figure 5.11. Double-beamed daily noise correlations (broadband). 117
Figure 5.12. Double-beamed daily noise correlations (5 to 10 sec periods). 118
Figure 5.13. Daily variations of the spurious phase and vespagrams of classified daily correlations. 119
Figure 5.14. Global map with array locations and M7+ earthquakes in 2008. 120
Figure 5.15. Comparisons of daily spurious phase with daily microseism noise level and seismicity in New Zealand. 121
Figure 5.16. Daily directional variations in the microseismic noise level in New Zealand in 2008.....123
Figure 5.17. Bathymetry around New Zealand, bathymetric amplification factors for P-type waves, annual average of equivalent surface pressure for microseism excitation in 2008, equivalent surface pressure modulated by the bathymetric amplification factors.....125
Figure 5.18. Map of weights created from bathymetric amplification and backprojection imaging. 126
Figure 5.19. Daily variations of the spurious phase and the microseism excitation, significant wave heights and winds in the effective noise source region.. 127
Figure 5.20. Spectrogram of seismograms at station NZ.APT from 04-27 to 05-04 of 2008. 129
Figure 5.21. FK maps of secondary microseisms recorded by GEONET on 04-29 and 05-01 of 2008. 129
Figure 5.22. Evolution of the microseism event around 2008-05-01. 132
Figure 5.23. Evolution of the microseism event around 2008-05-23. 135
Figure 5.24. Evolution of the microseism event around 2008-07-31. 139
Figure 5.25. Global maps of semi-annual mean significant wave height, correlation map of the spurious

phase and wave height, and links among global wave heights. 140
Figure 5.26. Global maps of semi-annual average intensity of oceanic microseism noise sources, correlation maps of the spurious phase with noise sources, and links among global noise sources. 142
Figure 5.27. True and spurious correlations between the spurious phase and microseism excitation. 143
Figure 6.1. Vespagrams of classified daily correlations. 146
Figure 6.2. Global map of annual intensity of oceanic microseism sources. 147
Figure 6.3. Correlation map of fake P arrival with oceanic microseism sources. 148
Figure 6.4. Schematic of the expected reconstruction of inter-receiver P wave from seismic noise. 149
Figure 6.5. Schematic of the emergence of noise-derived spurious P arrival due to localized strong sources in proximity to the expected effective sources. 149
Figure 6.6. Schematic of multipath interference due to mode conversion. 151
Figure 6.7. Schematic of multipath interference for noise-derived reflections. 152
Figure 6.8. Multipath interference for the inter-station PcP wave. 153
Figure 6.9. Effects of multipath interference on noise-based reflection imaging. 154
Figure 7.1. Geographic locations of Europe stations and China stations. 158
Figure 7.2. Global sections of synthetic seismograms for a 1D lossless acoustic Earth model. 161
Figure 7.3. Synthetic global sections of acoustic noise correlations. 162
Figure 7.4. Global section of virtual seismograms retrieved from noise correlations filtered in the period band of 25 to 100 sec, in comparisons with the global section of synthetic seismograms. 163
Figure 7.5. Global sections of TT, RR, and ZZ components of cross-correlation functions. 164
Figure 7.6. Cartoon illustration of the depth-dependent attenuation structure of Earth and the propagation of fundamental-mode and higher-mode oscillations. 165
Figure 7.7. Correlation of global seismicity with noise-derived long-period body waves. 166
Figure 7.8. Global section of virtual seismograms reconstructed from continuous seismograms. 167
Figure 7.9. Modal interpretation for the ScS-like arrival in the coda correlations. 168
Figure 7.10. Ray representation of spherical mode $_{52}S_{13}$ and time evolution of the associated rays. 169
Figure 7.11. Global sections of coda correlations created from observed and synthetic seismograms. ... 170

1. Winds, Ocean Waves and Seismic Noise

The incessant oscillations present on the seismograms have been observed from the very beginning of instrumental seismology, stretching back to the 19th century when the first seismometers were installed (Dewey and Byerly 1969; Bernard 1990; Ebeling 2012). The observed faint oscillations were termed “microseisms”. Figure 1.1 displays an example of the early observations. It was found that the persistent background oscillations could be observed ubiquitously, independent of geographic location, and even during seismically quite days and under calm local weather. The discovery of microseisms immediately attracted the interests of researchers. Very sooner, microseisms were found to be not caused by instrumental resonance but related to natural phenomena such as atmosphere processes and ocean wave activities. To the mid-twentieth century, the links between ambient seismic noise and ocean waves or storms had been clear. The theory of two different excitation mechanisms, which has been applied extensively in oceanography and seismology, was established by Longuet-Higgins (1950) and Hasselmann (1963) to explain the presence of two microseism peaks in the seismic noise spectra. Later, with the rapid development and increment of seismological apparatus and advances in computation power and digital storage, practical applications with ambient noise have been prospected and implemented in various scientific subjects.

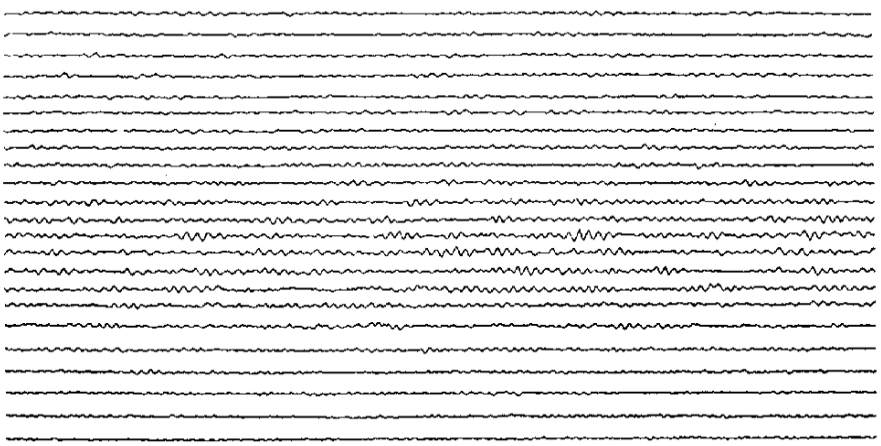

Figure 1.1. Pulsatory oscillations with a period of about 6 sec observed on September 6th and 7th, 1898, recorded by an Omori horizontal-pendulum seismograph in Tokyo. Reproduced from Journal of the College of Science, Univ. of Tokyo, 11, plate IV.

In order to have comprehensive knowledge about the nature and excitation mechanisms of the broadband spectrum of ambient seismic noise, it is necessary to consider the atmosphere, hydrosphere and solid Earth as an integrated system (Figure 1.2). In this chapter, we present introductions to global winds, ocean waves and seismic noise, along with their connections. Some illustrations in this chapter are adapted or reproduced from geophysical journal papers and oceanography textbooks like Garrison (2008) and Trujillo and Thurman (2008) published by Encyclopædia Britannica and Brooks/Cole-Thomson Learning (hereafter abbreviate the book title "Essentials of Oceanography" as EoO). The electronic versions of these figures are openly accessible from the Internet. Some figures are created from the hindcast data provided by the National Oceanic and Atmospheric Administration (NOAA), the European Centre for Medium-Range Weather Forecasts (ECMWF), and the Institut français de recherche pour l'exploitation de la mer (IFREMER).

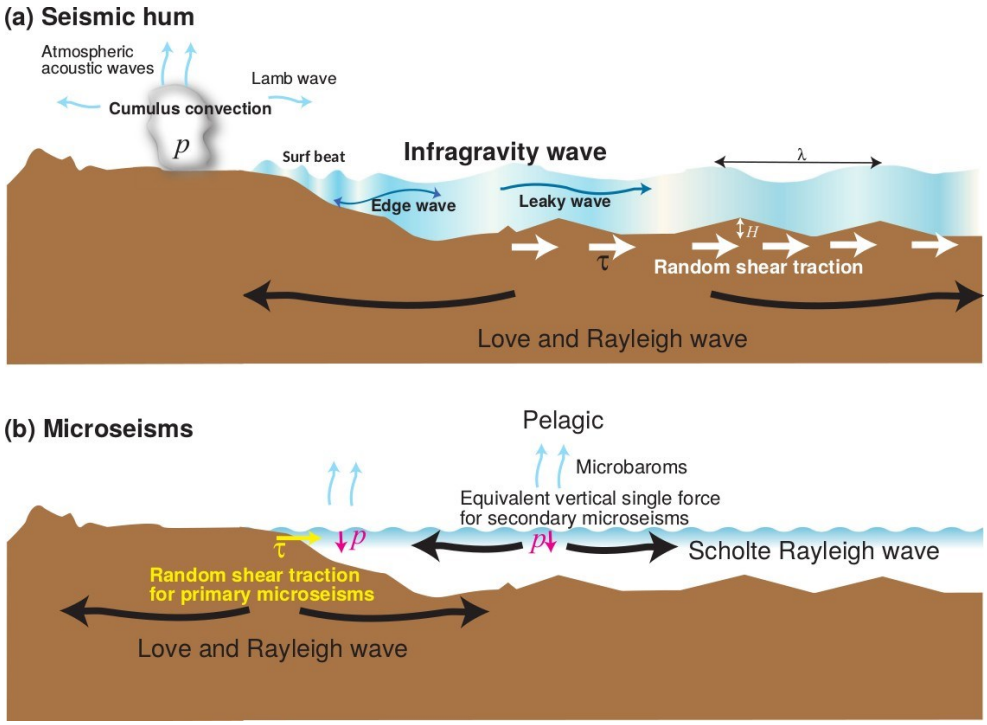

Figure 1.2. Excitation of ambient seismic noise by the coupling of atmosphere, hydrosphere, and lithosphere. (a) Schematic of the oceanic excitation of seismic hum by ocean infragravity waves (mechanism still in debate) and the atmospheric excitation of seismic hum caused by cumulus convection in the troposphere. (b) Schematic of the excitation mechanisms of the microbaroms (atmospheric infrasonic waves) and the primary and secondary microseisms. Reproduced from Figure 10 of Nishida (2017).

1.1. Global Winds

1.1.1. Driving Forces

The input of solar energy exhibits significant variations with latitudes. Surplus (Deficit) heat is received in the low-latitude (high-latitude) regions, leading to temperature gradients from the equatorial region toward the southern and northern polar regions (Figure 1.3).

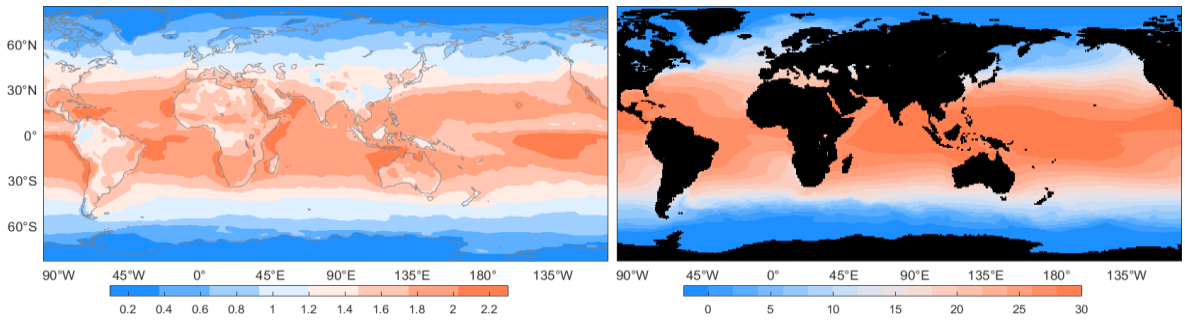

Figure 1.3. Global maps of annual average surface net solar radiation ($\times 10^7$ J·m^{-2}) and sea surface temperature (℃) in 2015 (data from ECMWF). The primary feature is the decrease of solar heating and temperature from equator to poles.

Because of the differential solar heating at low and high latitudes, differences in atmospheric pressures arise (Figure 1.4). Due to the tilt of Earth's rotation axis, the motions of Earth and the irregular distribution of continents and oceans, the global solar irradiance, temperature and atmospheric pressures are not only latitude-dependent, but also longitude-dependent and time-varying. The gradients in atmospheric pressure drive large-scale air movements called atmospheric circulations, to balance the pressure difference and transfer the surplus heat in the equatorial regions toward the polar regions. The circulations are also inevitably affected by the so-called Coriolis forces caused by the self-rotation of Earth and conservation of momentum. Typical examples of the Coriolis Effect are the counter-clockwise (clockwise) spiral of cyclones and the clockwise (counter-clockwise) deflection of the paths of cyclones in the Northern (Southern) Hemisphere. The Coriolis Effect and spiraling wind pattern can facilitate the formation of cyclones.

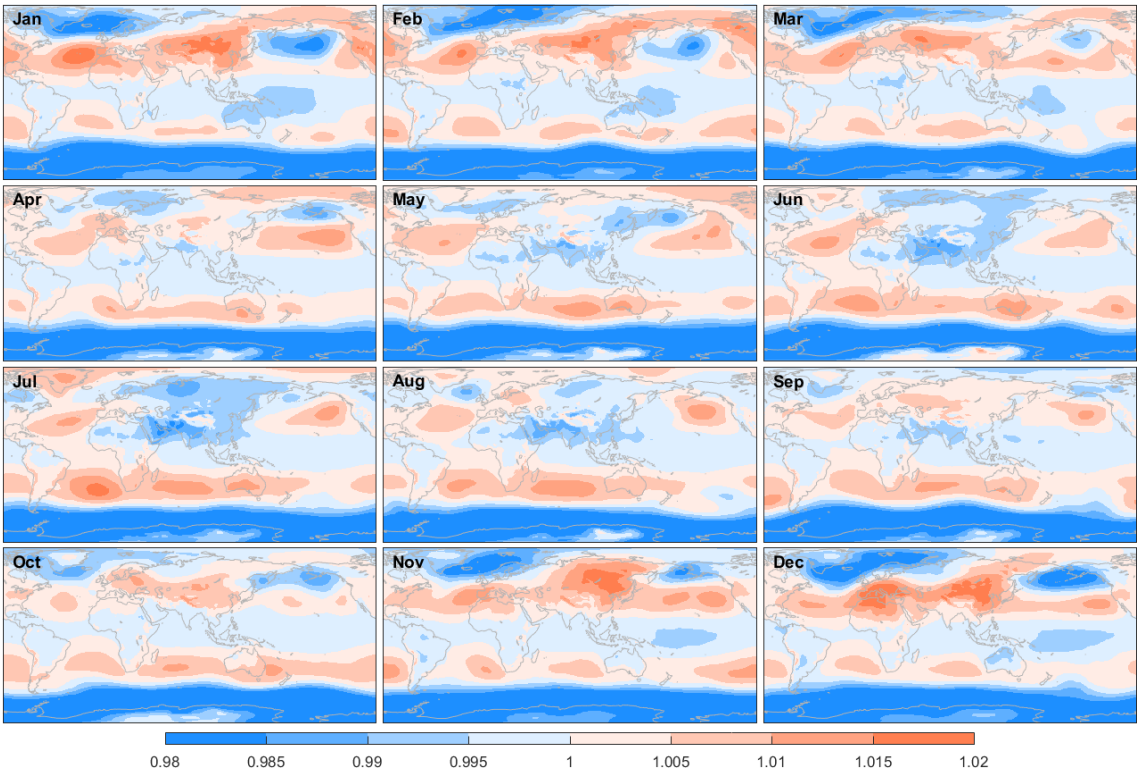

Figure 1.4. Global maps of monthly average atmospheric pressure at sea level in 2015 (data from ECMWF). The pressure is normalized by the standard atmosphere (1 atm = 101,325 Pa).

1.1.2. Global Patterns

As stated above, differential solar heating gives rise to atmospheric pressure gradients. As a consequence of the mixed effect of the pressure gradients and Coriolis forces, atmospheric circulations are driven to balance the distribution of thermal energy. The idealized pressure belts and global wind patterns are shown in Figure 1.5. The six large-scale atmospheric cells and seven pressure belts lead to three globally encircling easterly or westerly prevailing wind bands, namely, trade winds, prevailing westerlies and polar easterlies from equator toward pole in each Hemisphere. As for the real Earth, near-surface wind patterns (Figure 1.6) are further complicated by the seasonal variations in solar heating, the irregular distribution of oceans and continents, and also the land topography. On average, the strongest winds occur in the austral prevailing westerlies above the southern India Ocean. Seasonal variations of global winds are displayed in Figure 1.7. In addition to the seasonal fluctuations in wind speed, the geographic locations of the wind belts also change. The wind belts shift towards north during the northern summer and towards south during the southern summer.

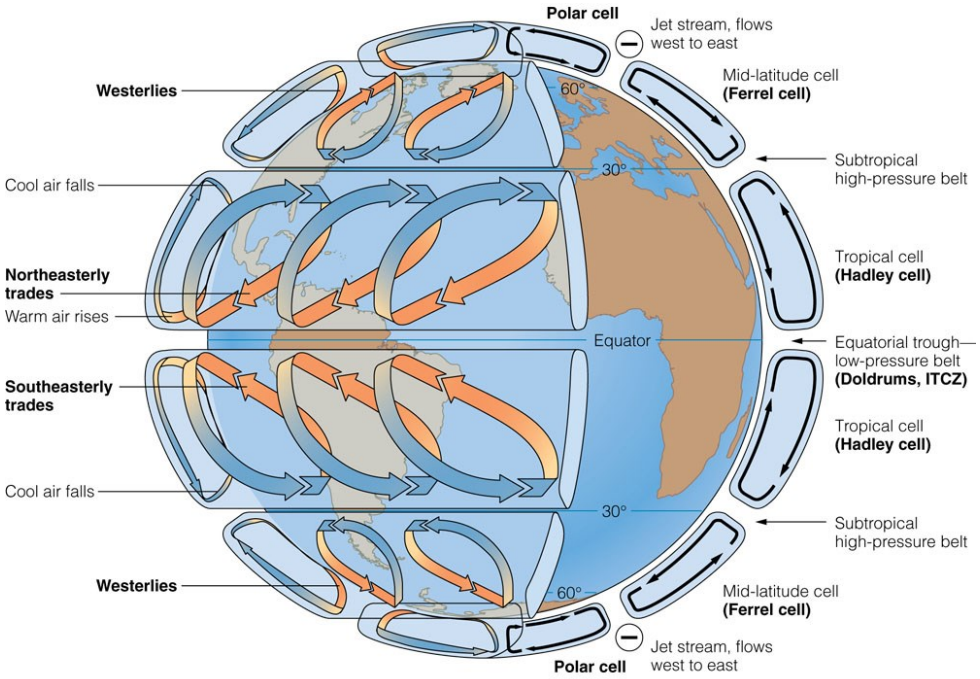

Figure 1.5. Idealized depiction of global wind patterns reproduced from EoO. Note the three-dimensionality of the circulations. There are six convection cells, three in each of the Northern and Southern hemispheres. From low to high latitudes are the Trade winds from the east, the Westerlies and the Polar Easterlies.

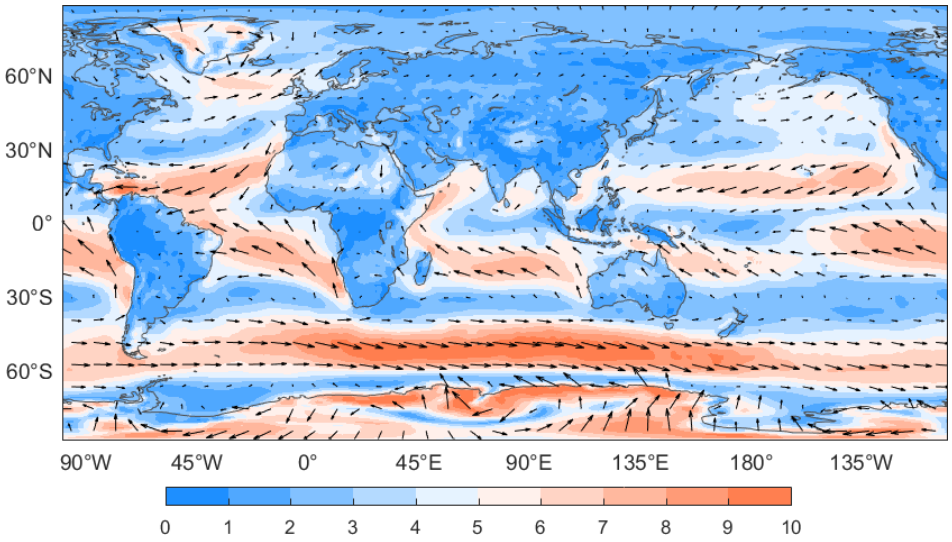

Figure 1.6. Global map of annual mean 10-meter wind speed (m/s) in 2015 (data from ECMWF). The background colored map and the arrows represent the scalar and vector averages of the wind speed, respectively.

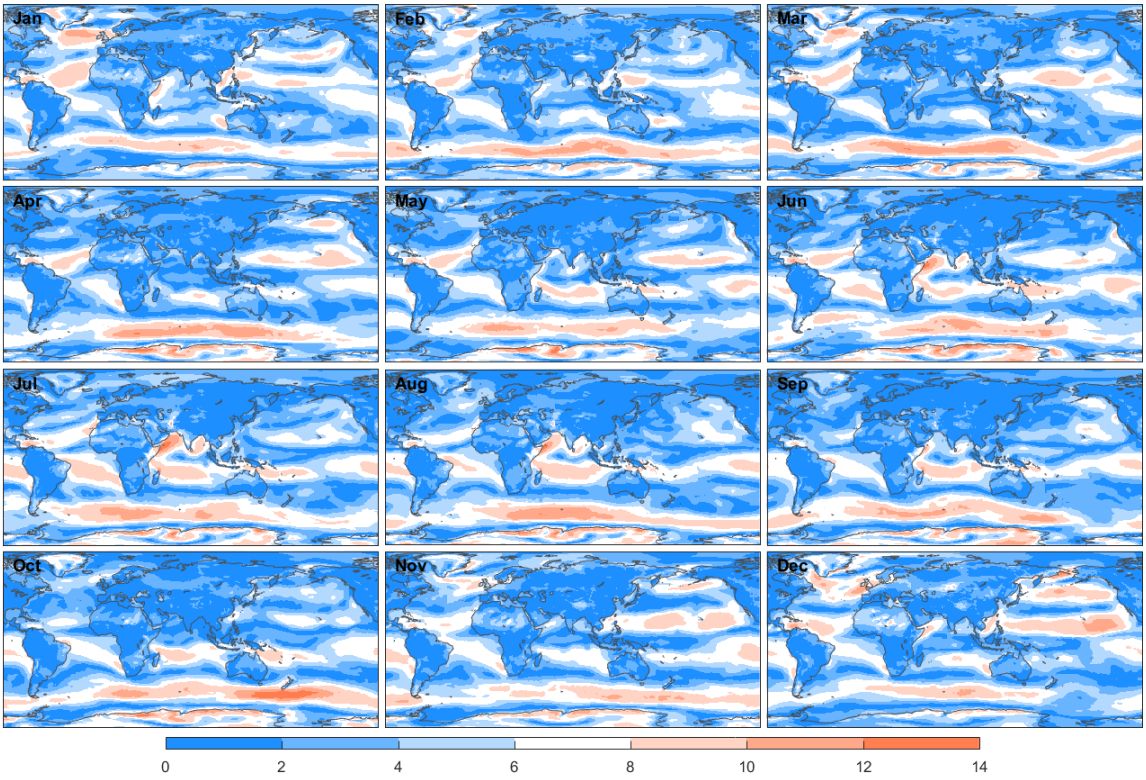

Figure 1.7. Global maps of monthly average 10-meter wind speed (m/s) in 2015 (data from ECMWF).

1.2. Ocean Waves

1.2.1. Types of Ocean Waves

Different types of ocean waves with their possible causes are summarized in Figure 1.8. Note that the boundary lines between different wave types are merely schematic, rather than being deterministic. Most ocean waves are wind-generated. When the wind blows over the water surface, the air-water interaction transmits energy from air to water and waves are formed under the frictional drag of winds. The typical order of development of ocean waves is, from ripples to wind seas, then to swells (after the wind has ceased or changed direction or the waves propagate away from the source area), and finally to surf (breaking waves when approaching the shoreline). Seas are forced waves by winds. Swells are free waves that can propagate over very long distance, even across oceans about half the circumference of Earth (Ardhuin et al. 2009). The scale of wind waves is governed by factors including wind speed, sustaining duration, and fetch length. When the wind speed increases, the ocean wave spectrum broadens

and the peak frequency decreases (Resio et al. 1999; Trujillo and Thurman 2008; Ebeling 2012). The celerity of wind waves is slower than that of the generating wind. The wave activity can be felt by the ocean bottom only in shallow water. As for waves in deep water, wave motions decrease with water depth and below the wave base (half the wave length), hardly any motions are caused by ocean waves. The wave celerity depends on both water depth and wave period.

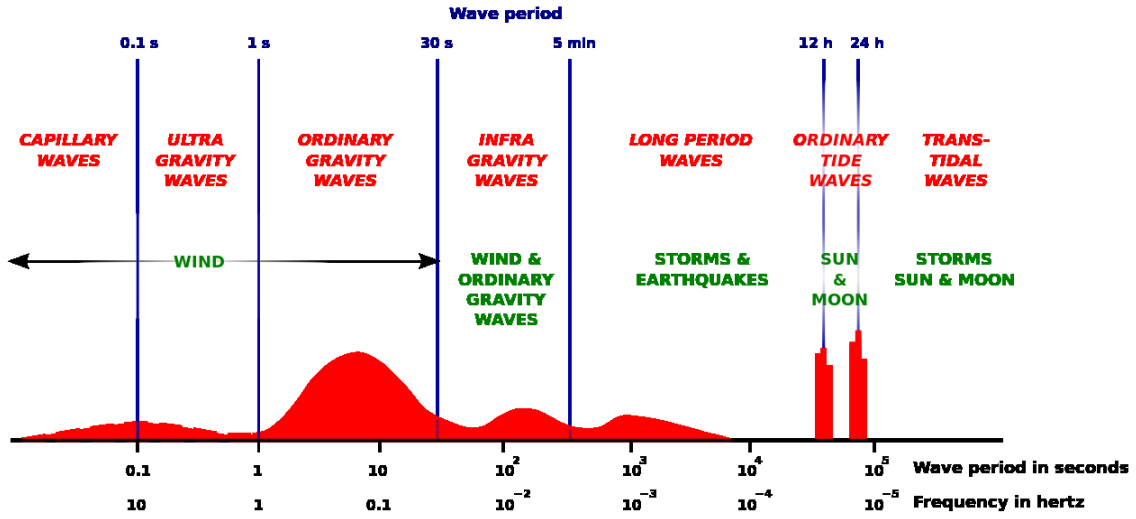

Figure 1.8. Idealized spectrum and causes of ocean waves. Reproduced from Munk (1950).

1.2.2. Global Patterns

The ocean wave height, vertical distance from crest to trough, is an important property of ocean waves and a convenient way to describe the size of ocean waves. The distribution of individual ocean wave heights can be well approximated by a Rayleigh distribution (Tayfun 1980). Because higher waves are easier to be observed and more significant in effect, it is customary to use a statistic called significant wave height, defined as the mean of the highest one-third of the waves or four times the standard deviation of the surface elevation or square root of the zeroth-order moment of the wave spectrum, measured over a stated interval of time. Other statistical measures of wave heights, such as the mean wave height and the root-mean-square wave height, are related to the significant wave height mathematically and can be mutually converted.

Storms are the main cause of significant ocean waves. In response to the geographical and seasonal variations of winds, global ocean wave height also exhibits remarkable geographic

and seasonal variations (Figure 1.9). The ocean wave activity is calm at low latitudes and energetic at mid-latitudes. In the Northern Hemisphere, the ocean activity in the north Atlantic and Pacific is most intense in winter (Dec, Jan and Feb) and weakest in summer (Jun, Jul and Aug). In a similar but anti-synchronized pattern, the ocean activity in the Southern Hemisphere also exhibits clear seasonal variations. The primary difference is that during the local summer, the wave height in the austral oceans is not as low as in the northern oceans. In contrast to the Atlantic and Pacific oceans, a unified seasonal pattern is peculiar to the Indian Ocean. The northern part of the Indian Ocean extends into the Northern Hemisphere, but note that the Indian Ocean is closed by circumjacent continents on the northern side. The northern Indian Ocean is governed by monsoons, rather than by the large ocean storms during the Northern Hemisphere winters as in Atalantic and Pacific.

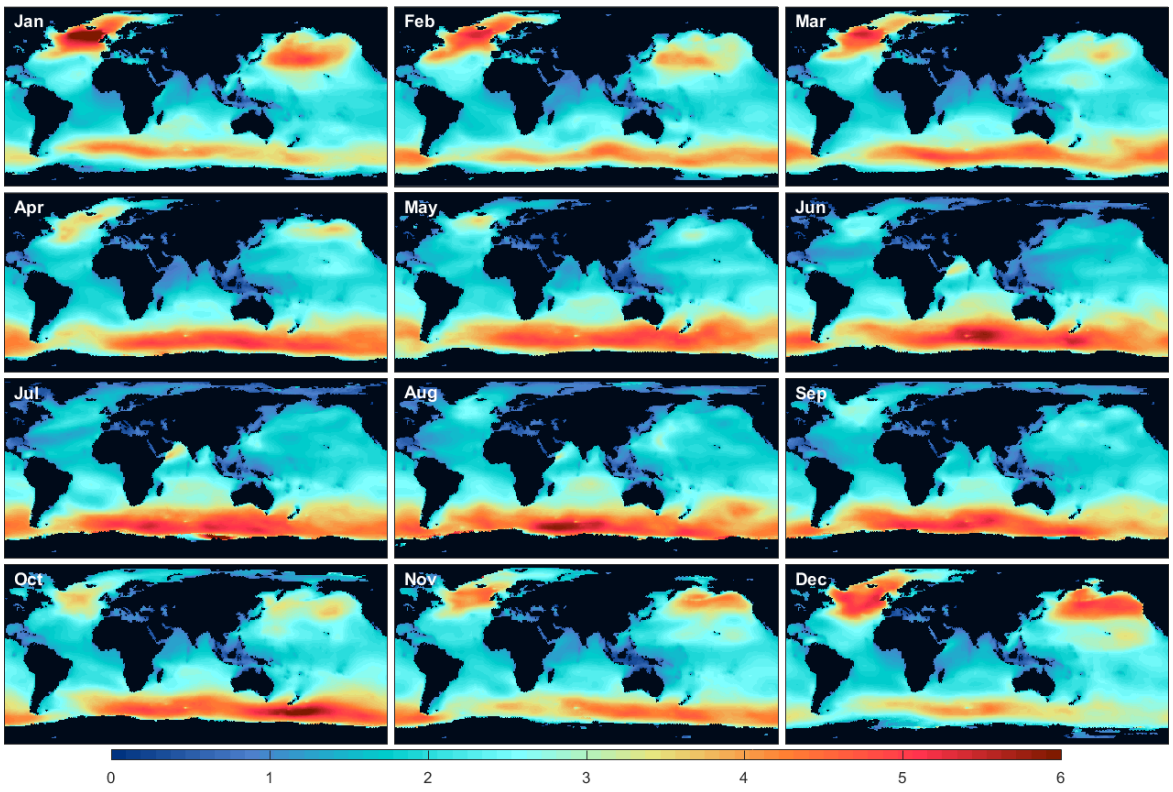

Figure 1.9. Global maps of monthly mean significant wave height (m) in 2015 (data from ECMWF).

Taking April to September as the austral winter half year and October to March as the northern winter half year, we average the global wave heights in these two half years and show the maps in Figure 1.10. During the northern winter, the wave activity is most intense in the North Pacific south of the Aleutian Islands and in the North Atlantic south of Greenland and Iceland. In the

Southern Hemisphere, intense wave activity circumscribes the Antarctic at around 50°S all through the year but more energetic during the southern winter. The annual average significant wave height (about 5 m) is highest in the southern Indian Ocean (see also "Science On a Sphere" established by NOAA at https://sos.noaa.gov/), in response to the highest annual mean wind speed in the austral westerlies (Figure 1.6).

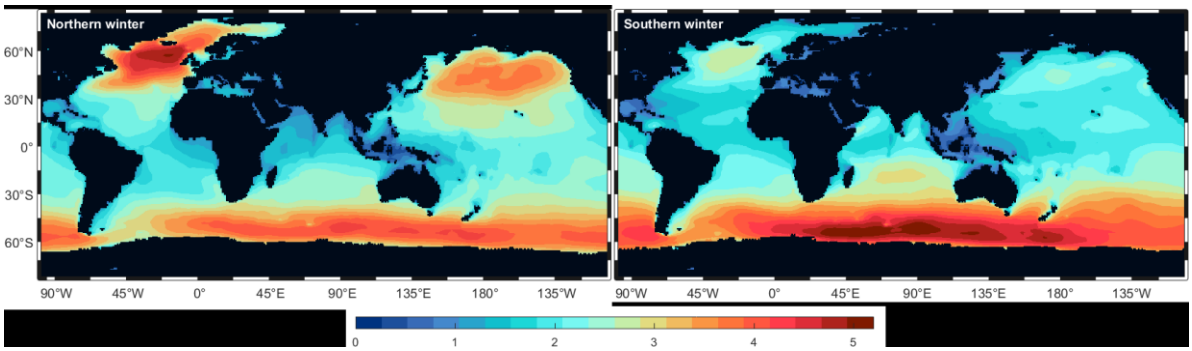

Figure 1.10. Global maps of mean significant wave height (m) in the northern and austral winter half years of 2015 (data from ECMWF).

1.2.3. Ocean Wave Spectra

The wind, the duration, the fetch, the water depth, together with the distribution of obstacles determine the height, peak period and propagation direction of waves (Young 1999a). Wind waves typically appear in a certain degree of randomness. Subsequent waves differ significantly in height, period and duration with little predictability. The sea state can be described as a superposition of waves of varying frequencies propagating in different directions (Figure 1.11). Mathematically, a comprehensive representation of the sea state is the two-dimensional direction-frequency spectra or directional wave spectra, which can be expressed in the form of $E(f,\theta) = S(f) \cdot D(f,\theta)$ with $S(f)$ the 1D spectrum of ocean waves describing the distribution of energy with respect to frequency and $D(f,\theta)$ the probability distribution function or directional spreading function in terms of frequency and propagation direction. The frequency spectrum $S(f)$ can be approximated by various empirical relationships like the modified Pierson-Moskowitz spectrum, the JONSWAP spectrum, the Ochi-Hubble spectrum, the Torsethaugen spectrum and the Gaussian Swell spectrum. The directional spreading function $D(f,\theta)$ is generally assumed to be trigonometric functions of propagation direction.

Ocean wave spectra can be obtained from in-situ measurements of buoys, ships and oil platforms, or inferred from observations of satellite altimetry and synthetic aperture radar from space. Statistical wave parameters like wave height, period and propagation direction, can all be derived from the ocean wave spectra. Wave hindcast and forecast can be achieved by numerically solving the wave action equations with spectral decomposition of sea states, for instance, the WAM model adopted by ECMWF and the WAVEWATCH III model adopted by IFREMER and NOAA. The accuracy of wave models depends on the numerical methods solving the wave action equations and the quality of inputs, including forcing fields (such as winds, currents, sea ice, bathymetry, bottom roughness) and parameterizations for wave growth and dissipation. Errors in the numerical modeling are generally largest at shallow waters due to the coarse discretization of coastlines (Rascle et al. 2008). The microseism excitation can be modeled from the ocean wave spectra (Longuet-Higgins 1950; Hasselmann 1963; Ardhuin and Herbers 2013).

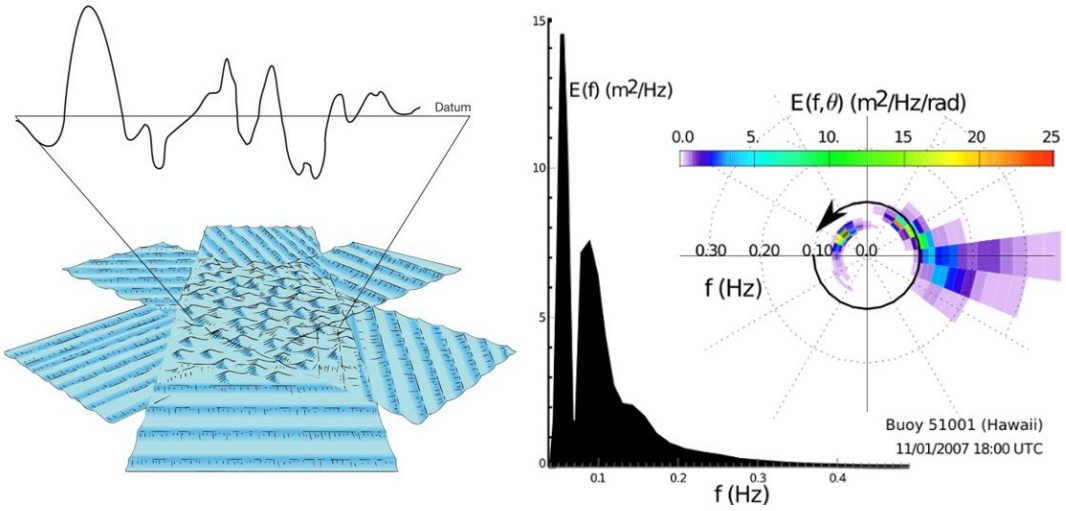

Figure 1.11. Left: fluctuations of water surface comprising waves of different frequencies propagating in varying directions (reproduced from EoO). Right: an example of 1D frequency spectrum and an example of 2D directional spectra of ocean waves from buoy recordings off Hawaii (reproduced from IFREMER webpage https://tinyurl.com/yddwvujp).

1.3. Seismic Noise

Seismic noise are man-made or caused by natural phenomena. Anthropogenic causes include human motions (Peck 2008), moving vehicles (Nakata et al. 2011; Behm and Snieder 2013;

Behm et al. 2014; Riahi and Gerstoft 2015), running trains and subway (Sheen et al. 2009; Nakata et al. 2011; Quiros et al. 2016; Green et al. 2017), flying helicopters (Riahi and Gerstoft 2015; Eibl et al. 2017), industrial production (Cara et al. 2010), etc. Natural causes include gust

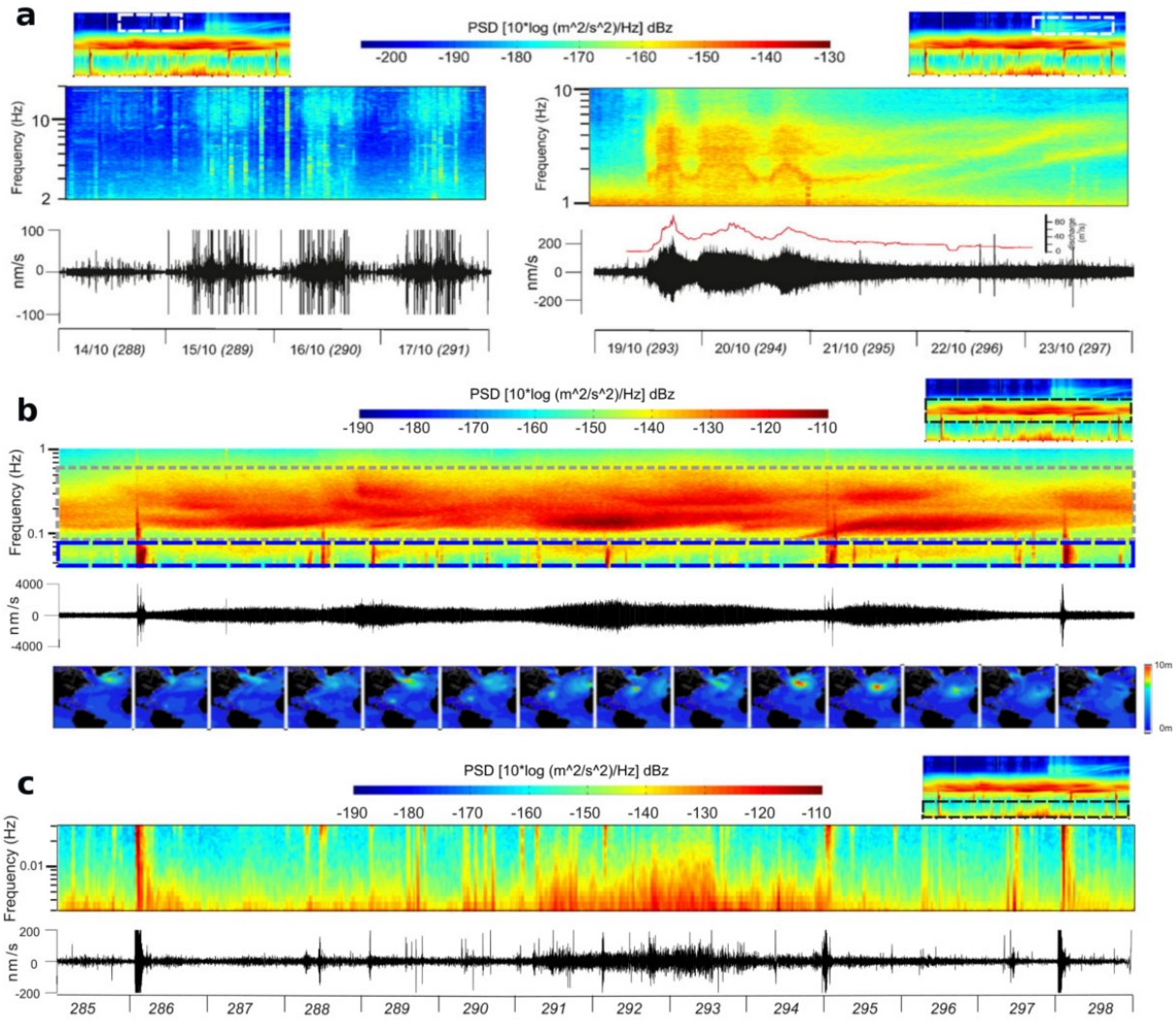

Figure 1.12. Vertical components of a two-week-long continuous seismogram (October 11-24, 2012) with corresponding spectrograms in the frequency bands of microtremor (a), microseism (b) and seismic hum (c). The data were recorded by a broadband station (LC.CANF) located in the Central Pyrenees (42.764°N, 0.517°W). The station is installed in a tunnel at a depth of 350 m and hence benefits from a lower level of cultural noise. The spike-like signals correspond to earthquakes. In (a), on the left, the cultural noise shows diurnal variations, and on the right, the spindle-like waveforms are generated by the discharge of a river about 350 m away from the station, after a significant rainfall episode (represented by the red curve). In (b), the smoothly changing amplitudes correspond to ocean wave activities in different regions of the Atlantic. Adapted from Figures 2 and 3 of Díaz (2016).

(Hu et al. 2017), tornado (Tatom and Vitton 2001; Valovcin and Tanimoto 2017), thunder (Lin and Langston 2007, 2009), temperature changes (Hillers and Ben-Zion 2011; Larose et al. 2015), torrential and fluvial processes (Hsu et al. 2011; Burtin et al. 2016; Roth et al. 2017), lake waves (Xu et al. 2017), ocean waves (Longuet-Higgins 1950; Haubrich and McCamy 1969; Cessaro 1994; Ardhuin et al. 2011), etc. Seismic noise contains information about the characteristics of noise sources and the properties of the hosting media, thereby valuable in many applications like surveying cultural activities, subsurface tomography, monitoring underground water table and fluvial processes, assessing wind and coastal wave energy, tracking storms, inferring wave climate, to cite only a few. Seismic noise originating from diverse sources can have different characteristic frequencies. Conversely, seismic noise with specific frequency content may have typical dominant causes. A real-data example is provided in Figure 1.12, gathering broadband seismic noise caused by traffic transportation, storms and ocean waves, distant and local earthquakes, and nearby river discharge.

1.3.1. Noise Spectrum

Ambient seismic noise can be deemed as a stationary stochastic process having an undefined phase spectrum (Bormann and Wielandt 2013), with significant variability in frequency content which is time-dependent and site-dependent. The amplitude of surface-recorded seismic noise is typically in the orders of 0.1 to 10 μm. Various noise models have been derived from seismic records to describe the variations of ground particle displacement, velocity or acceleration with seismic frequency or period. The noise model proposed by Brune and Oliver (1959) was ever the most popular reference for vertical component of ambient noise in the period range from 0.01 to 20 sec. The ground velocity spectral model proposed by Haubrich (1965) derived from stations near the coast, covered the period range from 2 to 200 sec. Fix (1972) established a very broadband noise model for a period range of 0.1 to 2560 sec, for both vertical and horizontal components, by using seismic recordings from a very quiet seismic station deployed in depth. Peterson (1980) derived noised models from seismic recordings of two stations only. Peterson (1993) provided a updated version of the noise models on the basis of continuous seismograms of 75 global broadband stations, which have been widely accepted as the standard curves for generally expected limits for the power spectral density (PSD) of seismic noise (Figure 1.13). As envelopes of seismic noise power spectra, the upper and lower envelope curves are generally referred to as the New High Noise Model (NHNM) and the Low Noise

Model (NLNM), respectively. The displacement power spectrum of ambient noise varies enormously from short to long periods. The dynamic range of the NLNM is ~260 dB for displacement (equivalent to 13 orders of magnitude in amplitude) in the period range of seismological interests. The range is reduced to ~130 dB for velocity power spectrum and to 50 dB for acceleration power spectrum. The noise models have been further updated by other authors with more recent data, for instance, the GSN Low Noise Model proposed by Berger et al. (2004). However, the NLNM and NHNM models proposed by Peterson (1993) are still the noise models most widely in use. Investigating the statistical characteristics of background seismic noise spectra is valuable for evaluating the performance of seismic stations, detecting operational problems, estimating the magnitude threshold of event detection, and optimizing the deployment of seismic networks (McNamara and Buland 2004; Vassallo et al. 2012; Möllhoff and Bean 2016; Hutt et al. 2017).

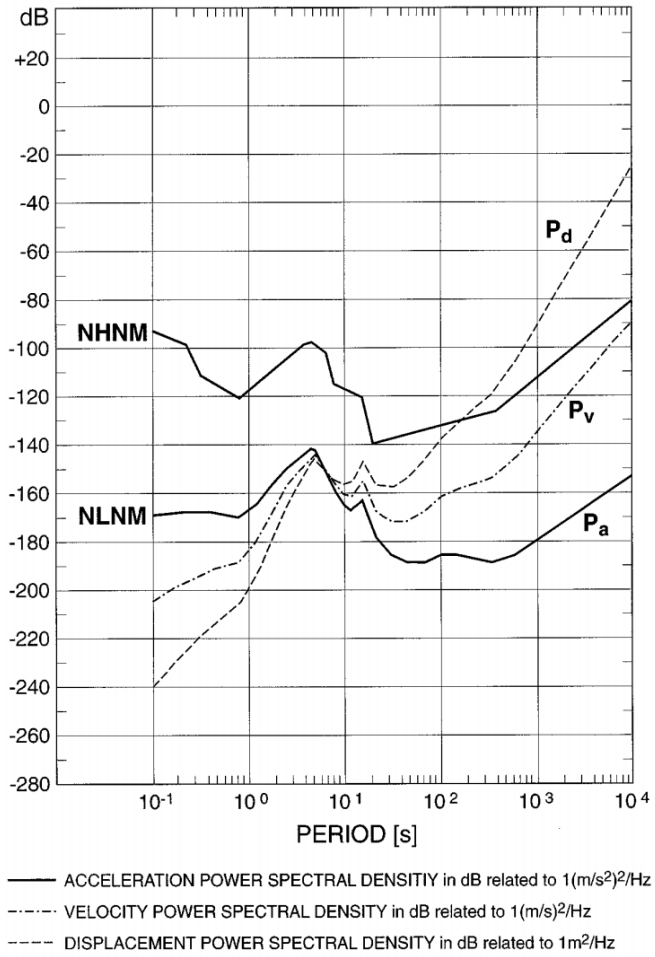

Figure 1.13. New low and high noise models proposed by Peterson (1993) for the power spectral density (PSD) of ground displacement, velocity and acceleration, derived from seismic noise recordings of 75 global stations. Reproduced from Figure 2 of Bormann (1998).

The spectrum of seismic noise can be classified into microtremor, microseism and seismic hum, from shorter to longer periods. Based on the typical frequencies, microseism can be further divided into the primary microseism and the secondary microseism. However, due to the large spatiotemporal variability in the frequency contents of noise spectra, the boundaries between different types of seismic noise are inherently vague. The definition of the frequency (period) bands for the classifications of seismic noise is more or less subjective and varies in different literature. The period of microtremor is generally shorter than 1 or 0.5 sec. The lower limit of the period of the secondary microseism ranges from 1 to 5 sec. The upper limit, which is also the boundary between the primary and secondary microseisms, varies from 8 to 12 sec and is commonly accepted to be 10 sec. The upper limit of the period of the primary microseism typically varies from 20 to 30 sec, and sometimes to 50 sec. The seismic hum starts from a period of 30 or 50 sec and ends at a period of hundreds or even thousands of seconds. Detailed introductions to different types of seismic noise are present in the following subsections.

1.3.2. Microtremor

1.3.2.1. Origins

The ambient vibrations at short periods below 1 sec, also referred to as microtremors, are generally man-made in inhabited regions, for example, by road traffic (Peck 2008; Behm and Snieder 2013; Riahi and Gerstoft 2015; Green et al. 2017; Albert and Decato 2017), vibrating heavy machinery (Bokelmann and Baisch 1999; Cara et al. 2010; Albert and Decato 2017), and swinging tall buildings (Cornou et al. 2004). The amplitude of short-period ground motions is generally in the orders of 0.01 to 1 μm. Under urban environments, the amplitude could be higher and exhibits significant site and time variability (Groos and Ritter 2009; Green et al. 2017; Albert and Decato 2017). The urban seismic noise is usually dominated by traffic noises with peak frequencies below about 25 Hz (Albert and Decato 2017) and exhibits conspicuous temporal and spatial variations, which is generally non-stationary and non-Gaussian (Groos and Ritter 2009; Steim 2015). Microtremors can also be caused by local meteorological factors such as winds (Carter et al. 1991; Vassallo et al. 2012), breaking waves (Poppeliers and Mallinson 2015) and temperature changes (Hillers and Ben-Zion 2011). The natural causes, especially winds, dominant in uninhabited areas. The wind-induced noise is wide-band, ranging from about 0.5 Hz up to about 15 to 60 Hz (Bormann and Wielandt 2013). Generally,

the short-period noise in urban and suburban regions is louder than in remote regions.

1.3.2.2. Spatiotemporal Variability

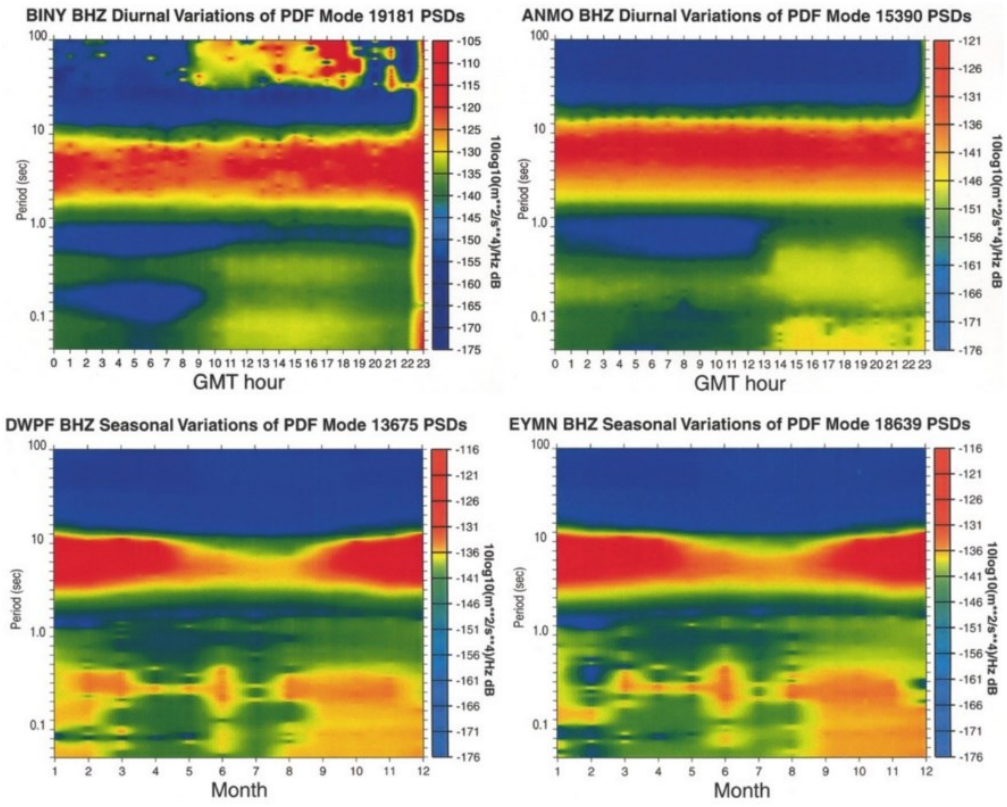

Figure 1.14. Examples of diurnal (upper) and seasonal (lower) variations in the power of seismic noise, reproduced from Figure 9 of McNamara and Buland (2004).

Due to the predominance of cultural origins, microtremors typically exhibit strong diurnal variations (McNamara and Buland 2004; Vassallo et al. 2008, 2012; Groos and Ritter 2009; Evangelidis and Melis 2012; Díaz 2016; Green et al. 2017), reaching the maximum (and exhibiting larger variations) during the daylight hours and the minimum during the night hours (see Figure 1.12 and Figure 1.14 for examples), and also probably weekly variations (Bonnefoy-Claudet et al. 2006; Green et al. 2017), louder on workdays and quieter during weekend. Observations of seasonal variations have also been reported (McNamara and Buland 2004; Koper and de Foy 2008; Hillers and Ben-Zion 2011). Since cultural and natural noise sources are predominantly located on the surface, microtremor noise amplitudes are higher and exhibit larger time variability near the surface than at depth (Carter et al. 1991; Bormann and Wielandt 2013; Hutt et al. 2017), such that installing seismometers at depth in boreholes, deep

caves, and tunnels can improve the capability of event detection. Short-period noise is generally much lower at seafloor than on land and thereby, a lower detection threshold is expected at ocean-bottom stations than at on-land stations (Vassallo et al. 2008).

1.3.2.3. Applications

Microtremor observations can provide useful information on dynamic properties of buildings and sites such as resonant frequencies, and thus can be employed in applications such as seismic microzonation (Nakamura 1989), soil classification and site effect evaluation (Bonnefoy-Claudet et al. 2006), and building health monitoring (Snieder and Şafak 2006; Nakata and Snieder 2014; Guéguen et al. 2017). Aki (1957) proposed a spatial autocorrelation method (SPAC) to evaluate the phase velocities of surface waves in shallow subsurface from noise recordings. The method was extended to attenuating media by Prieto et al. (2009). Claerbout (1968) proved that the reflection response of a horizontally layered structure can be synthesized from the autocorrelation of its transmission response. Capon (1969) proposed a modified formation for the frequency-wavenumber (FK) spectrum analysis. Nakamura (1989) proposed the horizontal-to-vertical spectral ratio (HVSR) method to derive resonance frequencies of sites responsible for seismic amplification during earthquakes. The HVSR method can also be used to derive shear wave velocity profile of shallow subsurface (Picozzi 2005; Cara et al. 2010; García-Jerez et al. 2016). Louie (2001) developed a so-called refraction microtremor (ReMi) technology which has been widely used in shear wave profiling and determining Vs30 or Vs100 for earthquake site response. More comprehensive review is provided by Okada (2003), Bonnefoy-Claudet et al. (2006) and (Lunedei and Malischewsky (2015). Many techniques originally proposed for imaging shallow structure using microtremors, are also applicable to microseisms (Tanimoto and Alvizuri 2006; Harmon et al. 2008; Ekström et al. 2009; Langston et al. 2009; Gal et al. 2014) and seismic hums (Tanimoto and Rivera 2008).

1.3.3. Microseism

The most striking peaks between 1 and 30 sec periods in the NLNM curve are termed microseisms. The presence of incessant microseisms on the seismograms was one of the phenomena observed and investigated from the very beginning of instrumental seismology. The earliest seismographs had already been able to record the background ground motions at a

predominant period of about 6 ± 2 sec (Figure 1.1). Later, it was found that the generation of microseisms are linked to storms and ocean wave activities. It was also recognized that one should discriminate two types of microseisms (Figure 1.15): a dominant noise peak at around 6 ± 2 sec period and a smaller noise peak at around 14 ± 2 sec period. Dominant periods of microseisms are linked to the characteristic periods of ocean waves. Spectral amplitudes of ocean waves and the consequent microseisms decline rapidly at periods longer than 25 sec (Bromirski et al. 1999; Bromirski 2002). Statistically, microseisms are long-continuing oscillations homogeneous over hours as ocean waves are. The amplitude of microseisms, typically in the orders of 0.1 to 10 μm, is commonly assumed to be stationary over time, with a histogram approaching a normal distribution (Haubrich 1965; Peterson 1993; Bormann and Wielandt 2013; Steim 2015).

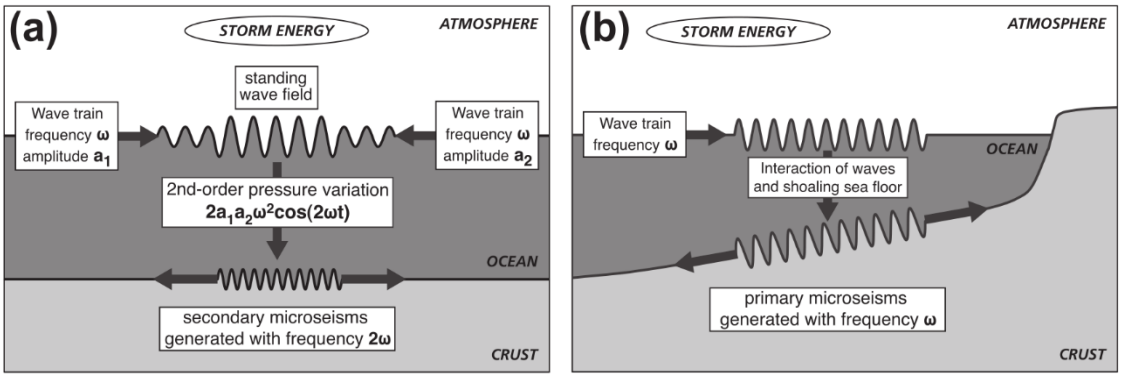

Figure 1.15. Cartoons explaining the generation mechanisms for the secondary (a) and primary (b) microseisms. Reproduced from Figure 1.7 of Ebeling (2012). Note that, more precisely, secondary microseisms are produced by interactions between waves with slightly different wave numbers instead of exactly equal and opposite wave numbers (Hasselmann, 1963).

1.3.3.1. Primary Microseism

The weaker microseism noise peak with longer periods, usually called the primary microseism, can be explained by the nonlinear interactions between ocean waves and bathymetry (Figure 1.15b), which transforms ocean wave energy into seismic energy. The generated microseisms have the same periods as the ocean waves, thereby also called single-frequency microseisms. Primary microseism energy decays rapidly from coast stations to inland stations (Haubrich and McCamy 1969). Since the pressure fluctuation caused by ocean surface gravity waves decays

exponentially with depth and vanishes below half the wavelength of the ocean wave, primary microseisms can only be generated in shallow waters. In other words, noise sources generating primary microseisms are typically located in coastal regions. In the center of continents or ocean basins, the primary microseisms are related to remote coastal waves (Cessaro 1994). The first detailed theory for the generation mechanism of primary microseisms was provided by Hasselmann (1963), assuming simplified model geometry with straight shoreline and constant slope. The theory was extended to slowly varying slopes by Ardhuin et al. (2015) but for seismic hum. Recently, Ardhuin (2018) extended the theory of Saito (2010), which was proposed to explain the origin of long-period Love waves, to explain the excitation of primary microseisms by considering both horizontal and vertical forces caused by the interaction of surface gravity waves with a wavy bathymetry. The primary microseism appears less sensitive to the incident angles of swell and the geometry of coastlines compared to the secondary microseism (Aster et al. 2010).

1.3.3.2. Secondary Microseism

The larger microseism noise peak with shorter periods, usually called the secondary microseism, is generally also the largest peak in the seismic noise spectra. The excitation of secondary microseisms is associated with the interactions between ocean waves with nearly equal frequencies but traveling in nearly opposite directions (Miche 1944; Longuet-Higgins 1950; Hasselmann 1963, 1966; Ardhuin and Herbers 2013). The standing waves are unattenuated with depth, leading to second-order pressure perturbations at the ocean bottom, which can be equivalent to vertical random forces applied to the free surface of water layer (Longuet-Higgins 1950; Hasselmann 1963). The excited microseisms have a frequency twice that of the ocean waves, thus also called double-frequency microseisms. An opposing pair of wave trains exciting the secondary microseisms could be swell from one storm meeting waves with the same period from another storm, or close to the coast due coastal reflections (Friedrich et al. 1998; Ardhuin et al. 2011). As for a fast-moving cyclone, the opposing pair could be the back-propagating waves driven by the cyclone and the forward-propagating swell generated earlier by the cyclone (Longuet-Higgins 1950; Ardhuin et al. 2011; Ebeling 2012; Bormann and Wielandt 2013; Farra et al. 2016). Due to their different excitation circumstances, the source regions for primary and secondary microseisms could be quite different. The location of secondary microseismic noise sources can be either coastal (Haubrich et al. 1963; Bromirski

2002; Essen et al. 2003; Schulte-Pelkum et al. 2004; Gerstoft and Tanimoto 2007; Yang and Ritzwoller 2008; Zhang et al. 2010a) or pelagic (Haubrich and McCamy 1969; Cessaro 1994; Bromirski et al. 2005; Kedar et al. 2008; Landès et al. 2010; Obrebski et al. 2012; Beucler et al. 2015; Liu et al. 2016a; Farra et al. 2016; Meschede et al. 2017), a consensus achieved in recent years. However, the relative contributions of coastal and pelagic sources are still not conclusive (Bromirski et al. 2013; Ying et al. 2014; Gualtieri et al. 2015). Bromirski (2001) advocated that the dominant source for the secondary microseism during the lifetime of two Atlantic storms is near the coast, instead of in the open ocean where the wind speed and ocean wave height are highest. Bromirski et al. (2005) proposed that secondary microseisms with periods longer than 5 sec are excited at coastal regions and the shorter periods are generated in open waters. Stutzmann et al.(2012) modelled seismic noise surface waves in various environments and showed that the major microseisms are generated in deep water, whereas coastal reflections generate numerous minor sources. Ying et al. (2014) concluded that land-observed microseisms are largely generated in shallow water on continental shelves. Gualtieri et al. (2015) claimed that land-recorded secondary microseisms for periods longer than 6 sec are mostly due to sources in deep waters and for shorter periods in relatively shallow water close to the shelf break. Davy et al. (2015) counted Rayleigh waves detected from the polarization analysis of seismic noise in the primary and secondary microseismic bands, and found that the secondary microseismic Rayleigh waves at most stations in and around the Indian Ocean they analyzed stemmed from distant sources in deep ocean but a station in western Australia was primarily affected by nearby coastal sources. They also observed that the Rayleigh-wave detection ratio was almost constant in the primary microseism band throughout the year, in contrast to the prominent seasonal variations in the secondary microseism band. Secondary microseism noise levels at near-coastal ocean bottom stations are consistently much higher than at coastal stations (Bromirski 2002), suggesting that the mode energy trapped in the water column dominate in the microseism spectrum at near-coastal ocean bottom. The average noise level at stations on the islands is typically much higher than on the mainland (Evangelidis and Melis 2012). Site geology is also a key factor controlling the noise amplitude (Koper and Burlacu 2015).

The power of secondary microseism sources can be modeled from the directional spectra of ocean waves according to the theory provided by Longuet-Higgins (1950) and Hasselmann (1963). Seismic spectra can then be modeled from distributed noise sources (Kedar et al. 2008; Ardhuin et al. 2011; Ardhuin et al. 2012; Ardhuin and Roland 2012; Hillers et al. 2012;

Stutzmann et al. 2012; Gualtieri et al. 2013; Ardhuin and Herbers 2013; Obrebsji et al. 2013; Farra et al. 2016). Ocean waves are composed of numerous wave trains in a wide frequency range and propagating in all directions (Figure 1.11). It is expected that there are always some opposing pairs of wave trains which excite microseisms. However, the excitation of secondary microseism is strongest only when there is a significant amount of gravity wave energy traveling in opposite directions, which means, an extreme wave height is not necessarily guaranteed to produce intense microseisms, providing that the wave train coming from the opposing direction is too weak.

Figure 1.16 shows the monthly global maps of the PSD of the secondary microseism excitation in 2015. Compared with the monthly wave heights in Figure 1.9, the intensity of microseism excitation exhibits a similar latitude-dependent distribution pattern, weak in low-latitude regions and strongest in mid-latitude oceans. Moreover, conspicuous seasonal variations in the microseism excitation can be seen from Figure 1.16, strongest in the northern and southern hemispheres during their own local winters and weakest during local summers. Besides the prominent geographic and seasonal variations, diurnal variations in microseisms can sometimes be observed, like at coastal stations due to the sea-land breeze. There are also obvious discrepancies between geographic patterns of wave height and microseism excitation, especially in the southern oceans. The longitudinal variations are more intense in microseism excitation than in wave height. The wave height in the North Indian Ocean shows a similar seasonal variation as in the Southern Hemisphere, whereas the microseism excitation is weak all through the year. The microseism excitation in the Northwest Pacific shows a pattern of moderate to strong strength in some months (e.g., August), which is not obvious for wave height. Integrating the monthly maps into maps for the northern and southern winter half years (Figure 1.17), it can be seen that the most intense regions of modeled microseism sources are in the North Atlantic south of Greenland and Iceland and the North Pacific between Japan and Alaska during the northern winter, and in the South Pacific between New Zealand and Antarctic during the austral winter. In contrast, the highest wave height occurs in the South Indian Ocean (Figure 1.10). Comparing wave height in Figure 1.9 and microseism excitation in Figure 1.16, one can easily find examples of large wave heights but with faint microseism excitations, or of strong microseism excitations but with wave height not so exceptional. These observations are not surprising according to our previous discussions. The maps shown in this section are raw PSD values of equivalent surface pressures. The intensity of microseism excitation can be significantly modified by the resonant effect in the water column, as will be introduced later.

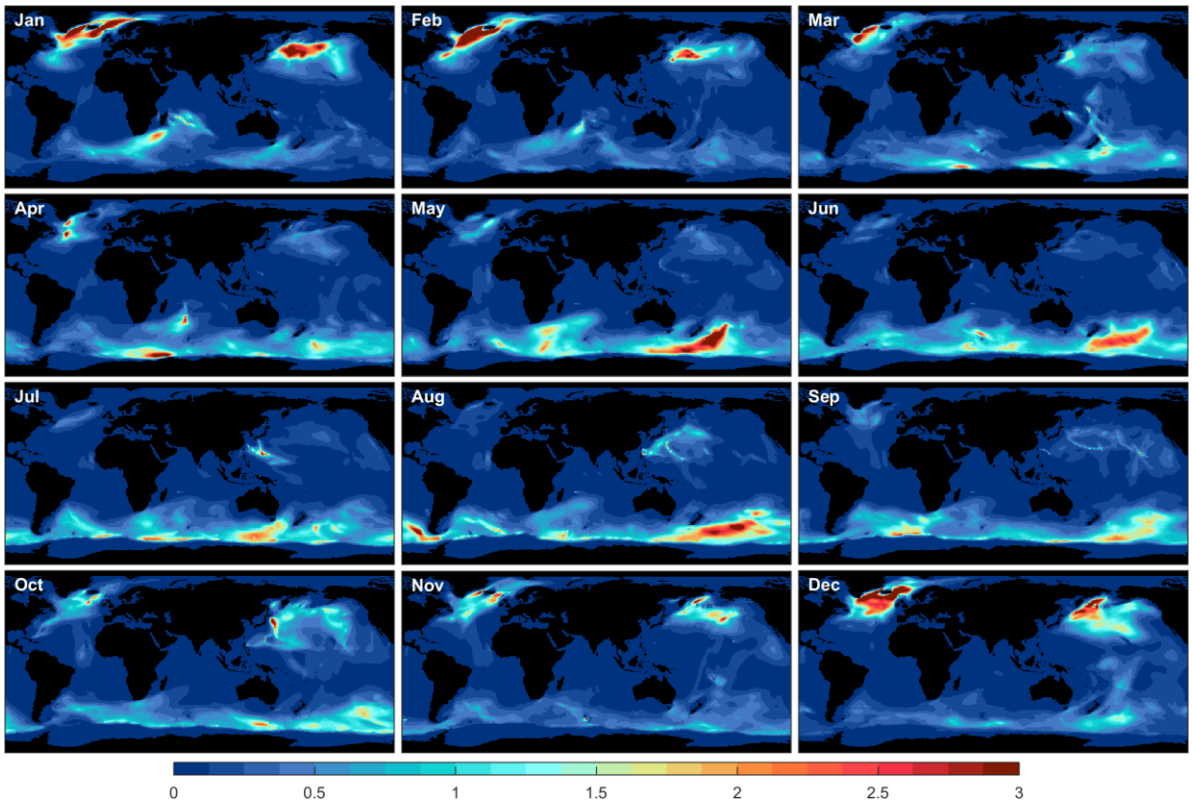

Figure 1.16. Global maps of monthly mean PSD of equivalent surface pressure ($\times 10^8$ $Pa^2 \cdot m^2$) for secondary microseism excitation in 2015 (data from IFREMER).

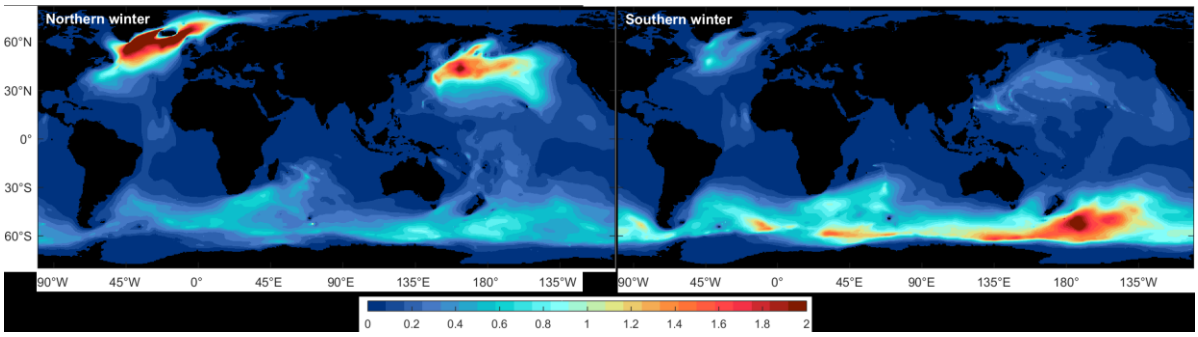

Figure 1.17. Global maps of the mean PSD of equivalent surface pressure ($\times 10^8$ $Pa^2 \cdot m^2$) for the northern (upper) and austral (lower) winter half years of 2015 (data from IFREMER).

1.3.3.3. Effects of Bathymetric Modulation

The depth of oceans varies significantly, with an average about 3.7 km and a maximum near 11 km at the Mariana Trench in the Pacific Ocean. The bathymetry from the ETOPO1 model

(Amante and Eakins 2009) is shown in Figure 1.18. The bathymetry plays an important role in amplifying or attenuating the microseism waves at source sites, for both surface waves (Longuet-Higgins 1950; Kedar et al. 2008; Ardhuin and Herbers 2013) and body waves (Ardhuin and Herbers 2013; Obrebski et al. 2013; Euler et al. 2014; Gualtieri et al. 2014; Farra et al. 2016; Meschede et al. 2017). Due to the resonance effect, a particular water depth favors some specific frequencies (Figure 1.19). Shallower water depth typically favors shorter periods. Consequently, the excitation of microseism noise is modulated by the bathymetry and the amplification depends on the seismic frequency and water depth. As for body waves, the amplification also depends on the take-off angle or slowness.

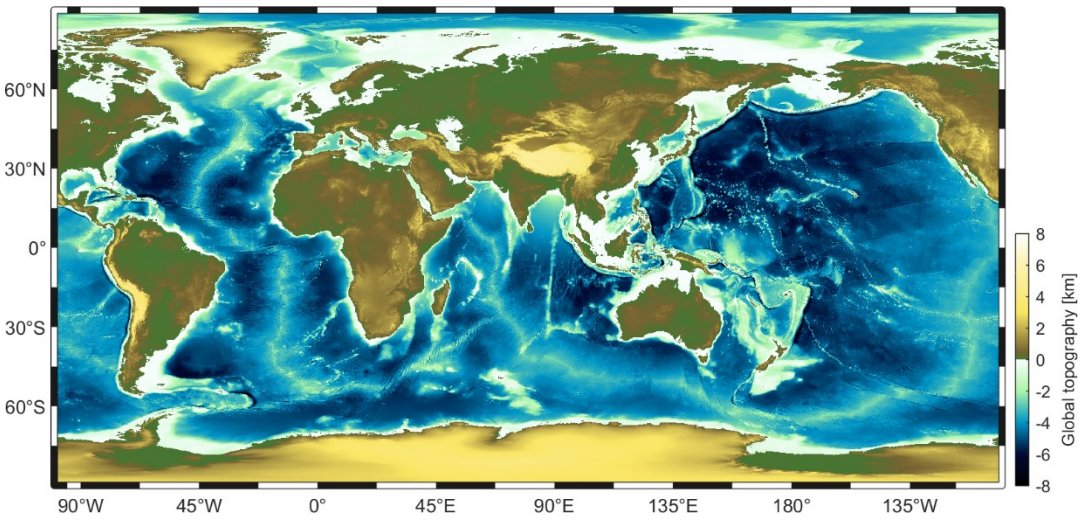

Figure 1.18. Global land topography and ocean bathymetry (data from the ETOPO1 model).

The modulation of the intensity of noise source by bathymetry was first proposed in Equation 184 of (Longuet-Higgins 1950; see also his Figure 2 and Table 1) without a specific name. The bathymetric modulation is referred to as **excitation function of microseisms** or **microseism excitation potential** by (Kedar et al. 2008), as **bathymetry-dependent amplification factor** by (Hillers et al. 2012), **coupling coefficient** by Ardhuin and Herbers (2013), as **ocean site effect** by Gualtieri et al. (2014), and as **bathymetric excitation factor** by Euler et al. (2014). The frequency-dependent bathymetric modulation changes the shape of the noise spectrum at source site. The bathymetric modulation is not the same for different wave types. It has been known that much more P waves than S waves are radiated from oceanic sources because of the nature of the excitation mechanism (Longuet-Higgins 1950; Hasselmann 1963; Ardhuin and Herbers 2013; Nishida and Takagi 2016). The larger amplification factor of P waves, as shown

in Figure 1.19, is another factor responsible for the stronger microseism P waves compared to S waves.

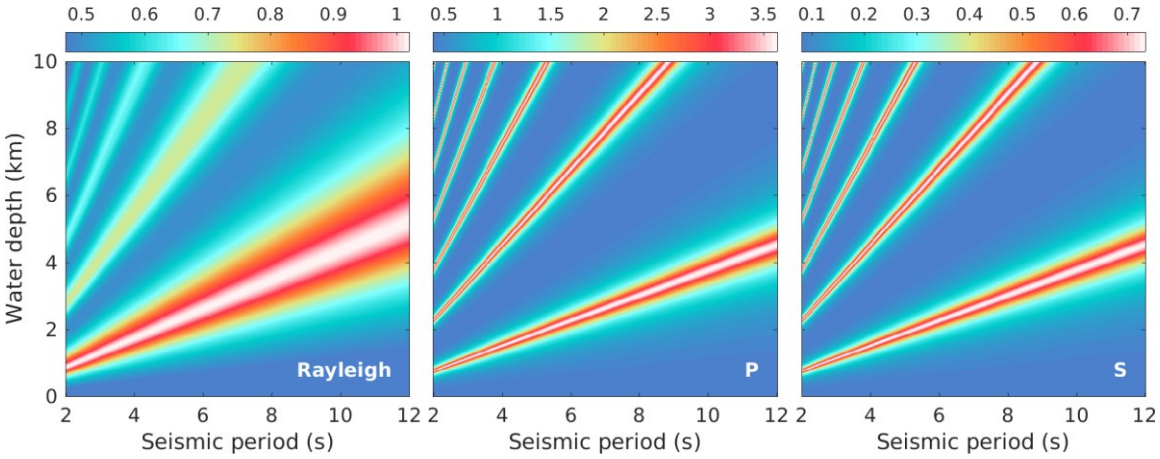

Figure 1.19. Bathymetric amplification factors for microseism Rayleigh, P and S waves, with respect to varying seismic periods and water depth. The amplification factors for Rayleigh waves are provided in Table 1 of Longuet-Higgins (1950). The amplification factors for body waves are calculated based on the equations of Gualtieri et al. (2014), for a slowness of 6 s/deg which corresponds to a take-off angle less than 5° in the water layer. For a specific seismic period, the water depth of peak amplification for Rayleigh waves is close to but generally larger than that for body waves.

1.3.3.4. Early History of Microseism Studies

Seismology became an independent science in parallel with the emerging and developing of seismological instruments. Our understanding about seismic noise has also been advancing in accompany with the improvements in seismological instruments. According to the review on the history of seismology by Dewey and Byerly (1969) and Ben-Menahem (1995), an Irish civil engineer named Robert Mallet, often referred to as the father of modern seismology, carried out a number of seismic experiments using explosives during the mid-nineteenth century and laid the foundation of instrumental seismology. The first mechanical seismometers were built by James David Forbes in 1841 and by Luigl Palmieri in 1855, and the first horizontal pendulum seismograph by Zöllner in 1869, the first functional seismograph system for recording local earthquakes by John Milne and his associates in 1880. In some literatures, it is claimed that the first seismograph was invented by Filippo Cecchi of Italy in 1875 and the

earlier ones were actually seismoscopes. However, Dewey and Byerly (1969) claimed that the apparatus made by Cecchi was rather insensitive and had relatively little impact on seismology compared to the contemporary seismographs built by the group of Britain researchers working in Japan. On 1889-04-17, the first teleseismic recording of an earthquake in Japan by Ernst von Rebeur-Paschwitz in Potsdam of Germany, marking the initiation of instrumental seismology in a global sense. From 1892 to 1894, John Milne and his associates developed the first portable seismograph system, facilitating the worldwide deployment of seismic stations. Emil Wiechert introduced the viscous damping to seismometers in 1898 and later built a three-component mechanical seismograph system in 1900, broadening the observable seismic wavefields. In 1925, Anderson and Wood developed the torsion seismometer. In 1935, Hugo Benioff designed a linear strain seismography, extending seismic observations to very long periods. With the increments and improvements in seismographs and the accumulation of observed seismic data, seismological phenomena could be studied in a quantitative way. In the mid-twentieth century, digital computers were first introduced into seismology. The earliest seismic arrays were built in order to improve the capability of monitoring nuclear tests. In 1962, the first digital broadband seismograph was operated at Caltech University. By the 1970s, high-gain digital seismological instruments had been deployed worldwide. Later, high-gain and high-dynamic-range broadband sensors and deployment of seismic arrays became popular.

The first pendulum seismographs in the late nineteenth century and early twentieth century, despite of the low sensitivity typically no more than 100 to 500 times magnification (Bormann and Wielandt 2013), had been able to record background oscillations lasting for hours or even days (see Figure 1.1 for example). These faint background oscillations, termed as microseisms afterwards, were found not instrumental and unrelated to earthquakes. Since as far back as 1643, early investigators had noticed the spontaneous motions of pendulum and reckoned that the spontaneous motions were “optical illusions” or caused by “local accidental causes” (Dewey and Byerly 1969). Timoteo Bertelli began the first systematic observation of the spontaneous pendulum motions in the 1870s and noted a dependence on regional meteorological conditions, with greater activity during winter and accompanying low-pressure zones. Until the end of the nineteenth century, the origin of the spontaneous motions was still debated and unclear. Bertelli believed that the pendulum motions were caused by natural forces acting on a regional scale. Monte ascribed the spontaneous motions to local causes such as air currents or cultural noise. Milne first suspected that the background vibrations were signatures of the preparing of earthquakes. After, he held that microseisms were caused by winds and could propagate to

windless regions. He also conjectured that microseisms were possibly caused by atmospheric pressure changes. By 1898, he changed the opinion again and concluded that most spontaneous pendulum motions were just instrumental disturbances or caused by purely local phenomena. In 1895, Jose Algue proposed that microseisms were likely produced by strong winds blowing against mountains. He noticed the phenomenon that the microseismic activity usually decreases when a cyclone crosses the coast from ocean to land. In 1899, Omori associated microseisms to strong local winds, but he also noted that the background oscillations could emerge on calm days.

The understanding of microseisms largely advanced during the first half of the twentieth century. In 1904, Wiechert proposed a theory about the generation of microseisms on the 2nd International Seismological Conference that microseisms are caused by the impact of ocean waves breaking on coast. In 1908, Karl Zoeppritz, an assistant of Wiechert who proposed the Zoeppritz equations, related microseisms to deep low-pressure systems in the atmosphere. In 1911, Beno Gutenberg, who was a student of Wiechert and famous for the discovery of the core–mantle boundary and other significant contributions, made the first major review on the nature and origin of seismic noise in his doctoral thesis (Bonnefoy-Claudet et al. 2006). Extensive evidences from worldwide observations linked microseisms to storms and ocean waves, and it was realized that microseisms can serve as a tool for storm forecasting (Harrison 1924). From 1924 to 1930, Banerji studied the connections between the Indian monsoons and microseisms in South Asia and inferred that microseisms were Rayleigh waves generated at the seafloor by the water wave trains maintained by the monsoon currents. Later, substantive attempts were made to explore the practical uses of microseisms in civil engineering and applied meteorology (Gutenberg 1947). In 1935, two years after the Mw6.4 Long Beach earthquake in California, a large experiment was implemented to record and analyze ambient vibrations in over 200 buildings. In 1943, the United States Joint Chiefs of Staff initiated a specific research project to track cyclones with microseisms (Ebeling 2012).

The atmospheric and oceanic excitation hypotheses were the major controversy concerning the origin of microseisms (Longuet-Higgins 1950; Hasselmann 1963; Bernard 1990; Nishida 2017). By the mid-twentieth century, it had been definitely clear that the microseism excitation should be ascribed to ocean wave activities. The effect of pressure fluctuations associated with atmospheric turbulence is found to be negligible (Hasselmann 1963). The theory proposed by Wiechert that microseisms were excited by waves shoaling and breaking on the coast, was

more favored, especially because a statistical correlation had been widely observed between the amplitude of microseisms and the height of coastal ocean waves. However, Wiechert's hypothesis could not explain the relation between the peak frequencies of microseisms and ocean swells found by Bernard (1941): the peak frequency of microseisms is twice that of ocean swells. It was recognized that it is necessary to discriminate the excitation mechanisms for the weaker primary microseism with the same frequency as the ocean waves and the stronger secondary microseism with twice the frequency as the ocean waves. Miche (1944) showed that the interaction of two wave trains in opposite propagation directions and with the same period can give rise to pressure fluctuations in the water column unattenuated with depth, thereby producing oscillations on the seafloor. On the basis of the empirical discovery by Bernard (1941) and the theoretical work by Miche (1944) and Longuet-Higgins and Ursell (1948), Longuet-Higgins (1950) developed a systematic theory for the excitation of secondary microseisms. While the first-order pressure fluctuation arising directly from the surface gravity waves decays exponentially with depth, the depth-independent second-order pressure fluctuation varies with an amplitude proportional to the product of ocean wave amplitudes and with twice the frequency of the interfering ocean waves [see Equation 34 of Longuet-Higgins (1950)]. The unattenuated pressure fluctuation arising from wave-wave interaction can be equivalent to a vertical random pressure applied to the ocean surface. The theory was soon verified by an experiment (Cooper and Longuet-Higgins 1951). The theory regarding the generation of primary microseisms, originally proposed by Wiechert in 1904, was provided in details by Hasselmann (1963). The theory regarding the generation mechanism of secondary microseisms was also discussed by Hasselmann (1963), who extended the theory of Miche (1944) and Longuet-Higgins (1950) to random waves. Hasselmann (1963) also emphasized that the secondary microseisms are actually produced by interactions between ocean waves with slightly different wave numbers, rather than by interactions between wave components having exactly equal and opposite wave numbers: the former gives rise to compressional waves with a finite horizontal phase velocity, which can be in resonance with a trapped mode of the wave guide; the latter leads to a theoretically infinite horizontal phase velocity for the generated compressional waves. The depth-independent nonlinear pressure is a direct consequence of the finite but high phase velocities caused by the former. The latter excites vertically propagating P waves only. Quantitative comparisons between the measured spectra of ocean waves and seismic noise by Haubrich et al. (1963) showed a good agreement with the theory of generation mechanisms for microseisms. Hasselmann (1966) introduced Feynman diagrams from quantum mechanics, to interpret the general case of wave-wave interactions, which, of course,

also include the two generation mechanisms of microseisms. Microseism was undoubtedly one of the topics that could attract interests from diverse branches of Earth science, including seismology, meteorology and oceanography. The study on microseisms were expansive and extensive. Gutenberg (1958) quoted over 600 references related to microseisms that were published in various languages and in many countries.

Further development in digital instruments and broadband seismometers, and rapid advances in computational power, allowed implementations of more advanced data analysis like polarization analysis and frequency-wavenumber analysis, for better understanding of noise phenomena. Particle motion analysis identified in ambient noise both Rayleigh and Love waves, which were theoretically predicted in 1885 and 1911, respectively. In the 1960s, P waves were discovered in ambient noise with the aid of array analysis (Backus et al. 1964; Lacoss et al. 1969; Vinnik 1973). More recent advances on microseism study are introduced in other sections.

1.3.3.5. Significance of Microseism Observations

Because of the close proximity to ocean waves and storms, microseisms can also be considered as meteorological signals and indicators of ocean activity and climate variability (Bromirski et al. 1999; Grevemeyer et al. 2000; Aster et al. 2008; Stutzmann et al. 2009; Ebeling 2012; Tytell et al. 2016; Jacques et al. 2017). Storms blowing over the ocean surface produce gravity waves responsible for the strongest microseisms. The intensity and peak frequency of ocean waves and microseisms are associated with the intensity of winds. Increasing wind speeds produce higher ocean waves and a broadening ocean wave frequency spectrum with a lower peak frequency, and hence stronger microseisms with lower dominant frequency. Microseisms generated by individual cyclones have been studied (Sutton and Barstow 1996; Bromirski 2001; Gerstoft et al. 2006a; Zhang et al. 2010b; Ebeling and Stein 2011; Davy et al. 2014; Sufri et al. 2014; Lin et al. 2014; Chen et al. 2015; Farra et al. 2016). The Indian Meteorological Survey has already employed seismic networks to track approaching monsoons for decades (Bormann and Wielandt 2013). It is feasible to monitor the evolution of storms using microseisms and identify undocumented historical storms from microseisms. However, it is noteworthy that in general the microseismic source locations, for both primary and secondary microseisms, do not directly follow the storm trajectories (Cessaro 1994; Ebeling 2012; Bormann and Wielandt

2013; Farra et al. 2016). As the storm moves over the ocean, it is possible to observe significant inconsistency between bearings toward the storm and the microseismic source regions (Friedrich et al. 1998; Bormann and Wielandt 2013). Storm moving faster than swell is a favorable condition for the presence of secondary microseismic sources near the parent storm. Haubrich and McCamy (1969) estimated a threshold of ~10° per day for the movement of storms.

The correlation of microseismic spectral power with the height and period of ocean waves suggests that microseismic observation could be a proxy for local sea states (Bromirski et al. 1999; Bromirski 2002; Ardhuin et al. 2012; Ferretti et al. 2013; Poppeliers and Mallinson 2015). Seismometers have been serving as a wavemeter system in superiority of continuous wave observations at low cost (Zopf et al. 1976; Tillotson and Komar 1997). It is also possible to infer remote wave climate from microseismic observations. Aster et al. (2010) observed from microseisms an increasing global trend in near-coastal ocean wave activity over the past decades in the Northern Hemisphere and a stable or slightly declining trend in the Southern Hemisphere. The wave climate prior to modern wave measurements is potential to be reconstructed from seismic noise data. However, it should be noted that, as mentioned previously, the power of secondary microseisms do not always correspond directly to ocean wave energy (Ebeling 2012; Obrebski et al. 2012). Also, note that microseisms could be significantly intensified or attenuated by the water column at source sites (Longuet-Higgins 1950; Kedar et al. 2008; Hillers et al. 2012; Ardhuin and Herbers 2013; Gualtieri et al. 2014; Meschede et al. 2017).

The instrumental observation of microseisms has a history more than one century, starting much earlier than the modern observations of storms and ocean waves. Before the era of satellite-based observations from the 1960s and aircraft reconnaissance from 1944, hurricane records were based upon land observations and ship logs (Ebeling 2012). The observations were sparse both in space and time, and could be of low accuracy. Unavoidably and undoubtedly, the documented storm records are limited. The short-term, incomplete records inevitably limit our understanding about the link between rising sea surface temperature and the frequency and intensity of storms, which are related to climate variability and global warming (Manuel et al. 2008; Ebeling and Stein 2011; Ebeling 2012). Analog seismograms in the late 19th century and early 20th century are possibly the only available instrumental records of high accuracy and high resolution. The digitalization of past analog seismograms has been

in progress (Ishii et al. 2015; Bogiatzis and Ishii 2016). The seismic recordings are prospected to expand the database of extremal atmospheric disturbance and ocean activities stretching back to one century ago or even earlier, which can have great significance in understanding the effects of anthropogenic global warming (Ebeling 2012). The database also allows to verify the conclusions derived from the reanalysis/hindcast data.

In contrast to long been considered as meteorological signals in climate science, microseisms were viewed as nuisance hampering the observation of earthquakes in seismology, possibly because monitoring earthquakes was the main interests of seismological observations. To avoid earthquake observations from being contaminated by the large microseism peaks, early seismometers were generally designed to be sensitive to frequencies above 1 Hz or below 0.1 Hz (Nishida 2017). Limited computation ability and storage resources at that time could be other important reasons. Benefiting from rapid development and falling cost of digital resources and high-gain broadband seismometers, the storage and processing of big seismic data have become feasible and the opinion on seismic noise has been changed. As advocated by Aki and Richards (2002), the definition of signal and noise is subjective. It has been realized that the ambient seismic wave filed contains rich information on medium properties and source characteristics. Various techniques have been developed to turn seismic noise into signals. For instance, the beam method (Rost and Thomas 2002) has been widely used to detect coherent microseismic signals and to locate microseismic noise sources (e.g., Friedrich et al. 1998; Landès et al. 2010; Zhang et al. 2010a; Kimman et al. 2012; Liu et al. 2016a; Neale et al. 2017b; Retailleau et al. 2018). The noise correlation technique (Campillo and Paul 2003; Shapiro and Campillo 2004; Shapiro et al. 2005), or seismic interferometry as named in the field of seismic exploration (Draganov et al. 2006; Curtis et al. 2006), is one of the most influential methods which opens a way to a better use of seismic noise data for probing the structure of Earth.

Microseisms, as well as seismic noise in other frequency bands, are also potential to contribute to the study in other physical scientific fields, such as astrophysics, cosmology or particle physics. The observation of gravitational waves, light-speed disturbances in the fabric of space-time incited by events like supernovae, the Big Bang and binary star systems, is critical to affirming the prediction and validity of the General Theory of Relativity (Abbott et al. 2016). Gravitational waves can interact with elastic bodies and give rise to vibrations. The major obstacle of observing gravitational waves directly is the extremely subtle strain of objects excited by the pass of gravitational waves, which is generally no more than 10^{-20} (as a

comparison, strains as large as 10^{-10} to 10^{-4} caused by earthquakes and tides are common in the solid Earth). The size of the detector is critical when extremely high resolution is hard to be reached. Some authors have proposed to take our Earth as an astrophysical observatory to identify gravitational waves from the background seismic noise (e.g., Dyson 1969; Gusev et al. 1990; Coughlin and Harms 2014a, b, c; Mulargia and Kamenshchik 2016; Mulargia 2017). Coughlin and Harms (2014b) inferred from global seismic noise data an upper limit of 1.2×10^8 for the energy density of gravitational wave on an isotropic stochastic gravitational-wave background in the frequency band of 0.05 to 1 Hz. Coughlin and Harms (2014c) obtained a better estimate of 1.2×10^5 in the frequency band of 0.1 to 1 Hz from lunar seismic noise data. Mulargia and Kamenshchik (2016) prospected the possibility to detect gravitational waves using global broadband seismic networks.

1.3.4. Seismic Hum

1.3.4.1. Discovery

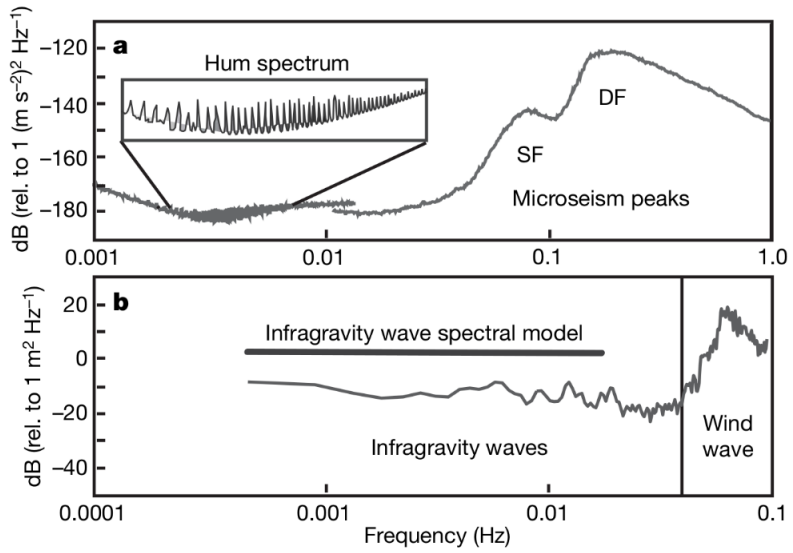

Figure 1.20. Vertical acceleration spectrum from the Black Forest Observatory (a) and ocean wave height spectrum from the shelf off Florida (b). Modal peaks between 1 and 10 mHz are shown magnified in the inset. Reproduced from Figure 1 of Webb (2007).

There is a smallest but still detectable peak in the NLNM curve at long periods (Figure 1.13), which is the incessant excitation of the Earth's free oscillations or normal modes, and often

referred to as seismic hum (Figure 1.20a). The Earth's free oscillations was first credibly observed after the huge 1960 Chile earthquake from the recordings of strain and pendulum seismographs (Alsop et al. 1961; Ness et al. 1961) and gravimeters (Benioff et al. 1961). However, almost forty years later the background long-period free oscillations were observed in the absence of significant earthquakes (Kobayashi and Nishida 1998; Suda et al. 1998; Tanimoto et al. 1998). And until very recently, the background free oscillations were first observed at ocean bottom seismometers (Deen et al. 2017).

Compared to the NLNM hum peak (Figure 1.13; roughly between 7 and 10 mHz), the modal peaks are observed primarily at lower frequencies (Figure 1.20; roughly between 3 and 7 mHz), matching the eigen-frequencies of fundamental spheroidal modes [see e.g., Figure 2 of Tanimoto (2005)]. Seismic hum has mainly been observed from vertical components of ground motions. Atmospheric pressure and temperature changes can lead to low-frequency tilts indistinguishable from horizontal motions (Rodgers 1968; Zürn et al. 2007; Hutt et al. 2017; Rohde et al. 2017). The noise level in horizontal components is often an order of magnitude higher than in vertical component (Tanimoto et al. 2015). An apparent diurnal variation in long-period noise is possible, caused by the thermal instability. The amplitude of seismic hum in the vertical component is generally no more than 0.1 or 1 nm/s^2. Tanimoto and Um (1999) estimated that the excitation of modal amplitudes observed requires an equivalent earthquake of magnitude 6 every day. Ekström (2001) estimated a similar equivalent magnitude of 5.75.

1.3.4.2. Open Questions on Origins

Since the first observation of seismic hum in 1998, seismologists have proposed various theories to explain the existence of these continuous oscillations, from atmospheric disturbances to ocean infragravity waves moving over the sea floor. However, the excitation mechanism for seismic hum is still not as clear as for microseisms till now. Tectonic processes, like the cumulative effect of small earthquakes, were the first causes excluded almost simultaneously with the discovery of seismic hum, because they were found incapable of reproducing the observed modal peaks (Kobayashi and Nishida 1998; Suda et al. 1998; Tanimoto et al. 1998). Another important evidence is the observation of seasonal variations in seismic hum amplitudes. The seasonal pattern has great implications in rejecting the tectonic causes in the solid Earth while favoring an atmospheric or oceanic origin (Ekström 2001;

Tanimoto et al. 2015). However, it has to be mentioned that controversy arises regarding the dominant seasonal pattern. Some authors (e.g., Tanimoto and Um 1999; Ekström 2001; Tanimoto 2005) reported a predominant 6-month periodicity with the maximum reached during the middle of January and July, whereas some others (e.g., Nishida et al. 2000) claimed a predominant annual seasonality. Regardless of the periodicities, the two seasonal patterns favor an atmospheric or oceanic origin.

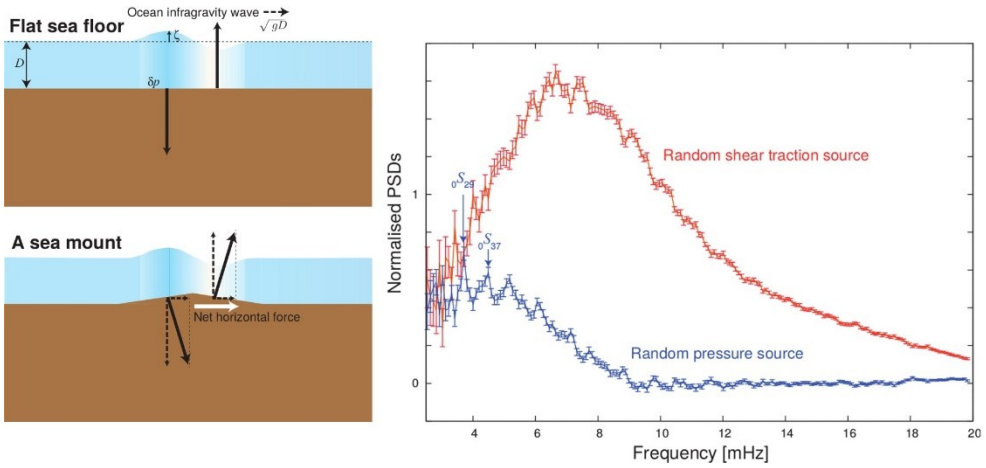

Figure 1.21. Left: schematic of random pressure and shear traction exciting seismic hum, originating from the interaction of ocean infragravity waves with ocean bottom. The topographic coupling is efficient when the wavelength of the infragravity wave matches the horizontal scale of the seamount. Right: Normalized PSDs of the effective pressure and shear traction, inferred from cross-spectra between pairs of 618 global broadband stations. The two local maxima of random pressure at 3.7 and 4.4 mHz as indicated by text arrows correspond to two acoustic coupling modes between the fundamental spheroidal and atmospheric acoustic modes. Reproduced from Figures 8 and 9 of Nishida (2017).

The atmospheric disturbance was initially recognized as the major excitation source by authors (Kobayashi and Nishida 1998; Tanimoto 1999; Tanimoto and Um 1999; Fukao et al. 2002). The direct coupling of atmospheric pressure variations into the solid Earth was proposed as the mechanism responsible of the excitation of the observed seismic modes. Now the oceanic excitation hypothesis is more favored (Rhie and Romanowicz 2004, 2006, Tanimoto 2005, 2007a, Webb 2007, 2008; Bromirski and Gerstoft 2009; Traer et al. 2012; Nishida 2014; Traer and Gerstoft 2014; Ardhuin et al. 2015; Bertin et al. 2018). It is proposed that the shear traction at seafloor, originating from the interaction between ocean infragravity waves and ocean

bottom topography (Figure 1.21), excites the background Rayleigh and Love waves composing seismic hum. Infragravity waves is one type of the ocean surface gravity waves with longer periods than wind seas and swells. The dominant period of infragravity waves typically ranges from 80 to 300 sec, between that of wind waves (typically 1 to 25 sec) and that of tsunamis (typically 10 min to 1 hr). Generally, infragravity waves are strongest at wavelengths between 2 and 10 km (Ardhuin et al. 2014). Infragravity waves propagate very fast in deep water, similar to tsunamis do. Some authors (e.g., Tanimoto et al. 2015; Nishida 2017) believe that, at very low frequencies, the atmospheric effects may still play a dominant role in exciting seismic hum.

Besides the uncertainty in the excitation mechanisms, the location of sources inciting seismic hum is also not definitive. It is generally considered that the dominant hum generation seems to be coastal (Webb 2007; Bromirski and Gerstoft 2009; Ardhuin et al. 2015; Nishida 2017), while hum can also be excited by free infragravity waves in the deep ocean (Webb 2008). Because of the long wavelength, the infragravity waves at very long periods can interact directly with the ocean bottom, even in the mid-ocean.

It is interesting that the exploration for the excitation mechanisms and source locations of seismic hum, more or less, mimics the history of microseism studies. It is confusing that it was not the oceanic excitation hypothesis but the atmospheric excitation hypothesis that had been considered in priority.

1.3.4.3. Implications

Seismic hum contains both surface waves and body waves (Nishida 2013; Boué et al. 2014a). The vertical component of seismic hum is dominated by fundamental Rayleigh waves (Nishida et al. 2002; Ardhuin et al. 2015). Studying seismic hum can improve our understanding about the nature of seismic wavefield at long periods and constrain the three-dimensional model of Earth structure at depth. Seismic hum has been applied in global surface wave tomography (Nishida et al. 2009; Haned et al. 2016). Because of its proximity to infragravity ocean waves, it is also promising to have applications in oceanography.

1.3.5. Persistent Localized Noise Sources

Besides the major classifications of seismic noise introduced above, some special spectral lines, originating from temporally persistent and spatially localized noise sources, have also been identified. Such phenomena have been observed at local (e.g., Bokelmann and Baisch 1999), regional (e.g., Gu et al. 2007) and global (e.g., Shapiro et al. 2006) scales.

Bokelmann and Baisch (1999) observed time-continuous spectral lines from the spectrogram of seismic recordings of the GERESS array between 2 and 3 Hz, with the most prominent one at ~2.083 Hz. They found that these narrow-band signals are regional *Lg* and *Sg* phases from an industrial origin near the German-Czech border. Gu et al. (2007) and Brzak et al. (2009) computed the noise correlation functions of vertical seismograms between station pairs in the southern Italy and observed considerable Rayleigh wave energy in the frequency band of primary microseisms, which originated from a dominant, persistent noise source near the Gargano promontory and a plausible secondary source near the Tyrrhenian Sea coast. Zeng and Ni (2010) observed stable seismic arrivals in the microseismic frequency band from the noise correlations of seismic stations in East Asia. The reconstructed seismic arrivals exhibited inter-annual rather than seasonal variations, rejecting the oceanic noise source excitation which has been known to vary in a seasonal periodicity. The authors attributed the excitation of the seismic noise to tremors due to volcano activities in Kyushu Island of Japan.

The most famous persistent localized noise source should be the globally observable 26 sec monochromatic noise. It was likely first observed by Oliver (1962) and after by many others (e.g., Holcomb 1980, 1998; Bernard and Martel 1990). The relative stability in observing at global sites suggests temporarily persistent, spatially stable noise sources responsible for the 26 sec spectral peak. The amplitude of the 26 sec noise shows seasonal variations and is largest during the austral winter. Shapiro et al. (2006) reconstructed the empirical Green functions from the ambient noise correlations and observed strong Rayleigh waves of 26 sec period propagating globally. Grid-search location unveiled that the noise source should be located in the Gulf of Guinea. Strong radiation directivity of the reconstructed Rayleigh waves were observed. Retailleau et al. (2017) obtained the same source location by beamforming and back-projecting spurious surface waves of 26 sec period reconstructed from noise correlations between European and American stations. By comparing Rayleigh waves from earthquake data and from ambient noise correlations, Zeng and Ni (2014) concluded that the antipodal region

of the Gulf of Guinea in the Pacific should be another independent 26 sec noise source.

Despite the decades long history of discovery, the excitation mechanism of the 26 sec seismic noise is still a mystery. Xia et al. (2013) ascribed the Gulf of Guinea noise source to volcano processes. Zeng and Ni (2014) also proposed that the Pacific 26 sec noise sources are long-period tremors excited by magmatic processes in Vanuatu volcanos. However, no strong evidence has been provided to support the hypothesis of volcanic origin. Xia et al. (2015) and Xie et al. (2018) utilized the correlation functions of the persistent 26 sec noise to detect clock drift of stations and synchronize seismic networks.

1.3.6. Composition of Seismic Noise

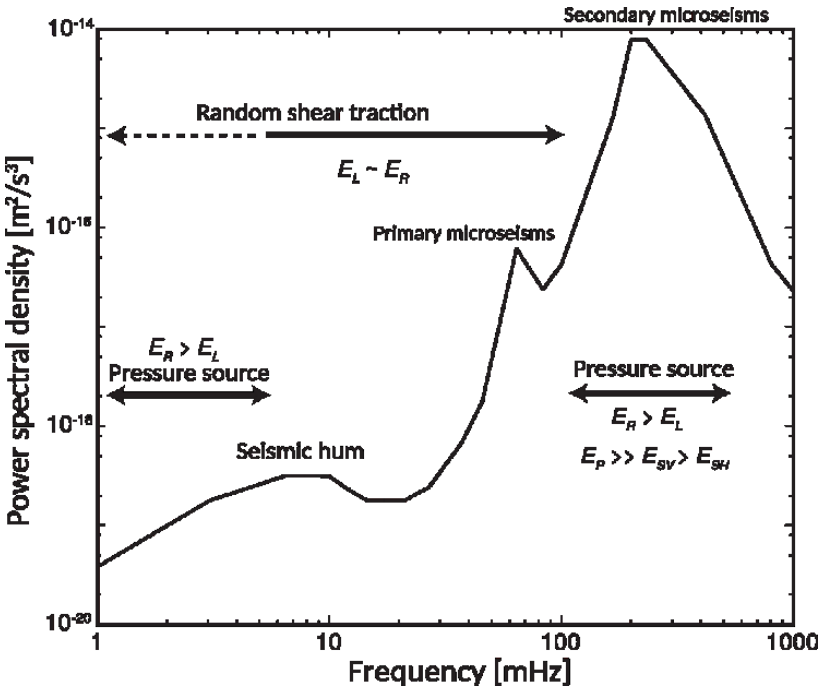

Figure 1.22. Typical power spectrum and causative forces of seismic noise in the microseismic and hum frequency bands. *E* with subscripts *R*, *L*, *P*, *SV* and *SH* refers to the energy of Rayleigh, Love, P, SV, and SH waves, respectively. Reproduced from Figure 1 of Nishida (2017).

Considering that most majority of seismic noise sources, either cultural or natural, are distributed on the Earth's surface, it has been consentaneous that seismic noise wavefields are predominated by surface waves (Bonnefoy-Claudet et al. 2006; Larose et al. 2006b; Ebeling

2012). Seismic noise also contains a small portion of body waves, including both P and S waves, which are generally observable by seismic arrays (Gerstoft et al. 2008; Koper et al. 2009, 2010; Zhang et al. 2010b; Landès et al. 2010; Pyle et al. 2015; Liu et al. 2016a; Nishida and Takagi 2016). Knowledge about noise source location and energy partition of different seismic wave types are helpful and critical for discerning their origins and excitation mechanisms. However, the relative proportion between different types of waves (body and surface waves, P and S waves, Love and Rayleigh waves, fundamental and higher modes), is indefinite and highly variable from site to site and from time to time (Bonnefoy-Claudet et al. 2006; Gualtieri et al. 2015; Tanimoto et al. 2016a, b). It is commonly presumed without further investigation in many applications that the (fundamental) Rayleigh waves are the most energetic surface waves making up the microseismic wavefield. Gualtieri et al. (2013) demonstrated that the main features of vertical-component microseism noise amplitude spectrum can be well reproduced by the fundamental Rayleigh waves. Nishida (2017) summarized the energy partition among different wave types and the force systems of excitation sources for microseisms and seismic hum (Figure 1.22). But counter-examples, particularly observations of more Love energy than Rayleigh energy, are easy to find (Bonnefoy-Claudet et al. 2006; Tanimoto et al. 2016a). At short periods (0.25 to 2.5 sec), there even exists observations of more P waves than Rayleigh waves (Koper et al. 2010). Another example in Kazakhstan was reported by Vinnik (1973) and was explained by Ardhuin and Herbers (2013).

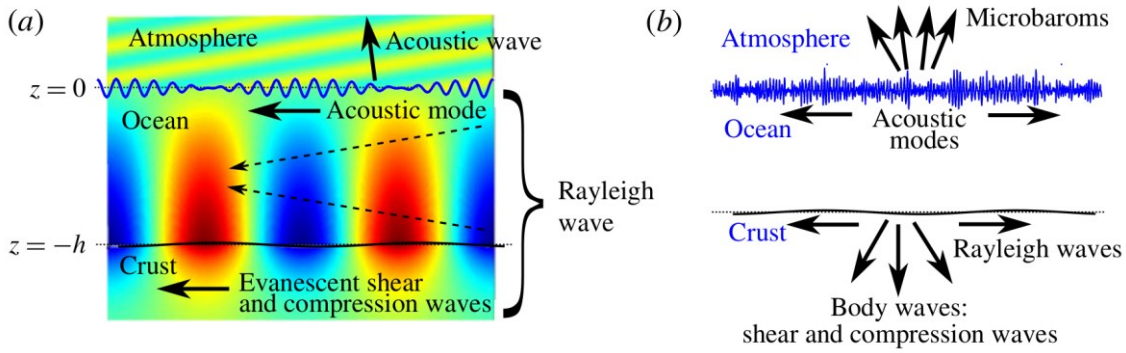

Figure 1.23. (a) Schematic of the second-order pressure field associated with the generation of secondary microseisms, forced by the interaction of a single pair of directionally opposing monochromatic ocean wave trains. (b) Schematic of ocean waves with a relatively broad spectrum, giving rise to the interaction of all possible pairs of wave-trains and noise radiation in all directions. Reproduced from Figure 2 of Ardhuin and Herbers (2013).

In the frequency band of secondary microseisms, the excitation of Rayleigh, P and SV waves can be easily understood through the nature of the excitation mechanism (Figure 1.23), which is equivalent to a vertical random pressure exerted on the free surface of water layer (Longuet-Higgins 1950; Hasselmann 1963). The dominance of Rayleigh waves is also well explained by the theory. It has been observed that the power of microseism P waves are much stronger than the S waves, which rely on the conversions from P waves at the fluid-solid interface (Gualtieri et al. 2014; Liu et al. 2016a; Nishida and Takagi 2016), and that the SV wave is stronger than the SH wave (Figure 1.24). These observations can also be explained by the theory of Longuet-Higgins (1950). However, the excitation mechanism for the transverse components (Love and SH waves) lacks a satisfactory explanation in the theory (Liu et al. 2016a; Tanimoto et al. 2016a). The origin of the transversely polarized waves is still obscure and confusing.

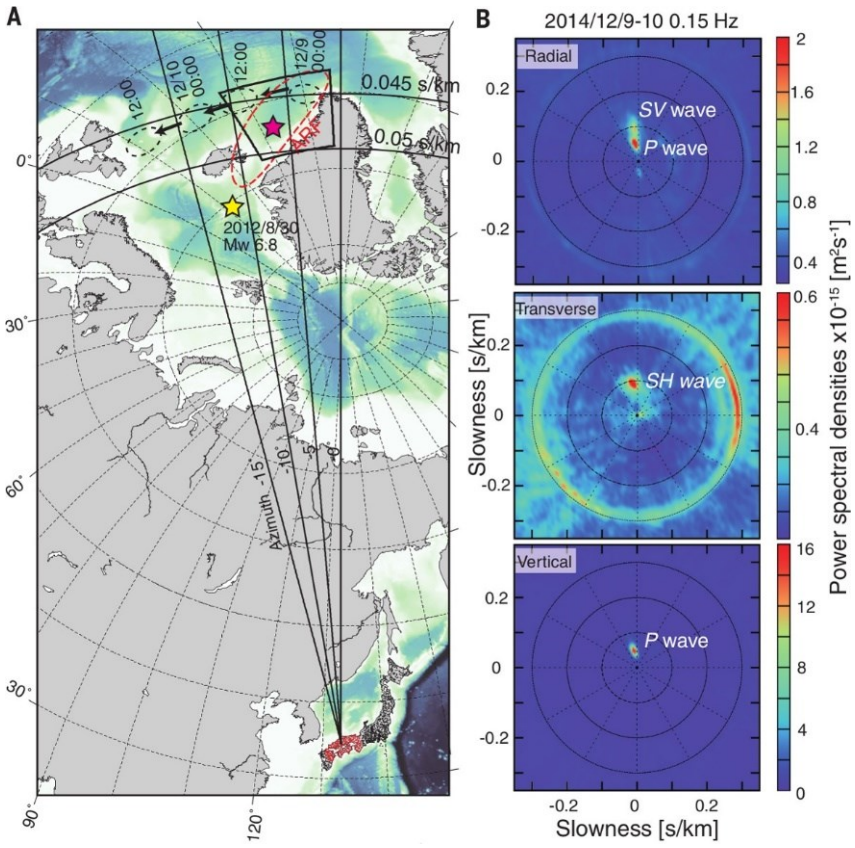

Figure 1.24. (A) Noise source location by back-projecting body-wave microseisms. Black and red dots indicate Hi-net stations. Red dashed line represents half peak of the array response function for a point source at the red star. (B) Frequency-slowness analysis of radial, transverse and vertical components at 0.15 Hz. The mean square amplitude of microseism SV (SH) waves is about 8% (3%) of that of microseism P waves. Reproduced from Figure 1 of Nishida and Takagi (2016).

1.4. Summary

In this chapter, we presented the relationships between the atmospheric motions, ocean waves and seismic noise. Their causative relationships are summarized in Figure 1.25. Solar energy is the ultimate power dictating the circulations of atmosphere and oceans, while the large-scale movements in the atmosphere and oceans are also deflected by the forces from the Coriolis Effect. Ocean waves are primarily produced under the force of winds. Nonlinear interactions between ocean waves (and solid Earth) then give rise to microseisms (and hum). The excitation mechanisms and traits of two types of microseisms are also summarized in the figure. The origins of microtremors are complicated and variable. The excitation mechanism of seismic hum is still under investigation and inconclusive. Therefore, they are not included in the figure. We also reviewed the history of seismic noise studies and various applications of seismic noise in multiple disciplines.

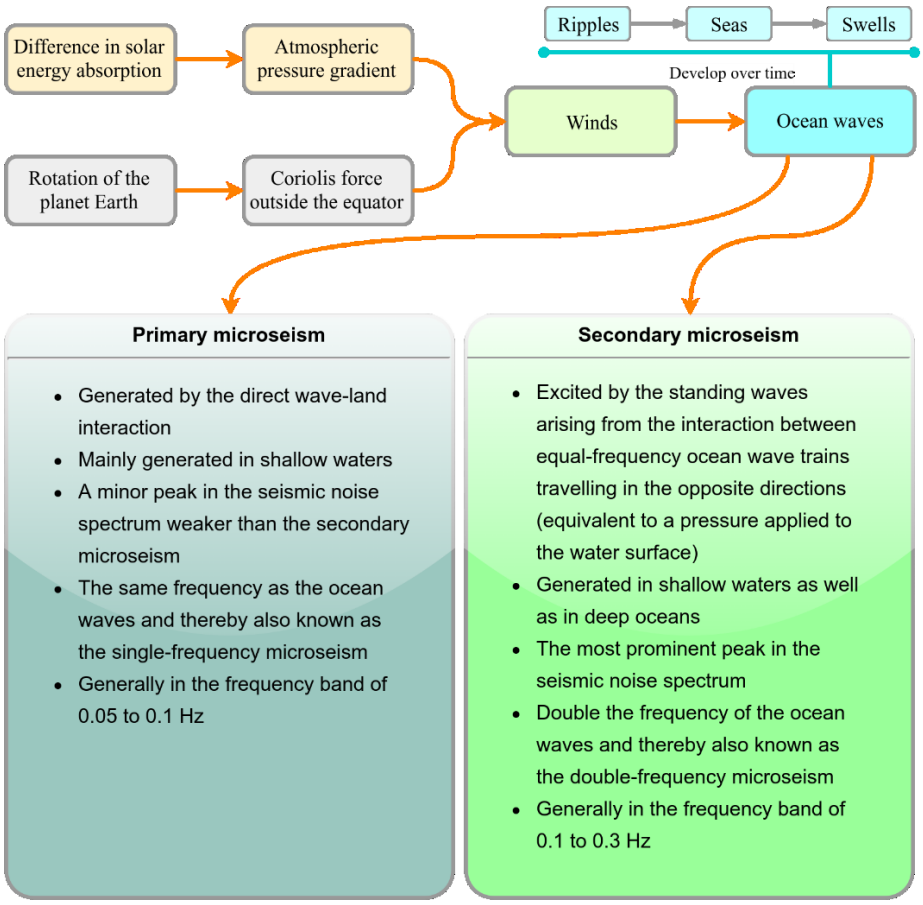

Figure 1.25. A summary over the relationships between winds, ocean waves and microseisms, and summaries of the primary and secondary microseisms.

2. Correlation Computation and Signal Construction

The ambient seismic wavefield is an enormous mine containing rich information but having been long buried. It contains information regarding both the characteristics of noise sources and the properties of hosting media. By computing the auto- or cross-correlation functions of continuous seismic recordings, explicit signals can be retrieved from the ambient wavefield. In this chapter, we present a brief overview on the history and development of the emerging noise correlation technique and its diverse applications in seismology. Also, we provide a summary over the methodological strategies concerning the computation of correlation functions and the processing of noise data and noise correlation functions. Furthermore, we make a survey on the descriptive statistics of seismic noise and introduce an extended median filter into the processing of seismic noise records. A kurtosis-based noise data selection filter and a modified scheme for calculating unattenuating correlation functions are also proposed.

2.1. A Literature Review

2.1.1. History and Current Status

The idea to extract seismic signals from random noise via correlation technique is not thoroughly new. Stretching back to over 60 years ago, Aki (1957) had developed a so-called SPAC method to estimate the phase velocity dispersion of surface waves from the spatial autocorrelations of stationary stochastic waves. The method required a seismic array deployed in a specific geometry and was successfully applied to microtremors (5-15 Hz) recorded in Tokyo. The original paper was published in Japanese. The author himself established a brief English translation eight years latter (Aki 1965). The explicit relationship between the spatial autocorrelation and the time-domain cross-correlation was clarified decades later (Sánchez-Sesma and Campillo 2006; Tsai and Moschetti 2010). In early seismological literatures, one can also find practical applications exploiting the correlation method similar to present. Douze (1967) detected the presence of both P waves and Rayleigh waves in the noise, from the cross-correlation and coherence between noise recordings at surface and in deep hole. Dziewonski and Landisman (1970) made use of the autocorrelations of earthquake codas containing the

multi-orbit Rayleigh and Love waves, to determine the average phase and group velocities of long-period surface waves along great circle paths. Ekström (2001) extended the method of Dziewonski and Landisman (1970) from earthquake recordings to long-period ambient noise to detect Rayleigh wave energy in seismic hum, and accordingly unveiled the dominant 6-month periodic pattern in the intensity of global seismic hum. Anyhow, the seismological community had been primarily relying on active sources or earthquakes to probe the inner structure of the Earth, until the successful recovery of the surface-wave parts of the Green function of medium from earthquake codas (Campillo and Paul 2003) and ambient seismic noise (Shapiro and Campillo 2004; Sabra et al. 2005a, b; Shapiro et al. 2005) by using the correlation technique. Since then, great interests have been aroused and studies based on the noise correlation technique enjoys a boom. Nowadays, the emerging correlation technique has been a routine method in seismology.

Before the introduction into seismology, the correlation method to recover Green functions from diffuse wavefield has been discussed and successfully applied in helioseismology (e.g., Duvall et al. 1993; Woodard 1997; Kosovichev et al. 2000; Rickett and Claerbout 2000) and acoustics (e.g., Weaver and Lobkis 2001; Lobkis and Weaver 2001; Derode et al. 2003a, b; Roux and Fink 2003). The theory behind the validity of approximating Green functions with noise correlation functions has been discussed by many authors (e.g., Weaver and Lobkis 2001, 2004; Lobkis and Weaver 2001; Wapenaar 2003, 2004, Snieder 2004, 2006, 2007; Roux et al. 2005b; Wapenaar et al. 2005, 2006, Nakahara 2006a, b; Sánchez-Sesma and Campillo 2006; Wapenaar and Fokkema 2006; Sánchez-Sesma et al. 2006; Godin 2006, 2007; Gouédard et al. 2008c; Tsai 2009, 2010, Sato 2009, 2010; Margerin and Sato 2011; Weaver 2013; Boschi and Weemstra 2015; Snieder and Sens-Schönfelder 2015; Wapenaar and Thorbecke 2017), under certain theoretical frameworks (Born approximation, fluctuation-dissipation theorem, modal equipartition, multiple scattering regime, radiative-transfer regime, reciprocity theorem, correlation representation theorem, stationary-phase approximation, time-reversal symmetry, …) and presumptions on the model geometry (one- or two- or three-dimensional, open or bounded, recorded on surface or in boreholes, ...), source characteristics (active or passive, stationary or transient, surrounding or one-sided, uniformly or non-uniformly distributed, …) and medium properties (acoustic or elastic, deterministic or random, attenuating or lossless, homogeneous or inhomogeneous, …). The theoretical studies have proved that it is the time derivative of the noise correlation function, rather than the correlation function itself, that converges towards the Green function of the system (e.g., Weaver and Lobkis 2001; Snieder

2004; Roux et al. 2005b; Weaver 2013; Campillo and Roux 2015). However, in real practices, it is conventional to use the correlation function itself rather that its time derivative to approximate the Green function, to prevent undesirable noise from performing the time derivative. In a finite frequency bandwidth, the waveform of the correlation function resembles that of the derivative, with a $\pi/2$ phase shift as the principal difference [see Figure 3 of Roux et al. (2005b)]. Besides, the derivative does not affect group velocity estimates. The correlation function is also referred to as the empirical Green function sometimes. Besides the theoretical works, the correlation method has also been validated through numerical modeling (e.g., Derode et al. 2003b; Paul et al. 2005; Draganov et al. 2006) and experiments in laboratory (e.g., Weaver and Lobkis 2001; Lobkis and Weaver 2001; Derode et al. 2003a; Larose et al. 2004, 2006c, 2007) and fields (e.g., Roux and Kuperman 2004; Draganov et al. 2007; Gouédard et al. 2008b).

In contrast to the parallel progress in the theoretical works, numerical modelling, experiments and practical applications in the fields of ultrasonics and marine acoustics, the development of the correlation technique in seismology started with real-data applications preceding the other aspects. The pioneering studies in seismology (Campillo and Paul 2003; Shapiro and Campillo 2004; Sabra et al. 2005a, b; Shapiro et al. 2005) testified the feasibility of applying the correlation method to random seismic noise by comparing with the results of earthquake recordings, and accordingly opened a new path to turning noise into seismic signals.

In the field of exploration seismology, the most original idea concerning the correlation technique is generally attributed to Claerbout (1968), who provided a theory for synthesizing reflection response of a horizontally layered medium from the autocorrelation of the acoustic transmission response, as if there were collocated source and receiver placed on the surface. The theory had been applied to micro-earthquake data to synthesize the pulse-echo response (pseudo-reflection seismograms) and accordingly to invert the velocity structure of shallow layers (Scherbaum 1987a, b; Tsutsui 1992; Daneshvar et al. 1995). Claerbout also conjectured that "*by cross-correlating noise traces recorded at two locations on the surface, we can construct the wavefield that would be recorded at one of the locations if there was a source at the other*" (Rickett and Claerbout 1996). However, the first field experiment attempting to attest Claerbout's conjecture led to inconclusive results (Baskir and Weller 1975). In 1987, another field experiment with 4096 geophones was implemented on the Stanford campus. Unluckily, it failed again to justify the conjecture (Rickett and Claerbout 1999), possibly due

to the short duration and poor quality of the records. Despite of the inconclusive tests in exploration geophysics, the application of the noise correlation technique succeeded in helioseismology (Duvall et al. 1993) and ultrasonics (Weaver and Lobkis 2001; Lobkis and Weaver 2001). Almost during the meantime as the introduction of the correlation technique into natural seismology (Campillo and Paul 2003; Shapiro and Campillo 2004; Shapiro et al. 2005), substantial progress in theories (Wapenaar 2003, 2004; Snieder 2004) and numerical examples (Schuster et al. 2004) was also achieved in the field of exploration seismology. In contrast to the situation in natural seismology that the stochastic source process is hardly known, the correlation method for the exploration purpose is primarily applied to seismic recordings from active sources, the source wavelets of which are controllable or easy to obtain. In the field of exploration seismology, the correlation technique is termed **seismic interferometry** (e.g., Schuster et al. 2004; Draganov et al. 2006; Curtis et al. 2006) or **virtual source method** (e.g., Bakulin and Calvert 2004, 2006; Snieder et al. 2006a; Mehta et al. 2007). Nowadays, the term seismic interferometry, coined by Schuster et al. (2004) and formerly referred to by Schuster (2001) as interferometric imaging, has been accepted as a synonym of the correlation technique by the whole seismological community and widely adopted in the publications. More related nomenclatures, like Redatuming and Marchenko, have been introduced/invented in exploration seismology. It appears that scientific researchers having connections with industry are more aware of/better at packaging and promoting new concepts/techniques.

2.1.2. Applications

Both body waves and surface waves can be extracted from noise correlations (see Figure 2.1 for a real-data example). Once the seismic phases are reconstructed, classical seismological methods, like seismic tomography, can be implemented. Seismic signals extracted from noise can be used alone, or joint with earthquake data to improve imaging resolutions (e.g., Yao et al. 2006, 2010; Liu et al. 2014a). Seismic imaging using the noise correlation technique is sometimes mentioned as **passive (seismic) imaging** (e.g., Wapenaar 2003; Snieder 2004; Weaver and Lobkis 2005; Campillo 2006; Larose 2006; Roux 2009). The greatest advantage of the emerging noise-based techniques is the availability in the absence of earthquakes or active sources. Active seismic survey is expensive and inconvenient to implement in densely inhabited regions, whereas passive imaging with ambient seismic noise can be cost efficient, environmentally friendly and easier to implement. Earthquakes occur sparsely over time and

are dominantly distributed along plate boundaries. With the noise correlation technique, the observation period can be largely shortened because there is no need to wait for enough number of significant seismic events. Besides, a better ray coverage can be achieved in passive imaging. Another superiority is the shorter dominant periods of the microseismic noise compared to the dominant periods of surface waves from distant large earthquakes. Shorter periods imply a higher resolution that is suitable for crustal imaging. However, short-period surface waves emanating from shallow earthquakes are attenuated rapidly by the scattering due to the presence of heterogeneities in the crust.

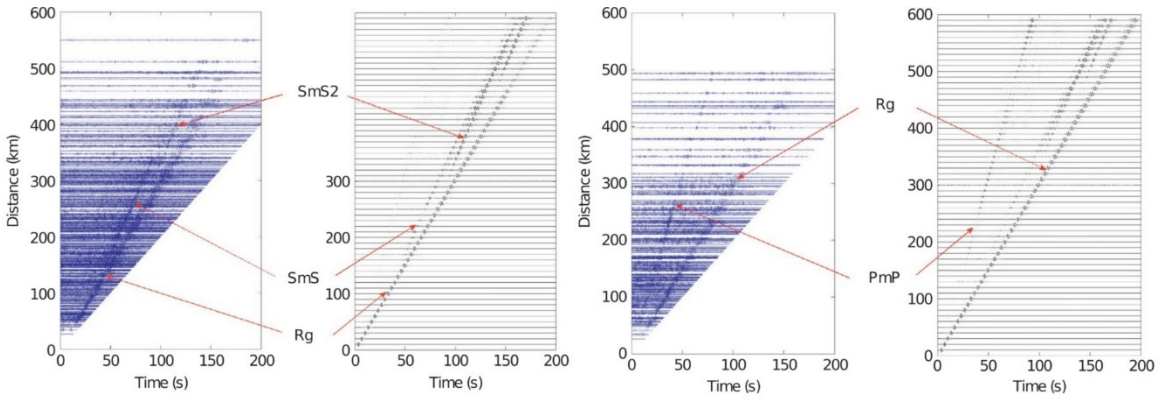

Figure 2.1. Emergence of coherent body wave reflections and Rayleigh waves in the correlation functions of seismic noise recorded by the LAPNET array in Finland (left: cross-correlation functions between the vertical components of seismic noise in comparison with the vertical component of synthetic seismograms for a vertical point force at the surface; right: cross-correlation functions between the radial components of seismic noise in comparison with the radial component of synthetic seismograms for a horizontal point force at the surface). The waveforms are bandpass filtered between 0.5 and 1.0 Hz. Adapted from Figure 6 of Poli et al. (2012b). Love waves are also reconstructed from the cross-correlation functions between transverse components but not shown here (see the reference for more information).

2.1.2.1. Surface Waves

Due to the fact that noise sources are primarily located on the surface of Earth, the ambient seismic wavefield is dominated by surface waves (see Chapter 1 for review). As a consequence, the first applications of ambient noise correlations were primarily the retrieval of surface waves for crustal shear wave velocity tomography (e.g., Shapiro and Campillo 2004; Paul et al. 2005;

Sabra et al. 2005c, a, b; Shapiro et al. 2005; Gerstoft et al. 2006b; Yao et al. 2006). Both Rayleigh waves and Love waves have been successfully extracted from seismic noise, since the very early stages of seismic interferometry (Campillo and Paul 2003). However, in most noise-correlation applications, only the vertical components of continuous seismograms are correlated to extract the dominating (fundamental) Rayleigh waves. The extraction of Love waves from ambient noise is not uncommon (e.g., Nishida et al. 2008; Lin et al. 2008; Bensen et al. 2008; Huang et al. 2010; Behm and Snieder 2013; Boué et al. 2014b; Mordret et al. 2015; Tomar et al. 2017; Ekström 2017), but relatively rare. The reason could be that the quality of horizontal components of seismograms are not as good as that of the vertical component, in that the horizontal components are more vulnerable to be affected by local site conditions and changes in ambient temperature and atmospheric pressure (Zürn et al. 2007; Bormann and Wielandt 2013; Tanimoto et al. 2015).

Till now, the noise-based surface wave tomography is undoubtedly the most common application of seismic interferometry. The noise-based tomography has achieved great successes at various spatial scales, from local (e.g., Brenguier et al. 2007; Renalier et al. 2010; Nakata et al. 2016; Boué et al. 2016; Lehujeur et al. 2017), to regional (e.g., Shapiro et al. 2005; Sabra et al. 2005b; Gerstoft et al. 2006b; Yao et al. 2006, 2008, Lin et al. 2007, 2008; Moschetti et al. 2007; Verbeke et al. 2012; Boué et al. 2014b), to continental (e.g., McNamara and Buland 2004; Yang et al. 2007; Zheng et al. 2008; Bensen et al. 2008; Ekström 2017), and until planetary scale (e.g., Nishida et al. 2009; Haned et al. 2016). Note that the noise-base velocity measurements are not only determined by the medium properties, but also affected by the spatial distribution of noise sources (Gouédard et al. 2008a; Weaver et al. 2009; Yao and van der Hilst 2009; Froment et al. 2010; Fichtner 2014, 2015). Some authors adopted the cross-validation, a method commonly used in machine learning, to test the sensitivity of the noise-based inversion to the distribution of noise sources. For instance, Ekström (2017) divided the dataset into winter and summer subsets corresponding to distinct oceanic microseism source distribution, and affirmed the reliability of the tomographic models by comparing the results for two subsets. With array observations, the velocity dispersion can also be estimated by other methods like SPAC (Aki 1957) or its variants (e.g., Bettig et al. 2001), beamforming (e.g., Harmon et al. 2008) and FK analysis (e.g., Capon 1969). Harmon et al. (2008) applied both the beamforming and correlation techniques to seismic noise recorded by a regional seismic array. They showed that the results of dispersion measurements for Rayleigh waves derived from both methods agree within 1%. Gouédard et al. (2008a) compared the performance of the

modified SPAC method, high-resolution FK analysis and the noise correlation technique in estimating the velocity dispersion of surface waves, with synthetic experiments for a complex layered model at a local scale. They showed that the correlation technique provides highly accurate measurements in a wider frequency band than other methods. The correlation technique is not the unique way for seismic velocity estimates, but it has distinct advantages in retrieving explicit signals that are directly associated to the Green functions of the propagation medium. Besides, in contrast to the average dispersion curve derived from the SPAC and FK methods for 1-D layered structure inversion, the correlation technique provides inter-receiver measurements available for 2-D or 3-D tomographic inversion.

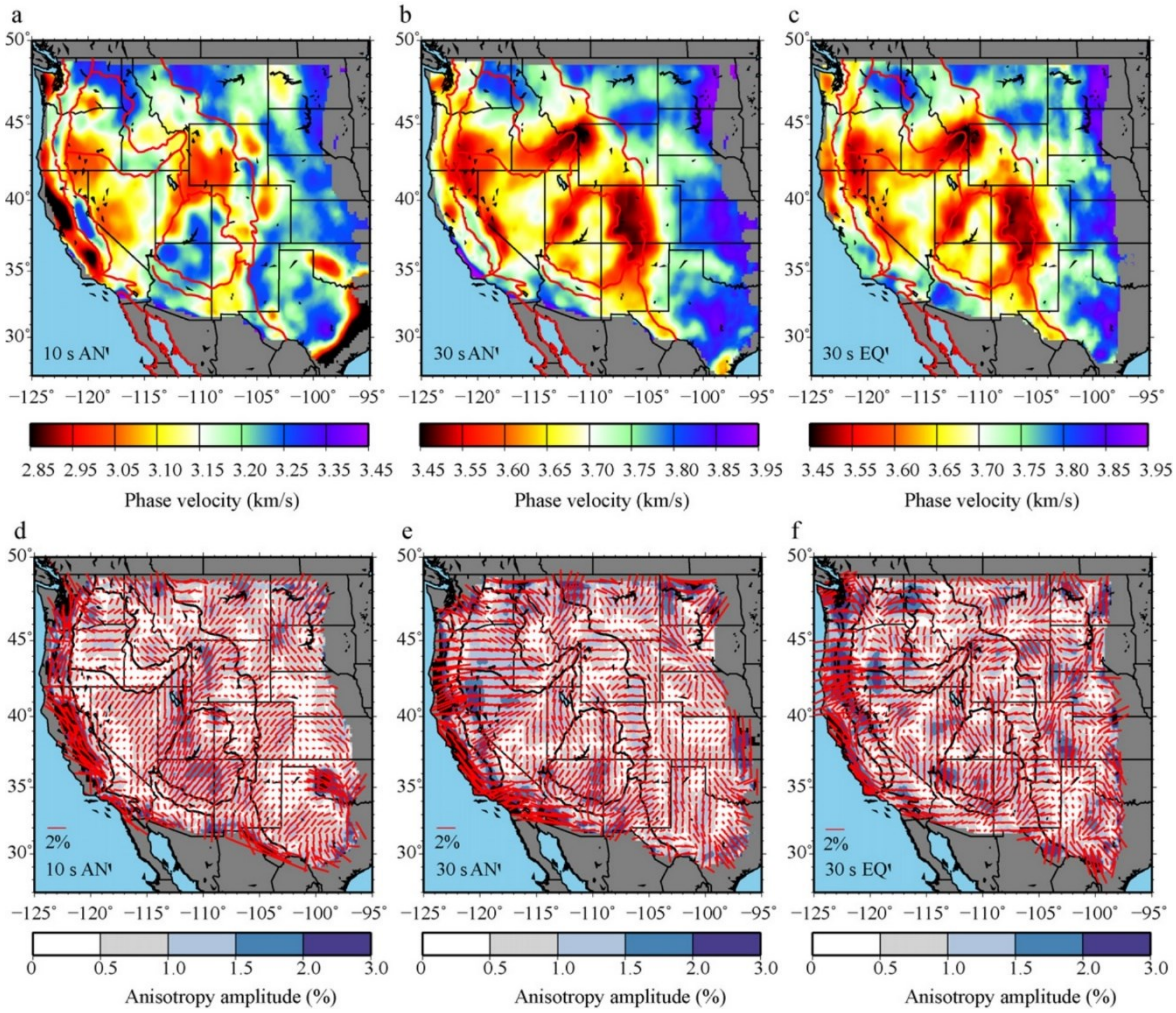

Figure 2.2. Maps of background phase velocity (a and b) and azimuthal anisotropy (d and e) of 10-sec and 30-sec period Rayleigh waves in western United States, in comparisons with the results obtained from teleseismic earthquake data (c and f). Reproduced from Figure 7 of Ritzwoller et al. (2011).

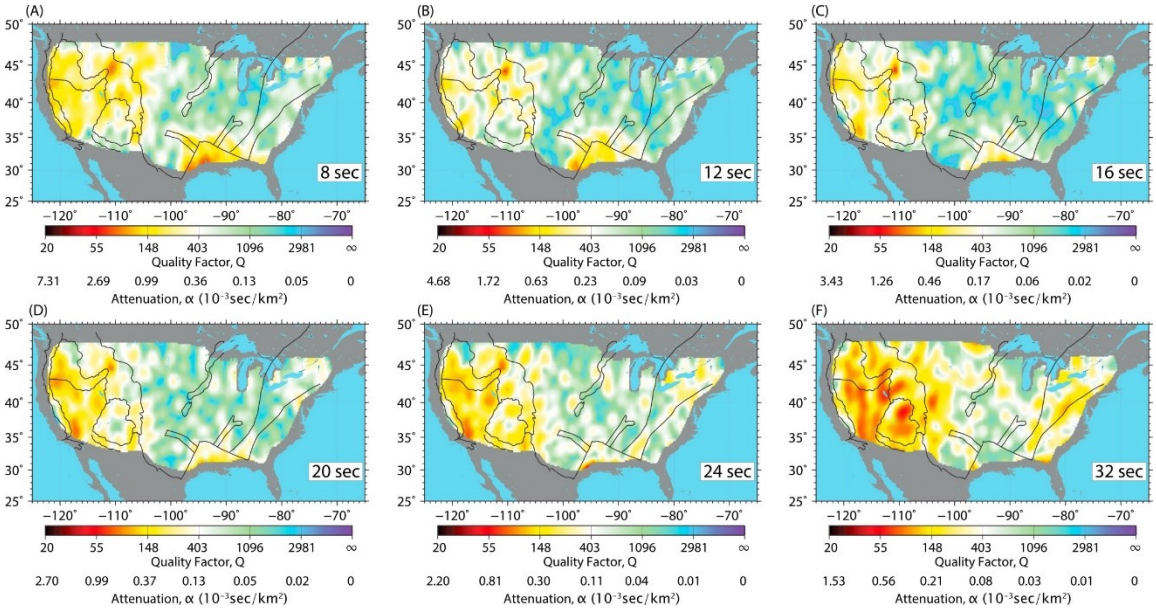

Figure 2.3. Maps of attenuations across the United States measured from noise correlations for different seismic periods. Reproduced from Figure 9 of Bowden et al. (2017).

The noise-based measurements can give rise to not only the background seismic wave speeds, but also the quantitative information on seismic anisotropy. Azimuthal anisotropy can be inferred from the directional dependence of the noise-based velocity measurements (e.g., Yao et al. 2010; Ritzwoller et al. 2011), and radial anisotropy can be obtained by combining the noise-based measurements for both Rayleigh and Love waves (e.g., Huang et al. 2010; Mordret et al. 2015; Tomar et al. 2017). Figure 2.2 demonstrates the noise-based tomography of seismic velocity and azimuthal anisotropy with a large seismic array (Ritzwoller et al. 2011). The amplitude of anisotropy is commonly within several percent (no more than 3% as for the example in Figure 2.2). The noise-base inversion for seismic anisotropy is particularly affected by the uneven distribution of noise sources, which may result in biased velocity estimates and apparent anisotropy at a similar level. Noise-based inversion on seismic attenuation has also been proposed to be feasible but still under debate (e.g., Prieto et al. 2009; Weaver 2011; Lin et al. 2011; Lawrence and Prieto 2011; Weemstra et al. 2013; Zhang and Yang 2013; Weemstra et al. 2014; Bowden et al. 2015, 2017; Liu et al. 2015; Stehly and Boué 2017). To retrieve seismic attenuations from noise correlations, Larose et al. (2008) suggested to avoid any normalization in the pre-processing of noise data. Campillo and Roux (2015) suggested to avoid mixing noise correlations of different station pairs arranged in varying azimuths. Figure 2.3 shows practical examples for the noise-based imaging of surface wave attenuation across

the United States at different seismic periods, by tracking the amplitudes of wavefronts derived from ambient noise correlations (Bowden et al. 2017).

The resolvable period band of surface waves is constrained by the observation geometry (array aperture and interstation spacing) and, of course, also by the nature of ambient wavefield. The depth sensitivity of surface waves depends on the seismic period, with larger penetrating depth at longer periods. Surface waves extracted from microtremors, microseisms and seismic hum, can be used to infer properties of the shallow structure, crust and upper mantle. The extraction of body waves from seismic noise is particularly attractive for its capability to probe the deep Earth.

2.1.2.2. Body Waves

Body waves in ambient noise had been detected from array observations decades ago (Backus et al. 1964; Douze 1967; Lacoss et al. 1969; Vinnik 1973). Specific ray paths such as P, PP and PKP waves, have been identified through array beamforming of noise data themselves or their correlations (e.g., Gerstoft et al. 2008; Koper et al. 2009, 2010; Zhang et al. 2010b; Landès et al. 2010; Pyle et al. 2015; Liu et al. 2016a; Nishida and Takagi 2016). Roux et al. (2005a) seems to be the first that has extracted explicit P signals from ambient noise, within a range of about 11 km. The noise-derived direct P waves were linearly polarized, with arrival times in agreement with the results predicted by an existing velocity model. Authors have also retrieved from the correlations of earthquake codas or ambient noise body wave reflections from discontinuities in shallow layers (e.g., Draganov et al. 2007, 2009), crust (e.g., Poli et al. 2012b), lithosphere (e.g., Ruigrok et al. 2010; Sun and Kennett 2017), mantle transition zone (e.g., Poli et al. 2012a; Feng et al. 2017), and core-mantle boundary (e.g., Boué et al. 2013a; Poli et al. 2015; Spica et al. 2017). Autocorrelations are of particular popularity in extracting body wave reflections to image discontinuities in shallow layers until the lower boundary of upper mantle (e.g., Ito and Shiomi 2012; Ito et al. 2012; Tibuleac and von Seggern 2012; Gorbatov et al. 2013; Kennett et al. 2015; Taylor et al. 2016; Oren and Nowack 2017; Phạm and Tkalčić 2017). Taking advantage of the antipodal focusing effects (Rial 1978; Retailleau et al. 2014), core phases have been extracted from auto-correlations or from cross-correlations of antipodal station pairs (Lin and Tsai 2013). At other distances, the extraction of core phases has also been affirmed (e.g., Lin et al. 2013; Xia et al. 2016; Wang and Song 2017). A comprehensive

reconstruction of global sections was accomplished by Nishida (2013), Boué et al. (2013a, 2014a) and Phạm et al. (2018). Seismic anisotropy can also be inverted from the noise-derived body waves (e.g., Miyazawa et al. 2008; Lewis and Gerstoft 2012; Wang et al. 2015; Wang and Song 2017; Chen et al. 2017). However, studies on seismic attenuation using noise-derived body waves appear still missing.

2.1.2.3. Scattering and Coda Waves

Seismic scattering due to medium heterogeneity is another important factor other than the intrinsic absorption that attenuates waves. In seismic interferometry, the effect of scattering is two-sided. Discontinuities and scatterers act as secondary sources redistributing the wavefield. The scattering makes the wavefield more close to the equipartition/diffusion status and accordingly facilitates the recovery of the empirical Green functions from seismic noise (Paul et al. 2005; Wapenaar 2006; Gouédard et al. 2008b; Larose et al. 2008; Campillo and Roux 2015). However, the scattering also attenuates the coherent waves passing across both receivers that contribute to the recovery of the Green function. The two effects are in competition and when the latter dominates in the case of strong scattering or large propagation distances, the reconstruction of the Green function is degraded by the scattering (Larose et al. 2008).

Numerical and real-data experiments have revealed that, in addition to the recovery of ballistic signals, coda arrivals can also be reconstructed from noise correlations (e.g., Gouédard et al. 2008b; Larose et al. 2008; Sato 2009, 2010; Dylan Mikesell et al. 2012; Colombi et al. 2014b; Hejazi Nooghabi et al. 2017). These studies affirmed that the scattering waves related to specific scatterers can be observed in the coda waves of noise correlations. However, they are not approving that the entire codas are perfectly recovered. A general mathematical proof on the equivalence between Green function and noise correlation function including the coda parts is provided by de Verdiere (2006), nevertheless, with rigorous prerequisite that the noise sources are uniformly distributed.

Some authors have paid attentions to the decay of the reconstructed coda waves in the noise correlations. Sens-Schönfelder and Wegler (2006) fitted a diffusion model to the coda envelopes of empirical Green function tensor retrieved from ambient noise in the context of a volcano. Wegler and Sens-Schönfelder (2007) estimated the coda decay rate from the envelope

of auto-correlation functions at a station near the Mw6.6 2004 Mid-Niigata earthquake in Japan. In principle, noise correlations are promising to infer scattering characteristics of the media (Weaver 2013). However, efforts on a formal inversion are still very rare. The studies of Olivier et al. (2015) and Chaput et al. (2015, 2016) are among the fewer trials.

2.1.2.4. Monitoring

Another important application of seismic interferometry is to detect changes in medium properties, a task that essentially relied on repeated earthquakes (e.g., Poupinet et al. 1984) or active sources (e.g., Niu et al. 2008). The noise-based measurements are easy to repeat and of low cost and high resolutions (generally at an order of 10^{-4}), enabling seismic interferometry an efficient monitoring tool. The passive monitoring technique has been applied in a wide range of context, to detect temporal changes in seismic velocity or anisotropy associated with earthquakes or active faults (e.g., Brenguier et al. 2008a; Wegler et al. 2009; Chen et al. 2010; Maeda et al. 2010; Durand et al. 2011; Lewis and Gerstoft 2012; Minato et al. 2012; Tonegawa et al. 2013; Froment et al. 2013; Riahi et al. 2013; Liu et al. 2014b; Obermann et al. 2014; Richter et al. 2014; Soldati et al. 2015; Stehly et al. 2015; Taira et al. 2015; Chaves and Schwartz 2016; Hobiger et al. 2016; Saade et al. 2017), volcanos (e.g., Grêt et al. 2005; Brenguier et al. 2008b, 2011, 2016; Duputel et al. 2009; Mordret et al. 2010; De Plaen et al. 2016), tides (e.g., Takano et al. 2014; Hillers et al. 2015b; Planès et al. 2017), atmospheric pressure and temperature (e.g., Larose et al. 2006a; Tanimoto et al. 2008; Sens-Schönfelder and Larose 2008; Eric and Stephen 2009; Hadziioannou et al. 2009; Richter et al. 2014), precipitation or water table (e.g., Sens-Schönfelder and Wegler 2006; Meier et al. 2010; Hillers et al. 2014; Ugalde et al. 2014; Larose et al. 2015; Lecocq et al. 2017), glacial mass (e.g., Mordret et al. 2016), landslide (e.g., Mainsant et al. 2012; Larose et al. 2015), structural failure (e.g., Larose et al. 2015; Salvermoser et al. 2015; Planès et al. 2016), etc.

The coda waves in noise correlations have been widely employed to infer seismic velocity changes in medium, by using the moving-window cross-spectral analysis (Poupinet et al. 1984) or the stretching method (Lobkis and Weaver 2003; Sens-Schönfelder and Wegler 2006). Coda-based measurements are believed to be more sensitive to weak changes and more robust than measuring the phase delay between direct ballistic waves (e.g., Hadziioannou et al. 2009; Colombi et al. 2014b).

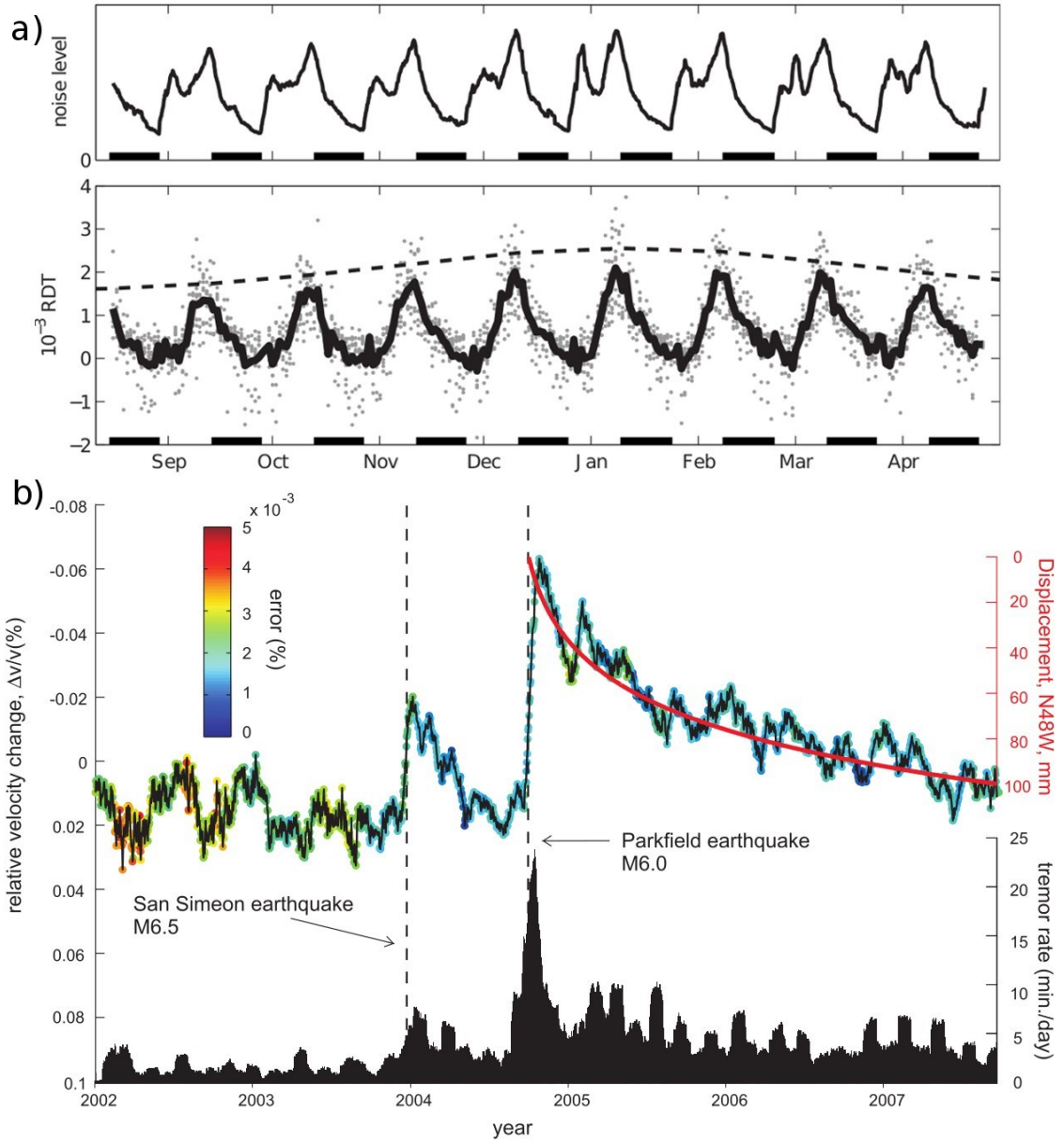

Figure 2.4. a) Temporal variations in lunar seismic noise level and noise-derived relative delay time (RDT). The lunar seismic noise data were recorded by the Apollo experiments. Light gray dots and thick solid curve denote individual and average measurements of RDT, respectively. Dashed curve represents the qualitative course of the inflow of thermal energy at lunar noon. Bold line segments at panel bottom indicate lunar night. Reproduced from Figure 2 of Sens-Schönfelder and Larose (2008). b) Temporal changes in seismic velocity estimated from noise correlation functions, in comparisons with the post-seismic surface displacements measured by GPS paralleling the San Andreas Fault and the 30-day running mean tremor activity near Parkfield. Reproduced from Figure 3 of Brenguier et al. (2008b).

There have been reports on the observations of precursory velocity changes before disaster events like volcanic eruption (e.g., Wegler et al. 2006; Brenguier et al. 2008b) and landslide (e.g., Mainsant et al. 2012). However, a confident observation of velocity changes prior to large earthquakes is still missing, though the changes associated with co-seismic failure and post-seismic relaxation have been intensively reported (e.g., Wegler and Sens-Schönfelder 2007; Brenguier et al. 2008a; Wegler et al. 2009; Froment et al. 2013; Liu et al. 2014b; Obermann et al. 2014; Stehly et al. 2015).

Figure 2.4 presents an example of noise-based measurements of seismic velocity changes in the shallow lunar crust resulting from the temperature variations caused by periodic solar heating, and an example of noise-measured seismic velocity changes related to co-seismic damage in the shallow layers and to deep co-seismic stress change caused by large earthquakes, and post-seismic stress relaxation within the San Andreas Fault Zone. Note that for the monitoring purpose, the equivalence between correlation function and Green function is not a necessary condition (Hadziioannou et al. 2009). Instead, the stability of measurements is most critical to passive monitoring.

2.1.2.5. Noise Source Location

As mentioned earlier, ambient seismic wavefield contains information of not only the sampled structure but also the sources exciting the ambient noise. It is feasible to investigate noise sources using noise correlation functions. One can infer the directions of dominant noise sources and their temporal variations from the particle motions of surface waves in ambient wavefields (e.g., Davy et al. 2015) or from the azimuthal variations of the amplitude of surface waves reconstructed from noise correlations (e.g., Stehly et al. 2006). More knowledge on the noise sources radiating ambient surface waves can be inferred from grid-search results based on noise-derived travel times (e.g., Shapiro et al. 2006), beamer of noise-derived signals (e.g., Ermert et al. 2016, 2017; Retailleau et al. 2017), or envelopes of noise correlations (e.g., Sadeghisorkhani et al. 2016). Figure 2.5 shows an example of localized, energetic noise sources outside the stationary-phase regions, located by beamforming the coherent, spurious early surface waves retrieved from noise correlations between European and North American stations. A higher resolution of noise source imaging can be obtained by back-projecting the beamer output of seismic noise or noise-derived body waves onto surface grids (e.g., Zhang et

al. 2010b; Landès et al. 2010; Euler et al. 2014; Pyle et al. 2015). An example of the body-wave backprojection can be found in Figure 1.25. The computation of noise correlations is not mandatory. There are also publications that directly beamed seismic noise (e.g., Vinnik 1973; Obrebski et al. 2013; Liu et al. 2016a; Nishida and Takagi 2016; Neale et al. 2017a, b; Meschede et al. 2017; Retailleau et al. 2018). The results of noise source imaging based on noise beamer and noise correlation beamer should be almost identical (Ruigrok et al. 2017). Since noise interferometry can provide explicit signals, it is more intuitive to work with noise correlations.

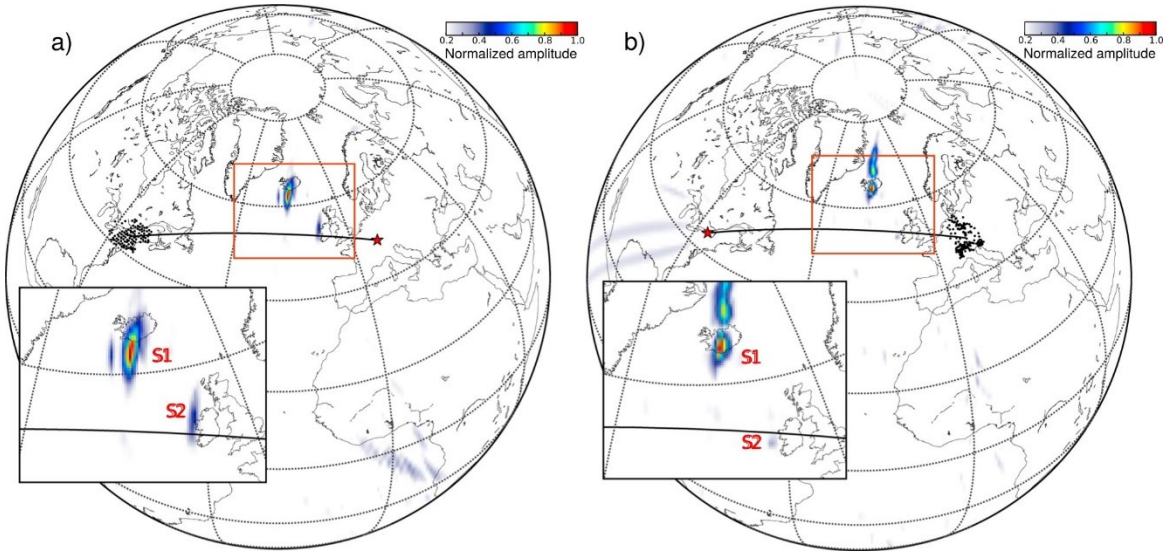

Figure 2.5. Grid-search imaging to locate noise sources responsible for the presence of spurious surface waves in the period band of 15 to 25 sec in the noise correlations between a station in Europe and a network in the United States (a), and between a station in the United States and a network in Europe (b). Reproduced from Figure 5 of Retailleau et al. (2017).

The empirical Green functions reconstructed from noise correlations suffer from the trade-offs between the subsurface structure and the distribution of noise sources (Weaver et al. 2009; Yao and van der Hilst 2009; Froment et al. 2010; Fichtner 2014, 2015; Fichtner et al. 2017). The ideal, uniform distribution of noise sources for the perfect reconstruction of the Green function is typically not satisfied in seismological observations. The worse fact is that, neither the structure nor the noise sources are perfectly known. In practical applications, it is typical to ignore one and focus on inverting only the other. In the case of noise-base tomography, it is commonly assumed that the Green function of the medium between stations can be well approximated by the ensemble-averaging correlation, or cross-validate the results by splitting

the dataset into subsets or by comparing with results from other sources. Efforts have been made to reduce the effects of source directivity on the reconstruction of Green functions, by applying some specific processing to the noise data (e.g., Bensen et al. 2007) or to the correlations (e.g., Roux 2009; Moreau et al. 2017). In the case of noise source location, the complexity in the subsurface structure is generally ignored, which may lead to significant bias in the source location (Liu et al. 2016a; Nishida and Takagi 2016).

2.1.2.6. High-Order Correlations

The inter-receiver noise correlation function contains both ballistic and coda arrivals. One can continue to apply the correlation technique to the coda parts of noise correlations, which also leads to the reconstruction of ballistic waves and codas between two receivers. The coda correlations require fewer noise sources and show less sensitivity to the noise source distribution (Gouédard et al. 2008b; Stehly et al. 2008; Froment et al. 2011; Colombi et al. 2014b; Hejazi Nooghabi et al. 2017), whereas a uniform distribution of noise sources is generally required by the interferometry of ballistic wavefields to guarantee the convergence of the correlation function towards the Green function. The correlation of coda waves builds both the ballistic part and the coda part of the Green function, whereas the correlation between ballistic paths contributes fewer and merely to the reconstruction of ballistic waves (Hejazi Nooghabi et al. 2017). For short, Stehly et al. (2008) denoted the conventional ambient noise correlation as C^1 and the correlation of coda waves of C^1 as C^3. The computation of correlations of codas of correlations can proceed recursively and thereby it has been named as iterative or high-order correlations, or in a more compact form, C^{2N+1} (Stehly et al. 2008; Garnier and Papanicolaou 2009; Froment et al. 2011). In this sense, the correlation of earthquake codas can be denoted as C^2 and this family of high-order correlations as C^{2N}. As for the family of C^{2N+1}, in general, C^3 would be sufficient. Higher-order correlations like C^5 are of course feasible but not attractive, since they do not bring further improvements (Froment et al. 2011).

A theoretical study on C^3 was provided by Garnier and Papanicolaou (2009) based on the stationary-phase analysis. The empirical Green function between a pair of stations operating in different time periods, can be obtained from the C3 functions by taking other stations having common operation times with both stations as virtual sources (Curtis and Halliday 2010; Ma and Beroza 2012). Spica et al. (2017) extracted ScS waves from C^3 to image the core-mantle

boundary under Mexico at a regional scale. The recovery of amplitude is more sensitive to the distribution of noise sources than that of the phase (Yoritomo and Weaver 2016). Zhang and Yang (2013) compared Rayleigh wave attenuations of the western United States derived from C^3 and from earthquake data, and concluded that C^3 can effectively reduce bias caused by the uneven distribution of noise sources and accordingly allows for more reliable attenuation estimates from seismic noise. Haendel et al. (2016) estimated the attenuation of Love waves recovered from C^3 in the Euroseistest area of Greece.

2.1.2.7. More Applications

In addition to the typical applications introduced above, seismic interferometry can also be applied in evaluating existing tomographic models (e.g., Ma et al. 2008), predicting ground motions (Prieto and Beroza 2008; Denolle et al. 2013, 2014, 2018; Sheng et al. 2017), testing building response (e.g., Snieder and Şafak 2006; Prieto et al. 2010; Mordret et al. 2017), complementing the database of Green functions, event location (e.g., Barmin et al. 2011), network synchronization (e.g., Stehly et al. 2007; Sens-Schönfelder 2008; Xia et al. 2015; Xie et al. 2018), to cite only a few. Concerning the asymmetry in the acausal and causal parts of the correlation function caused by instrumental clock drift, the bias is a global shift of the whole correlation function, discriminable from the modification in waveform caused by changes in medium properties and the bias caused by the uneven illumination resulting from an uneven noise source distribution (Campillo and Roux 2015).

It is worth mentioning that Earth is not the only context nor the limit of size to apply interferometry. It can also be applied to seismograms recorded on other celestial objects. For instance, authors have applied the technique to lunar seismic noise for subsurface imaging and monitoring (Larose et al. 2005; Tanimoto et al. 2008; Sens-Schönfelder and Larose 2008). The passing of light-speed gravitational waves incited by big cosmic events (Abbott et al. 2016), induces feeble oscillations of objects, which, of course, include astrophysical bodies like Earth and Moon. Coughlin and Harms (2014c) correlated ambient seismic noise recorded by the Apollo lunar seismic array and borehole seismometers on Earth, and inferred from the Earth-Moon correlation analysis an upper limit of an order of 10^5 for an isotropic stochastic gravitational-wave background in the frequency band of 0.1 to 1 Hz.

2.2. Schematic of Seismic Interferometry

We have provided a quick literature review covering the historical and recent developments of the theories and applications of the correlation technique in the previous section. In this section, instead of striving to explain seismic interferometry by providing the theoretical details, we are devoted to interpreting the idea behind the correlation technique schematically, which allows for a more intuitive understanding of the method. Systematic review on interferometric theories can be found in recent book chapters like Sato et al. (2012) and Campillo and Roux (2015).

2.2.1. Typical Model Geometry

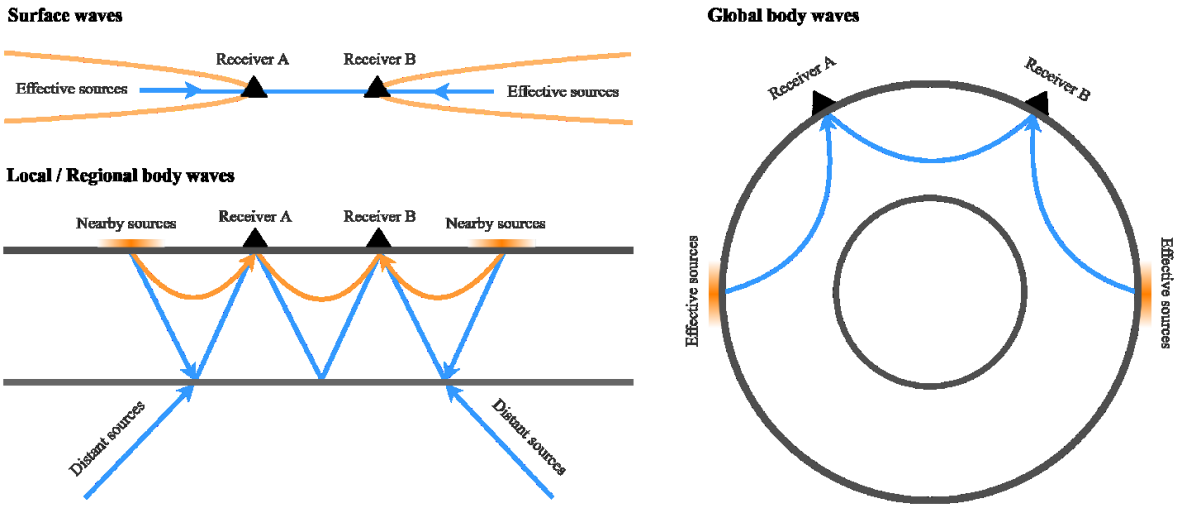

Figure 2.6. Geometry of typical configurations to retrieve seismic signals from noise correlation functions. Waves traveling along the shown paths imping at one receiver and then arrive at the other. The inter-receiver ballistic phases are extracted from the noise correlation functions as a result of the canceling of the common paths by the correlation operation. Higher-order multiples can also contribute to the reconstruction of signal but are not shown in the schematic of body waves.

We present in Figure 2.6 typical configurations of the observation system for extracting surface waves (e.g., Campillo and Paul 2003; Shapiro and Campillo 2004; Shapiro et al. 2005; Sabra et al. 2005b; Yao et al. 2006; Yang et al. 2007), local/regional transmitted/reflected body waves (e.g., Roux et al. 2005a; Draganov et al. 2007, 2009; Zhan et al. 2010; Ruigrok et al. 2010; Tibuleac and von Seggern 2012; Poli et al. 2012b, a; Feng et al. 2017), and teleseismic body

waves (e.g., Boué et al. 2013a, 2014a; Lin et al. 2013; Nishida 2013; Huang et al. 2015; Wang et al. 2015; Xia et al. 2016), from ambient noise or seismic coda waves. The reconstruction of surface waves from noise correlations have been investigated intensively and extensively (e.g., Snieder 2004; Gouédard et al. 2008c; Weaver et al. 2009; Yao and van der Hilst 2009; Froment et al. 2010; Wapenaar et al. 2010a). Here we devote the discussions, which generally hold in a general sense, primarily to the retrieval of body waves from seismic noise.

2.2.2. Signal Retrieval

The ambient wavefield can be described as a superposition of random waves emanating from diverse anthropic and/or natural noise sources with an arbitrary distribution of amplitudes (Aki 1965; Cox 1973; Weaver and Lobkis 2004; Nakahara 2006b). A noise source could be an "active" one that excites ambient ground vibrations, or a "passive" one that redirects waves emanating from other sources and accordingly acts as a secondary source. Active noise sources can be either man-made or natural, which are primarily distributed on or close to the Earth's surface. Passive noise sources could be seismic scatterers or discontinuities inside the Earth (Wapenaar 2006; Colombi et al. 2014a; Campillo and Roux 2015; Yoritomo and Weaver 2016). For the sake of simplicity, in this thesis we consider merely the surface noise sources if without instruction.

Provided that a wave emitted from any source located at the right place passes through one receiver and subsequently arrives at the other receiver, the correlation operation applied to the recordings at these two receivers will cancel the effect of the common path from the source to the first receiver, and retain only the phase delay due to the remnant path between the receivers (Figure 2.7). Here we refer to such noise sources as **effective sources** and by analogy, the paths of the correlated waves as **effective paths,** the corresponding rays as **effective rays**. The sharing of the common path between the correlated effective rays implies a common ray parameter, which corresponds to a stationary-phase location for the time delay varying with the source location. Due to the finite frequency bandwidth of data, the valid location of effective source is not confined to a single point but actually within a bounded region referred to as **effective region** hereafter. The time delay between correlated waves at two receivers from any source in the effective region is close enough to the expected time delay for the inter-receiver ballistic wave, meaning that the signals in the source-wise correlation functions are

coherent. The recovery of the ballistic signal is ascribed to the constructive stacking of the correlation functions for all sources in the effective region. The effective region has been referred to by authors as **end-fire lobe/area** (Roux and Kuperman 2004; Froment et al. 2010; Leroy et al. 2012; Boué et al. 2014a; Campillo and Roux 2015; it is a term introduced from the antenna theory in radio science), or **stationary-phase region/location** (Snieder 2004; Ruigrok et al. 2008; Wapenaar et al. 2010a; Olivier et al. 2015; Boschi and Weemstra 2015). Note that coherent waves emanating from an effective source can reach the receivers following paths other than the effective paths. In other words, even if the waves are emitted from the effective source, not all but only the ones propagating along the effective paths, are effective.

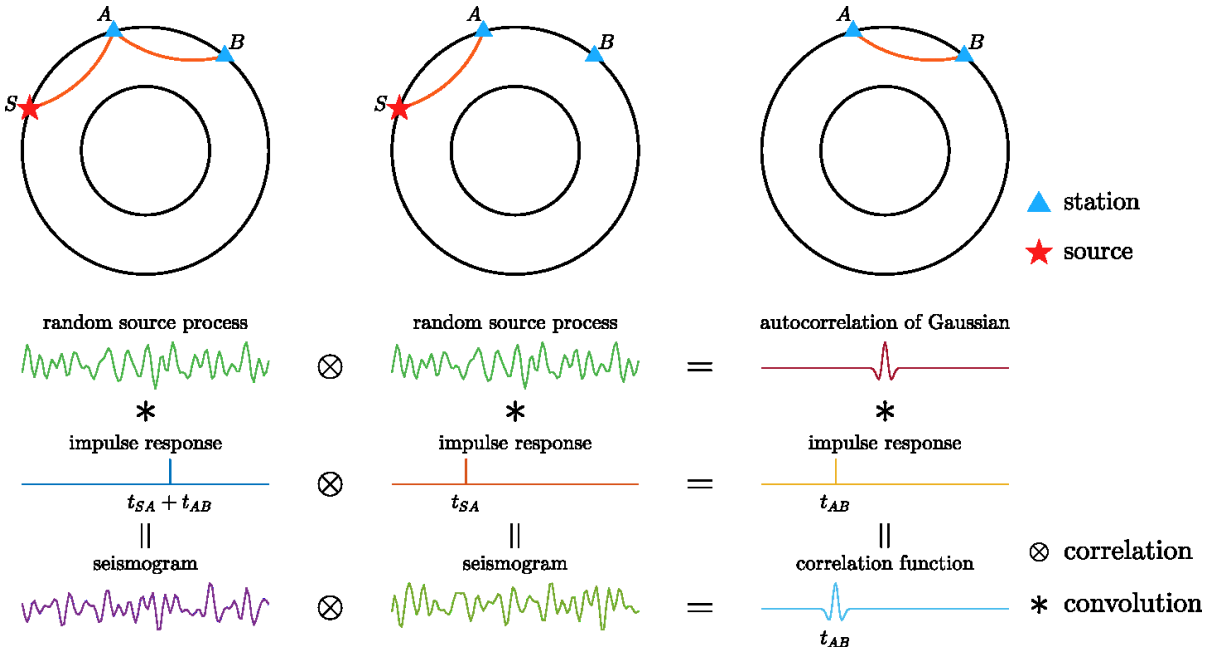

Figure 2.7. Signal recovery from the interferometry of coherent waves that emanate from an effective source and propagate following the effective paths. Neglecting the instrumental response, the noise recording is the source-receiver Green function of the medium convolved with the source process. The process of a stationary stochastic noise source is usually assumed to be Gaussian. The cross-correlation function between seismograms at two receivers equals to the convolution between the inter-receiver Green function and the autocorrelation of the random source time function. The correlated waves share a common path from the source to the first receiver, and thereby a common slowness. Higher-order surface-reflected multiples with more common paths extending to farther effective sources, can also contribute to the building of the ballistic signal from the correlation but are not shown for simplicity.

For coherent waves emitted from a noise source outside the effective region, a signal can also be built in the correlation function, but usually emerge at a time delay distinct from the expected traveltime between the two correlated receivers (Figure 2.8). The noise sources outside the effective region are accordingly termed **ineffective sources**. The time delays between correlated waves from ineffective sources varies remarkably and thereby the corresponding signals are incoherent with each other. When integrating over sources, such signals will be incorporated into the background noise in the correlation function which is mentioned as correlation noise in some literatures (e.g., Ruigrok et al. 2008), and under an ideal situation, such signals can cancel each other in the stacking, leading to a perfect recovery of the interstation Green function of the medium. Waves from ineffective sources can be scattered by heterogeneities in the effective region and some of the scattering waves can propagate following the effective paths. In such situations, we deem the scatterers in the effective region as secondary, passive sources, so that the ballistic wavefield from any ineffective source can be simply classified as **ineffective wavefield**.

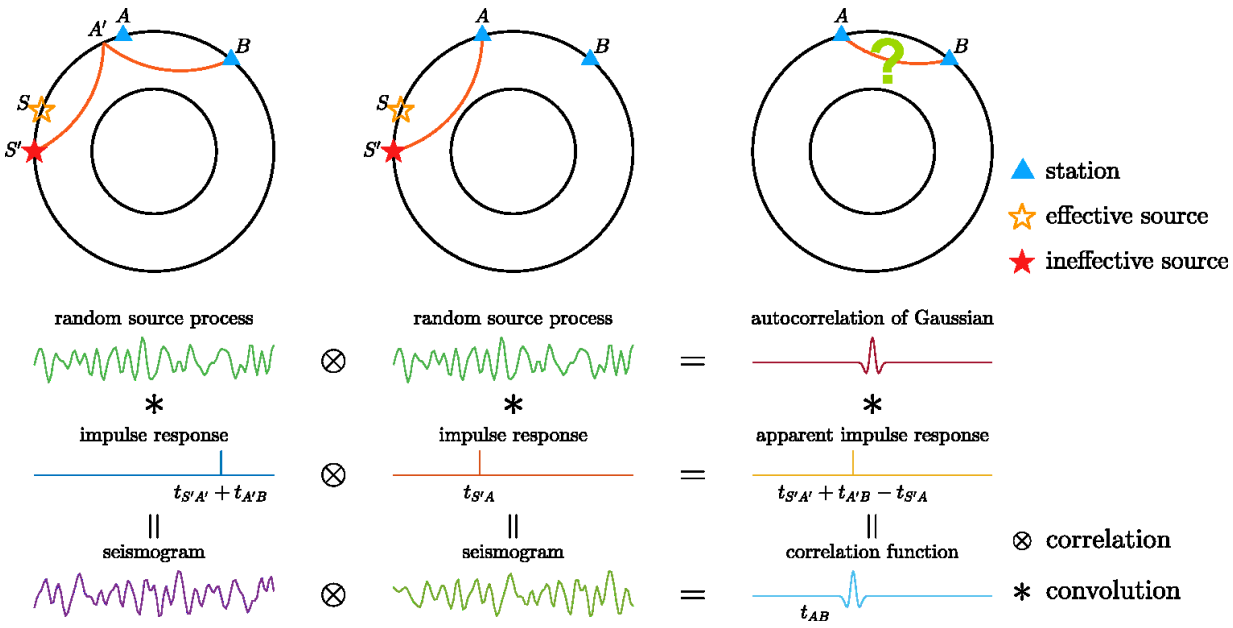

Figure 2.8. Inter-receiver interferometry of coherent waves emanating from an ineffective noise source. The correlating waves propagate along separated paths with different slownesses. In such a case, the signal built by the correlation operation is usually present at a time delay other than the expected traveltime between receivers. Such signals built from the correlations for ineffective sources at varying locations will be incorporated into the background noise in the final inter-receiver correlation function.

2.2.3. Source Averaging

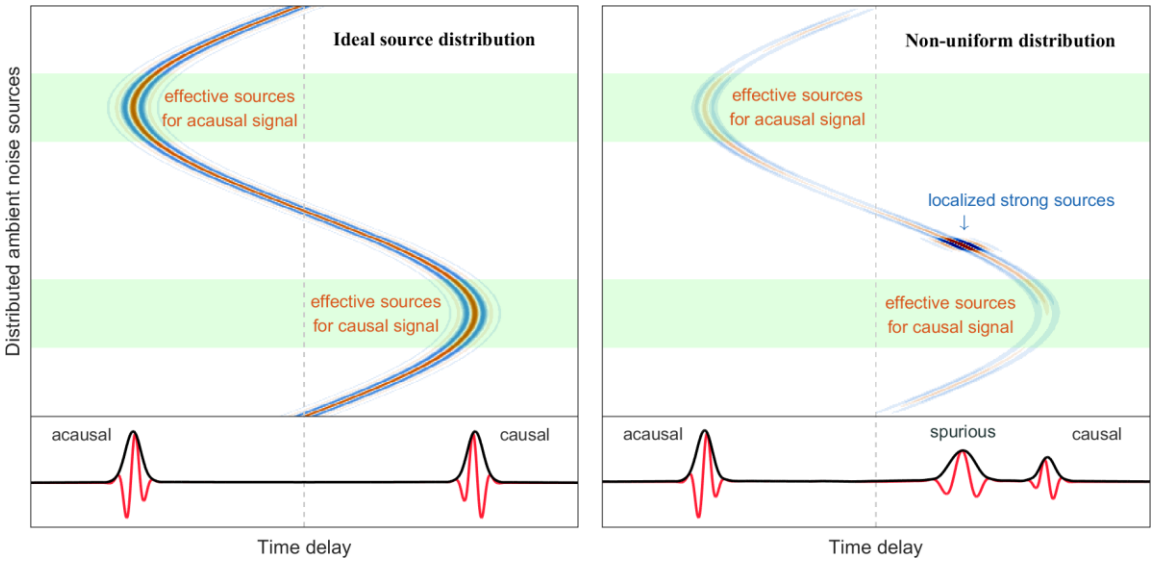

Figure 2.9. Construction of the causal and acausal signals via source averaging, for an ideal case of uniform source distribution (left) and for a more "realistic" case of non-uniform source distribution (right). Each row of the image represents an inter-receiver correlation function for waves from a single source, constructed by convolving a Gaussian pulse with the time delay. The noise sources are assumed to be distributed in all directions and the uniformity of source distribution refers to the spatial variation in the strength of noise sources, which is reflected by the amplitude of correlation functions. Shaded areas represent the effective source regions responsible for the reconstruction of the causal and acausal signals from the source averaging. Below the image is the stacked correlation function with its envelope. The ideal example demonstrates a perfect reconstruction of inter-station Green function from noise correlations, with the causal and acausal signals symmetrical in both time and amplitude. The other synthetic example shows the asymmetry of the causal and acausal parts of the recovered Green function caused by the non-uniform distribution of noise sources, and the presence of a spurious phase due to an energetic, localized noise source outside the effective region. Inadequate source sampling may lead to artificial background fluctuations in the stacked correlation functions.

Assuming uncorrelated noise sources, the coherence between the source time functions of different noise sources converge toward zero in the long range. Thus, we can ignore the interference between waves from different sources and consider only the inter-receiver correlation between waves from each independent source. The final correlation function between wavefields at two receivers is thereby equivalent to an integral over the inter-receiver

correlation function for every single source. The integral procedure is referred to by authors as **source averaging** (e.g., Larose et al. 2004, 2006b, 2008), or **stationary-phase integral** (e.g., Snieder 2004; Snieder et al. 2006b; Ruigrok et al. 2008; Boschi and Weemstra 2015; Snieder and Sens-Schönfelder 2015).

We show in the left panel of Figure 2.9 a synthetic experiment of source averaging for an ideal distribution of noise sources, which generally means an even distribution of noise sources as assumed in many literatures. Such a demonstration has also been presented by many others [see e.g., Figure 3 of Gouédard et al. (2008b); Figure 3 of Yao and van der Hilst (2009); Figure 6 of Wapenaar et al. (2010a)]. As described in the previous subsection, the reconstruction of the ballistic parts of the Green function is ascribed to the interference between effective rays from effective sources. The signals generated by correlating waves from effective sources are aligned somewhat in phase and can stack constructively, while those generated by ineffective sources are out of phase and cancel each other in the source averaging. In other words, the source averaging tends to select the contributions from the effective sources. In this ideal synthetic experiment, a perfect recovery of signal is achieved. However, such an ideal distribution of noise sources is hardly met in real cases. A practical distribution of noise sources is typically inhomogeneous over both space and time (e.g., see the spatiotemporal variations in the global distribution of oceanic microseism sources in Figures 1.16 and 1.17). The ambient wavefield is commonly observed to be dominated by waves from one or several directions, implying heavily non-uniform distribution of noise sources (e.g., Schulte-Pelkum et al. 2004; Roux 2009; Behr et al. 2013; Poli et al. 2013; Tian and Ritzwoller 2015; Chen et al. 2016; Sadeghisorkhani et al. 2017). The directivity of wavefield can lead to bias or error in the recovery of the medium's Green function.

A typical, direct consequence of the directivity of ambient wavefield is the directional (azimuthal) variations in the amplitude (and possibly the arrival time) of the signals recovered from noise correlations (e.g., Sabra et al. 2005b; Stehly et al. 2006; Gerstoft et al. 2006b; Pedersen et al. 2007; Roux 2009; Macquet et al. 2014; Seydoux et al. 2017). The amplitude of the retrieved signal approaches the maximum when a pair of receivers are aligned along the direction of the dominant energy flux. The asymmetry in the causal and acausal parts of the recovered Green function is also a commonly observed azimuthally-dependent phenomenon related to the non-uniformity of source distribution [see e.g., Figure 1 of Stehly et al. (2006)]. In the presence of an energetic, localized source outside the effective region, the corresponding

signal cannot be canceled by the source averaging and consequently a spurious phase emerges in the recovered Green function [see e.g., Figure 11 of Zhan et al. (2010)]. We show in the right panel of Figure 2.9 a synthetic experiment including both the asymmetry of the recovered Green function and the emergence of a spurious phase. In this example, the effective sources are much weaker than the localized strong ineffective sources. However, benefiting from the stationary nature, the stacking of the coherent signals in the correlation functions for the effective sources are more efficient than the stacking of non-stationary signals in the correlation functions for the stronger ineffective sources. Depending on the relative strength of noise sources, the spurious phase is of course plausible to be stronger than the regular stationary phase (cf. the spurious phase and the causal regular phase). It suggests a risky possibility in the presence of a localized strong source close to the effective region with very weak effective sources. In this case, the recovered regular phase could be biased by the partial superposition of a strong spurious phase, or even worse if taking the spurious phase as the regular phase. The bias in the waveform of regular phase will lead to errors in the measurements of arrival time and seismic velocity, apparent seismic anisotropy, artificial velocity changes, as well as mislocation of subsurface structural heterogeneities. Such effects are referred to as the **source-structure trade-offs** in literatures as Fichtner (2015) and Fichtner et al. (2017). Fichtner (2015) asserted that the source-structure trade-offs are inherent and unavoidable, and decay with increasing attenuation. Fichtner et al. (2017) claimed that the trade-offs are likely to be most important when scattering is dominant, i.e., for high frequencies and long propagation distances. However, on the contrary, Derode et al. (2003a) observed from ultrasonic experiments that in the presence of multiple scattering, the accuracy of the signals reconstructed from noise records were significantly improved (see their Figure 3).

An examination over the time symmetry of regular phases can reduce the risk of taking spurious phase as regular phase, since there are much less odds to have strong localized ineffective sources that produce time-symmetric spurious phases close to the regular phases on both sides of the empirical Green function. Some data processing techniques, as will be introduced later, can be applied to noise data or correlation functions, to equalize the spatial distribution of noise sources. Fichtner et al. (2017) proposed a corollary based on their theoretical and numerical studies that no processing scheme can produce an effective perfectly homogeneous source distribution from an original heterogeneous source distribution. Another solution, possible the best, is to directly account for the source distribution in the recovery of Green functions from noise correlations (Woodard 1997; Fichtner et al. 2017).

2.2.4. Noise Source Classification

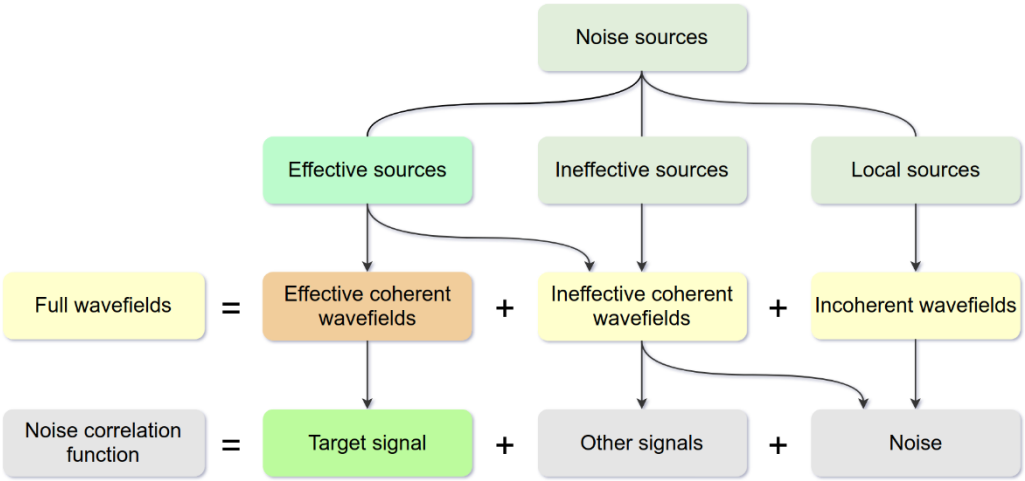

Figure 2.10. Classification of noise sources and decomposition of ambient wavefields based on their contributions to the reconstruction of the target signal from noise correlations between two receivers. The full ambient wavefields are decomposed into coherent and incoherent parts. The coherent parts are further divided into effective and ineffective parts. A noise source or a wavefield is considered to be effective if it has positive contributions to the retrivial of the target signal, or otherwise, it is deemed to be ineffecitve. Regarding the coherency, any motions perceptible by both receivers are regarded as part of the coherent wavefields. Conversely, the signals recorded by one sensor but not by the other compose of the incoherent wavefields.

Consider the situation of retrieving a specific seismic phase (termed target signal hereafter) from the noise correlation function between two receivers. Following conventions mentioned in the previous subsections, we say a wave is **coherent** if it is registered at both receivers, and a wave or a source is **effective** if it contributes to the building of the target signal from noise correlations. The inter-receiver noise correlation consists of the target signal, other signals and background noise. Based on the contributions to the target signal, we decompose the ambient seismic wavefield into three parts:

- ✧ The **effective coherent part**, registered at both receivers and responsible for the building of the target signal;
- ✧ The **ineffective coherent part**, registered at both receivers but having no contributions to the building of the target signal;
- ✧ The **incoherent part**, recorded by only one of the receivers being correlated.

Accordingly, we can classify seismic sources into three types:

- ✧ The **effective sources** that radiate coherent waves recorded by both receivers and having contributions to the target signal;
- ✧ The **ineffective sources** that radiate coherent waves recorded by both receiver but having no contributions to the target signal;
- ✧ The **local sources** that produce signals perceptible by only one receiver in two.

The decomposition of wavefields and classification of noise sources described above, together with their connections to the constituents of inter-receiver correlation function, are summarized in Figure 2.10.

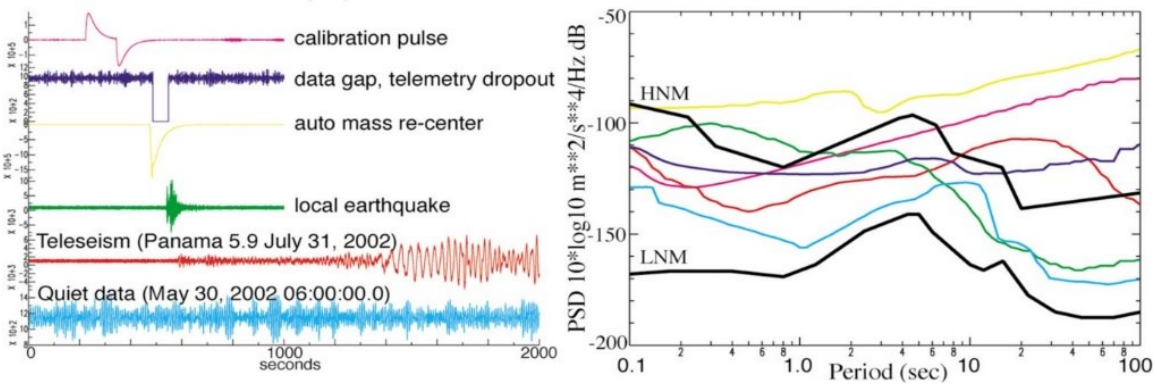

Figure 2.11. Examples of various types of recordings in seismograms (left: waveforms; right: the corresponding spectra). Reproduced from Figure 7 of McNamara and Buland (2004).

The recovery of the target signal is exclusively ascribed to the interferometry between the effective coherent wavefields emanating from the effective sources. However, note/recall that not all waves emanating from the effective sources can be labelled as being effective. The effective sources radiate waves propagating following the effective paths but also waves in other directions. The former constitute the effective coherent wavefields, while the latter belong to the ineffective coherent wavefields. In other words, the effective sources produce coherent wavefields partly effective and partly ineffective. The sources other than the effective ones are all ineffective. Some of them radiate coherent waves recorded by both receivers, but the correlations between these waves yield background noise in the correlation function, or possibly contribute to the recovery of signals other than the target signal. Typically, the global significant earthquakes are classified into this category. The ballistic wavefields from large earthquakes are coherent but ineffective for the recovery of the target signal. There are some other ineffective sources that are felt by only one of the receivers being correlated. We separate such sources from the category of ineffective sources and classify them as an independent

category termed local sources. Local sources produce incoherent wavefields only, which are pure nuisance always hampering the signal recovery from seismic interferometry. Small local events recorded by one receiver but not the other are examples of local sources. Instrumental self-noise and artifacts are other examples. Figure 2.11 shows several real seismogram examples containing operation problems, local and distant earthquakes, and relatively stationary ambient noise, along with their power spectral densities (PSD).

The classifications and decompositions in Figure 2.10 can be simplified as shown in Figure 2.12. The local sources are merged into the category of ineffective sources. The ineffective coherent wavefields and the incoherent wavefields are combined to ineffective wavefields. Noise correlation function constitutes the target signal and the remnant.

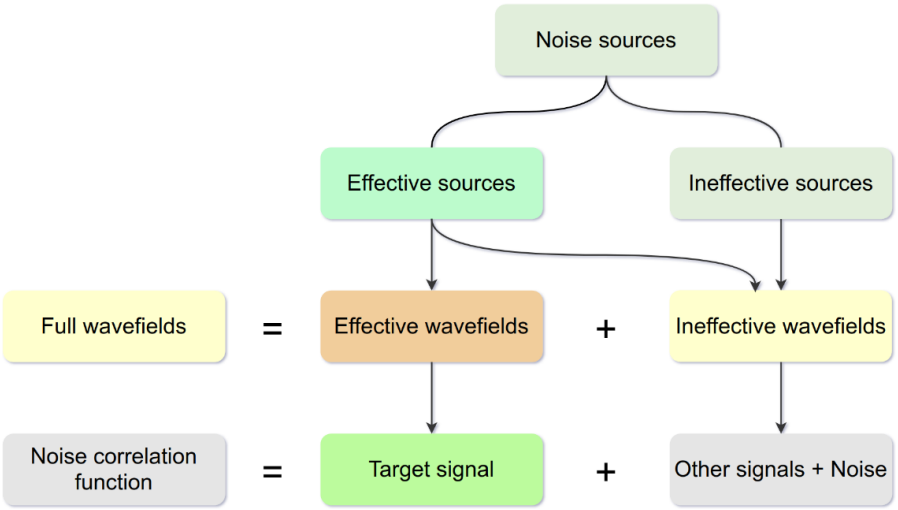

Figure 2.12. Classification of noise sources and decomposition of ambient wavefields based on their contributions to the reconstruction of the target signal from noise correlations between two receivers. The effectiveness of a noise source or a wavefield refers to if it contributes to the retrieval of the target signal from noise correlations.

To conclude, the proportion of the effective coherent wavefields in the full wavefields is the key factor that determines the quality of signal extraction from noise correlations. The effective sources must be (relatively) strong enough to guarantee the recovery of the target signal. The strength of effective sources is necessary but not sufficient for a successful signal recovery from noise correlations. The directivity of source radiation (radiation pattern) and the time-dependent decay of effective wavefields (geometrical spreading, intrinsic absorption, random scattering, reflection and transmission) are also important factors.

2.3. Processing of Noise Data

In principle, a stringent equivalence between the (time derivative of) correlation function and the Green function between two receivers generally requires that the modes of the system are uncorrelated and perfectly equipartitioned, or that the noise sources are independent from each other and uniformly distributed. However, the theoretical requirements can scarcely be well fulfilled in practical seismological observations, conflicting with the great success of seismic interferometry achieved in practical applications. To reconcile the interferometric theory with the seismological practices, some authors (e.g., Tsai 2009, 2010; Godin 2009) have attempted to extend the theory to weaker mathematical prerequisites which are closer to real situations. Besides the theoretical efforts, authors also proposed various pre-processing techniques to improve the signal-to-noise-ratio (SNR) of the empirical Green function or to reduce the bias in the empirical Green function brought by the imperfect equipartition of wavefields or the non-uniformity of noise source distribution. In this section, we give a brief introduce to the existing techniques for pre-processing seismic noise data. We also propose new processing methods based on the statistics of seismic noise.

2.3.1. General Processing Flow

In early acoustic literatures concerning the noise correlation technique, authors correlated the raw records from ultrasonic experiments or numerical modelling. However, seismological observations are generally far from the mathematical requisites of the interferometric theory, pre-processing of continuous seismograms is usually necessary and useful for improving the quality of signals recovered from seismic noise. Besides the routine signal processing such as de-meaning, de-trending, bandpass filtering, instrumental response correction and resampling, which are basic steps necessary in seismic data processing of almost all seismic applications, the most common pre-processing of seismic noise data includes the **time-domain** or **temporal equalization** and the **frequency-domain** or **spectral equalization**. The first systematic survey on the performance of different normalization techniques have been made by Bensen et al. (2007). Later, some authors (e.g., Groos et al. 2012; Macquet et al. 2014) have done similar works in comparing different processing strategies. General workflow of noise data processing and noise-based applications has been described by authors like in Figure 2 of Bensen et al. (2007) and Figure 4 of Larose et al. (2015).

Transient signals from earthquakes dominating in the seismograms can badly deteriorate the retrieval of the inter-receiver empirical Green functions. The strong coherent ballistic waves from earthquakes give rise to large spurious signals in the correlations. A natural choice would be rejecting seismic records of earthquakes in the light of event catalogue. However, not every earthquake is present in the seismograms of all stations. Rejecting earthquake records based on event catalogue may remove seismic records with pure ambient noise. Also, not all earthquakes, especially the small-magnitude local events, have been included in the catalogue. Furthermore, there are other large transient impulses other than earthquakes (see Figure 2.11 for examples). Thus, even after rejecting windows containing earthquakes based on event catalogue, further processing is still needed in most cases to improve the temporal stationarity of seismic noise records. The most frequently-used methods for temporal equalization are the one-bit normalization (e.g., Campillo and Paul 2003; Larose et al. 2004; Shapiro and Campillo 2004; Paul et al. 2005; Shapiro et al. 2005; Stehly et al. 2006; Brenguier et al. 2007; Cupillard et al. 2011; Hanasoge and Branicki 2013; Chen et al. 2016; Oren and Nowack 2017), waveform clipping (e.g., Sabra et al. 2005a, b; Roux et al. 2005a), and running-absolute-mean (RAM) normalization (e.g., Bensen et al. 2007). The one-bit technique, which replaces the waveform with the signs, is most radical and simplest. In the first formal application of the noise correlation technique in seismology, Campillo and Paul (2003) reconstructed the inter-station surface waves by correlating one-bit coda signals of regional earthquakes. The amplitude level of coda waves decreases significantly with time lapse. The one-bit replacement complements the amplitude decay at later times. It is amazing that this simple replacement brings significant improvements in the quality of signal recovery, enabling the one-bit technique one of the best temporal normalization methods. Larose et al. (2004) highlighted that one-bit correlations need fewer noise sources, because the one-bit processing tends to increase the weight of longer and more diffracted paths, enhancing the role of multiple scattering in favor of the recovery of signals from noise correlations. Some authors (e.g., Cupillard and Capdeville 2010; Cupillard et al. 2011; Weaver 2011) even proposed that seismic attenuation can be inferred from the correlations of one-bit signals. The clipping method was introduced by Sabra et al. (2005a). Waveforms in a daily seismogram are clipped at a threshold which is generally set to several times of the standard deviation of the daily trace. Concerning the comparison between the one-bit and clipping methods, different authors (e.g., Larose et al. 2004; Gerstoft et al. 2006b) have drawn different conclusions, likely because they chose different thresholds for the clipping and/or worked with different datasets. An extreme clipping would be equivalent to the one-bit operation. The RAM normalization method first proposed by Bensen et al. (2007) normalizes

the daily seismogram with the RAM version of the seismogram bandpass filtered in the dominant period band of surface waves from large earthquakes (e.g., 20 to 100 sec, or 15 to 50 sec), thereby suppressing the large amplitudes from earthquakes and enhancing the faint amplitudes of background noise. It is equivalent to an auto gain control (AGC) procedure. There are some varieties of the RAM method. For instance, Shen et al. (2012) normalized the daily seismograms filtered in different frequency bands by their RAMs and then summed the normalized traces into a single trace.

Repelling the temporal equalizations that lead to severe nonlinear modifications to the seismic noise records, some authors favor retaining the raw waveforms to the largest extent. The selection filters for discarding impulsive windows and retaining stationary noise windows are among such endeavors (e.g., Prieto et al. 2011; Poli et al. 2012b, a, Boué et al. 2013a, 2014a; Macquet et al. 2014). At early stages, authors were accustomed to process and correlate noise data on a daily basis (e.g., Sabra et al. 2005a; Roux et al. 2005a; Yang et al. 2007; Bensen et al. 2007; Zheng et al. 2008; Yao et al. 2008), which was plausibly a spontaneous choice since the continuous seismic data were usually organized and stored by dates. Daily-based processing is still popular in recent literatures, but correlations based on shorter time windows have been increasingly favored (e.g., Seats et al. 2012; Poli et al. 2012b, a, Boué et al. 2013a, 2014a; Macquet et al. 2014; Oren and Nowack 2017; Ekström 2017). We refer to the latter as segment-based hereafter, and for time windows varying from one to several hours as used in different literatures, they are referred to as hourly-based hereafter. In the case of coda correlations, the segment-based correlations were calculated by Campillo and Paul (2003). They found that the results of stacked coda-segment-based correlations are very similar to the results of one-bit correlations. In the case of ambient noise correlations, the major operation of a segment-based processing is to detect and discard segments containing large transients. From the viewpoint of the theory of effective wavefields as introduced in subsection 2.2.4, the ineffective wavefields dominate in these segments and the proportion of effective wavefields is too low to have significant contributions to the recovery of signals from noise correlations. Zhao et al. (2015) compared the surface waves reconstructed from the correlations of one-bit daily traces and of hourly-based noise segments. The seismic noise data they used were the vertical components of continuous seismograms of one-year long, which were recorded by a portable seismic array in western Sichuan of China and were polluted by numerous aftershocks of the 2008 Wenchuan earthquake. Their Figure 2 showed that the signal-to-noise ratio (SNR) of the Rayleigh waves recovered from hourly-based correlations increases monotonously with shorter time window

length, until the saturation for windows no longer than two hours. If the time window is shorter (longer) than 3-4 hours, the SNR of the surface waves recovered from hourly-based correlations is significantly higher (lower) than that recovered from the one-bit correlations. Also, the average of correlations using 1-hour window shows a faster convergence rate compared to the one-bit processing. Another advantage of using short time windows is its higher efficiency in CPU time. The most time consuming operations for the noise data process and correlation are the forward and inverse Fast Fourier Transforms (FFT). The computational complexity of the FFT algorithm is $O(N \cdot \log N)$. Subdividing N samples into k segments, the time complexity is reduced to $O(N \cdot \log(N/k))$.

As for the spectral equalization, one can either smooth the amplitude spectrum of noise data using an AGC method, or totally discard the amplitude information (spectral whitening) and correlate the phase spectra directly. It seems to be unclear who is the first having introduced the spectral equalization into seismic interferometry. It is possibly ascribed to Bensen et al. (2007) if there are no earlier ones. Even if a spectral equalization is missing in noise data processing, applying the spectral normalization is natural and necessary for the estimates of surface-wave velocity dispersion.

The equalization strategies are generally useful in improving the traveltime measurements, but are not mandatory in seismic interferometry. Sometime, it has even been proposed to avoid any normalizations (e.g., Larose et al. 2008), especially in applications aiming to extracting both phase and amplitude information from noise correlations (e.g., to infer seismic attenuations). The nonlinear modifications to the waveforms of raw records can potentially lead to biased or wrong results.

2.3.2. Segment-Based Noise Data Processing

In this thesis, we adopted the segment-based noise data processing. The processing workflow is illustrated in Figure 2.13. First, the routine signal processing procedures, including gap filling, mean and linear trend removal, bandpass filtering, time correction, 5 Hz resampling and instrumental response deconvolution, were applied to the raw seismograms. We still refer to the seismograms after the routine processing as raw seismograms, since no artificial changes have been applied to the waveforms. Second, the continuous seismograms were subdivided

into 4-hr segments and their frequency spectra were whitened between 1 and 100 sec. An additional waveform clipping could be applied to the spectral-whitened waveform. However, as can be seen from the comparisons between the processing of stationary noise and earthquake segments, the clipping is useful in removing large spikes in the earthquake window, but is not necessary for the stationary noise. Last, a sifting operation was applied to the segments to reject those containing large transient pulses like earthquakes and electronic glitches. Segments with nulls over 5 percent were also discarded. It can thus be seen that the key step in the noise data processing is the detection of segments with large transients. In the following subsections, we introduce the methods based on the statistical characteristics of continuous seismograms.

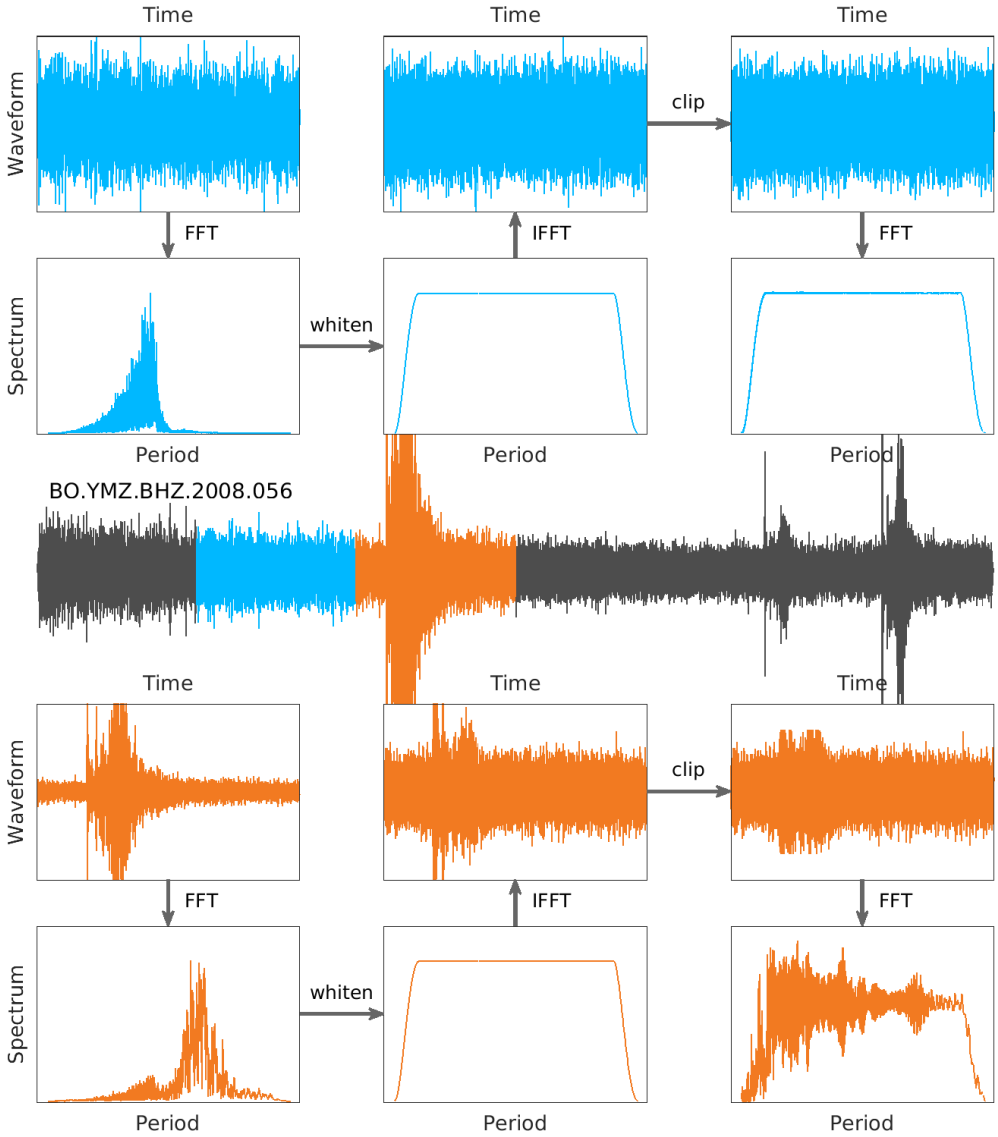

Figure 2.13. Workflow of noise data processing. The continuous seismogram is divided into segments. A segment with stationary noise on a daily seismogram is used to demonstrate the processing. The trapezoidal spectral whitening discards amplitude information and retains only

the phase spectrum. The waveform clipping after whitening is an optional operation, depending on whether to retain segments with limited local spikes. The processing of the successive earthquake window is just a demonstration to be compared with the processing of the stationary noise window. In the practical noise data processing, the segments containing earthquakes or other transients are directly rejected by a detection algorithm.

2.3.3. Descriptive Statistics of Seismograms

The distribution of amplitudes of vibrations in the seismograms can be regarded as a random distribution. Mathematically, the statistical characteristics of a random distribution can be described by its moments. The concept of moments in mathematics is closely related to that in physics. In mechanics, the mass of object is the zeroth moment, the center of mass is the first moment normalized by the zeroth moment, and the rotational inertia is the second moment. In statistics, the zeroth moment is the total probability which always equals to unit. The first to forth moments, which are frequently-used in real practices, are related to the mean, variance, skewness and kurtosis of the distribution, respectively. The mean represents the central location of the distribution, and the others describe the spreading and shape of the distribution. Moments of further higher orders are rarely used. In this subsection, we review the concepts of the first to forth moments and apply them to real seismograms. Part of the contents come from the Wikipedia items and Wolfram documentation.

2.3.3.1. Lower-Order Statistics: Mean and Variance

The ***n*-th moment** of a probability distribution of random variable $\boldsymbol{X}$ is defined as the expected value of the *n*-th power of $\boldsymbol{X}$, namely, $m_n = \mathbf{E}[X^n]$, where $\mathbf{E}[\cdot]$ is the expectation operator. The first moment is the **mean** of $\boldsymbol{X}$, namely $\mu = m_0 = \mathbf{E}[\boldsymbol{X}]$. The raw moments for $n > 1$ are rarely preferred. Instead, it is more favored to use the ***n*-th central moment**, which is defined as the moment about the mean, namely $\widetilde{m}_n = \mathbf{E}[(X-\mu)^n]$. The second central moment of $\boldsymbol{X}$ is the **variance**, namely $\sigma^2 = m_2 = \mathbf{E}[(X-\mu)^2]$, with σ the standard deviation (std). In some applications of data analysis, it is common to normalize observed data with the mean and the std, namely, the so-called z-score standardization $Z = (X-\mu)/\sigma$. Considering that demeaning is a routine operation in seismic data pre-processing, we can ignore the difference between m_n

and $\widetilde{m}_n$ for $n > 1$ and use the notations $\boldsymbol{X}$ and m_n directly. For the zero-mean series, the variance is equivalent to the energy. Theoretically, a unique determination of a distribution in a bounded interval requires a full set of moments of orders from 0 to ∞. However, for some particular distributions, like the Gaussian distribution, the statistical characteristics can be fully described by the mean and the variance.

2.3.3.2. Higher-Order Statistics: Skewness and Kurtosis

At orders higher than two, the standardized moments are in preference to the ordinary moments. The ***n*-th standardized/normalized (central) moment** is defined as $s_n = m_n/\sigma^n$, that is the *n*-th raw central moment divided by the *n*-th power of std. The normalization makes the quantities dimensionless and independent from scaling. The first normalized moments always equals to zero and the second normalized moment is always unit. The third normalized moment is called **skewness** γ, which is a measure of the asymmetry of the distribution about the mean. If the distribution is symmetric with respect to the mean (e.g., the Gaussian distribution), the skewness equals to zero and the mean equals to the median. If the distribution is skewed to the left/right of the mean (longer tail on the left/right), the skewness is negative/positive and the mean is on the left/right of the median. The forth normalized moment is called **kurtosis** κ, which is a measure of the heaviness of the tail in the distribution, or the impulsiveness (Westfall 2014). The definition of kurtosis varies in different literatures. It is common to modify the formula of the forth normalized moment with a shift of 3, namely,

$$\kappa = \frac{m_4}{\sigma^4} - 3 = \frac{\mathbf{E}[(X-\mu)^4]}{(\mathbf{E}[(X-\mu)^2])^2} - 3. \quad \text{..... (2.1)}$$

With this modification, the kurtosis of any Gaussian distribution goes to zero. To distinguish between the two definitions of kurtosis, the original definition of kurtosis (the forth normalized moment) is also called the **non-excess** or **historical kurtosis**, while the definition in Equation 2.1 is referred to in some literatures as the **excess kurtosis** or **kurtosis excess**. In this thesis, we adopt Equation 2.1 as the definition of kurtosis. Probability distributions with zero, positive, and negative kurtosis are called mesokurtic or mesokurtotic, leptokurtic or leptokurtotic, and platykurtic or platykurtotic, respectively. The normal distribution family are typical mesokurtic distributions ($\kappa = 0$), but not the unique ones. Typical manifestation of a leptokurtic distribution ($\kappa > 0$) is its heavy or long tails. On the contrary, thin or light tails are traits of platykurtic distributions ($\kappa < 0$). The super-Gaussian distribution family (like the exponential distribution, Laplace distribution, Poisson distribution, Rayleigh distribution, and Student's t-distribution)

are prominent examples of leptokurtic distribution. The sub-Gaussian distribution family (like the uniform distribution, Bernoulli distribution, and raised cosine distribution) are examples of platykurtic distribution.

The significance of the higher-order statistics is not easy to be seen from their mathematical definitions. Most of our knowledge are based on rules of thumb. In fact, there are still debates in the significance of the kurtosis (Westfall 2014), especially in if kurtosis is a measure of the peakedness of a distribution.

2.3.3.3. Statistics of Continuous Seismogram

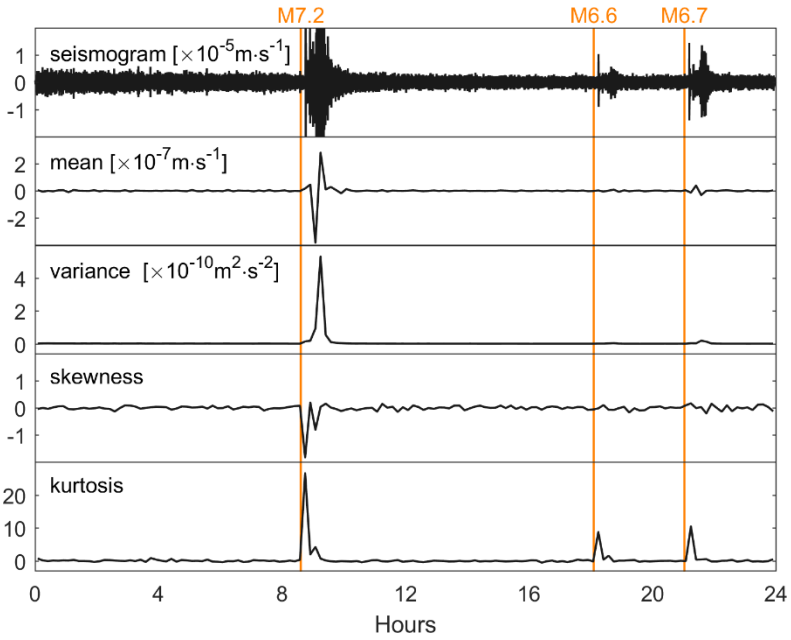

Figure 2.14. The first- to forth-order descriptive statistics of the same daily seismogram as used in Figure 2.13. The time series of statistics are calculated with a sliding window of 15 min without overlaps. Three significant earthquakes in Indonesia ~54° away from the station BO.YMZ in Japan are labeled at their origin times. The time series of mean can be regarded as a low-pass version of the raw seismograms. The largest M7.2 earthquake is highlighted in the time series of variance and skewness. The other two M6+ events are not clearly visible in the series of variance because the corresponding spikes are much lower than the spike for the M7.2 event. All three large teleseisms are clearly identified in the time series of kurtosis.

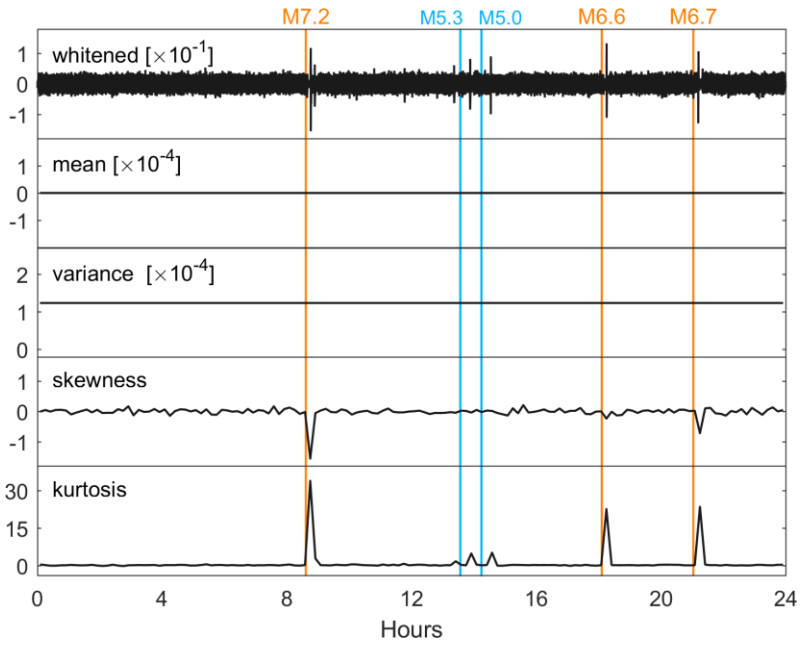

Figure 2.15. Similar to Figure 2.14 but for spectral-whitened segments. Earthquakes are labelled at their origins. The time-independent mean and variance imply that the spectral whitening enables the seismogram stationary to at least second order. Kurtosis exhibits better performance in identify earthquakes than skewness.

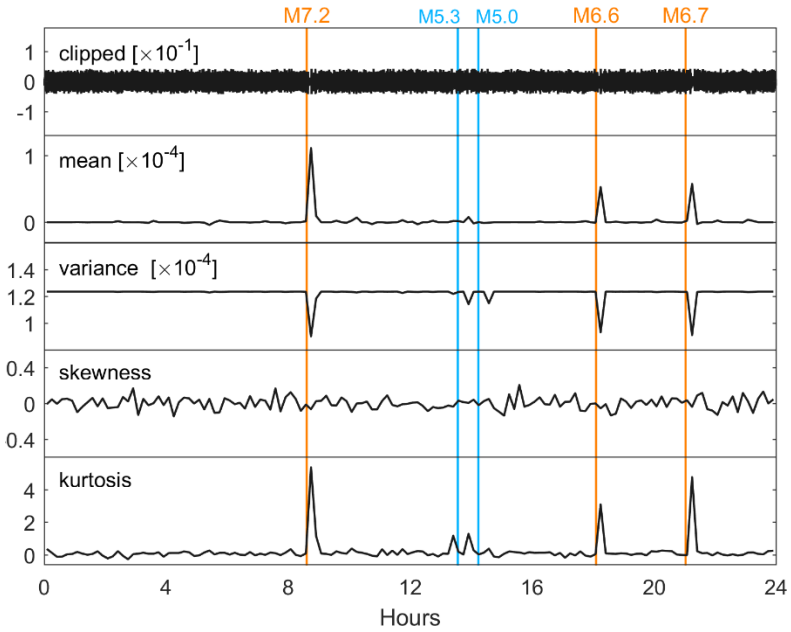

Figure 2.16. Similar to Figure 2.14 but for segments after spectral whitening and waveform clipping. After clipping, the daily waveform appears more stationary over time. The clipping also makes earthquakes emerging in the time series of mean and variance, but disappearing from the time series of skewness. Kurtosis still exhibits the best performance in detecting segments with earthquakes.

The daily seismogram used in Figure 2.13 contains both stationary noise and earthquake, a good example for us to demonstrate the capability of the statistical parameters introduced above in identifying large-amplitude transients from the background seismic noise. We computed the mean, variance, skewness and kurtosis of the raw, spectral-whitened and clipped seismograms as illustrated in Figure 2.13, with a moving window of 15-min length. There were no overlaps between successive windows. The results were plotted from Figure 2.14 to Figure 2.16. It can be seen that kurtosis is the best indicator of segments containing earthquakes.

2.3.4. Selection Filters for Noise Data Processing

As mentioned early, the key step in segment-based noise processing is the selection of segments with stationary noise, or in other words, the detection and rejection of segments with large transients like earthquakes. Therefore, the event detection algorithms in earthquake seismology are also available to be the selection filter for noise data processing. In this subsection, we introduce the variance-based (or energy-based or power-based) and kurtosis-based methods as candidate selection filters.

2.3.4.1. Variance-Based Selection Filter

Due to the large amplitudes of transient impulsive signals relative to background noise, it is natural that many of the event detection methods are energy-based. The famous STA/LTA (short-term-average over long-term-average ratio) triggering algorithm (e.g., Allen 1982; Withers et al. 1998; Trnkoczy 2012) belongs to such a category. The energy-based selection filter employed by Poli et al. (2012b) and Boué et al. (2013a), by comparing the power of a segment with the power of the daily trace, can be regarded as a rough version of the STA/LTA detection. The power of seismic noise can fluctuate in a wide range spanning over several orders. A hard threshold applied to the noise power is impractical. The STA/LTA-like detection can be adapted to the temporal variations in the power of ambient noise. It works well in most cases, whereas false detections still potentially occur in some cases. In the presence of frequent or periodic impulses, the power of segments may remain relatively stable at hourly-based scales. In these cases, impulsive segments may pass the power-based selection filter. If the ambient noise experiences a rapid change over time, it is plausible that segments with ambient noise of high energy are discarded by mistake.

2.3.4.2. Kurtosis-Based Selection Filter

In subsection 2.3.3, we have shown that kurtosis is highly sensitive to impulsiveness (Westfall 2014) and that kurtosis is a more robust estimator in detecting large transients than the other statistical parameters. In earthquake seismology, kurtosis-based characteristic functions have been widely used in event detection, location and phase identification (e.g., Saragiotis et al. 2002; Gentili and Michelini 2006; Küperkoch et al. 2010; Baillard et al. 2014; Langet et al. 2014; Ross and Ben-Zion 2014; Olivier et al. 2015).

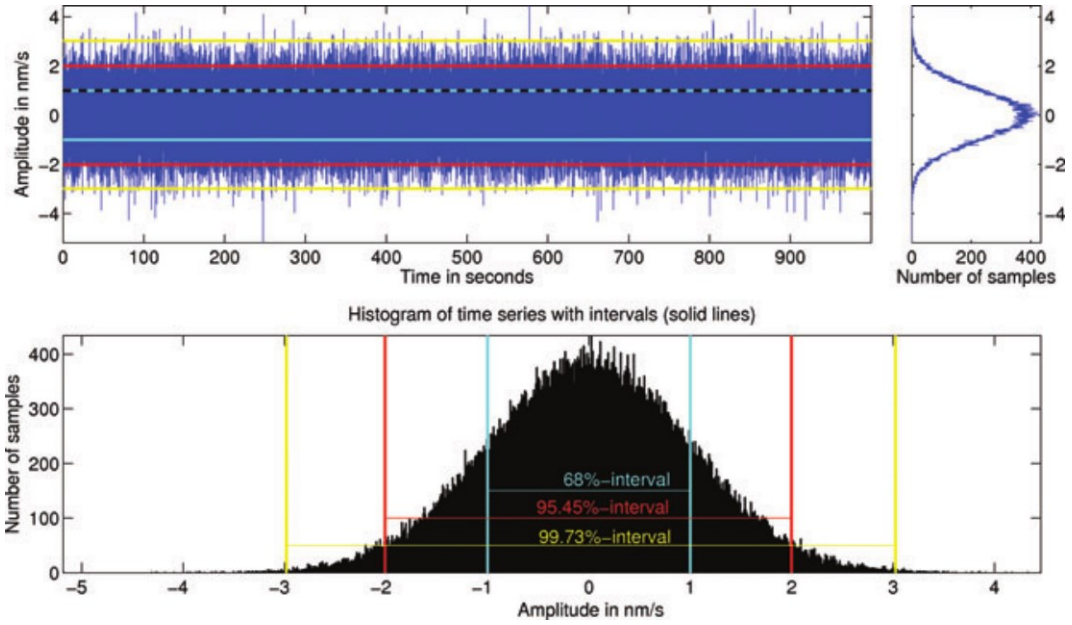

Figure 2.17. An example of stationary noise with the histogram of amplitude distribution which can be approximated by a Gaussian stochastic process. The cyan, red and yellow lines indicate the intervals of 68%, 95.45% and 99.73%, respectively. Reproduced from Figure 4 of Groos and Ritter (2009).

It is commonly assumed that the amplitude distribution of broadband or long-period seismic noise is approximately Gaussian [Figure 2.17; see also Figures 16 and 17 of Peterson (1993) and Figure 2 of Steim (2015) for more examples], implying that the kurtosis is supposed to approach zero. At short periods, when cultural noise dominates, large-amplitude transient or periodic signals degrade the Gaussianity (Figure 2.18). Groos and Ritter (2009) showed that 60% of their analyzed seismic noise data under the urban environment were not normally distributed and that deviations from the normal distribution were commonly due to the presence of large-amplitude transient signals. Groos and Ritter (2009) thus proposed to use the ratio

between different intervals as an indicator of the presence of large transient signals. The idea is somewhat similar to the kurtosis estimator proposed here, but the latter is more convenient.

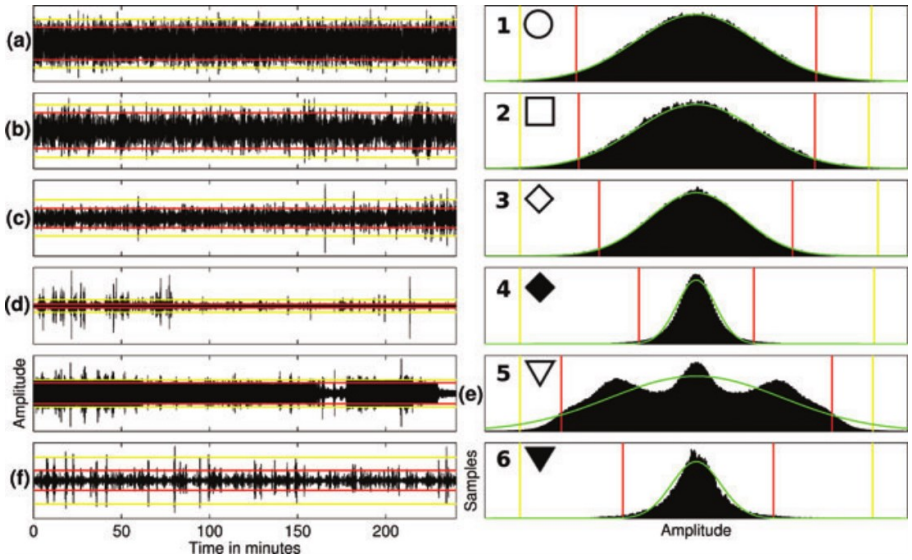

Figure 2.18. Examples of six typical classes of vertical-component seismic noise recorded at different sites in the city of Bucharest with their amplitude histograms: (a) Gaussian distributed (0.25–0.6 Hz), (b) nearly Gaussian distributed (0.04–0.09 Hz), (c) dominated by short transient noise signals (0.18–0.25 Hz), (d) heavily dominated by short transient noise signals (1–25 Hz), (e) multimodal distribution (1–25 Hz), and (f) asymmetric distribution (0.04–0.09 Hz). Red and yellow lines indicate the 95.45% and 99.73% intervals, respectively. Green lines in the right panels are the Gaussian distributions estimated from the mean and std. Reproduced from Figure 5 of Groos and Ritter (2009).

We aim to discriminate segments of stationary noise from transient impulses in the continuous seismogram. The application of kurtosis-base selection filter for such a purpose is illustrated in Figure 2.19. It can be seen that for the segment of stationary noise, the kurtosis always equals to zero, as expected. For the segment with the presence of the M7.2 teleseism, the values of kurtosis for the raw and whitened waveforms are up to tens or hundreds. The waveform clipping significantly reduces the value of kurtosis to 2.3, justifying the high sensitivity of kurtosis to the presence of impulsiveness. In this thesis, we take an empirical threshold of 1.5 for the kurtosis-based selection filter. The selection filter can be applied to any of the raw, whitened and clipped waveforms. Compared to the energy-based selections, the kurtosis-based selection relies on the statistics of the segment itself only and is more robust when the amplitude level of seismic noise experiences rapid changes.

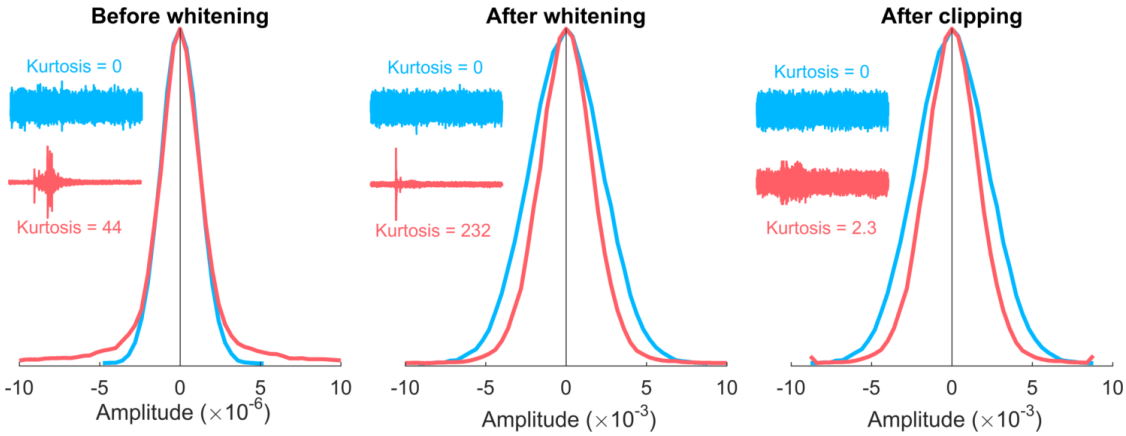

Figure 2.19. Kurtosis-based selection filter to determine segments of stationary noise or with the presence of large-amplitude transient signals. The two segments used here, one with stationary noise (dodger blue) and the other with a teleseism (coral), are the same as in Figure 2.13. The raw, spectral-whiten and clipped waveforms and their amplitude histograms are plotted in the left, middle and right panels, respectively. For the sake of display, waveforms are plotted in different scales, amplitude histograms are normalized by their own maximum and tails outside the horizontal axis limits are cropped. The value of kurtosis for each segment is labeled. One can reject segments containing large impulses by applying an upper threshold to the kurtosis value at one or more of the three stages shown here.

2.3.5. Separation Filters for Noise Data Processing

In some context (like in latter chapter of this thesis), we need to extract the time series of the power of background seismic noise from continuous seismograms. This is generally obtained from the piecewise variance of seismograms. However, the presence of earthquakes or other large-amplitude transient pulses in the seismograms severely affects the extraction. Generally, these transient signals appear as isolated spikes or outliers in the noise power time series. Removal of these large transient impulses are necessary for unbiased estimates of noise power. The selection filters introduced in the previous subsection are available for this task. However, they produce missing samples in the time series of noise power. In this subsection, we introduce several filters that can separate ambient noise from transient signals and introduce no new gaps in the time series.

2.3.5.1. Mean and Median Filters

Mean (median) filter replaces a sample with the mean (median) of a local window around the sample. The only parameter is the size of the sliding window to compute the local mean or median. Mean and median filters are denoising techniques widely used in the data processing of many fields, such as imaging processing and machine learning. They are equivalent to nonlinear lowpass filters that can suppress high-frequency noise (Astola and Kuosmanen 1997). In trend analysis, denoising with mean and median filters improve the clarity the longer-period trends. In regression, they can stabilize the fit. The median filter is more robust than the mean filter due to its lower sensitivity to outliers. Suomela (2014) proposed that median filtering is equivalent to piecewise sorting. Mean and median filters can reduce high-frequency noise or isolated outliers but they unavoidably blur the data. To reserve some useful high-frequency features in the data, variants of median filter have been proposed to improve the adaptability to non-uniform variations in data (e.g., Hwang and Haddad 1995; Chen and Wu 2001). In some seismological literatures (e.g., Hillers and Ben-Zion 2011; Liu et al. 2016a), the median filter has been used to suppress earthquake signals in the piecewise seismic noise power estimates.

2.3.5.2. Hampel Filter

Mean and median filters can suppress outliers. However, they changes values of all the samples. A better strategy is to use a variant of the median filter called Hampel filter. The Hampel filter is an effective technique for outlier detection and removal popular in data science, but its use in seismology appears still rare. In contrast to the median filter that replace all samples with local medians, the Hampel filter detects outliers by compare a sample with the neighboring samples. A sample is replaced by the local median only if its deviation from the local median is several times of the mean or median absolute deviation (MAD), or else the sample remains the old value. The despiking process using the Hampel filter can be executed recursively.

2.4. Computation of Correlation Functions

As for the computation of correlation functions, the conventional method has some drawbacks requiring refinements. In this section, we propose a modified method to compute the correlation function.

2.4.1. Conventional Scheme

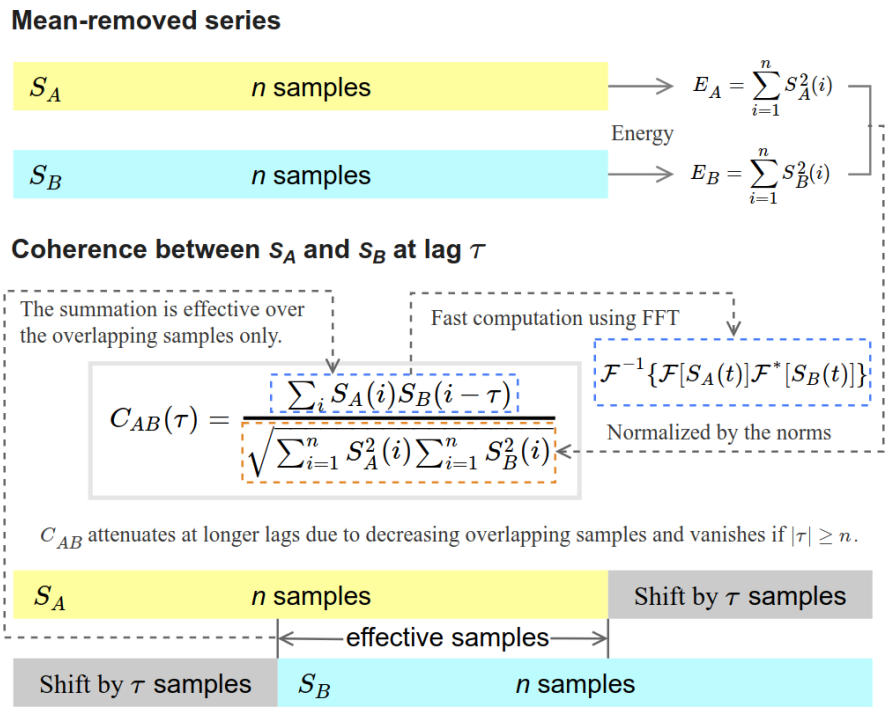

Figure 2.20. Schematic diagram of computing correlation functions in the conventional way.

The traditional way to calculate the correlation function between two time series of the same length is summarized in Figure 2.20. The correlation function can be computed either in the time domain (t-domain) or in the frequency domain (f-domain). Undoubtedly, computing with t- and f-domain formulae leads to the same result. The computation using the t-domain formula is more effective only if the maximum lag (maxlag) is short. In seismic interferometry, the maxlag is generally not so small that it is popular to compute the correlations with the aid of the Fast Fourier Transform (FFT).

Nonetheless, the t-domain formula is more explicit for an intuitive understanding of the computation of the correlation function. The denominator in the t-domain equation equals to the product of the *L2* norms of two series being correlated, which is invariant at any lag. The numerator is equivalent to the inner product between the overlapping parts of the two time series being correlated. It is obvious that the correlation function decays at large lags due to the decrease in the amount of overlapping samples. When the lag is greater than the length of the time series, the correlation function goes to zeros.

2.4.2. Modified Scheme

In the previous subsection, we introduced the traditional scheme for computing the correlation function. There are some limits to calculate the correlation function with the traditional scheme.

- ✧ The time series being correlated should have the same size.
- ✧ The maxlag should be less than the length of time series.
- ✧ The amplitude of the correlation function attenuates at large lags.

The last point is of particular importance because it degrades the recovery of signals emerging at long traveltimes.

To overcome the drawbacks of the conventional scheme, we propose a modified scheme by simply padding zeros to one of the correlated time series. We present the new scheme in Figure 2.21, which is self-explained. The modified scheme possesses the following advantages.

- ✧ The maxlag and the length of the (short) time window are independent from each other.
- ✧ The time window can be any short (but no less than several cycles of the longest period of interests, of course). Shorter windows cost less CPU times in FFT calculations, and allows higher time resolution in monitoring.
- ✧ The amount of effective samples is invariant, meaning that the correlation coefficient does not suffer from the amplitude decay at large lags caused by the decrease in the amount of effective samples.
- ✧ The lag time of the correlation function can be nonsymmetrical with respect to zero lag. In other words, the two correlated time windows need not to be synchronous. One can choose to calculate the correlation function merely for a range of time delay including the signals of interests. For instance, if we are only interested in the P wave traveling from station A to station B, we can correlate a time window of station A from t_0 to $t_0 + n$ with a time window of station B from $t_0 + t_P - m$ to $t_0 + t_P + n + m$, where t_P is the predicted time of the P wave. In this case, the corresponding lag time ranges from $t_P - m$ to $t_P + m$. In the case of the auto-correlation function, one can choose to compute only one side of the time-symmetric full auto-correlation, and thereby speed up the computation.

The computation of the correlation function using the modified scheme still follows the same equation as used in the conventional scheme. There are two choices for the normalization factor in the formula of correlation function: a rolling normalization with the norms of the n effective samples only, or a constant normalization with the norms of the whole windows.

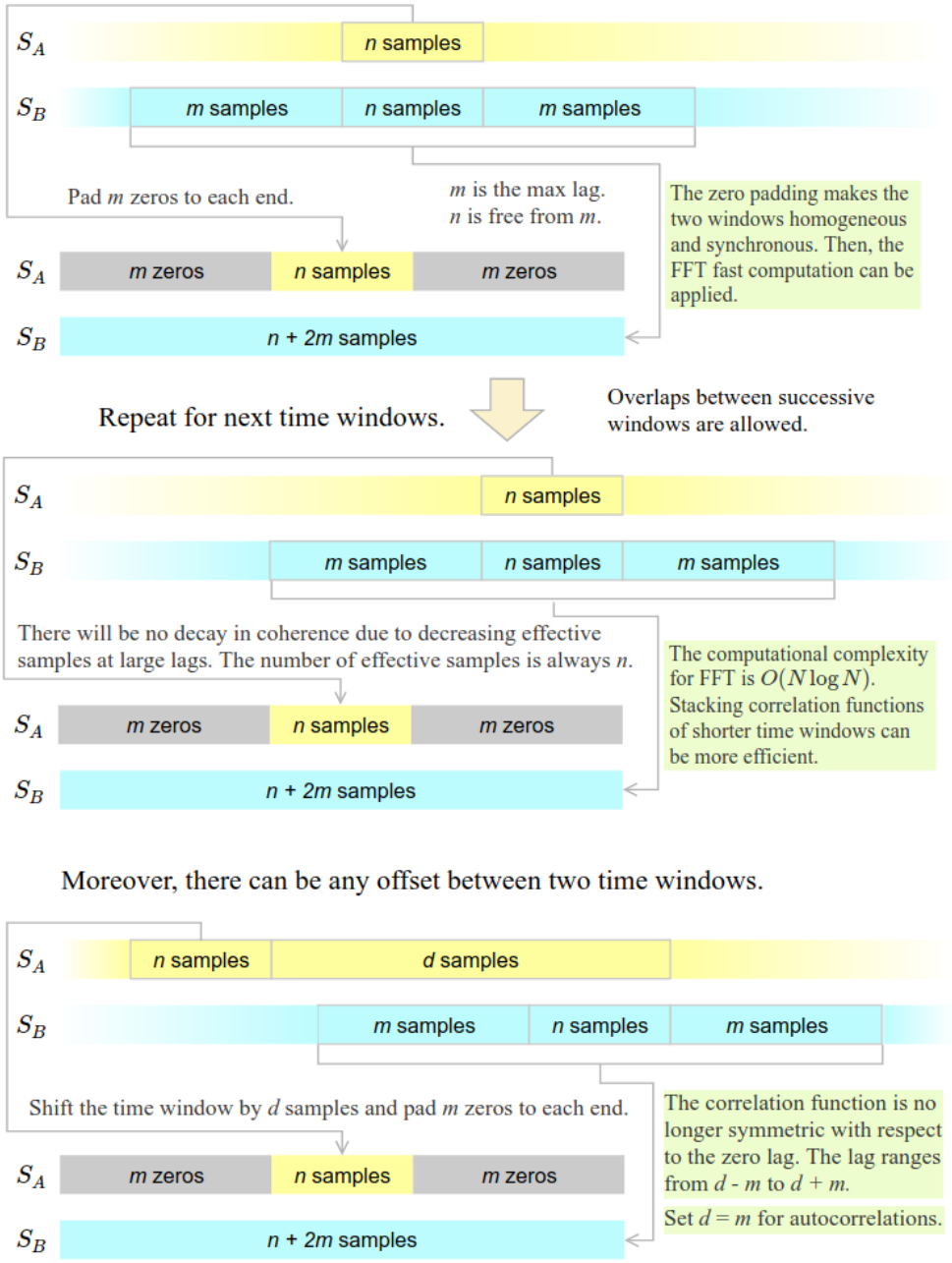

Figure 2.21. Schematic diagrams of the new scheme for calculating unattenuated correlation functions. The two time windows being correlated are in different length. By padding *m* zeros to the ends of the shorter window, the two time windows are in the same length and then the correlation function can be calculated from the conventional way. The denominator in the formula of correlation function can be the product of the *L2* norms of either the whole windows or only the effective parts. The correlated time windows can be asynchronous and the lag time can be asymmetric. In the case of auto-correlation, the conventional scheme leads to an exact time-symmetric auto-correlation, whereas the causal and acausal parts of the auto-correlation calculated by the modified scheme are not time-symmetric any more.

2.4.3. Numerical Comparisons

To demonstrate the difference between the correlation functions calculated using the traditional scheme and the modified scheme, we present a numerical example in Figure 2.22. Two random time series of 10,000 samples are cross-correlated. The maximum lag is 12,000, longer than the length of the time series. As can been seen from the figure,

- ✧ the correlation function by the traditional scheme decays at large lags and vanishes when the lag exceeds the series length;
- ✧ the correlation functions by the modified scheme do not attenuate at large lags;
- ✧ all correlations are in good semblance at short lags, while the difference between the traditional and modified schemes is clear at large lags;
- ✧ the correlation functions by the modified scheme with different normalizations are almost identical except an overall scaling, naturally resulting from the facts that the correlated time series are stationary at second order and that the constant normalization overestimates the normalization factor in contrast to the rolling normalization.

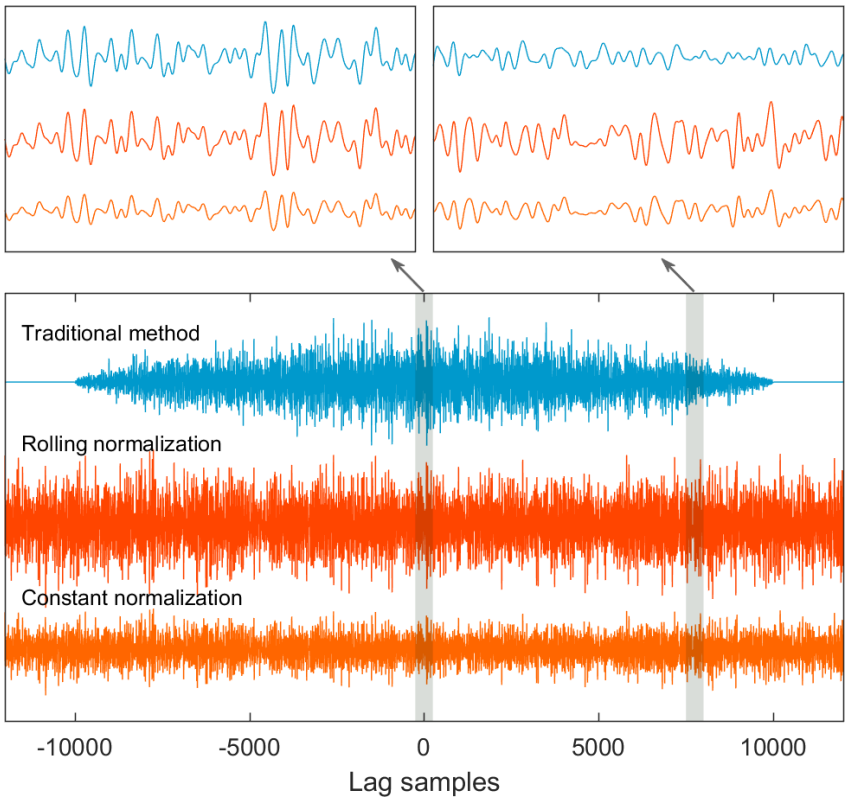

Figure 2.22. Numerical comparisons between the attenuated correlation function calculated with the conventional scheme and the unattenuated correlation functions calculated with the modified scheme with two kinds of normalization.

2.5. Processing of Correlation Functions

Theoretically, the inter-receiver Green function of medium can be reconstructed from the correction between ambient noise records at two receivers. However, due to various limits in real observations, the reconstruction can never be perfect. Many authors have surveyed the errors in the noise-derived empirical Green functions (e.g., Weaver and Lobkis 2005; Douma and Snieder 2006; Larose et al. 2008; Lin et al. 2008; Weaver et al. 2009, 2011; Tsai 2009; Yao and van der Hilst 2009; Froment et al. 2010; Clarke et al. 2011; Zhan et al. 2013; Hanasoge 2013; Yoritomo and Weaver 2016; Liu and Ben-Zion 2016; Liu et al. 2016b; Sadeghisorkhani et al. 2017). Toward improving the quality of signal recovery from noise correlations, there are not only strategies that are applied to seismic noise data, but also some others that are applied to the noise correlations. The latter can be classified into two main sorts: one toward the improvement of the SNR of noise-derived signals and the other toward the reduction of bias in the noise-based estimates.

A straightforward strategy to improve the SNR of noise-derived signals is to stack the inter-receiver noise correlations over a long time. For inter-receiver noise correlations at different time slots, the signals associated to the deterministic structure of Earth are supposed to be coherent and can be enhanced in the stacking, while the incoherent random background noise in the correlations is reduced due to unconstructive stacking. A squared-root dependence of the SNR of noise-derived Rayleigh waves on the noise record length, which is consistent with the prediction of signal processing, has been reported by authors (e.g., Snieder 2004; Sabra et al. 2005a; Gerstoft et al. 2006b). The dependence of SNR on the square-root of noise source density observed by Yoritomo and Weaver (2016) is an equivalence. Medeiros et al. (2015) discussed analytically the minimum amount of noise data necessary for the extraction of coherent signals from ambient noise.

Stacking over space has the same effects as stacking over time in enhancing the signal clarity. It is also called the slant stack or beamforming (e.g., Rost and Thomas 2002; Gu and Sacchi 2009; Nakata et al. 2015), which is a spatial filter that can enhance signals from specific direction and with specific slowness. The beamforming is particularly useful when the duration of array observation is limited, or in the scenarios requiring fine time resolution, such as for monitoring purpose with high temporal resolution requisite or if the medium is flowing or fluctuates with time significantly (Leroy et al. 2012). A more advanced double beamforming

method has been applied to noise correlations by authors (e.g., Roux et al. 2008, 2016; Leroy et al. 2012; Boué et al. 2013b, 2014a; Nakata et al. 2016). In the next chapter, we provide particularly an introduction to the family of such techniques.

Similar to the selection of stationary noise data, it is a natural strategy to apply a selection filter to the noise correlations (e.g., Nakata et al. 2015; Olivier et al. 2015), or make a quality control on the dispersion estimates (e.g., Lin et al. 2007; Bensen et al. 2007).

Various denoising filters in signal processing have also been applied to noise correlations, including S transform (e.g., Baig et al. 2009; Hadziioannou et al. 2011), curvelet transform (e.g., Stehly et al. 2011, 2015), adaptive covariance filter (Nakata et al. 2015), SVD-based filter (SVD is the abbreviation of Singular Value Decomposition) (e.g., Melo and Malcolm 2011; Leroy et al. 2012; Melo et al. 2013; Moreau et al. 2017), Wiener filter (e.g., Moreau et al. 2017), phase weighted stack (e.g., Schimmel et al. 2011; Haned et al. 2016; Ventosa et al. 2017), to cite only a few.

A main cause for the bias in the noise-derived signals is the non-uniformity in the distribution of noise source. Mathematically, a perfect recovery of inter-receiver Green function from noise correlations requires a uniform distribution of noise sources. However, the strict mathematical prerequisite is scarcely fulfilled in seismological practice. It is expected that through long-term observations, the average distribution of noise sources can converge toward the condition acceptable by the mathematical requisite (Campillo and Roux 2015). This expectation is not always able to be realized, especially for noise-derived body waves that are ascribed to noise sources in specific, confined regions. To reduce the bias in the noise-derived Green functions, authors proposed analytical corrections (e.g., Weaver et al. 2009; Tsai 2009) as well as new processing strategies, such as the multi-dimensional deconvolution (Wapenaar et al. 2011a, b) and passive inverse filter (Gallot et al. 2012). Recently, a SVD-based spatial equalization was introduced to improve the azimuthal balance of the noise source distribution (Seydoux et al. 2016, 2017). The method is the same as the PCA whitening popular in data pre-processing in machine learning. PCA is the abbreviation of the Principle Component Analysis, which is also called the Empirical Orthogonal Function (EOF) in climate science. PCA is commonly implemented by calculating the eigenvalues and eigenvectors of the covariance matrix from SVD. In seismology, the SVD-based polarization analysis (Jurkevics 1988) can be regarded as a special case of the PCA application. The SVD-based denoising filter assumes that the largest

eigenvalue corresponds to the signal of interests, implying that it is required that the interested signal must be stronger than the incoherent noise. The SVD-based spatial equalization whitens the significant eigenvalues of the covariance matrix (that is why it is called PCA whitening) of array noise correlations and accordingly improve the azimuthal balance of the noise source distribution. However, Fichtner et al. (2017) concluded that no processing scheme is capable of producing a homogeneous effective source distribution from a heterogeneous original distribution. Seydoux et al. (2017) proposed that the SVD-based spatial equalization can be applied to either noise data or noise correlations, but less efficient for large inter-receiver distance.

2.6. Summary

In this chapter, we reviewed the correlation technique, or seismic interferometry, from its origins to its data processing strategies to its wide applications. The general workflow for the data processing and applications of seismic interferometry is summarized in the panel of Figure 2.23. For more information, we refer to the recent reviews (Campillo and Roux 2015; Larose et al. 2015; Wapenaar et al. 2017; Wapenaar and Thorbecke 2017) as well as some earlier ones (Campillo 2006; Larose et al. 2006b; Larose 2006; Weaver and Lobkis 2006; Gouédard et al. 2008c; Snieder et al. 2009; Wapenaar et al. 2010a, c; Sato et al. 2012).

We explained schematically how signals are retrieved from noise correlation functions. The reconstruction of regular seismic phases is exclusively ascribed to the interference between the coherent wavefields emanating from the effective sources in the stationary phase locations, propagating along the effective paths and recorded by the receivers being correlated. The interfering waves following the effective paths share a common slowness and consequently the inter-receiver time delay corresponds to an extreme value (a stationary location) on the curve or map of time delay with respect to the location of noise source.

We surveyed the lower- and higher-order descriptive statistics of continuous seismograms and accordingly proposed a kurtosis-based filter to discard earthquakes and select time windows with stationary noise which are desirable for the correlation technique. We also introduced the Hampel filter to separate earthquakes and other impulses from the power series of seismic noise. Moreover, we implemented some simple modifications in the computation of correlation

functions, enabling the choice of window size free from the maxlag and the amplitude of resultant correlation functions unattenuating at long lags.

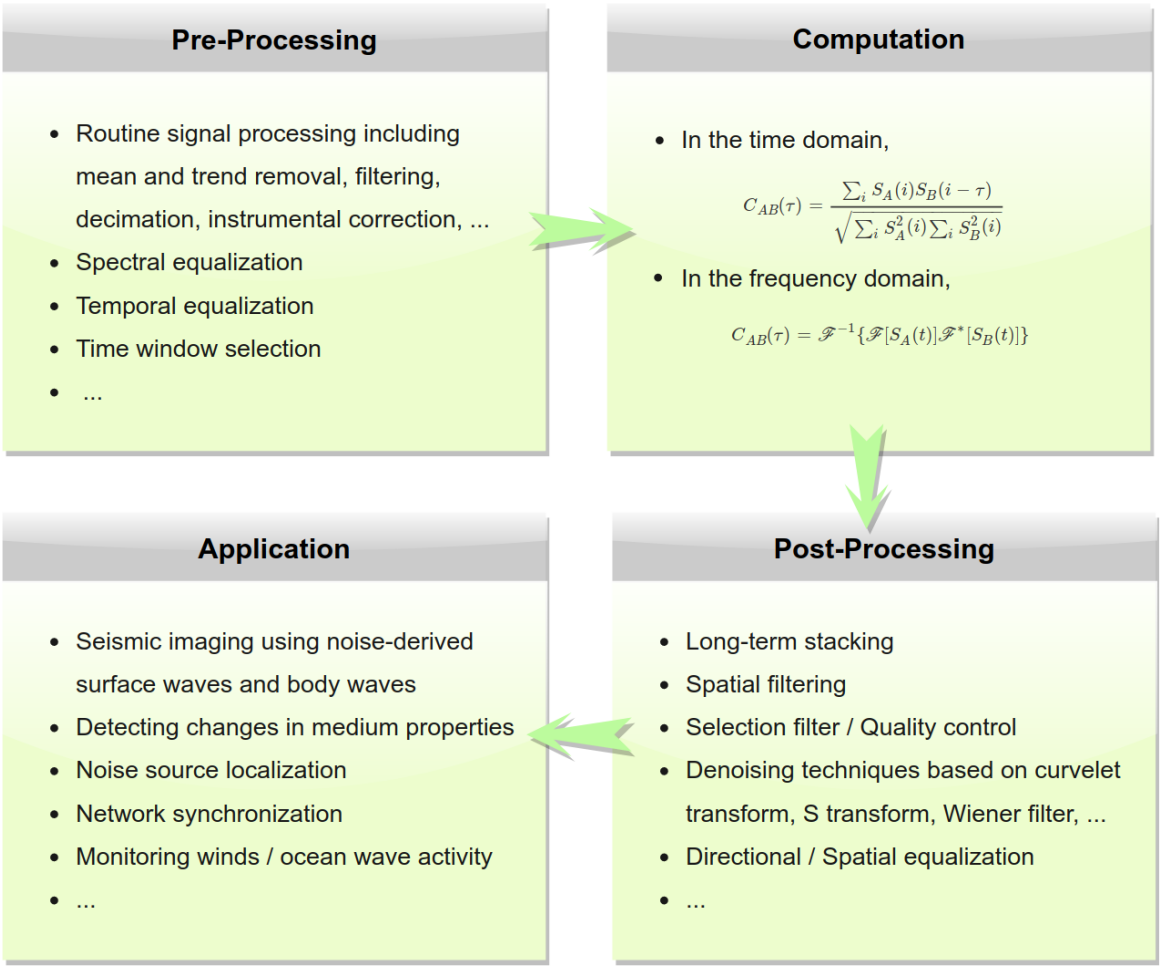

Figure 2.23. General workflow of noise correlation applications

3. Radon-Based Techniques in Double-Array Interferometry

In the previous chapter, we introduced various techniques for processing seismic noise data and correlation functions, aiming at improving the quality of signal recovery from seismic noise. Here, we introduce several Radon-based techniques for the applications of noise correlations, with a particular emphasis on the configuration of double-array correlations.

3.1. Double-Array Interferometry

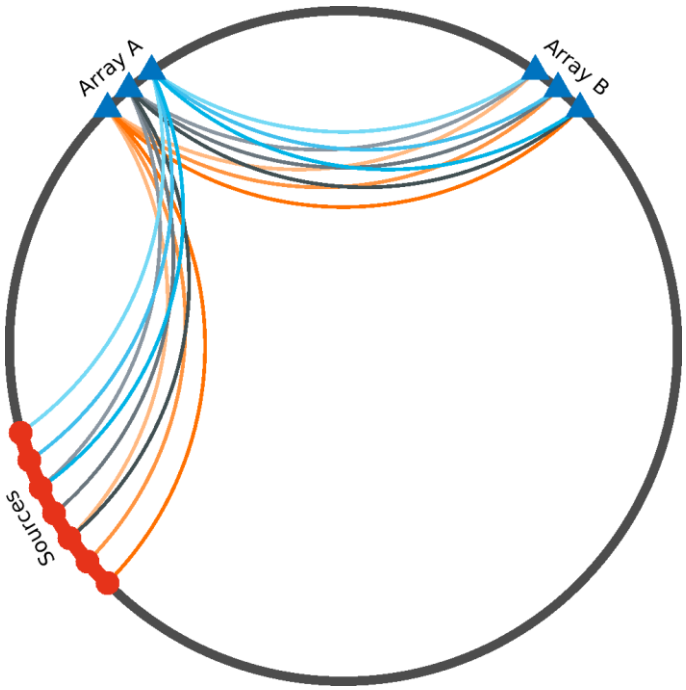

Figure 3.1. Ray representation of double-array interferometry.

In this thesis, we focus on the retrieval of seismic signals from the correlation functions between stations of two arrays. Let us denote the seismic arrays being correlated as array X ($X = A$ or B). A simplified model demonstrating the geometry of the interferometry between arrays A and B is displayed in Figure 3.1. For each pair of array A station and array B station, we compute the correlation function between the seismic noise records at two stations. The gather of correlation functions for all station pairs are called **double-** or **inter-array correlation**

functions. Note that the signals retrieved from correlation functions of different station pairs stem from separated effective noise sources.

3.2. Radon-Based Applications

3.2.1. Classic Radon Transform

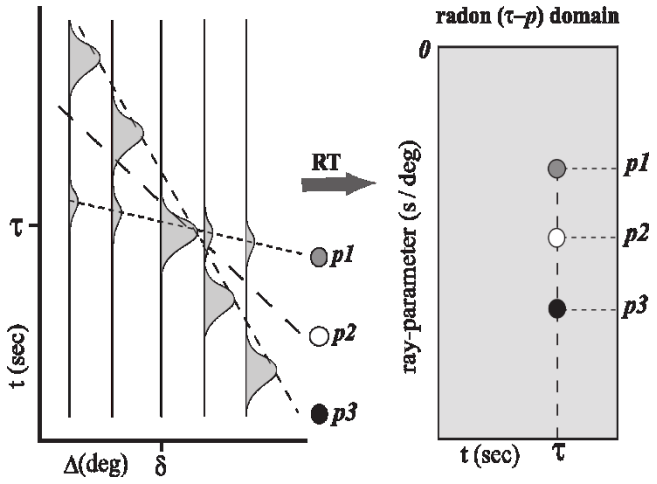

Figure 3.2. A cartoon depicting the Radon transform. Ray parameters *p1*, *p2* and *p3* correspond to a weak signal, no coherent signal, and a large-amplitude signal, respectively. Reproduced from Figure 1 of Schultz and Jeffrey Gu (2013).

The Radon transform is a kind of integral transform that projects data from the time-distance domain to the time-slowness (*tau-p*) domain. In different context, the discrete form of Radon transform is also known as slant stack, beamforming, fan filtration or *tau-p* transform (Gu and Sacchi 2009). The schematic in Figure 3.2 explains the basic idea of Radon transform. The implementation of Radon transform is based upon the delay-and-sum operation which is also called the slowness slant stacking. The resultant beam of a slant stack is given by

$B(t) = \sum_i w_i \, s_i(t + \Delta t_i)$, ... (3.1)

where $s_i(t)$ is the *i*-th trace of dataset comprising *N* traces, w_i is the normalized weight for s_i and Δt_i is the time delay between s_i and a reference. In a normal beamforming, w_i is uniform and thus equals to *1/N*. The beam equation can be written in a compact form as

$B(t) = \langle s_i(t + \Delta t_i) \rangle$, ... (3.2)

with $\langle \cdot \rangle$ the operator of ensemble (weighted) average. Depending on the relationship assumed between distance and time delay, there are different variants of Radon transforms [linear,

parabolic, hyperbolic, etc.; see Equation 6 of Gu and Sacchi (2009)]. The beam method is the basis of the applications in the following subsections.

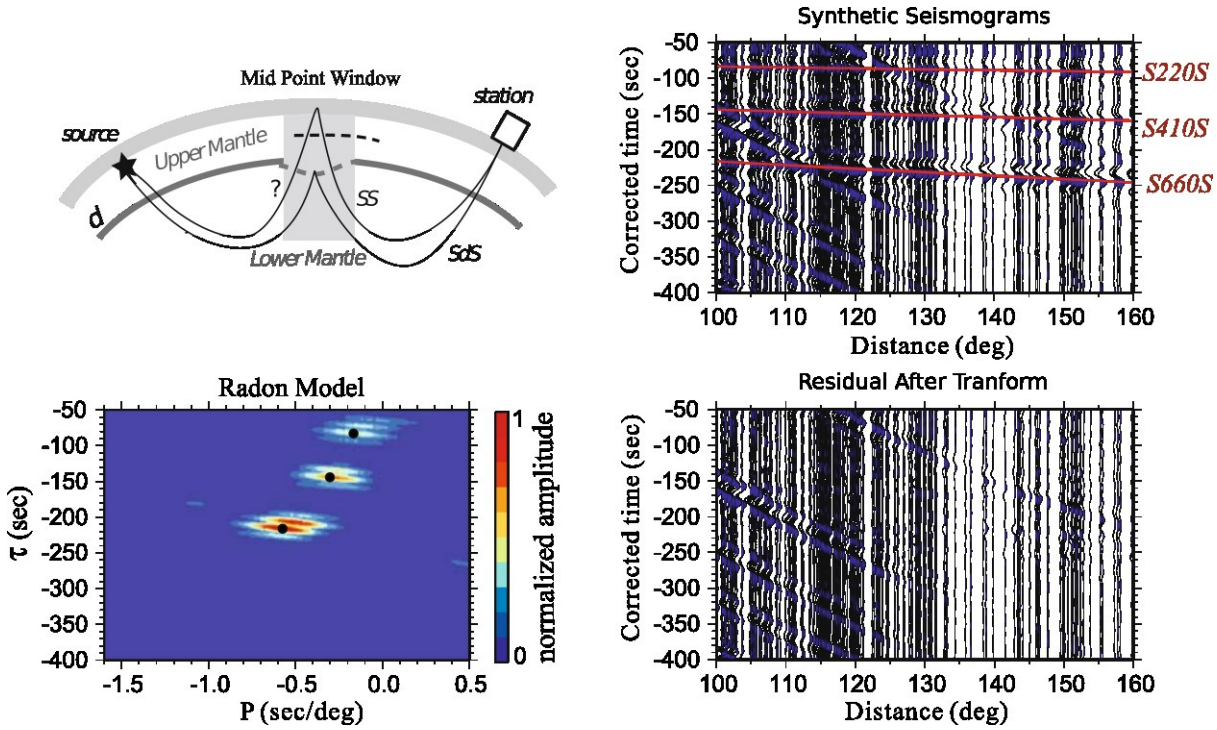

Figure 3.3. Synthetic example illustrating the use of Radon transform in wavefield decomposition and signal extraction. a) Schematic ray diagram for the SS phase and the precursor phase S*d*S due to the reflection at the bottom of an interface in mantle transition zone (*d* represents the interface depth). b) Synthetic seismograms aligned on SS. c) Radon solution for S*d*S phases. d) Difference between the original data and the reconstructed seismograms after filtering in the Radon domain. Undesired arrivals with different slowness from phases of interest are effectively filtered out. Reproduced from Figures 1 and 6 of Gu and Sacchi (2009).

As shown in Figure 3.2, by integrating along ray parameters, the coherent signals in the time-distance domain are mapped into energy foci in the Radon domain. We abundant Radon-based applications in seismology, such as signal identification, phase isolation, removal of multiples, signal enhancement, and spatial interpolation, to cite only a few. An example of the application of Radon transform in seismology is presented in Figure 3.3. For more comprehensive details on the mathematical formulations, code implementations and practical applications of the Radon-based methods in seismology, we refer to several concerned review papers (Rost and Thomas 2002, 2009; Gu and Sacchi 2009; Schultz and Jeffrey Gu 2013).

3.2.2. Double-Beam Method

Providing that *X{i}* means the *i*-th station of array *X* and $C_{ij}(t)$ is the correlation function between *A{i}* and *B{j}*, the slant stack of the inter-array correlations can be expressed as

$B(t) = \langle C_{ij}(t + \Delta t_{ij})\rangle$, ……. (3.3)

which is substantially equivalent to Equation 3.2 except the changes in the notations to make it compatible with the configuration of double-array interferometry. The equation is known as the double-beam method (Krüger et al. 1993; Rost and Thomas 2002) or double-beamforming (Roux et al. 2008, 2016; Leroy et al. 2012; Boué et al. 2013b, 2014b, Nakata et al. 2015, 2016).

The key of applying the double-beam equation to the double-array correlations is the calculation of the time delay between the station pair of *A{i}* and *B{j}* and the reference station pair. Depending on the way to computing the time delay, one can implement different Radon-based applications as introduced in the following subsections.

3.2.3. Vespagram

As for the geometry of double-array interferometry, assuming a linear path-function, the time delay can be calculated from (Schultz and Jeffrey Gu 2013)

$\Delta t_{ij} = p \cdot (d_{ij} - d_0)$, ……. (3.4)

with p the slowness, d_{ij} the distance between *A{i}* and *B{j}* and d_0 the distance between the reference station pair. By repeating the double-beam process for a range of slowness, one can obtain a *tau-p* diagram named vespagram. In some literatures, the vespagram is also called velocity spectral analysis or vespa process (e.g., Davies et al. 1971). In the vespagram, coherent signals are stacked constructively when integrating over some specific slowness. Accordingly, isolated and enhanced energy foci emerge at the location with correct slowness and arrival time.

3.2.4. Slowness Analysis

An underlying assumption in Equation 3.4 is that the slowness is the same at both arrays *A* and *B*. However, this assumption is potentially not always true. Allowing distinct slownesses at two arrays, one has

$$\Delta t_{ij} = \boldsymbol{x}_i^A \cdot \boldsymbol{p}^A + \boldsymbol{x}_j^B \cdot \boldsymbol{p}^B, \quad \text{..... (3.5)}$$

where $\boldsymbol{x}_k^X$ denotes the local coordinates of station $X\{k\}$ and $\boldsymbol{p}^X$ is the horizontal slowness vector of the wave at array X. The origin of the local coordinate system for array X is generally chosen at the array center. Equation 3.5 allows to estimate the slownesses and azimuths of the interferometric wavefields at arrays A and B.

3.2.5. Noise Source Imaging

In the context of forward modeling of the noise correlations for given noise sources, or imaging noise sources by back-projecting the noise correlations to potential locations, one can calculate the time delay with the aid of the *Taup* program (Crotwell et al. 1999) and the reference Earth models like the *PREM* model (Dziewonski and Anderson 1981), the *IASP91* model (Kennett and Engdahl 1991) and the *AK135* model (Kennett et al. 1995). Given the seismic phase and source-receiver distance, it is easy to obtain the predicted traveltime of the phase traveling from the source to the receiver (Figure 3.4).

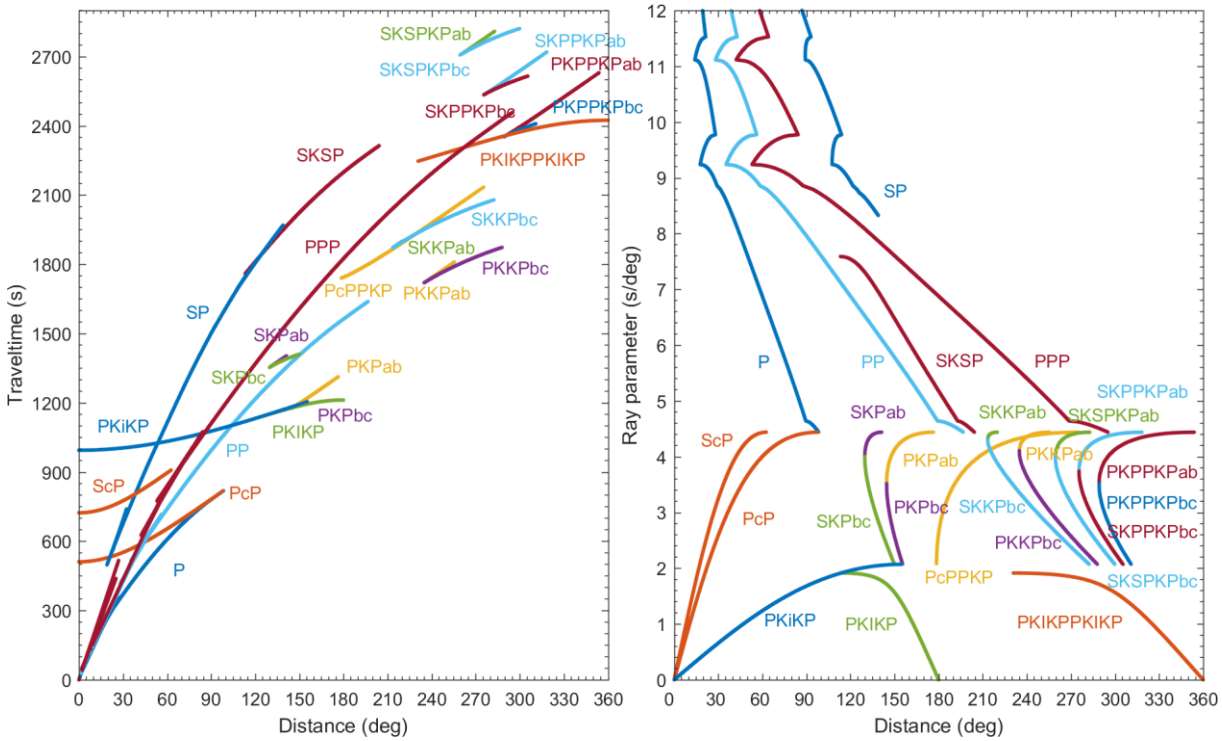

Figure 3.4. Theoretical curves of traveltimes and ray parameters for typical seismic body phases, predicted by the *Taup* program base on the *IASP91* model.

Using t_k^X to denote the traveltime of a seismic phase *X* from a noise source to station *X{k}*, the time delay between phase *A* at station *A{i}* and phase *B* at station *B{j}* is given by

$\Delta t_{ij} = t_i^A - t_j^B$, ... (3.6)

which predicts the emerging time of a signal in the inter-receiver correlation function resulting from the correlation between phase *A* at station *A{i}* and phase *B* at station *B{j}*. By stacking the signals in all double-array correlations based on Equation 3.3, one can assign the power of the double-beam to the presumed noise source location as its potential. Repeating the process for all possible locations, one can obtain the imaging of noise sources. The choosing of seismic phases can refer to the observed earthquake seismograms (see Figure 3.5 and Figure 3.6).

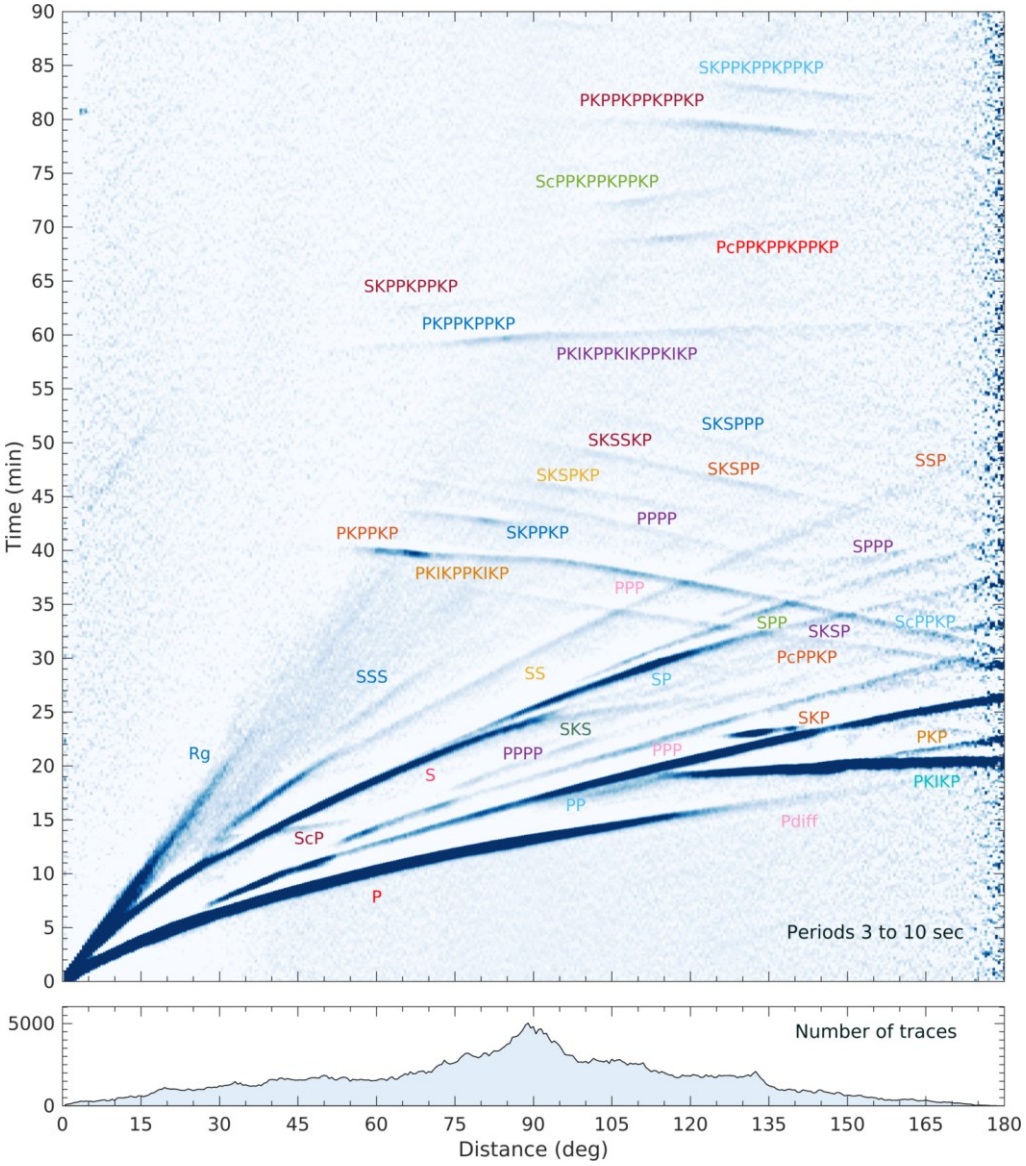

Figure 3.5. Global stacks of vertical components of earthquake seismograms in the period band of 3 to 10 sec (data provided by IRIS). Discernible seismic phases are labeled.

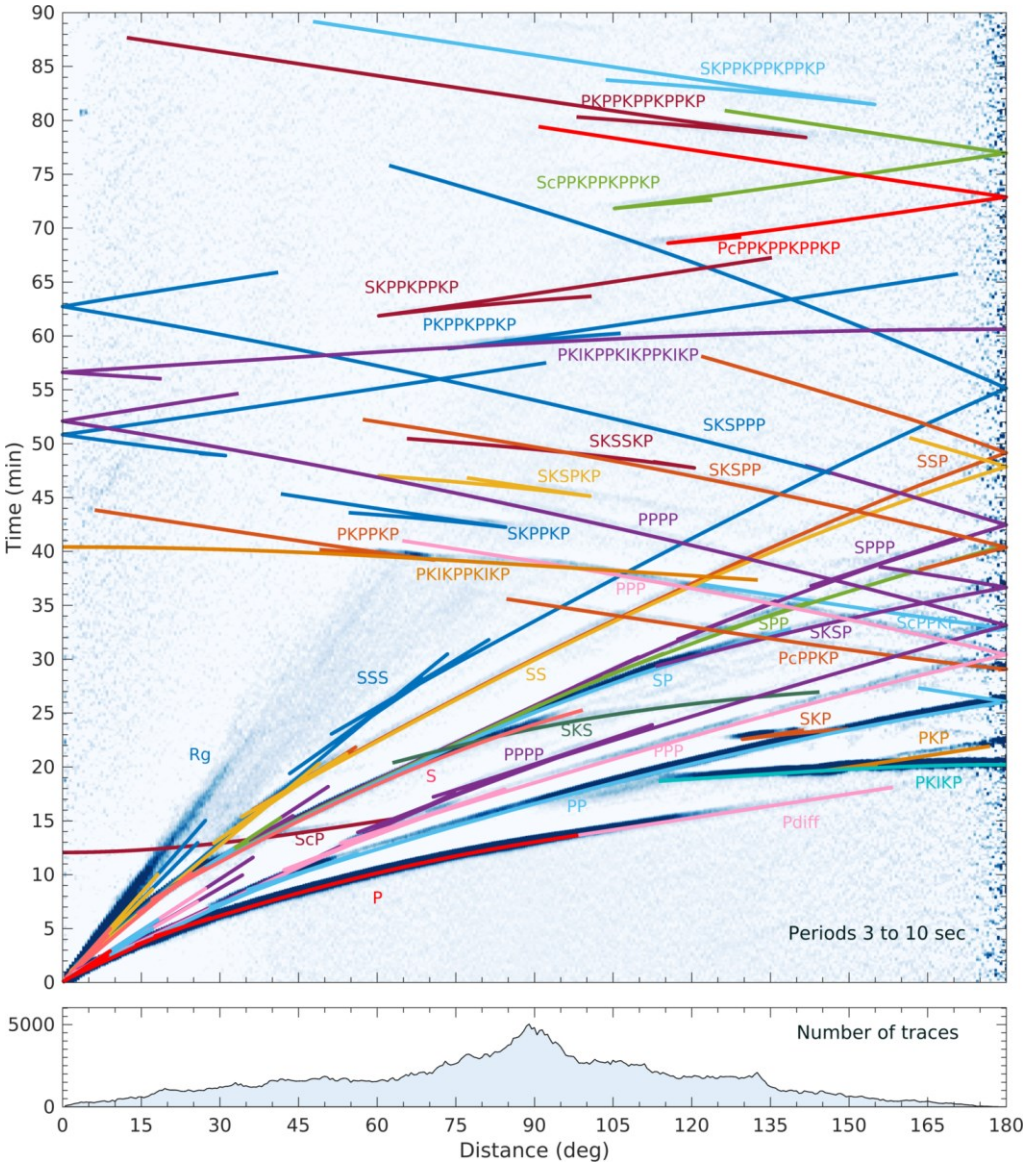

Figure 3.6. The same as Figure 3.5 but with theoretical traveltime curves plotted.

The back-projection technique based on single-array beamforming has been widely applied in earthquake seismology to image the rupture process of large earthquakes (e.g., Kiser and Ishii 2017), or in ambient noise seismology to locate noise sources (e.g., Gerstoft et al. 2008; Landès et al. 2010; Farra et al. 2016; Retailleau et al. 2018). However, as can be seen from Figure 3.4, multiple body waves can share the same slowness and a single array cannot distinguish between seismic ray paths of the same slowness. Consequently, even if a strong energy burst is detected by the single-array beamforming, it cannot determine a unique location for the noise source. The back-projection based on double-array correlations has distinct advantages over that based on single-array beamforming.

3.3. Summary

In this chapter, we introduced the vespagram method, slowness analysis and noise source imaging based on the double-beamforming of inter-array correlations. In the subsequent chapters, these techniques are applied to real data to study the extraction of seismic body waves from inter-array correlations.

4. Body Waves in Double-Array Noise Correlations

To investigate the recovery of deep body waves from ambient noise using the correlation technique, we cross-correlated in this chapter the continuous seismic data recorded by two broadband seismic networks separated at a teleseismic distance. The noise data processing and correlation function computation followed the methods introduced in Chapter 2. Preliminary results are descripted in this chapter. In subsequent chapters, the techniques proposed in Chapter 3 will be applied to the correlations computed in this chapter for further detailed investigations.

4.1. Seismic Networks and Noise Data

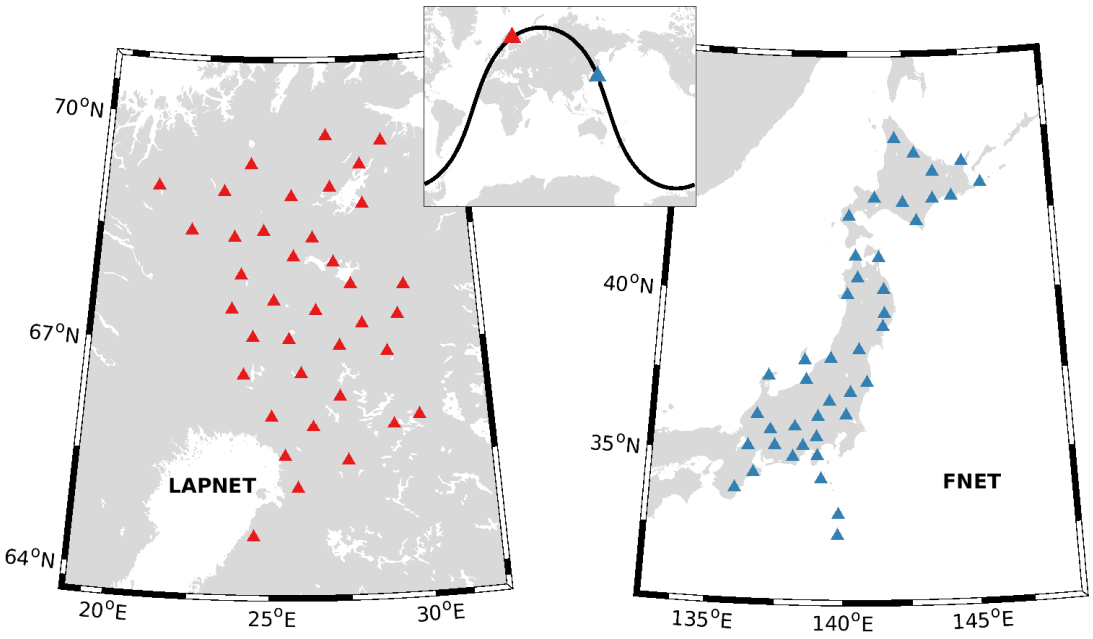

Figure 4.1. Geometry of the LAPNET array in Finland and the FNET array in Japan. The LAPNET array includes 38 broadband seismic stations, and the FNET array is composed of 41 stations. The inset shows the geographic locations of the two arrays on the global. The thick line represents the great circle across two arrays. The aperture of LAPNET is ~700 km and it is twice for FNET.

The vertical components of continuous seismograms recorded by the Full Range Seismograph Network of Japan (the FNET array) and the northern Fennoscandia POLENET/LAPNET seismic network (the LAPNET array), were used to reconstruct seismic body waves from ambient noise. The seismic data of FNET and LAPNET were obtained from data centers of the National Research Institute for Earth Science and Disaster Resilience (NIED) and the Réseau Sismologique et Géodésique Français (RESIF), respectively. The geographic distributions of the stations of the two seismic networks were present in Figure 4.1. The FNET array is a permanent network with long-term high-quality seismic data available. FNET covers the whole area of Japan but only 41 of the stations were chosen here. The LAPNET array is a portable seismic network that operated between mid-2007 and mid-2009. The seismic data of LAPNET are complete through the year of 2008. Only the 38 broadband LAPNET stations were selected and the short-period stations were rejected. The aperture of LAPNET is about 700 km. FNET has an aperture nearly double that of LAPNET but in an elongated shape.

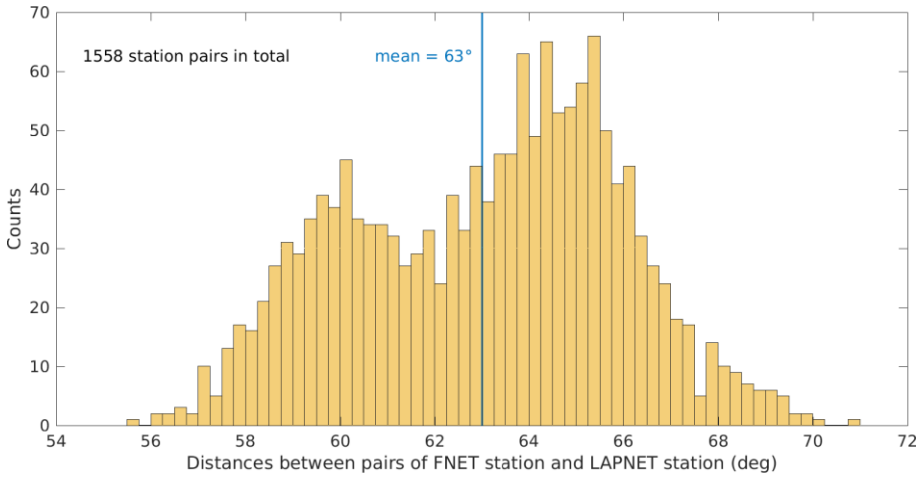

Figure 4.2. Histogram of the inter-station distances between all FNET-LAPNET station pairs. The width of a bin is 0.25°.

There are 1558 pairs of FNET station and LAPNET station in total. The statistical distribution of the inter-station distances is present in Figure 4.2. The inter-station distance ranges from 55.6° to 70.8°, with an average value of 63° and a standard deviation of nearly 3°. Most of the inter-station distances fall between 60° and 66°.

4.2. Double-Array Noise Correlations

4.2.1. Broadband Waveform Sections

We calculated the cross-correlation functions between all the 1558 pairs of FNET and LAPNET stations, for the year of 2008 and in the period band between 1 and 100 sec. The correlations were computed on an hourly basis. The hourly-based correlations were stacked into daily and annual traces, for further processing and analysis. The noise correlations of the same datasets had been computed by Boué et al. (2013a) and Boué et al. (2014a) to illustrate the extraction of teleseismic body waves from noise correlations, and by Poli et al. (2015) to determine the depth of the D″ structure under Siberia.

The annual stacks of the noise correlations between each pair of a FNET station and a LAPNET station were sorted by distance and plotted in sections shown in Figure 4.3. From the station-pairwise sections, one can easily identify the direct P arrivals in both the acausal and causal correlations, which implies that the reconstruction of teleseismic P waves is feasible even for a single station pair. The PcP arrivals are not easy to be identified visually (possibly discernible visually a bit in the causal section). Another striking feature shown in Figure 4.3 is the presence of a coherent phase in the acausal section at arrival times between 400 and 450 sec and at distances between 61° and 66°. The strange arrival is hundreds of seconds earlier than the direct P wave that is expected to be the primary arrival. Such an earlier arrival has neither been observed on real earthquake seismograms nor is predicted by classic seismological theories and is undoubtedly spurious.

To improve the visibility of the coherent arrivals reconstructed from seismic noise, we stacked the noise correlations in small distance bins. The binned sections were displayed in Figure 4.4. In the binned sections, the PcP arrivals hidden from the station-pairwise sections in Figure 4.3 became discernible. From the binned acausal section shown in Figure 4.4, one can observe that the spurious arrival is mostly clear between 61° and 66°, partly because of the denser available FNET-LAPNET station pairs in this distance range. In the binned causal section, a spurious phase corresponding to the one in the acausal section is still hardly discriminable.

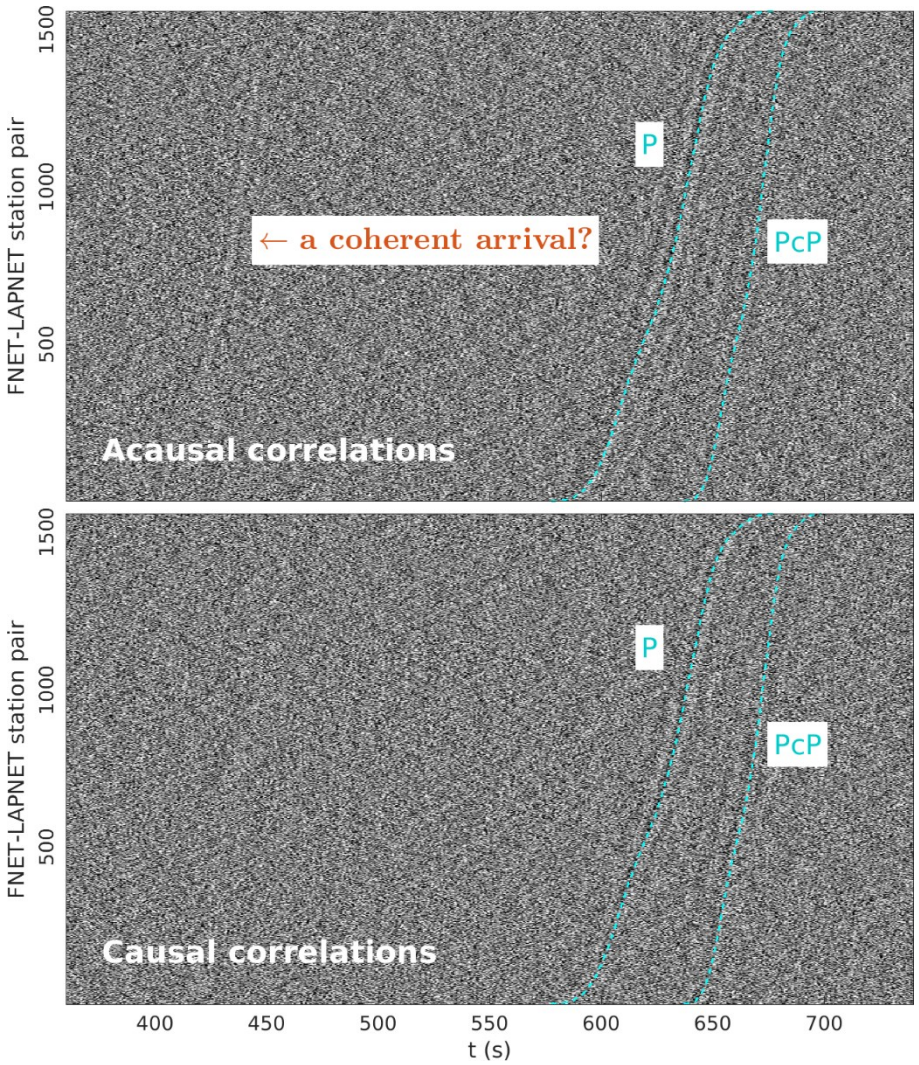

Figure 4.3. Broadband acausal and causal cross-correlation functions between all FNET-LAPNET station pairs. Each row of an image corresponds to the annual stack of the noise cross-correlations between a FNET-LAPNET station pair. The noise correlations are sorted with respect to the inter-station distance. The theoretical arrival times of the P and PcP waves predicted by Taup program are indicated by dashed lines. The acausal (causal) correlation functions correspond to seismic waves travelling from FNET to LAPNET (from LAPNET to FNET). The direct P waves are visible in both acausal and causal sections. The PcP waves, especially the acausal PcP wave, are hardly visible. In the acausal section, a coherent arrival is present about 200 sec prior to the P wave. No such an arrival is visible in the causal section.

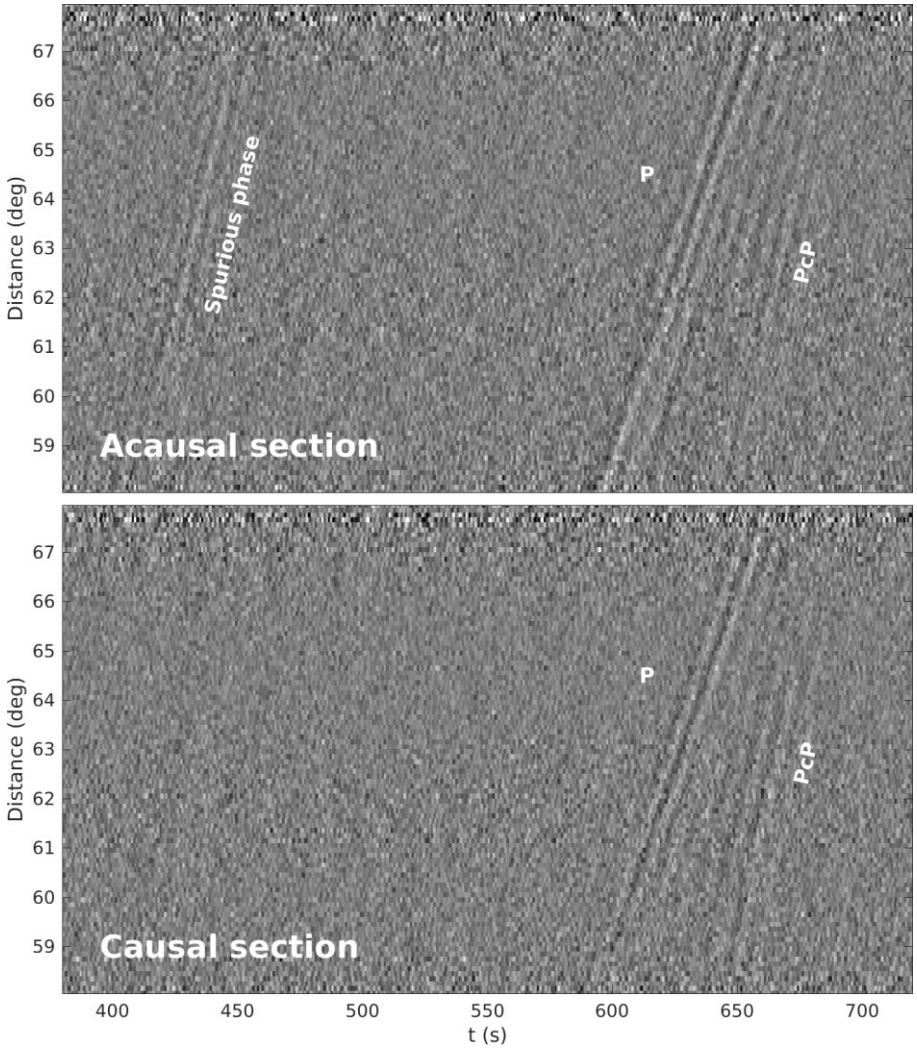

Figure 4.4. Broadband acausal and causal FNET-LAPNET noise correlations stacked in 0.1° bins.

4.2.2. Broadband Vespagrams

Vespagram is a better representation than the waveform section in the identification of coherent seismic arrivals. We computed the vespagrams from the annually stacked noise correlations of all FNET-LAPNET station pairs, with respect to a reference distance of 63°. The results were shown in Figure 4.5. At 63° distance, the theoretical traveltime and slowness are 628 sec and 6.7 s/deg for P, and 666 sec and 4.1 s/deg for PcP arrivals, respectively. It can be seen from the vespagrams that the P wave is strongest in both acausal and causal correlations. Between the P and PcP waves, there are several spots, likely the P reflections from the D″ layers (PdP waves). The acausal spurious phase is weaker than the P wave but stronger than the PcP wave. Again,

the corresponding causal spurious phase is missing. In the acausal vespagram, there appears to be another arrival a bit earlier than the P wave and with smaller slowness. This arrival is indiscernible in the waveform sections.

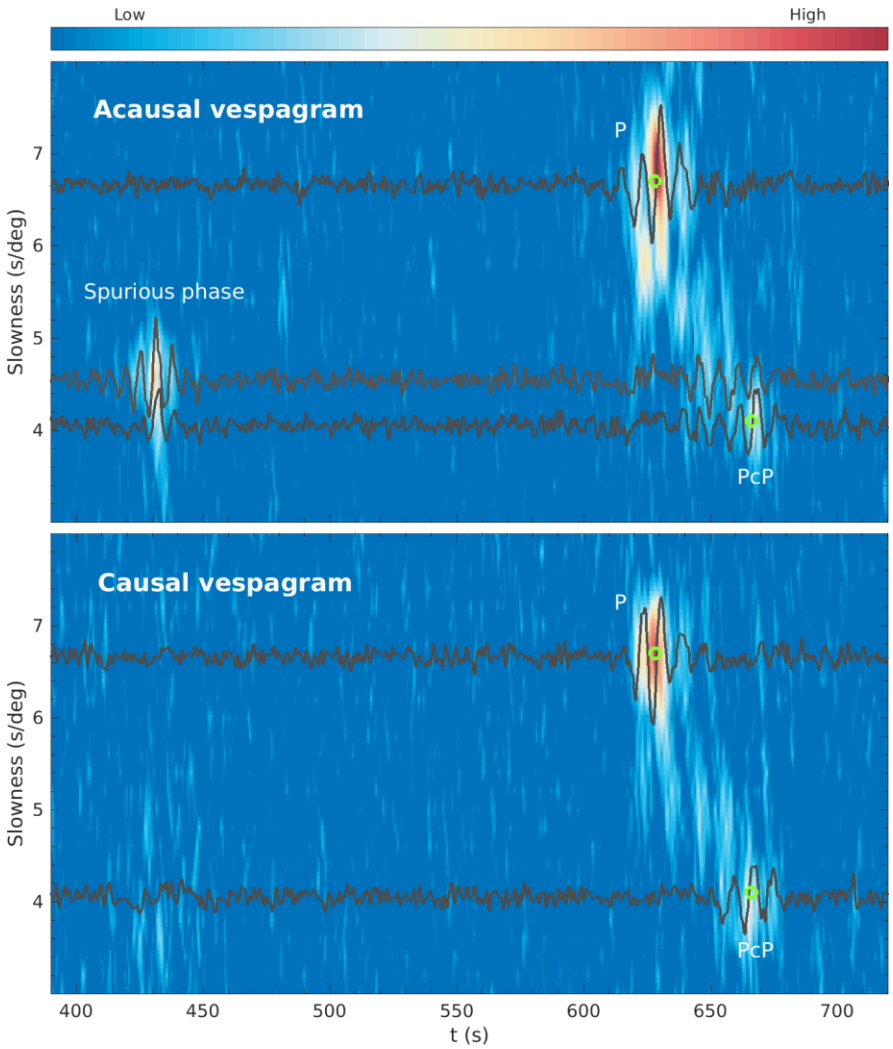

Figure 4.5. Acausal and causal vespagrams of the annual FNET-LAPNET noise correlations. The double-beamed waveforms for the acausal and causal P and PcP waves and the acausal spurious phase are plotted overlying the vespagrams. The theoretical P and PcP arrivals predicted by Taup program for a distance of 63° are indicated by open dots (628 sec and 6.7 s/deg for the P arrival; 666 sec and 4.1 s/deg for the PcP arrival).

4.3. Spectral Analysis of Reconstructed Seismic Phases

The double-beamed waveforms of the reconstructed seismic phases were plotted in Figure 4.6.

The discrepancy in the waveforms of the noise-derived acausal and causal P waves is small. However, the recovered PcP waves are apparently not time-symmetric. Spectral analysis can provide details in the frequency contents. We windowed the waveforms around the seismic phases and calculated their Fourier spectra, the magnitudes of which were shown in Figure 4.6. The peak periods estimated from the amplitude spectra are 6.2 sec for the acausal spurious phase, 7.7 (7.5) sec for the acausal (causal) P wave and 7.4 (7.9) for the acausal (causal) PcP wave. All the peak periods are typical for secondary microseisms. The frequency contents of the acausal and causal P or PcP waves are not perfectly consistent, which is ascribed to the different microseism excitations in the respective source regions. The spurious phase has a dominant period distinct from the P and PcP waves, signifying that the spurious phase is likely to originate from microseismic noise source distinct from the P and PcP waves. The differences in the source regions for the noise-derived body waves also imply that the amplitude ratios between different noise-derived phases are not expected to equal to the ratios derived from earthquake seismograms.

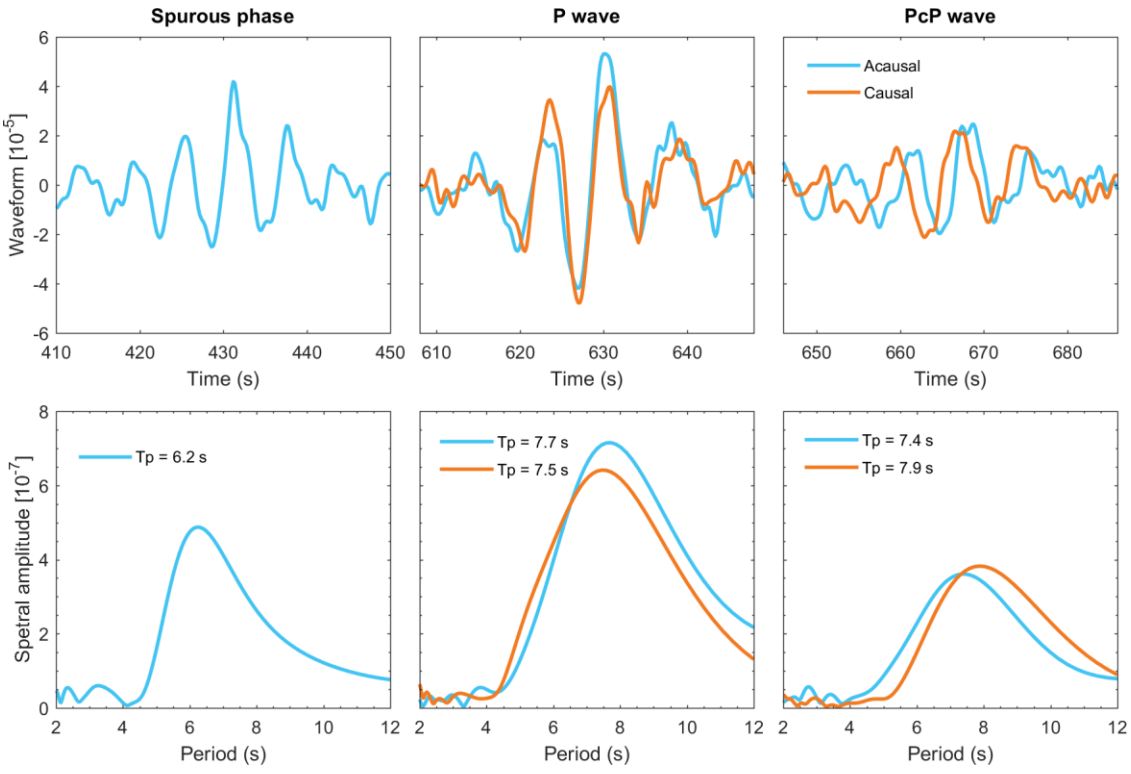

Figure 4.6. Double-beamed waveforms and spectral magnitudes of seismic body waves retrieved from the FNET-LAPNET correlations. Peak periods (Tp) of the phases are labeled on the panels.

4.4. Correlations in Secondary Microseism Frequency Band

4.4.1. Filtered Waveform Sections

Since the dominant frequencies of the reconstructed seismic phases all fell in the typical frequency band of secondary microseisms, we filtered the double-array noise correlations in the frequency band of 0.1 to 0.2 Hz. The filtered acausal and causal sections were shown in Figure 4.7. The coherent arrivals in the filtered sections are all visible through almost the full distance range displayed. The spurious arrival is most legible between 60.5° and 66.5°.

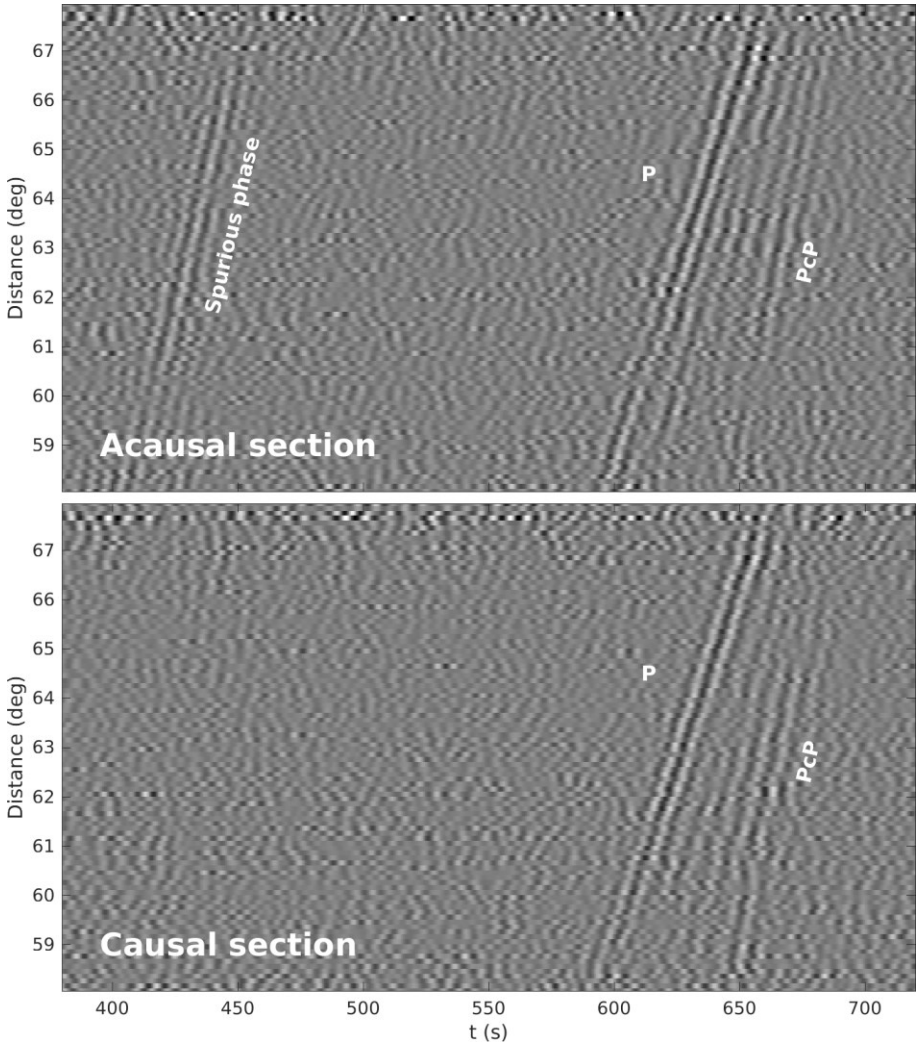

Figure 4.7. Sections of the acausal and causal FNET-LAPNET noise correlations bandpass filtered in the secondary microseism period band (5 to 10 sec).

4.4.2. Filtered Vespagrams

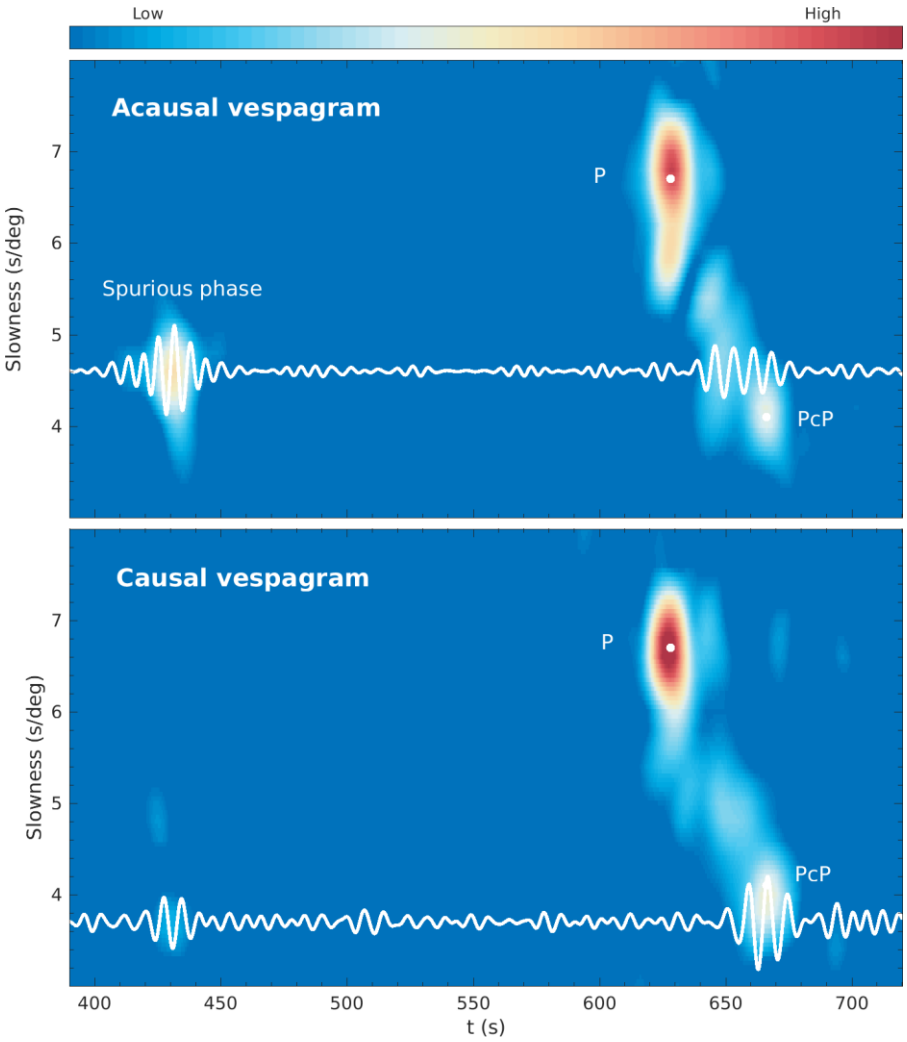

Figure 4.8. Acausal and causal vespagrams of the FNET-LAPNET noise correlations filtered between 5 and 10 sec. The theoretical P and PcP arrivals are indicated by white dots. The arrival time and the slowness of the acausal spurious phase are 430.8 sec and 4.6 s/deg, respectively. In the causal vespagram around 430 sec, there seems to be a weak phase but with a smaller slowness (3.6 s/deg) compared to the acausal spurious phase. The corresponding double-beamed waveforms are plotted overlying the vespagrams.

The vespagrams were also bandpass filtered and were displayed in Figure 4.8. From the acausal vespagram, we estimated that the arrival time and slowness of the acausal spurious phase are 430.8 sec and 4.6 s/deg, respectively. In the causal vespagram around 430 sec, there seems to be a weak spot with a smaller slowness of 3.6 s/deg compared to the acausal spurious phase. Regarding the P waves, the causal and acausal waveforms are quite similar (see Figure 4.6).

However, the arrival time and slowness estimated from the acausal vespagram are a bit larger than those estimated from the causal vespagram. The time difference is even beyond 1 sec. It seems that highly accurate absolute traveltime estimates are difficult.

4.5. Summary

In this chapter, we computed the noise cross-correlation functions between 1558 pairs of FNET station and LAPNET station in 2008. Inspecting the waveform sections and the vespagrams, we found that the teleseismic P and PcP waves were recovered from seismic noise. Deep P reflections (PdP waves) were also likely reconstructed. In addition to the regular seismic phases, we observed the presence of a prominent spurious phase arriving much earlier than and another spurious phase in proximity to the direct P arrival in the acausal correlations. The P wave and the early spurious phase were discernible even in the annual noise correlation between a single station pair. All these phases have peak frequencies in the frequency band of secondary microseisms. In the following chapters, we shall explain the origins of the reconstructed body waves, with emphases on spurious phases.

5. Seismic Interferometry of Quasi-Stationary Phase

In Chapter 4, we computed the cross-correlation functions between the FNET-LAPNET station pairs and briefly described the results. It was shown that even though the receivers were separated at teleseismic distances, deep body waves could still be successfully retrieved from seismic noise. However, in contrast to the seismograms from earthquake observations, some anomalous, coherent arrivals were observed from the virtual seismograms reconstructed from seismic interferometry. The most prominent one is the early spurious arrival in the acausal noise cross-correlations. In this chapter, we are committed to unveil the origin of the spurious phase and accordingly propose a new mechanism explaining the generation of stable spurious phases in noise correlations.

5.1. Observation of Coherent Spurious Arrival

At the beginning of this chapter, we make a quick review over the observation of the spurious phase that has been discovered in Chapter 4, and present more examples concerning the observation of the spurious phase in daily correlations.

5.1.1. A Quick Review

In the acausal noise correlations between FNET and LAPNET, which are supposed to be the empirical Green functions for seismic waves traveling from FNET toward LAPNET, we have observed a coherent spurious arrival with a slowness of 4.6 s/deg emerging about 200 sec prior to the direct P arrival. Spectral analysis revealed that the spurious phase has a peak period of 6.2 sec, a typical value for the secondary microseisms. The dominant period of the spurious phase is distinct from those of the P and PcP wave which are between 7 and 8 sec, indicating a separated source region for the spurious phase from the source regions for the P and PcP waves. A corresponding time-symmetric spurious phase is missing in the causal noise correlations.

Based on the estimates of the slowness and emerging time of the spurious phase, we shifted the annual noise correlations for all 1558 FNET-LAPNET station pairs to make them aligned at the spurious phase. The broadband (1 to 100 sec) and filtered (5 to 10 sec) sections of aligned

noise correlations were plotted in Figure 5.1. The spurious phase is visually discernible from the sections composed of noise correlation functions of single station pairs, namely, it can be reconstructed from the annual stack of noise correlations of a single station pair. The spurious phase is most easily discernible between 61° and 66°.

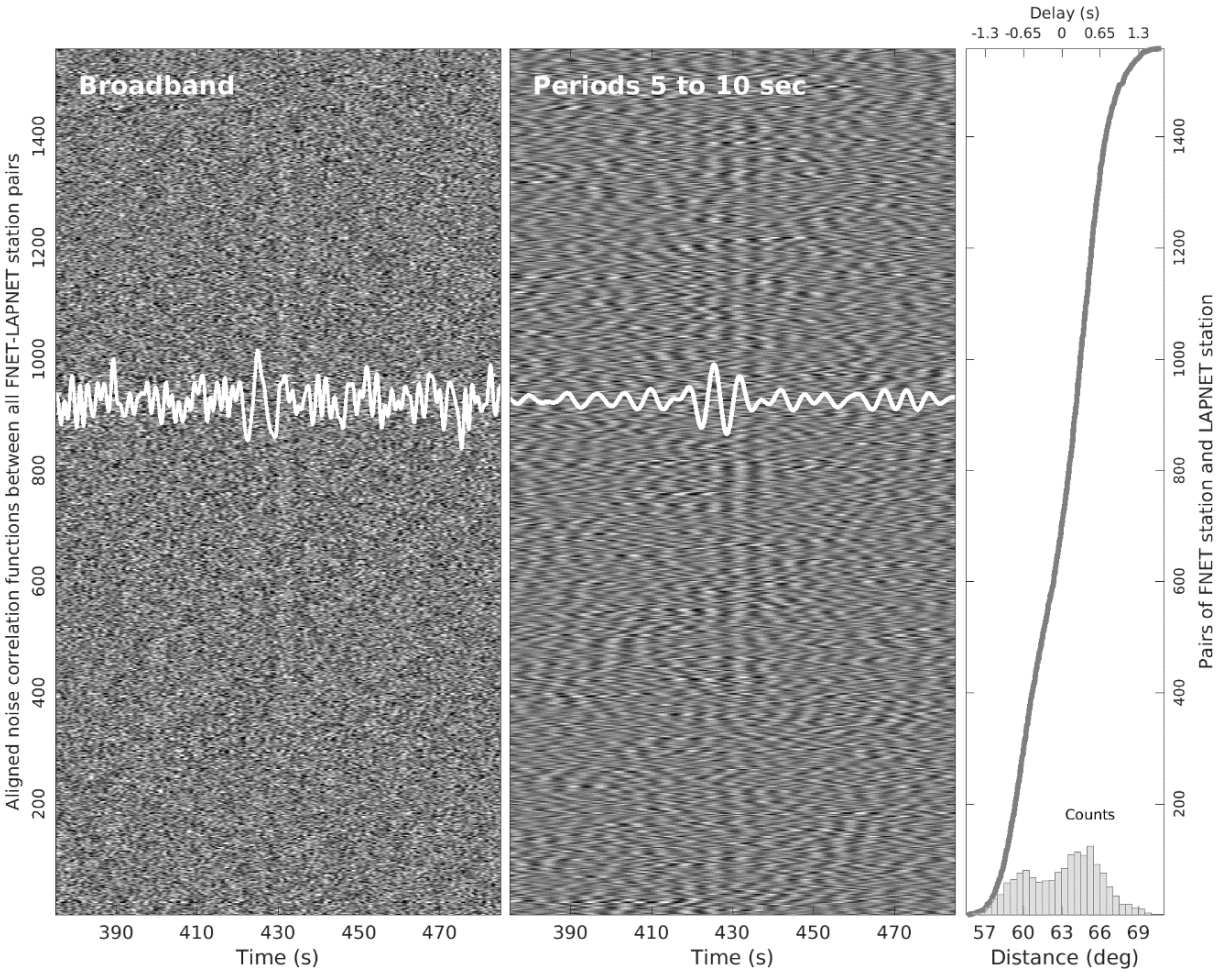

Figure 5.1. Broadband (periods from 1 to 100 sec) and bandpass-filtered (periods from 5 to 10 sec) acausal cross-correlation functions between all FNET and LAPNET station pairs, aligned and windowed around the spurious phase. Each row of an image corresponds to the annual correlation function between a single station pair. The correlation functions are shifted by a time delay determined from the inter-station distances (relative to a reference distance of 63°) and the slowness of the spurious phase (4.6 s/deg). The waveforms overlying the images are the broadband and filtered correlation functions for the pair of FNET station BO.TTO and LAPNET station XK.LP72. The distribution of inter-station distances and the corresponding time delays are shown in the rightmost panel.

5.1.2. Daily Noise Correlations

The spurious phase can not only be retrieved from the long-term stack of noise correlations between a single station pair. It is even feasible from single-station-pair noise correlations on some single days. In Figure 5.2, we showed such an example for the date of 2008-05-01. There are 1280 station pairs available for this date. The spurious phase are retrieved from the daily noise correlations of the majority of available station pairs. The binned waveform section and the vespagrams for this date are plotted in Figure 5.3 and Figure 5.4, respectively.

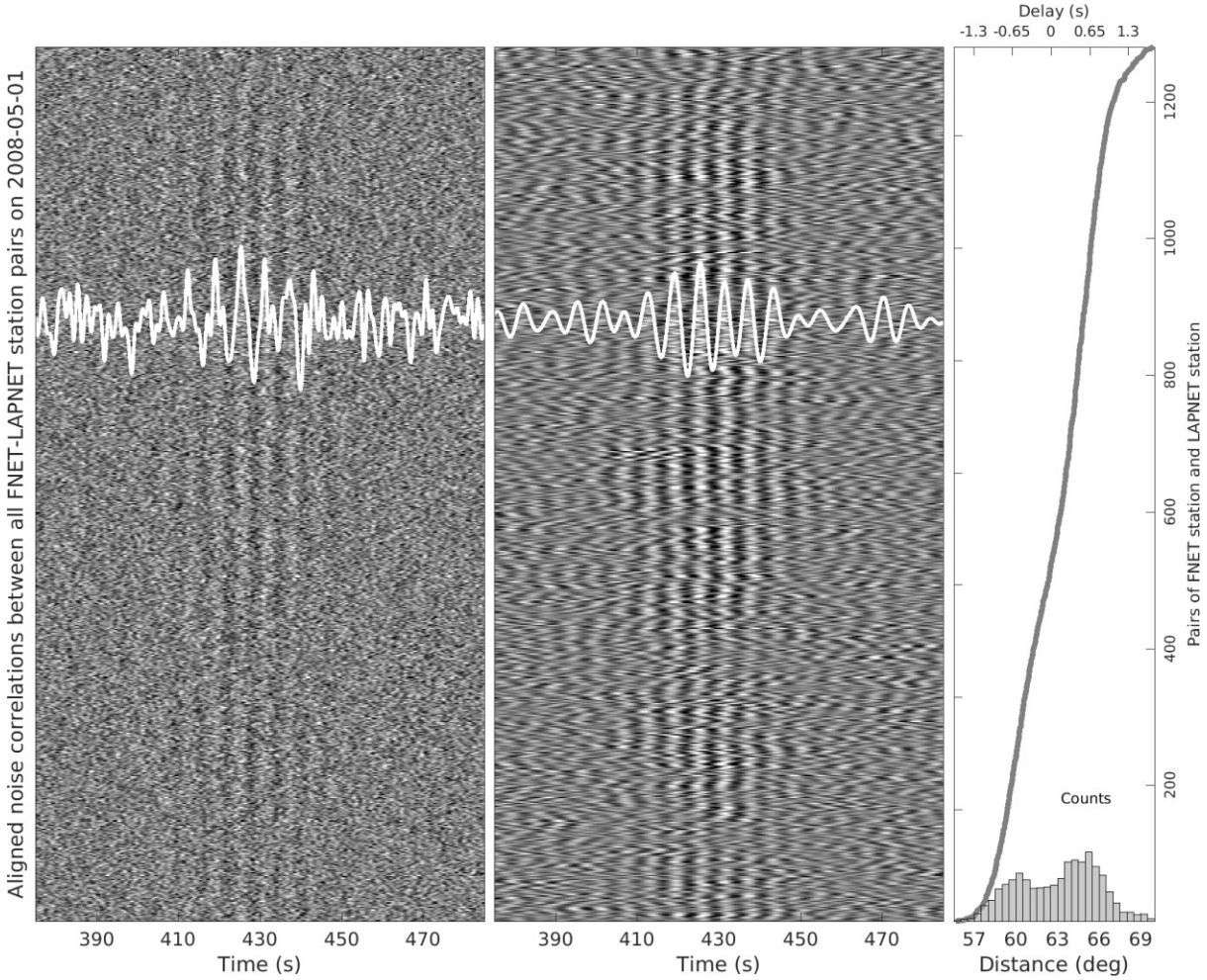

Figure 5.2. Broadband and bandpass-filtered acausal noise correlations between all available FNET and LAPNET station pairs on 2008-05-01, aligned and windowed around the spurious phase. Each row of an images represents the correlation function of a station pair shifted by a time delay determined from the inter-station distance and the slowness of the spurious phase. The waveforms overlying the images are the broadband and filtered noise correlations between a selected station pair. The distribution of inter-station distances and the corresponding time delays are displayed in the rightmost panel.

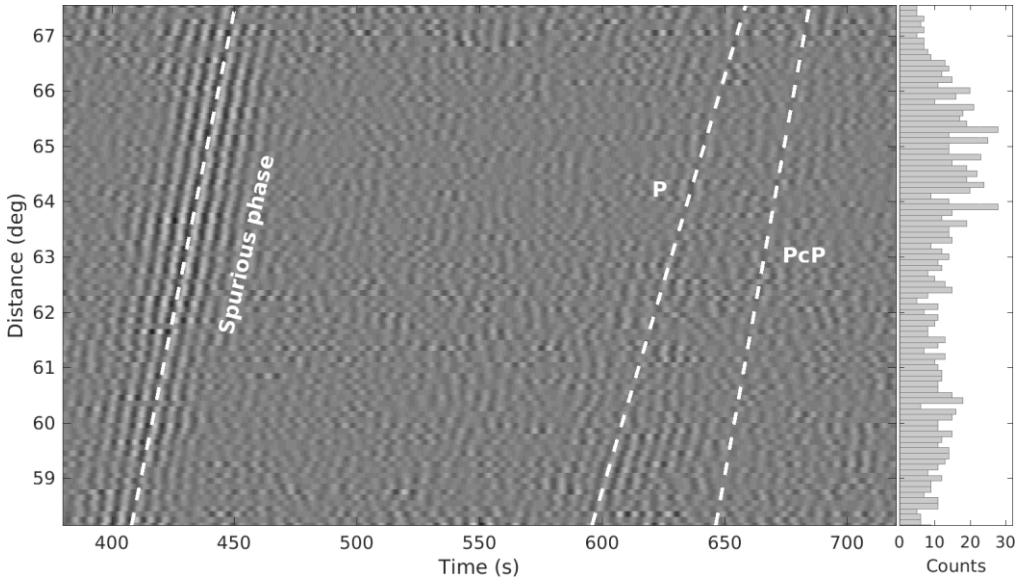

Figure 5.3. Waveform section of the acausal noise correlations on 2008-05-01. The daily noise correlations for station pairs are binned in an interval of 0.1°. The counts of available station pairs in each bin are shown in the right panel. Dashed lines indicate the predicted arrival times of the spurious phase, P and PcP waves. Prominent spurious phase is retrieved from the daily correlations.

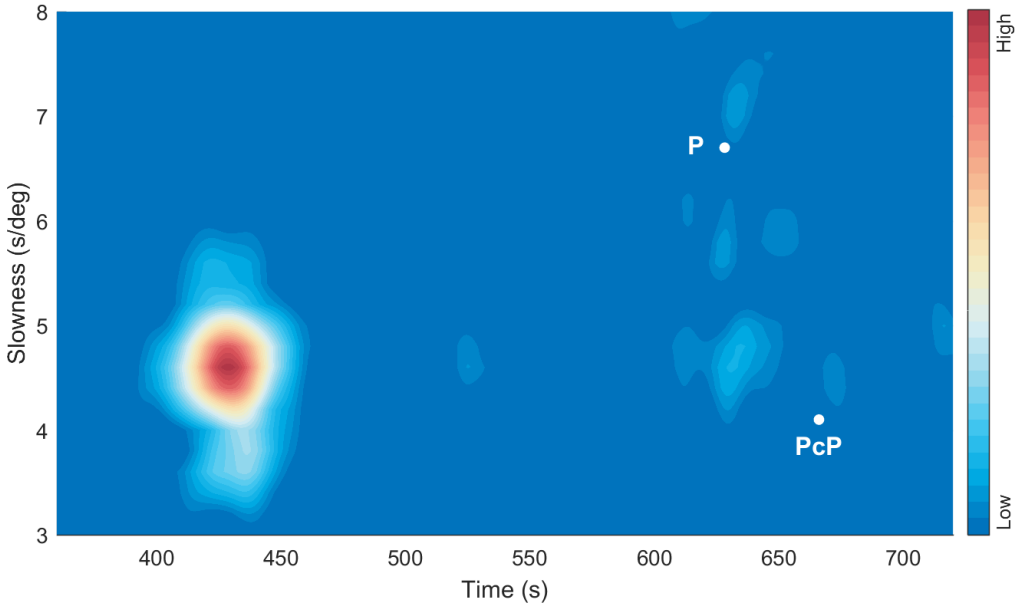

Figure 5.4. Vespagram of the acausal noise correlations on 2008-05-01. The spurious phase is strong on this date, while P and PcP waves are not reconstructed from the daily correlations. The theoretical P and PcP arrivals are marked by white dots.

5.2. Origin of Spurious Phase

The theory of stationary phase is usually used to explain the reconstruction of seismic phases from noise correlations (Snieder 2004; Schuster et al. 2004; Ruigrok et al. 2008; Wapenaar et al. 2010b, 2012; Boschi and Weemstra 2015). According to the theory of stationary phase, in 1D Earth model, the slownesses of two interferometric wavefields yielding a regular seismic phase are expected to be the same at both receivers. In this case, the delay between the traveltimes from effective noise source to the receivers being correlated corresponds to an extreme value (stationary location) on the curve of time delay between receivers with respect to the source-receiver distance. It is believed that the reconstruction of regular seismic phases can be explicable in the manner. However, it is not yet a certainty that the emergence of the spurious phase can also be explained in the same way.

5.2.1. Double-Array Slowness Analysis

In order to estimate the slownesses and backazimuths of the interferometric waves at FNET and LAPNET, we applied the double-array slowness analysis to the acausal spurious phase in the annual noise correlations of single station pairs. The station-pairwise correlations were modulated by a 30 sec window centered on the spurious phase before being double-beamed to eliminate amplitudes other than the spurious phase. The position of the spurious phase on each noise correlation was predicted by $t_{ij} = t_0 + (d_{ij} - d_0) \cdot p$, with i and j the station index, t_{ij} the emerging time of the spurious phase in the correlation function, t_0 and p the emerging time (431 sec) and slowness (4.6 s/deg) of the spurious phase estimated from the acausal vespagram, d_0 the reference distance (63°) and d_{ij} the inter-station distance. The results of the slowness analysis were plotted in Figure 5.5. It can be seen that the backazimuths of the interferometric waves are well confined in the great-circle directions. However, the slowness at FNET (4.7 s/deg) and the slowness at LAPNET (4.2 s/deg) are quite different from each other. In the framework of stationary phase and assuming that the lateral variations are neglectable (i.e., in 1D Earth model), the slowness is expected to be the same at both arrays, in contradiction with our observations. To rule out the possibility that the lateral heterogeneities of Earth's structure led to the discrepant slownesses, we also applied the double-array slowness analysis to the acausal P wave. The slownesses of the interferometric waves for the P wave are almost coincide at both arrays. The results for the P wave were consistent with the prediction of the theory of

stationary phase, implying that the slowness discrepancy for the spurious phase is not caused by the lateral heterogeneities. It can thus be concluded that the spurious phase cannot be explained by the theory of stationary phase and should stem from some other mechanism. In the following subsection, one will see that the double-array slowness estimates obtained here are the key to solving the puzzle.

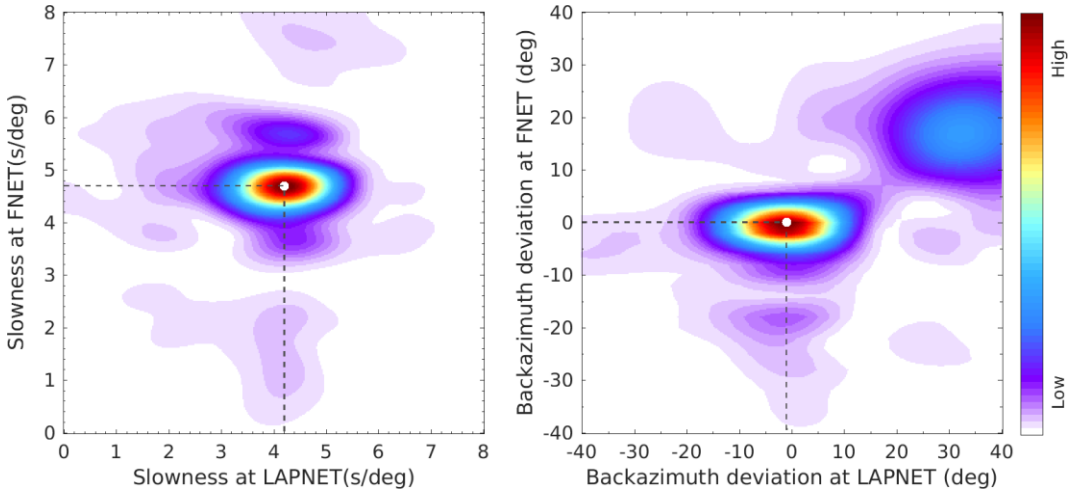

Figure 5.5. Power maps of double-beamed noise correlations for estimating the slownesses and backazimuths of the interferometric wavefields at FNET and LAPNET which are responsible for the generation of the spurious phase. The backazimuth deviation is defined as the clockwise azimuthal deviation from the great circle across FNET and LAPNET. The optimal estimates are indicated by white dots. The backazimuths are well confined in the sagittal plane but the slowness at FNET (4.7 s/deg) is distinct from the slowness at LAPNET (4.2 s/deg).

5.2.2. Tracking Paths of Interferometric Waves

From the acausal vespagram in Chapter 4, we obtained the emerging time of the spurious phase (about 430 sec), which corresponded to the time delay between the interferometric waves at two receivers separated by 63°. From the slowness analysis in the previous subsection, we obtained the respective slownesses of the interferometric waves. One can check which couple of ballistic seismic phases can fulfil the source-receiver geometry and the estimates of slowness and time delay. When coming to the selection of candidate seismic phases, the existing seismic recordings from earthquakes can provide us a good reference. Figure 5.6 displays the global section of earthquake seismograms filtered around 6 sec period, which is close to the dominant

period of the spurious phase. Visually discernible seismic body waves are labeled in the global section of earthquake seismograms. Theoretical studies have revealed that the dominant source of secondary microseisms, the oceanic wave-wave interactions, can be equivalent to a random vertical pressure field applied to the free surface of the water layer (Longuet-Higgins 1950; Hasselmann 1963; Ardhuin and Stutzmann 2012). The excitation mechanism of the strongest microseisms implies that the microseismic body waves are dominated by P waves. Seismological observations have also confirmed that P waves are much stronger than S waves in microseisms (Liu et al. 2016a; Nishida and Takagi 2016). Furthermore, we are studying the noise correlations between the vertical components of seismograms. All these reasons support to take into account P-type phases as candidates in priority. However, here we still considered all the labeled seismic phases in the global section of earthquake seismograms as candidates responsible for the generation of the spurious phase from noise correlations.

The ballistic seismic phases are generally valid only in specific ranges of slowness. Therefore, some invalid phases could be excluded with ease by the estimated slownesses. The remaining phases were taken into further considerations. For clarity, we only plotted in Figure 5.7 the theoretical traveltime and ray parameter curves of several typical P-type phases, including P, PP, PcP and PKP branches PKPab, PKPbc and PKPdf (PKIKP). There are several couples of seismic phases sufficing the source-receiver geometry and time delay constrains, for instance, PcP at FNET with PKPab at LAPNET or P at FNET with PKPbc at LAPNET. However, the full constrains can only be met by a combination of the P wave at FNET with the PKPab wave at LAPNET. The slowness estimates played critical roles in the unique determination of the interfering seismic phases.

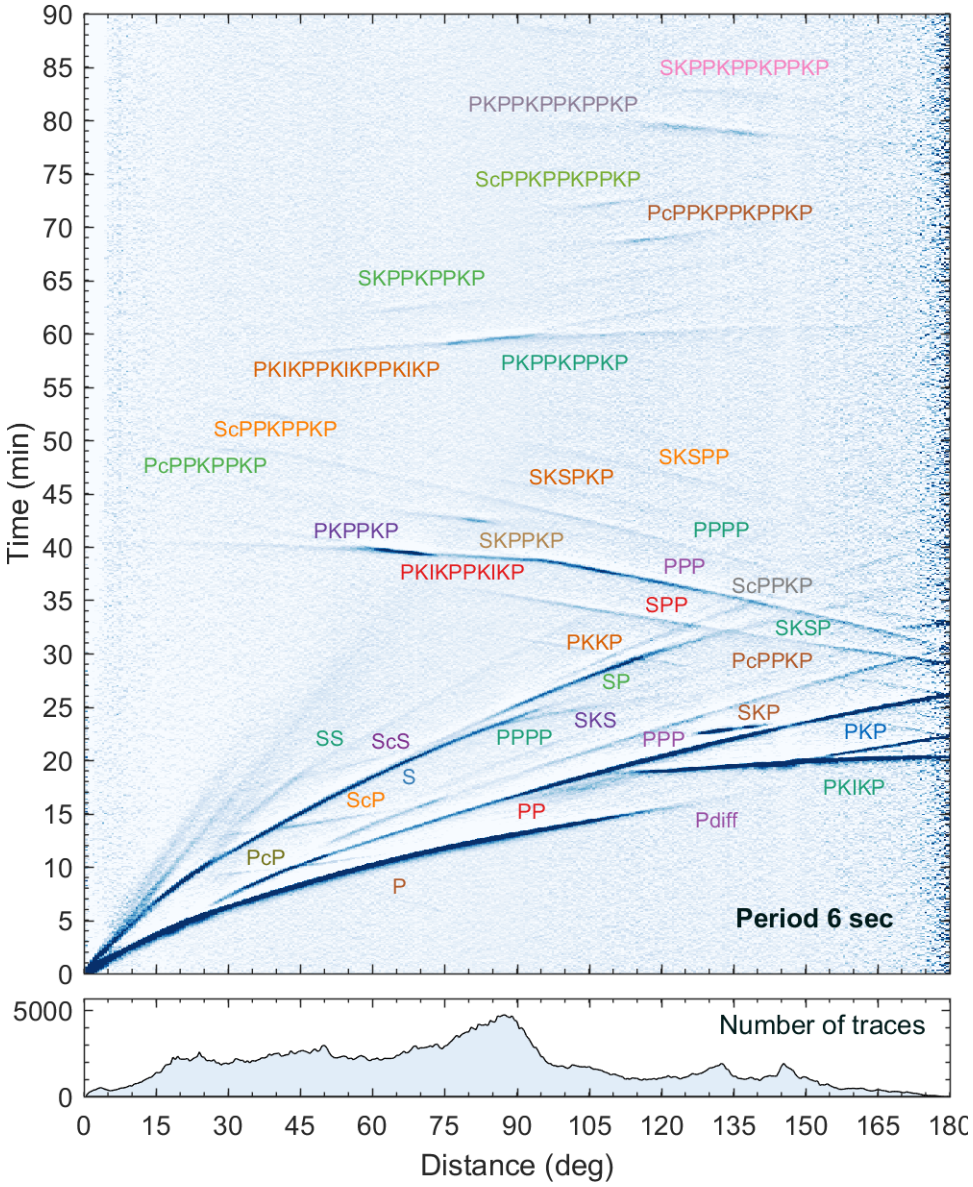

Figure 5.6. Global stacks of vertical components of earthquake seismograms with discernible seismic body phases labeled. A quality control is applied to over 600,000 seismograms from more than 2,500 earthquakes occurring between 1995 and 2013 with event depth shallower than 50 km and magnitude no less than 5.4. The selected seismograms are filtered around a period of 6 sec and converted into traces of the short-term-average over long-term-average (STA/LTA) ratios. The STA/LTA traces are binned by epicentral distances with an interval of 0.5°. The stacked traces are normalized before plotting. More details regarding the retrieval and processing of the data used in this plot can be found from the IRIS Data Services Products webpage (https://ds.iris.edu/ds/products/globalstacks/).

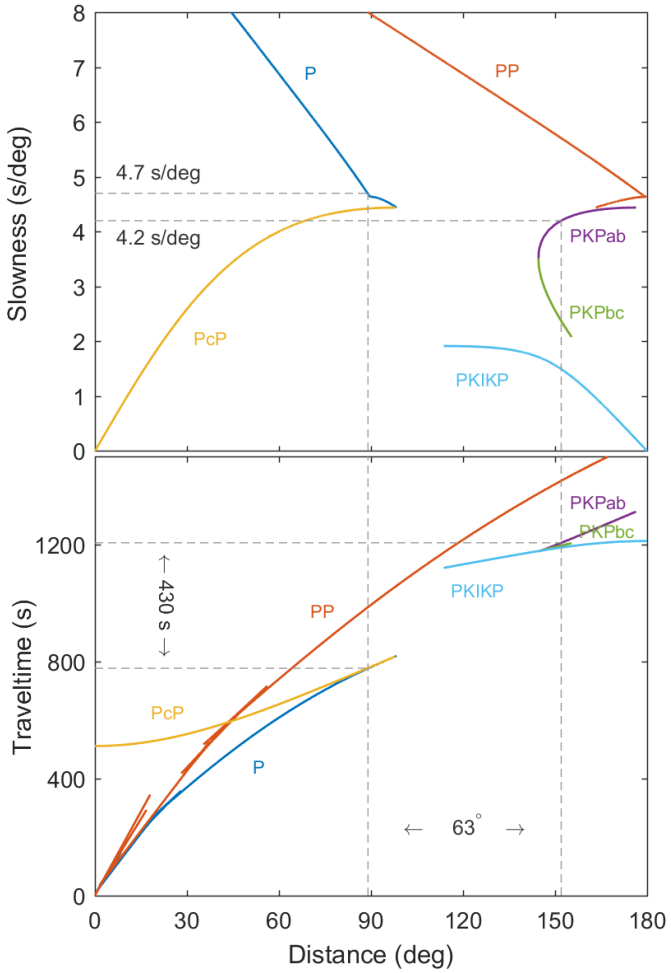

Figure 5.7. Theoretical curves of ray parameter (upper) and traveltime (lower) with respect to source-receiver distance for typical P-type phases (P, PcP, PP, PKP). Based on the inter-receiver distance (63°) and time delay (~430 sec), and the estimated slownesses of 4.7 s/deg at FNET and 4.2 s/deg at LAPNET, one can find that a combination of the P wave at FNET and the PKPab wave at LAPNET can suffice all the constrains. Accordingly, the microseism noise source should be 89° away from FNET and 152° away from LAPNET, at around [45°S, 174°E] south of New Zealand.

5.2.3. Noise Source Imaging

Once the ray paths of the interferometric waves have been known, one can apply the Radon-based noise source imaging to the double-array noise correlations. The results for annually averaged noise sources and daily noise sources on 2008-05-01 are shown in Figure 5.8. In both images, the spots of microseismic noise sources are always well focused in the ocean south of New Zealand, surrounding the point source location determined from Figure 5.7. In the image

of annual noise sources, there is a secondary spot to the south of the Australian Tasmania Island and to the west of New Zealand, possibly a localized strong noise source (evidence will be shown later).

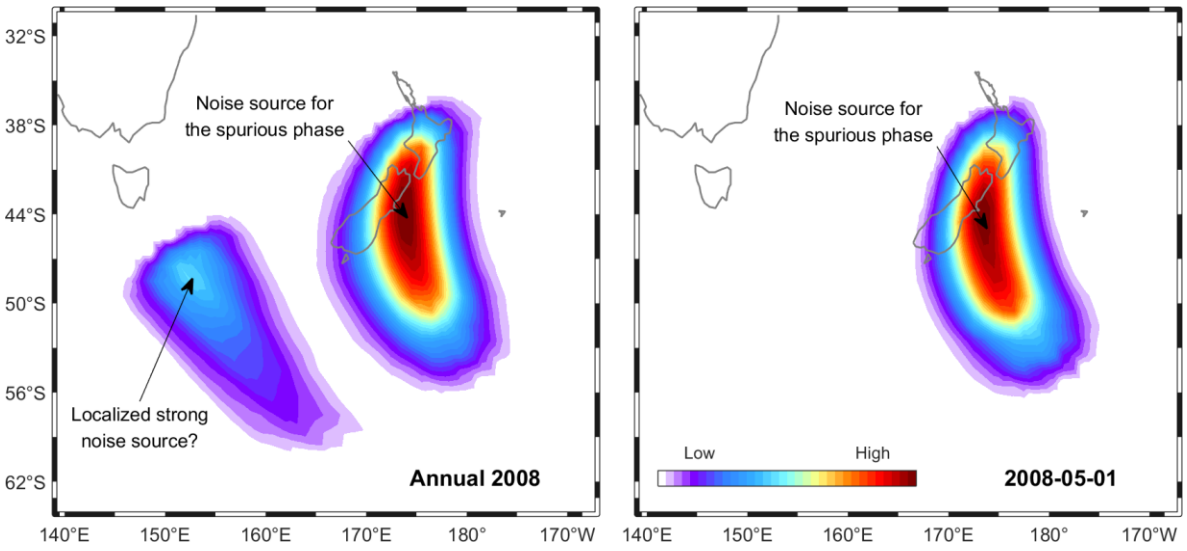

Figure 5.8. Maps of the probability of noise source distribution. Left: Noise source imaging for annual noise correlations. Right: Noise source imaging for daily correlations on 2008-05-01. The global surface is discretized into 1° × 1° grids as distributed noise sources. Based on the predicted time delays between the P waves at FNET stations and the PKPab waves at LAPNET stations for each grid point, the noise correlations of single station pairs are double-beamed and the power of the double-beam is assigned to the grid point as the probability. Grid points with fewer than 800 available pairwise correlation functions (about half the total number of the FNET-LAPNET station pairs) are skipped.

5.2.4. Quasi-Stationary Phase Interferometry

We have proposed that the spurious phase is not yielded by the same mechanism as regular seismic phases which can be explained by the theory of stationary phase. To have an intuitive understanding on how the correlation between the P and PKPab waves can give rise to the spurious phase, we made a simplified synthetic experiment based on ray theory. The model geometry and the P-PKPab time delay were presented in Figure 5.9. The P-PKPbc ray paths and time delay were also plotted for comparison. The P-PKPab combination is valid in a broader distance range than the P-PKPbc combination. Furthermore, the variations in time

delay are smaller for P-PKPab than for P-PKPbc. Based on the ray-derived time delays, one can synthesize the inter-receiver correlation function via source averaging. The results for the correlation function between the P and PKPab waves were plotted in the left panel of Figure 5.10. Despite that there is no stationary location on the curve of P-PKPab time delay as expected by the theory of stationary phase, the correlation functions for the sources at larger distances are more or less aligned in phase and can still be stacked constructively in source averaging. Consequently, a clear signal emerges in the stacked correlation function. In our numerical tests, the stack can stay effective at 1 sec or even shorter periods. Referring to the mechanism of stationary phase to explain regular seismic phases reconstructed from noise correlations, we propose to name the mechanism as the P-PKPab correlation illustrated here the interferometry of **quasi-stationary phase**. Note that we ignored the amplitude variations in the source-wise correlation functions, which implies that the presence of the spurious phase does not result from localized strong noise source (non-uniform distribution of noise sources) as demonstrated in Figure 2.9.

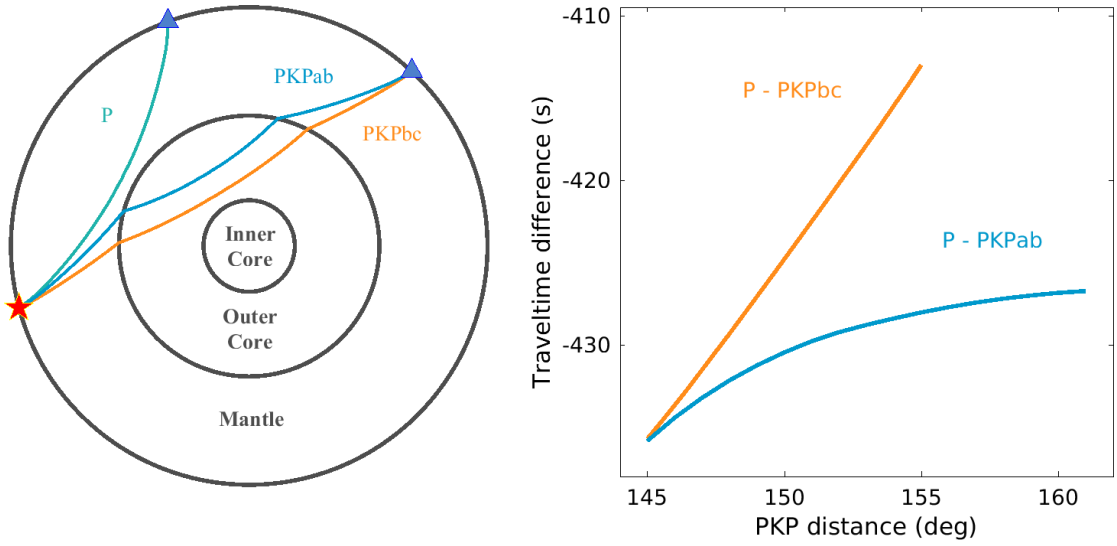

Figure 5.9. Left: Ray paths of P and PKP waves being correlated. The source and receivers are represented by the star and triangles, respectively. Right: Time delays between the P and PKP waves at a pair of 63°-separated receivers, for sources distributed at varying distances. No stationary points with zero slope exist on the curves of time delay.

From the experience of earthquake observations, PKPbc is generally the dominant PKP branch at distances from the PKP caustic at about 144° until around 153° (Kulhánek 2002). Array observations of microseism noise also reported that PKPbc is more prominent (Gerstoft et al.

2008; Landès et al. 2010). To demonstrate why the correlation between the P and PKPbc waves failed to produce the spurious phase, we synthesized the results of source averaging for the P-PKPbc correlation. As shown in the right panels of Figure 5.9 and Figure 5.10, the time delay between the P and PKPbc waves varies almost linearly against the distance and the broader dynamic range of P-PKPbc time delay leads to that the signals in the source-wise correlation functions are out of phase and consequently the source averaging is ineffective.

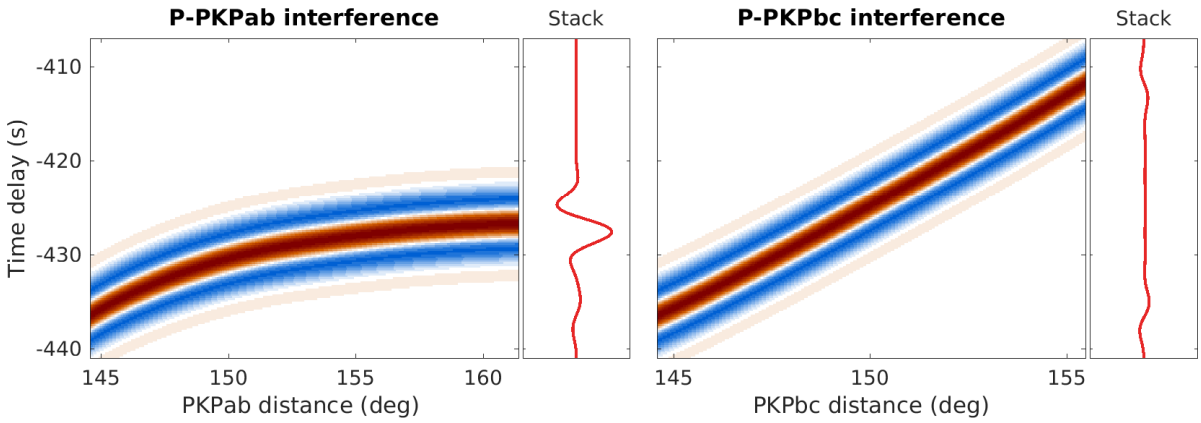

Figure 5.10. Synthetic experiments to explain the building of the spurious phase from seismic interferometry of quasi-stationary phase. We convolve the P-PKP time delay as shown in Figure 5.9 with a second-order Gaussian pulse with a dominant period of 6.2 sec, to mimic the cross-correlation function between the P and PKP waves from a corresponding noise source. For simplicity, the amplitude variations of the correlation functions with respect to the distance are neglected. The correlation functions for all valid sources are stacked to synthesize the final noise correlation function between two receivers. It can be seen that the stack is constructive in the case of P-PKPab interference (left) but destructive in the case of P-PKPbc interference (right). The building of the signal from the stack of P-PKPab correlations is mainly ascribed to the sources at larger distances where the P-PKPab time delay curve is sub-horizontal (quasi-stationary).

5.3. Temporal Variations of Spurious Phase

Recall that in subsection 5.1.2, we presented examples of daily noise correlations with strong spurious phase. In this section, we make a survey on the daily variations of the spurious phase throughout a full year. The results presented in this section are the basis of the investigations in later sections.

5.3.1. Daily Variations of Spurious Phase

We double-beamed the daily noise correlations with the slowness of the spurious phase estimated from the annual vespagram. The broadband and filtered daily double-beams and the derived daily strength were plotted in Figure 5.11 and Figure 5.12, respectively. In principle, a slant stack based on the double-array slowness estimates should give better beamforming. However, from our tests, the double-beamed waveform is not so sensitive to the limited changes in slowness. The resultant double-beams using a unique slowness or respective slownesses does not lead to nontrivial difference for our studies.

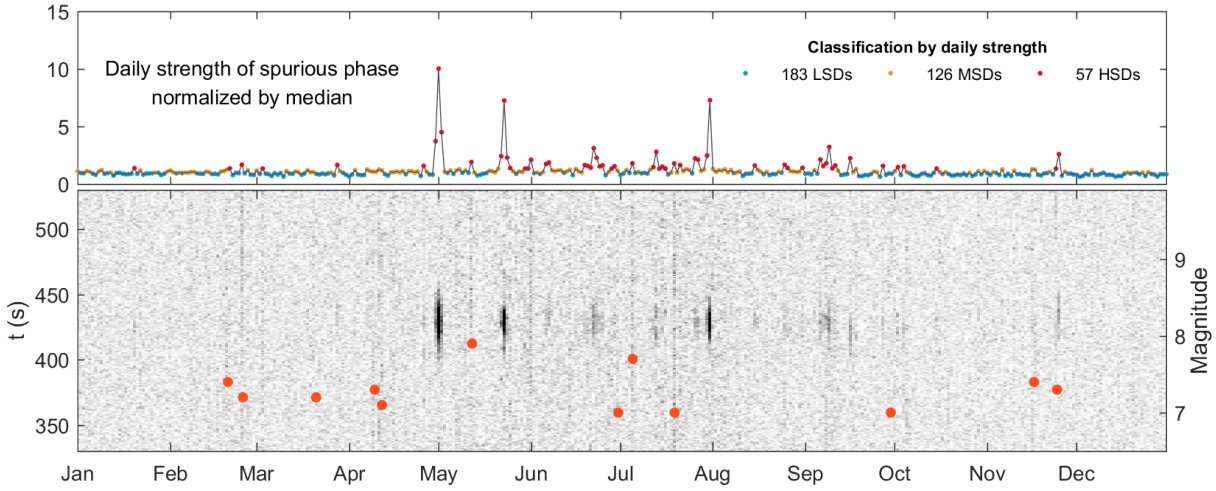

Figure 5.11. Envelopes of double-beamed daily noise correlations (lower) and variations in the strength of the daily spurious phase (upper). The noise correlations are broadband. Global M7+ earthquakes are plotted at their origin times overlying the image of daily double-beams. The strength of the spurious phase is computed from the average of the envelope of daily double-beam in a 60 sec window around the spurious phase. The strength is normalized by the median of the strength on all days. The daily double-beams of noise correlations are classified into three groups according to their strength. The 183 days (half of all days) with strength lower than the median of all days (low-strength days; LSDs) constitute the largest group. The 130 days (~35% of all days) with strength between the median and the sum of median and mean absolute deviation (MAD) of all days (moderate-strength days; MSDs) make up the second group of an intermediate size. The remaining 53 days (~15% of all days) with strength above median plus MAD (high-strength days; HSDs) belong to the last and smallest group. In other words, the three groups are divided by the 50 and 85 percentiles.

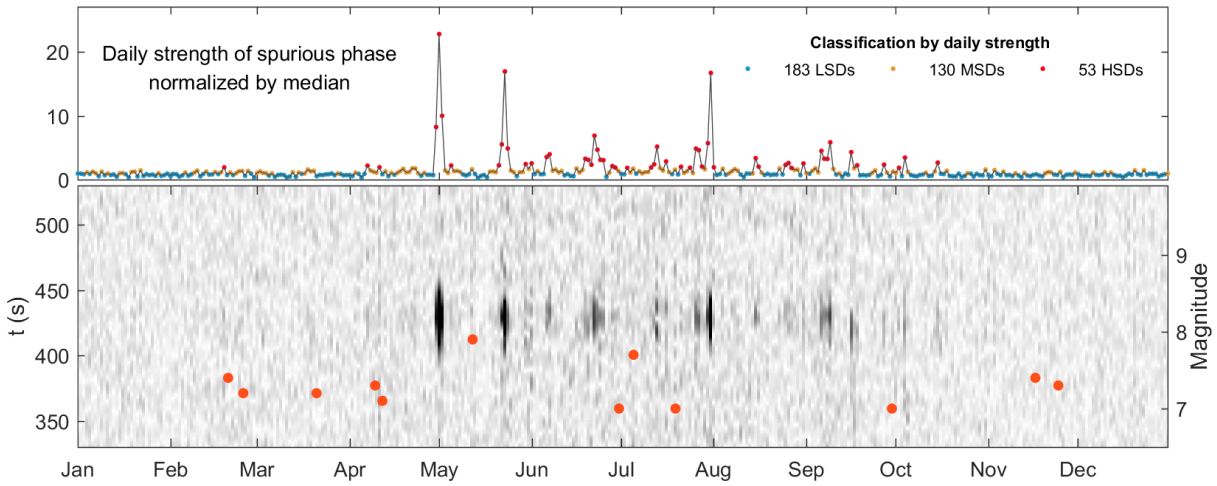

Figure 5.12. Envelopes of double-beamed daily noise correlations (lower) and variations in the normalized strength of the daily spurious phase (upper). The noise correlations are filtered between 5 and 10 sec. Global M7+ earthquakes are plotted at their origin times overlying the image of daily double-beams. The shape of the strength curve does not change significantly compared to the curve derived from the broadband double-beams.

It can be seen from the figures that the daily strength of the spurious phase exhibits dramatic fluctuations. The strength on some days (05-01, 05-23 and 07-31 for examples) can be one or two orders higher than on other days. The drastic temporal variability implies that it is hard to have a simple universal rule of thumb on how many data are enough to reconstruct a seismic body phase. At an overall sight, the daily strength exhibits a clear seasonal variation pattern, consistent with the well-known feature of the temporal variations in the global ocean wave activities or oceanic microseismic noise sources (e.g., Young 1999b; Stehly et al. 2006; Tanimoto 2007b; Gerstoft and Tanimoto 2007; Gerstoft et al. 2008; Yang and Ritzwoller 2008; Stutzmann et al. 2009; Hillers et al. 2012; Koper and Burlacu 2015). The vast majority of HSDs concentrates in the austral winter months (defined as six months from April to September in this chapter; the northern winter months comprising the remaining six).

5.3.2. Classification of Daily Noise Correlations

Based on the daily strength of the spurious phase, we divided the daily correlations into three groups: the LSD group for low-strength days, the MSD group for mediate-strength days, and the HSD group for high-strength days. The vespagrams for the three groups were plotted in

Figure 5.13, which reveals that the building of the spurious phase is predominantly attributed to the smallest but strongest HSD group. The contribution of the MSD group is limited. The largest but weakest LSD group, make no contributions.

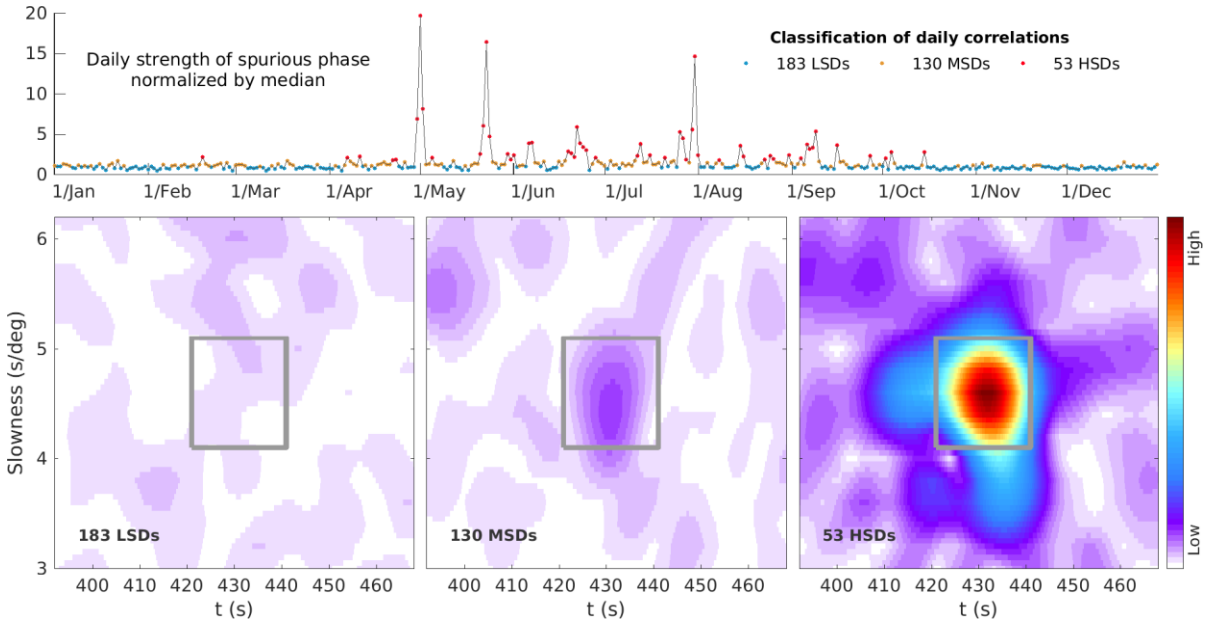

Figure 5.13. Upper: Daily variations in the strength of the spurious phase derived from daily vespagrams and classifications of the daily correlations. Lower: Vespagrams for the three groups. The strength is computed from the average in the box surrounding the spurious phase in the vespagram, so that the shift of the daily spurious phase due to the wandering of noise sources is considered. The vespagram-derived daily strength brings no clear changes to the temporal variations and classifications of daily correlations.

5.4. Comparisons with Seismological Observations

In section 5.2, we have discovered that the correlation between the P waves at FNET and the PKPab waves at LAPNET should be responsible for the emergence of the spurious phase with a typical dominant period of secondary microseisms. By correlation-based double-array back-projection, we located the noise source in the ocean south of New Zealand. In this section, we exclude the possibility of seismicity being the origin of the spurious phase on the one hand. On the other hand, we compare the daily spurious phase with the daily noise level at seismic stations close to the source region, which can be a direct evidence supporting our results. The availability of the broadband GEONET network deployed in New Zealand (see Figure 4.1)

offers us the great opportunity to verify the results of noise source imaging. The seismic noise data in New Zealand are provided by the GEONET Data Center.

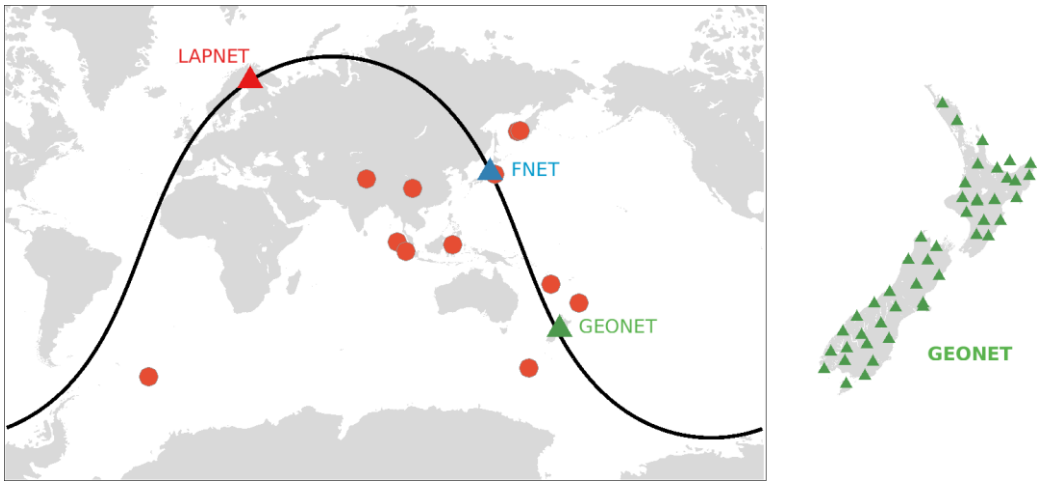

Figure 5.14. Global map with array locations and M7+ earthquakes in 2008. The earthquakes are marked by dots. The geographic locations of the FNET, LAPNET and GEONET arrays as indicated by triangles. The thick line is the great circle crossing all three networks. The center-to-center distance is 85° (148°) between GEONET and FNET (LAPNET). The distribution of the 46 elementary stations of GEONET is shown on the right side.

5.4.1. Comparisons with Global Large Earthquakes

It has been revealed that late codas of large events contain a fair portion of steeply traveling body waves (Sens-Schönfelder et al. 2015; Poli et al. 2017), or say, reverberations between primary interfaces like free surface and core-mantle boundary (Boué et al. 2014a; Phạm et al. 2018). It is thus unlike that the presence of strong daily spurious phases should be related to the coda wavefields which are not abundant in mantle refracted P waves. Moreover, the coherent phases extracted from coda correlations are generally at longer periods outside the period range of microseisms (Poli et al. 2017; Phạm et al. 2018; Wu et al. 2018). On some of the days with large earthquakes, one can observe from the broadband panel in Figure 5.11 the conspicuous vertical stripes resulting from the correlation of highly coherent earthquake coda waves. These stripes disappear from the filtered panel in Figure 5.12, affirming the difference in the frequency contents.

Nonetheless, considering that the late coda waves from large earthquakes were not discarded intentionally in our noise data processing, it is not totally redundant to survey the links between the occurrence of global large earthquakes and the emergence of strong spurious phases. From Figure 5.11 or Figure 5.12, one can find no correspondence between global large earthquakes and strong daily spurious phases. Thereby, we have confidence to conclude that the emergence of the spurious phase is not related to large earthquakes.

5.4.2. Comparisons with Seismicity in New Zealand

Large earthquakes have been found to have no connections with the spurious phase. However, considering that the noise source locates in proximity to New Zealand, a tectonically active region lying on the deforming boundary zone between the Australian and Pacific plates, one cannot reject the possibility that the seismicity in New Zealand, specifically the highly-frequent small earthquakes, led to the emergence of the spurious phase in the noise correlations. With the event catalogue provided by the GEONET Data Center, we computed the accumulated seismic moment of M2+ events in New Zealand on each day and compared the daily seismic moment with the daily spurious phase (Figure 5.15). It can be observed that no connections exist between the spurious phase and the seismic moments in New Zealand.

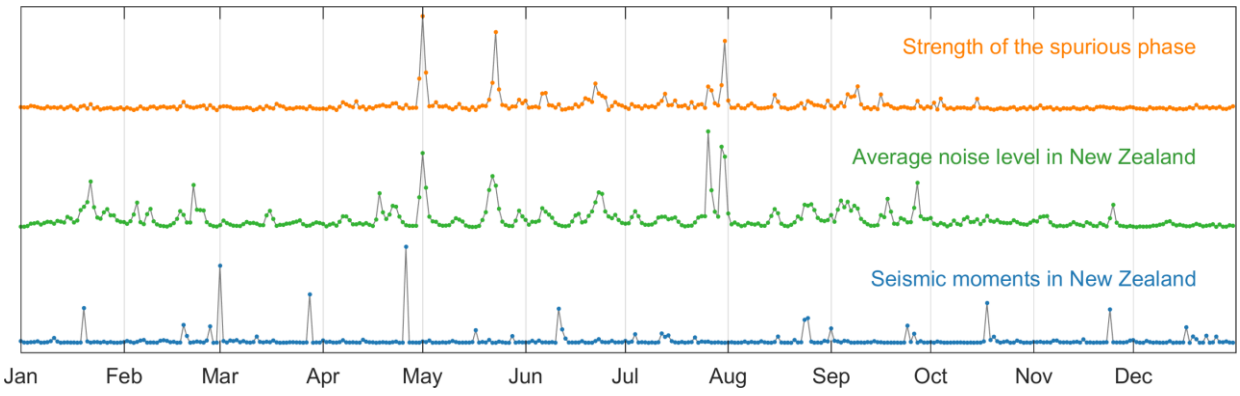

Figure 5.15. Comparisons between the daily variations in the strength of the spurious phase and the daily variations in the average level of secondary microseisms and seismicity in New Zealand. The curves are normalized for display purpose. The three strongest spurious phases appeared on 05-01, 05-23 and 07-31. The highest two peaks for the noise level arose on 07-26 and 07-30.

5.4.3. Comparisons with Microseisms in New Zealand

In the previous subsections, we presented evidences to prove that both the worldwide large earthquakes and low-magnitude seismicity around the source region have no causative relations with the spurious phase. Here we exploit the GEONET noise data to investigate in a fine time resolution the connections between the spurious phase and the microseismic noise source.

The vertical components of the GEONET noise data in 2008 were filtered between 5 and 10 sec and were divided into 30-min segments to generate a time series of secondary microseism noise level in New Zealand. Subsequently, the Hampel filter was applied to the time series to extract a new time series for the pure microseismic noise. The time series of microseismic noise level was averaged in daily bins. We repeated the procedures to extract the time series of daily microseismic noise level for every GEONET station. The array-averaged daily microseismic noise level was plotted in Figure 5.15, together with the daily strength of the spurious phase and the daily accumulated seismic moments in New Zealand. The decorrelation between the noise level time series and the seismic moment time series justifies the effectiveness of using Hampel filter to separate transient impulses from background microseism noise. In contrast, the noise level appears to be highly correlative with the strength of the spurious phase. The Pearson's correlation coefficient between them is as high as 0.7. The peaks in time series of the strength of spurious phase exhibit good correspondences with high microseism noise levels in New Zealand: a strong spurious phase arose only on days of high noise level in New Zealand (see 05-01, 05-23 and 07-31 for examples). However, it is not always true in reverse: a high noise level in New Zealand did not necessarily correspond to a simultaneous strong spurious phase. The most arresting examples could be observed on 07-26 and 07-30, when the noise level in New Zealand reached the highest peaks but only moderate spurious phase was generated. It is also noticeable that a high noise level in the northern winter months generally fails to produce a prominent spurious phase. In the austral winter months, the correlation coefficient between the strength of spurious phase and the noise level is as high as 0.74 with a nearly zero p-value, whereas in the northern winter months the correlation coefficient is merely 0.16 with a p-value of 0.03.

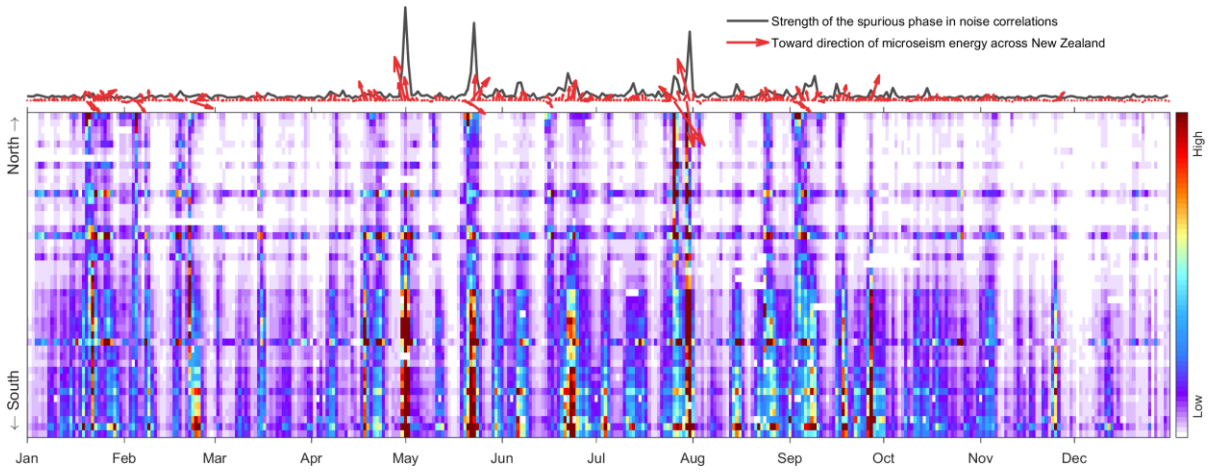

Figure 5.16. Daily directional/station-wise variations in the level of secondary microseismic noise in New Zealand in the year of 2008. Each row of the image corresponds to an annual time series of daily noise level at a GEONET station. Some visual horizontal stripes corresponds to stations deployed close to the coast with relatively higher microseism noise level. Each column shows the station-dependent variations of daily noise levels. The stations are sorted by latitudes along the vertical axis so that changes in colors along columns reflect the azimuthal variations of the microseism noise sources. Take 05-01 for instance, it can be seen from the image that the noise energy flux was attenuating from south to north, implying that the dominant microseism noise sources located in the south of New Zealand. The rapid station-dependent decay indicates that the sources are supposed to be not too distant away. However, it should be kept in mind that due to the NE-SW prolonged shape of New Zealand, microseism energy coming from the west/east shows similar patterns as coming from the south/north. By fitting a three-dimensional plane to the station-wise noise levels in each column, one can estimate the direction of the dominant microseism energy flux propagating towards. The daily dominant microseism energy flux are indicated by the red arrows on top of the images. The arrow size represents the amplitude of array-averaged daily noise level in New Zealand, while the arrow direction stands for the toward direction of dominant microseism energy flux across New Zealand. The daily strength of the spurious phase is also plotted for comparisons.

Inspecting the spatiotemporal variations in the station-dependent daily microseism noise levels in New Zealand can provides more information. We sorted the GEONET station by latitude and plotted the station-wise noise level series in an image as shown in Figure 5.16. It can be observed that the strength of spurious phase shows a dependence on the direction/location of the dominant microseism noise sources around New Zealand. A strong spurious phase emerges

only when the dominant microseism energy flux comes from the south, or say, only when the microseism noise sources in the south of New Zealand are sufficiently energetic. During the days with bursting southerly microseism energy (e.g., on 05-01, 05-23 and 07-31), one can observe a rapid decay in the energy flux from southern stations to northern stations. These observations implies that the effective noise sources for the spurious phase are expected to be in the south of New Zealand but not too distant away, which are direct evidences supporting the noise source imaging in Figure 5.8. We have observed from Figure 5.15 that on the dates of 07-26 and 07-30, the GEONET noise level showed two peaks but only moderate spurious phases were produced. From Figure 5.16, one can see that the dominant noise sources located to the north of New Zealand, outside the effective source region for the spurious phase. Consequently, a high level of microseismic noise was observed at GEONET, but the secondary microseism excitation in the effective source region was not so energetic to produce large spurious phase. More detailed and straightforward observations explaining these phenomena are provided in the images of the next subsection.

5.5. Comparisons with Hindcast Data

In the previous sections, we have found that the noise source responsible for the spurious phase located in the ocean south of New Zealand and provided independent evidence from the practical observation of microseisms in New Zealand to support the noise source location. The noise source imaging agrees with the well-known fact that the dominant source of secondary microseisms is the oceanic wave-wave interaction (Longuet-Higgins 1950; Hasselmann 1963; Kedar et al. 2008; Hillers et al. 2012; Ardhuin and Herbers 2013). In this section, we inspect and discuss the links between the spurious phase and the ocean waves and microseism excitations in the source region.

5.5.1. Hindcast Data Surrounding Source Region

The interaction between ocean gravity waves of nearly the same frequency travelling in nearly opposite directions creates an unattenuated second-order random pressure fluctuation with a frequency double that of the colliding ocean waves. The interacting ocean waves can be wind waves and swells from storms, or waves reflected by barriers like icebergs and coast lines. The wave-wave interactions have been proved to be equivalent to random pressures acting onto the

free surface of the water layer (Longuet-Higgins 1950; Hasselmann 1963; Ardhuin and Herbers 2013) and are the main excitation sources of secondary microseisms. The resonance effect of bathymetry can play an important role in amplifying or attenuating the seismic waves at source sites (Euler et al., 2014; Gualtieri et al., 2014; Hillers et al., 2012; Kedar et al., 2008; Longuet-Higgins, 1950; Meschede et al., 2017).

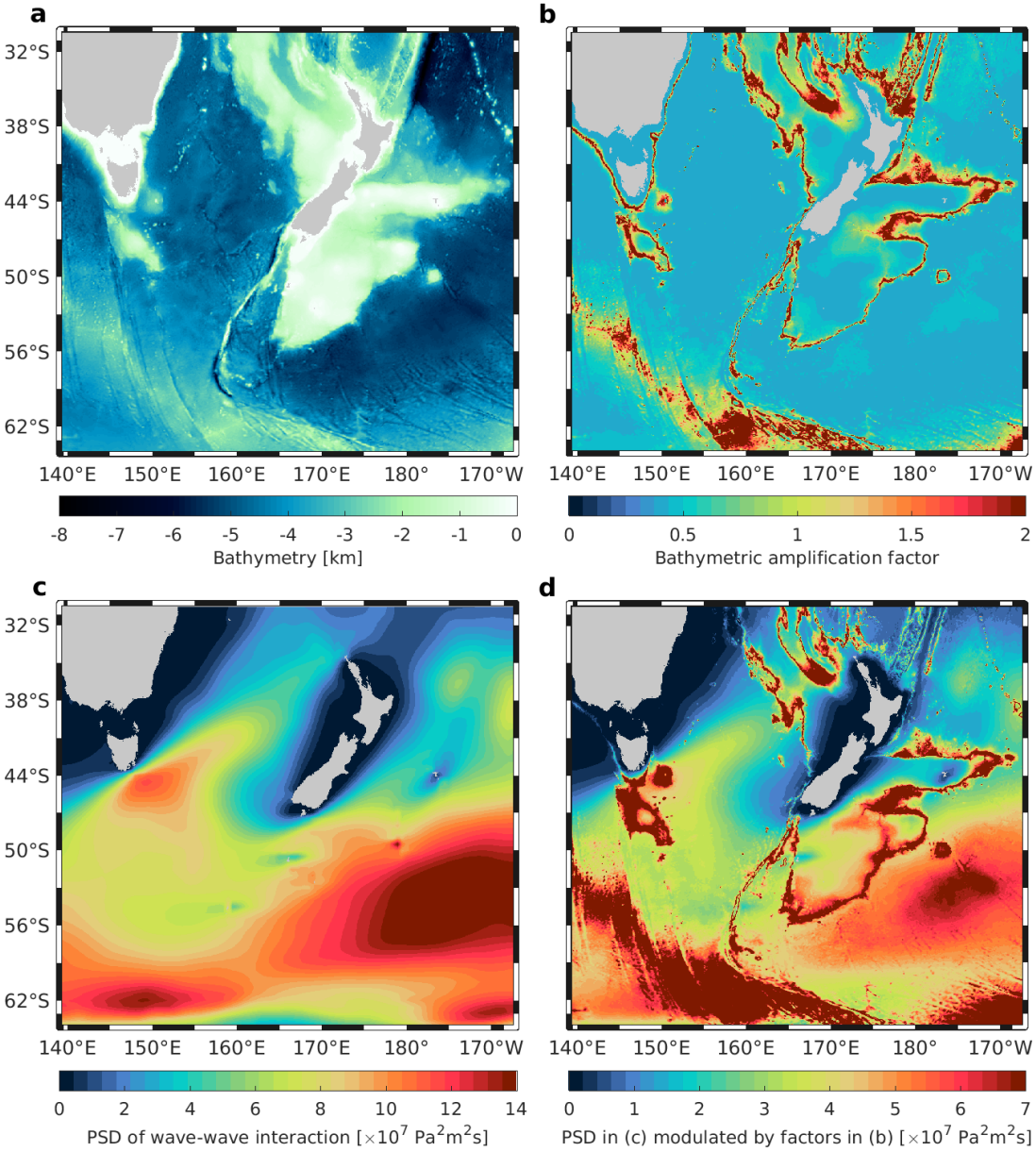

Figure 5.17. Bathymetry around New Zealand (a), bathymetric amplification factors for 6.2 sec period P-type waves with a slowness of 4.6 s/deg (b), annual average PSD of equivalent surface pressure caused by wave-wave interactions in 2008 (c), equivalent surface pressure modulated by the bathymetric amplification (d). The map of microseism excitation in (d) agrees with the backprojection imaging of noise source in Figure 5.8.

Figure 5.17 shows the bathymetric effect on altering the pattern of equivalent surface pressures of wave-wave interactions surrounding New Zealand. The bathymetry data are from ETOPO1 Global Relief Model (Amante and Eakins 2009). The bathymetric amplification factors are computed from the equations given by Gualtieri et al. (2014). The PSD data of equivalent surface pressure were described by Rascle and Ardhuin (2013). It is obvious that the ocean bathymetry significantly modifies the spatial pattern of the equivalent surface pressure PSDs. Compared to the raw PSD map for wave-wave interaction in Figure 5.17c, the PSD map in Figure 5.17d with the consideration of the bathymetric effects agrees much better with the noise source imaging in Figure 5.8, highlighting the importance to take into account the bathymetric effect on the generation of secondary microseisms.

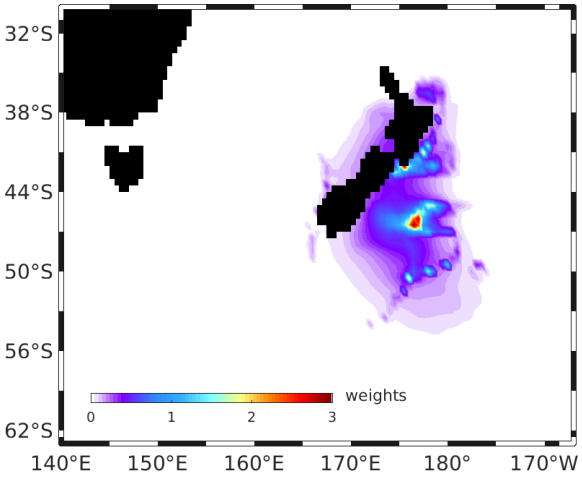

Figure 5.18. Map of weights for computing the averages of wind speeds, ocean wave heights and microseism noise source PSDs in the effective source region. The weights are the product of the double-beam back-projection imaging in Figure 5.8 with the bathymetric amplification factors in Figure 5.17b.

To obtain the time series of averaged daily wind speed, significant wave height and secondary microseism excitation in the noise source region to be compared with the time series for the spurious phase, we computed a map of weights from the noise source imaging in Figure 5.8 and the bathymetric amplification factors in Figure 5.17b. The weights were displayed in Figure 5.18. Applying the weights to the hindcast data of winds, ocean waves and microseism excitations in 2008, we obtained the time series of hindcast data as shown in Figure 5.19. The reanalysis data of winds are provided by the ECMWF. In agreement with the observations from Figure 5.15, the strength of spurious phase is highly correlated with the intensity of microseism

excitation in the effective source region; the microseism excitation is more intense during the austral winter months; not all intense microseism excitation, especially during the northern winter months, can produce energetic spurious phase. The significant wave height is highly correlated with the local wind speed, indicating the dominance of wind waves in the wave spectra rather than swells from distant storms. However, one can observe that the wave height is not significantly correlated with the strength of spurious phase, nor with the microseism excitation. For some large spikes appearing in the time series of microseism excitation intensity, the corresponding wind speed and wave height is only moderate or even lower. These may imply the critical role of swells in the wave-wave interactions and also signify that strong microseism excitation caused by wave-wave interactions does not necessarily require extreme local winds or wave heights.

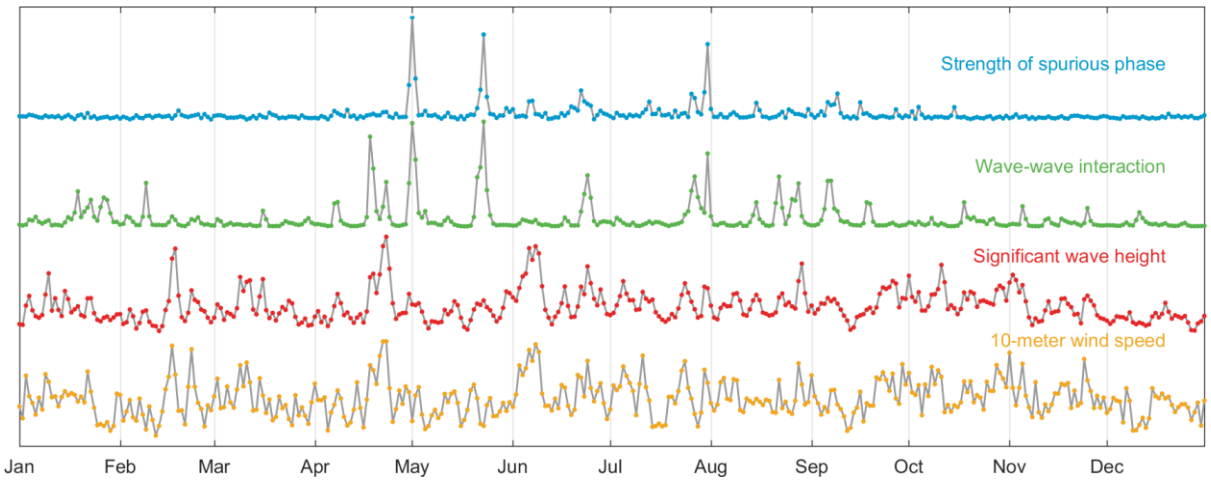

Figure 5.19. Daily variations of the strength of spurious phase and the average intensity of wave-wave interactions for microseism excitation, significant wave heights and winds in the effective source region in Figure 5.8. The average over the hindcast datasets is weighted by the backprojection imaging in Figure 5.8. The intensity of wave-wave interaction is additionally weighted by the bathymetric amplification factors in Figure 5.17b. The averaged microseism excitation intensity ranges from 0 to 4×10^{7} Pa^2m^2. The averaged wave height ranges from 1.5 to 5.7 m. The averaged wind speed ranges from 4 to 12.5 m/s. All time series are normalized for display. The correlation coefficients are, respectively, 0.7 between the strength of spurious phase and the intensity of wave-wave interaction, 0.16 between the strength of spurious phase and significant wave height, 0.25 between the intensity of wave-wave interaction and significant wave height, and 0.74 between significant wave height and wind speed.

5.5.2. Oceanic Microseism Events

In subsection 5.3.1, we observed large spurious phase on some single days. In subsection 5.2.3, we located the effective noise source for the spurious phase in the ocean south of New Zealand. In subsection 5.4.3, we revealed the highly correlated temporal variations of the spurious phase and the microseism noise level at GEONET stations that are adjacent to the effective source region. In subsection 5.5.1, we showed the annual average PSDs of oceanic microseism noise sources in the effective source region and compared the time series of the strength of spurious phase and of the averages of microseism noise source PSDs, significant wave heights and winds in the effective source region. On some dates, microseism energy bursts in the effective source region, leading to strong spurious phase in daily correlations. Hereafter, we refer to the burst of microseism excitation as **microseism event.** The temporal evolution of microseism event is closely related to the life circle of the causative storms that drive ocean waves colliding with each other.

To have perceptual observations on the growth and vanish of the oceanic microseism events in the effective source region, in this subsection we show the images of hindcast winds, ocean wave heights and microseism noise source PSDs for the microseism events around 05-01, 05-23 and 07-31 of 2008.

5.5.2.1. Event around 2008-05-01

The proximity of GEONET to the effective source region enables the seismic noise recorded by GEONET agency of the microseism events in the source region. As for the largest daily spurious phase on 2008-05-01, it can be observed from Figure 5.15 and Figure 5.19 that the noise level at GEONET stations and microseism excitation in the effective source region were prominently high on this date. We showed in Figure 5.20 the spectrogram of the vertical-component seismogram recorded by the GEONET station NZ.APT between the dates of 04-27 and 05-04 of 2008. One can observe that the microseism energy started to increase from before the middle of 04-30, reached the maximum on 05-01, and vanished on 05-03. The FK map of microseisms at GEONET stations on 05-01 were provided in Figure 5.21, which shows the dominant microseism energy flux coming from the south and southeast. The temporal characteristics were compatible with the time evolution of the microseism event in the effective

source region shown in Figure 5.22. The time evolution of the microseism events around 05-23 and 07-31 were presented in Figure 5.23 and Figure 5.24, respectively. All these events are good examples of strong microseism excitation and large-amplitude spurious phase caused by merely moderate or lower ocean wave heights. The images for the dates 07-29 and 07-30 demonstrate how a storm hitting New Zealand from the north led to the high noise level at GEONET stations but failed to produce a strong spurious phase.

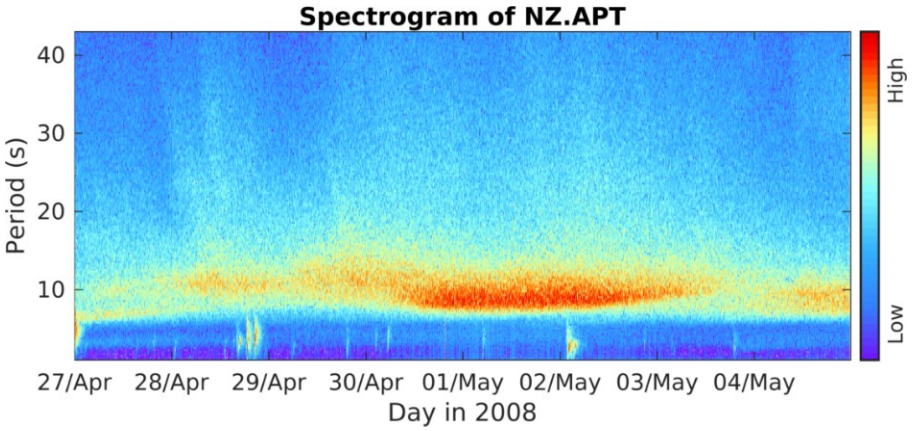

Figure 5.20. Spectrogram of the vertical component of seismograms recorded by the GEONET station NZ.APT, from 04-27 to 05-04 of 2008. One can observe a striking increased microseism PSD between 04-30 and 05-03.

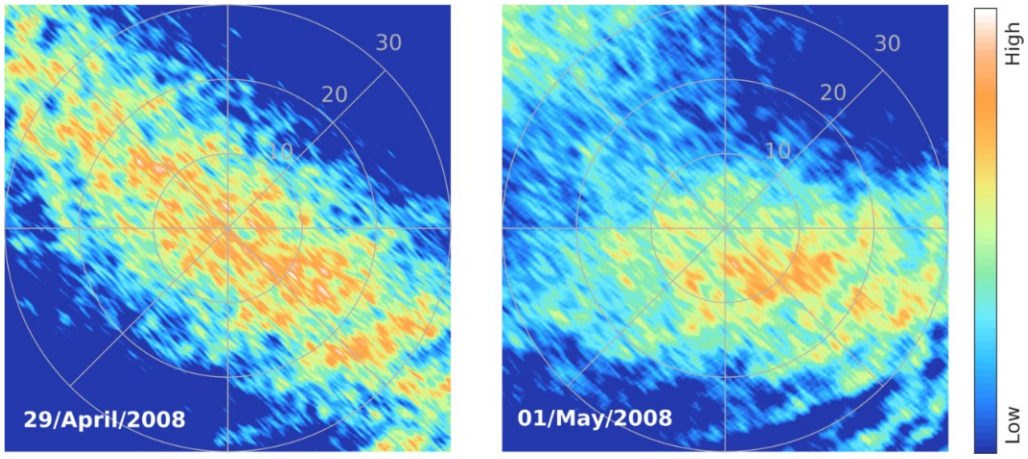

Figure 5.21. FK maps of secondary microseisms (periods of 5 to 10 sec) recorded by GEONET on 04-29 and 05-01 of 2008. The radial number labels are slownesses in s/deg. The azimuth stands for the coming direction of the microseismic energy flux. The map for 05-01 with the strongest spurious phase shows dominant microseism energy flux originating from the south. The map for 04-29 with a weak spurious phase is presented for comparison.

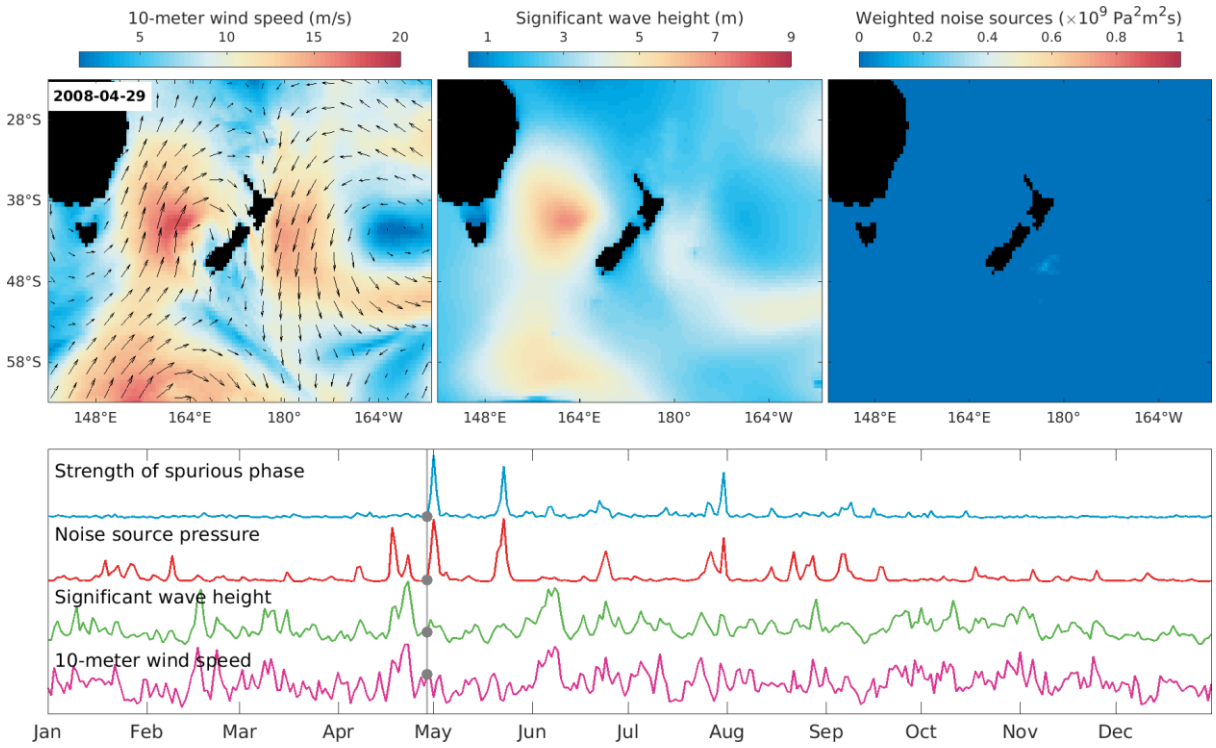
10-meter wind speed (m/s)
5 10 15 20
Significant wave height (m)
1 3 5 7 9
Weighted noise sources (×10^9 Pa^2m^2s)
0 0.2 0.4 0.6 0.8 1
2008-04-29
28°S
38°S
48°S
58°S
148°E 164°E 180° 164°W
Strength of spurious phase
Noise source pressure
Significant wave height
10-meter wind speed
Jan Feb Mar Apr May Jun Jul Aug Sep Oct Nov Dec

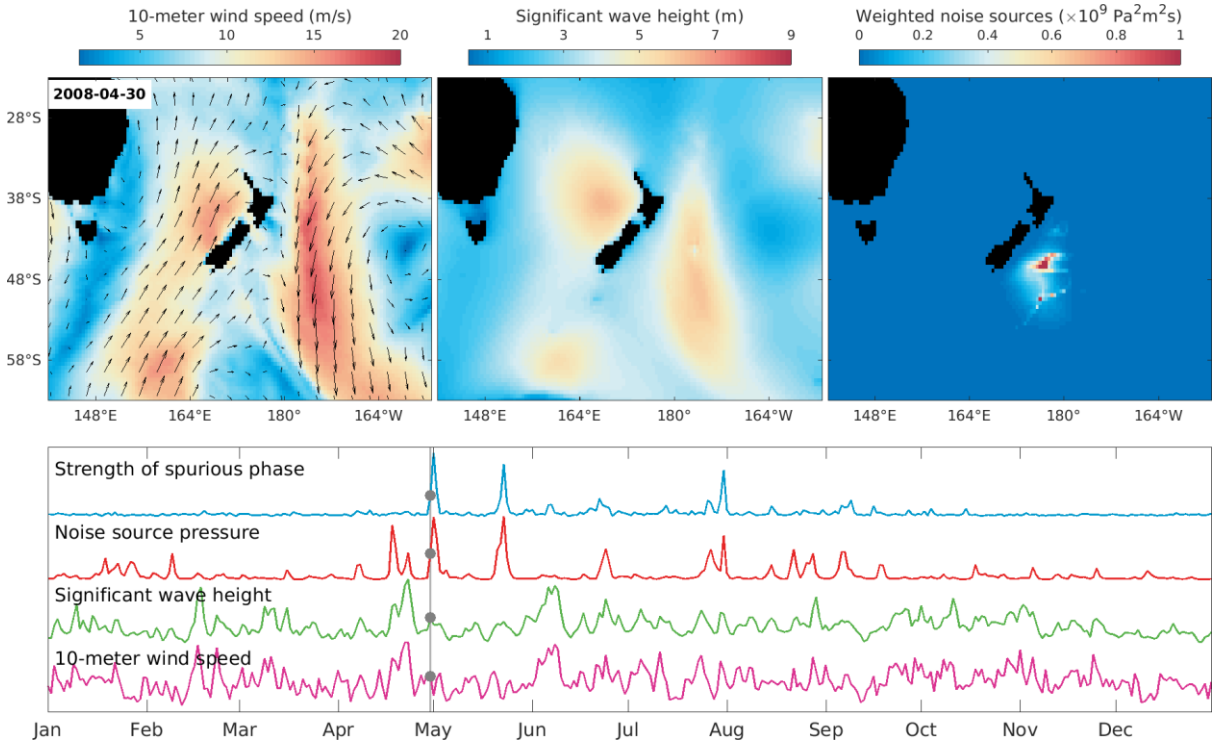
10-meter wind speed (m/s)
5 10 15 20
Significant wave height (m)
1 3 5 7 9
Weighted noise sources (×10^9 Pa^2m^2s)
0 0.2 0.4 0.6 0.8 1
2008-04-30
28°S
38°S
48°S
58°S
148°E 164°E 180° 164°W
Strength of spurious phase
Noise source pressure
Significant wave height
10-meter wind speed
Jan Feb Mar Apr May Jun Jul Aug Sep Oct Nov Dec

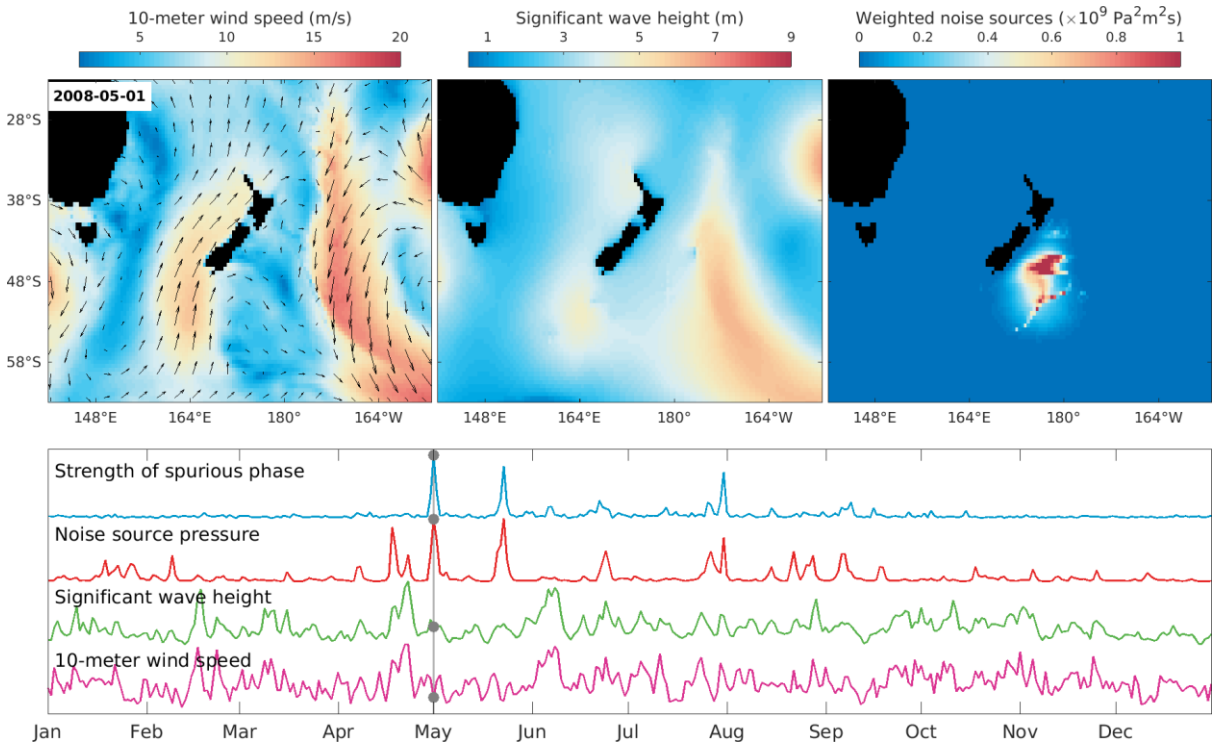
10-meter wind speed (m/s)
5 10 15 20
Significant wave height (m)
1 3 5 7 9
Weighted noise sources (×10^9 Pa^2m^2s)
0 0.2 0.4 0.6 0.8 1
2008-05-01
28°S
38°S
48°S
58°S
148°E 164°E 180° 164°W
Strength of spurious phase
Noise source pressure
Significant wave height
10-meter wind speed
Jan Feb Mar Apr May Jun Jul Aug Sep Oct Nov Dec

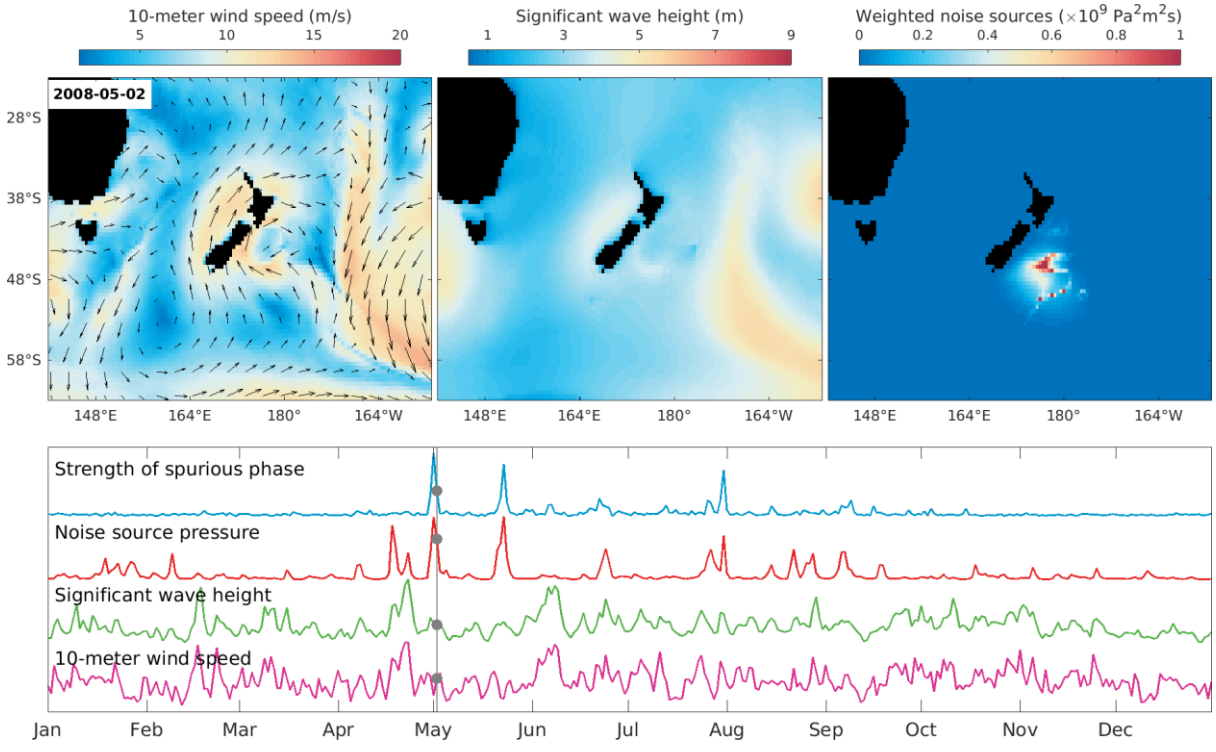
10-meter wind speed (m/s)
5 10 15 20
Significant wave height (m)
1 3 5 7 9
Weighted noise sources (×10^9 Pa^2m^2s)
0 0.2 0.4 0.6 0.8 1
2008-05-02
28°S
38°S
48°S
58°S
148°E 164°E 180° 164°W
Strength of spurious phase
Noise source pressure
Significant wave height
10-meter wind speed
Jan Feb Mar Apr May Jun Jul Aug Sep Oct Nov Dec

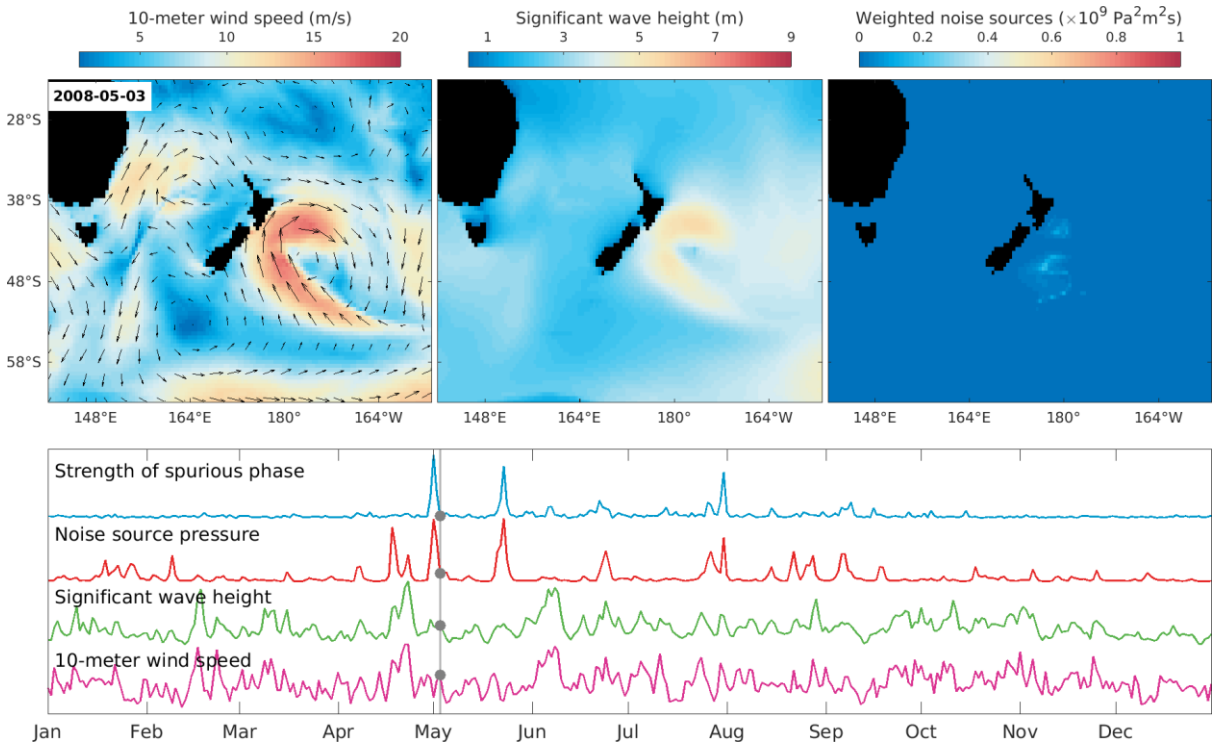

Figure 5.22. Evolution of the winds, ocean waves and oceanic noise sources for the microseism event around 2008-05-01. As for the winds, the colored image and arrows represent the daily averages of scalar and vector wind speeds, respectively. As for the noise sources caused by the oceanic wave-wave interactions, the daily average PSDs of equivalent surface pressure at a seismic period of 6.2 sec are modulated by the back-projection map in Figure 5.8 as well as the bathymetric amplification factors in Figure 5.17b. The time series below the images are labelled and detailed explanations can be found in the legend of Figure 5.19. The daily images display that the ocean waves generated by two weather systems, one from northeast and the other from southwest, collided with each other in the effective source region. The microseism excitation for P waves was largely amplified by the bathymetry around [47°S, 177°E]. The microseism excitation reached maximum on 05-01 but the wave height in the effective source region was merely moderate on that day. On 05-03, there was a local storm in the effective source region. However, the microseismic P-wave excitation was weak due to the lack of colliding waves from the opposite directions against the wind waves.

5.5.2.2. Event around 2008-05-23

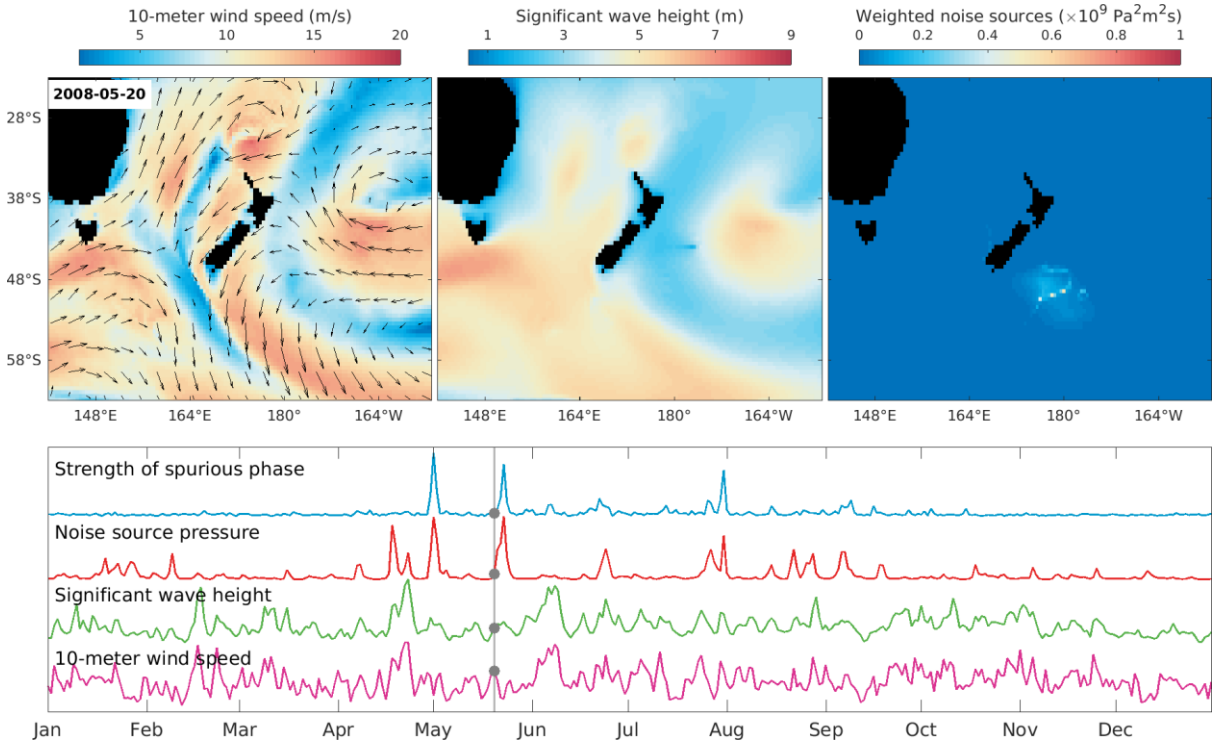

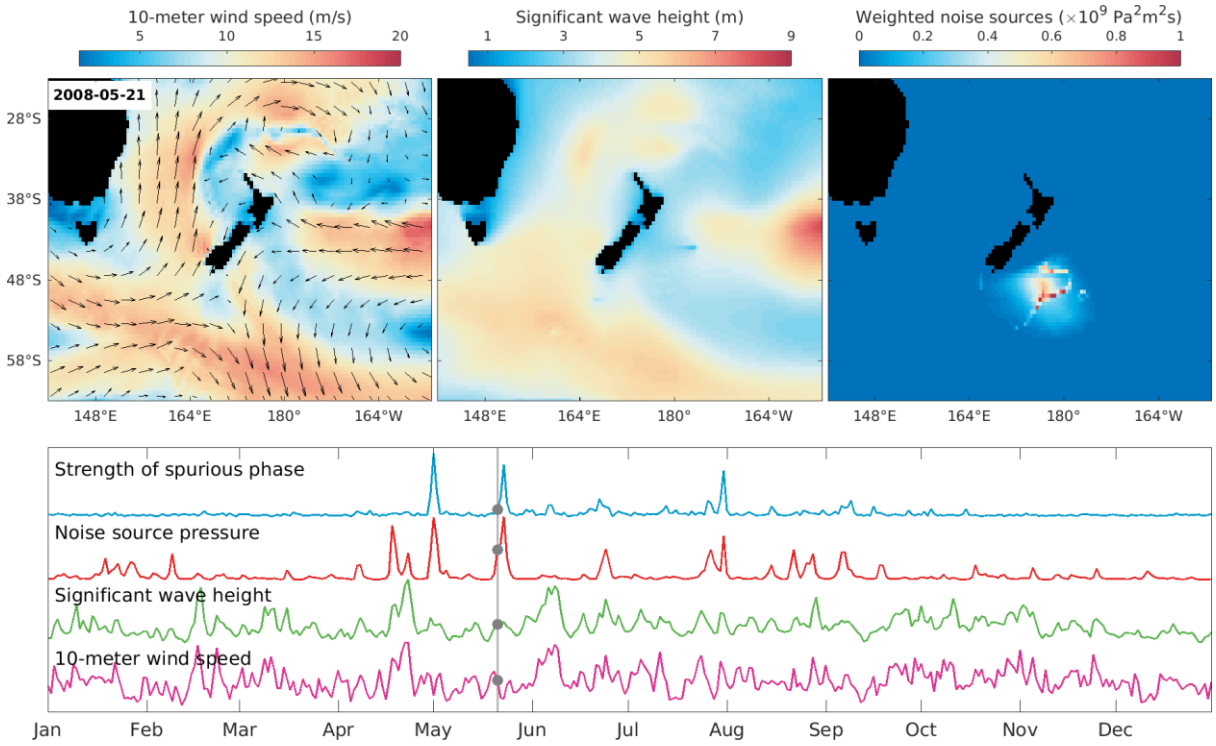

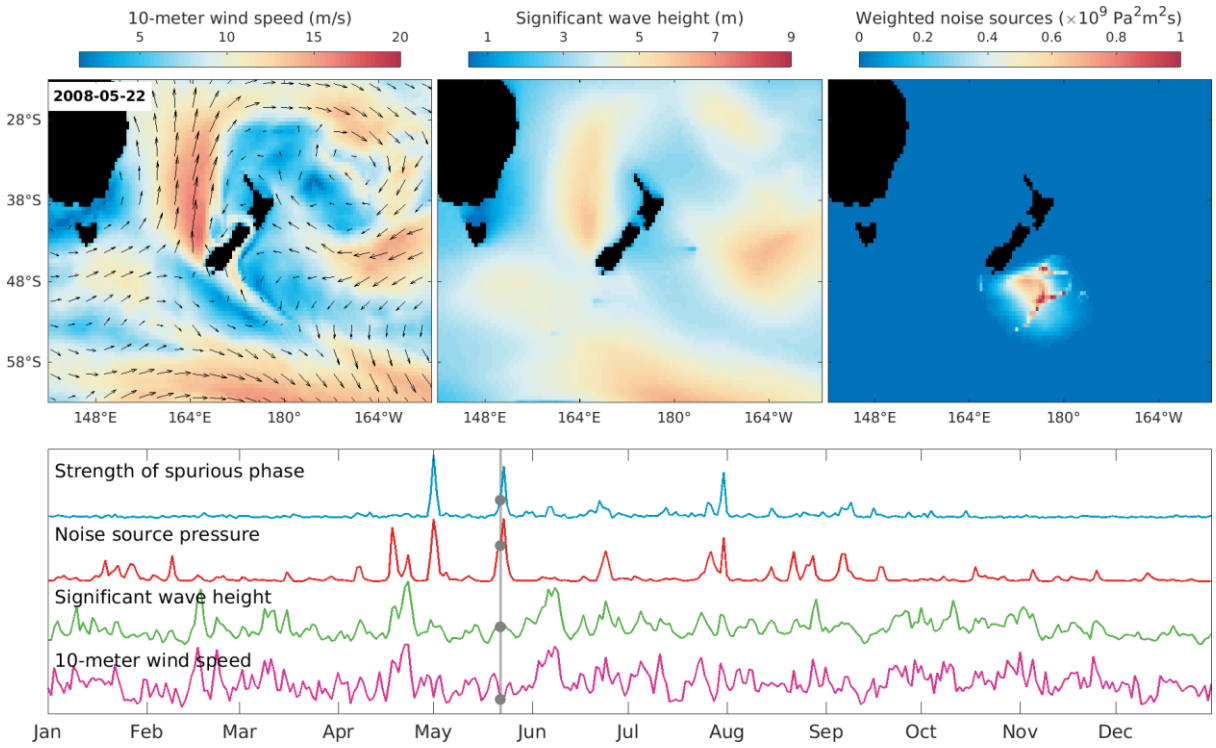
10-meter wind speed (m/s)
5 10 15 20
Significant wave height (m)
1 3 5 7 9
Weighted noise sources (×10^9 Pa^2m^2s)
0 0.2 0.4 0.6 0.8 1
2008-05-22
28°S
38°S
48°S
58°S
148°E 164°E 180° 164°W
Strength of spurious phase
Noise source pressure
Significant wave height
10-meter wind speed
Jan Feb Mar Apr May Jun Jul Aug Sep Oct Nov Dec

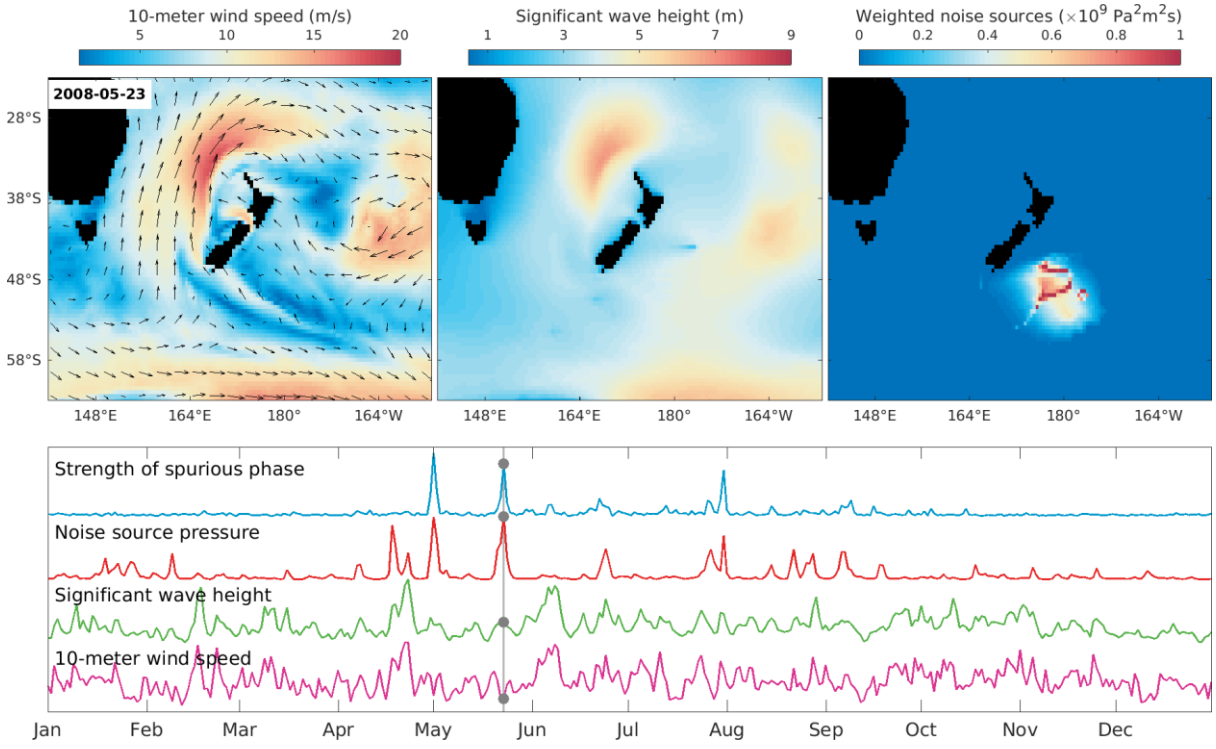
10-meter wind speed (m/s)
5 10 15 20
Significant wave height (m)
1 3 5 7 9
Weighted noise sources (×10^9 Pa^2m^2s)
0 0.2 0.4 0.6 0.8 1
2008-05-23
28°S
38°S
48°S
58°S
148°E 164°E 180° 164°W
Strength of spurious phase
Noise source pressure
Significant wave height
10-meter wind speed
Jan Feb Mar Apr May Jun Jul Aug Sep Oct Nov Dec

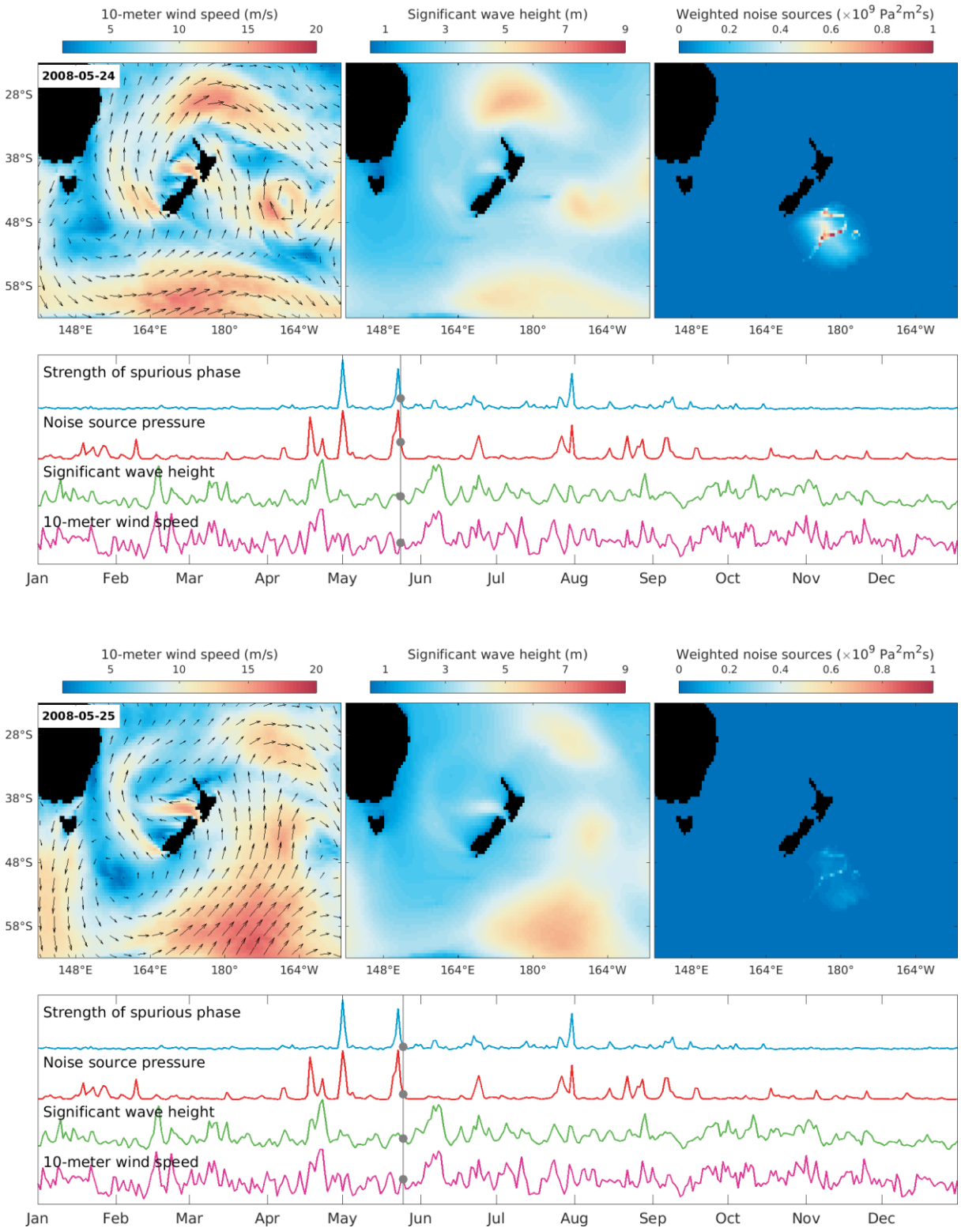

Figure 5.23. Evolution of the winds, ocean waves and microseism event around 2008-05-23. See the legend of Figure 5.22 for more details.

5.5.2.3. Event around 2008-07-31

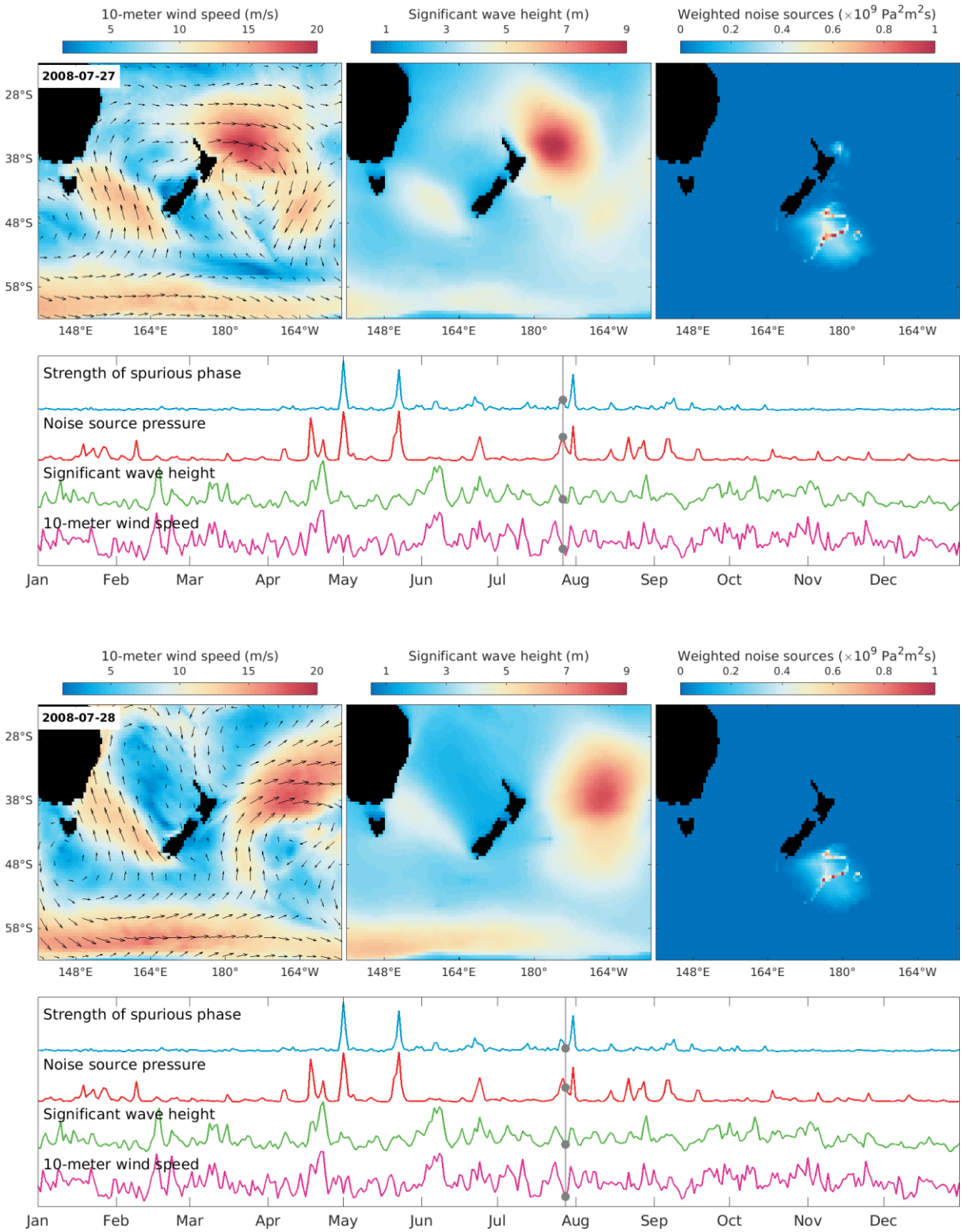

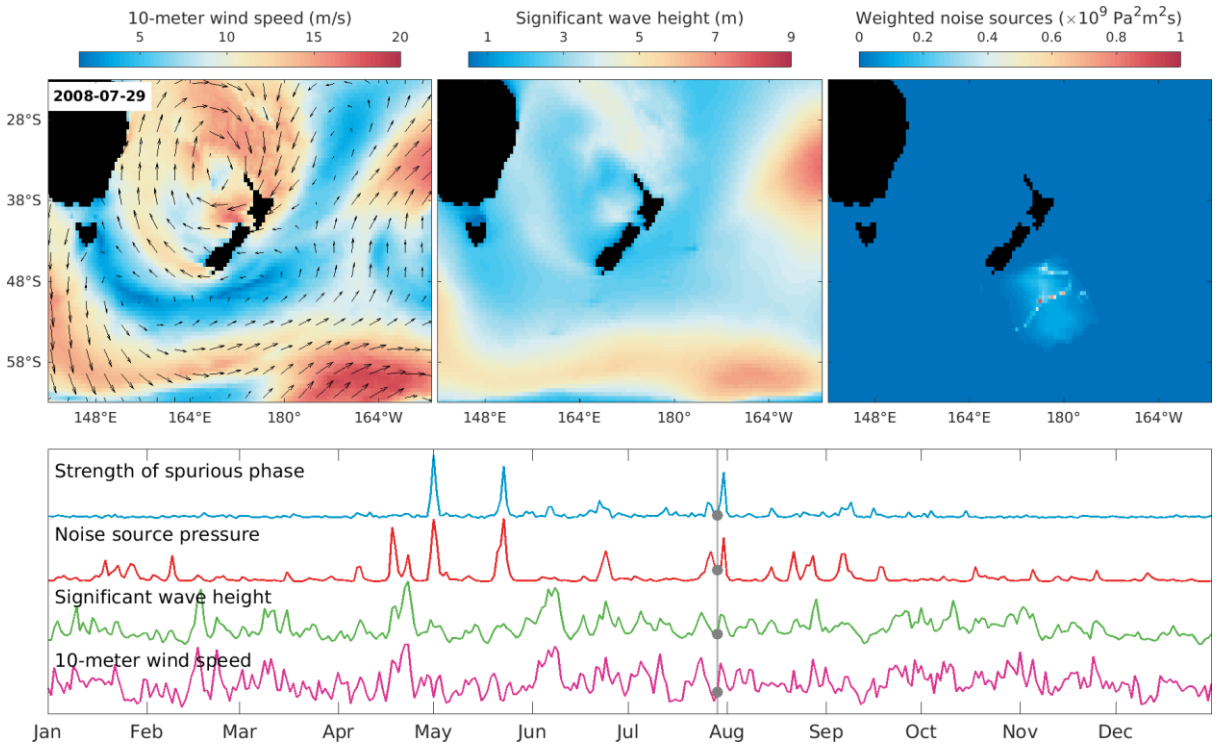
10-meter wind speed (m/s)
5 10 15 20
Significant wave height (m)
1 3 5 7 9
Weighted noise sources (×10^9 Pa^2m^2s)
0 0.2 0.4 0.6 0.8 1
2008-07-29
28°S
38°S
48°S
58°S
148°E 164°E 180° 164°W
Strength of spurious phase
Noise source pressure
Significant wave height
10-meter wind speed
Jan Feb Mar Apr May Jun Jul Aug Sep Oct Nov Dec

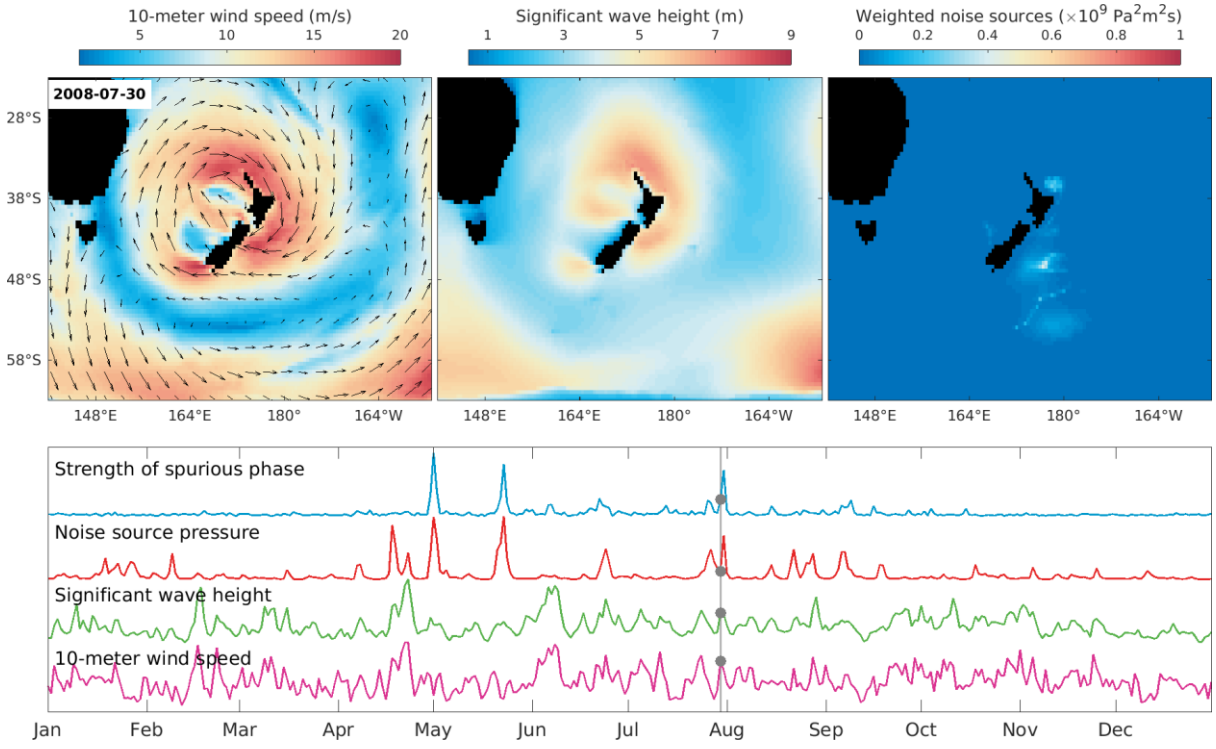
10-meter wind speed (m/s)
5 10 15 20
Significant wave height (m)
1 3 5 7 9
Weighted noise sources (×10^9 Pa^2m^2s)
0 0.2 0.4 0.6 0.8 1
2008-07-30
28°S
38°S
48°S
58°S
148°E 164°E 180° 164°W
Strength of spurious phase
Noise source pressure
Significant wave height
10-meter wind speed
Jan Feb Mar Apr May Jun Jul Aug Sep Oct Nov Dec

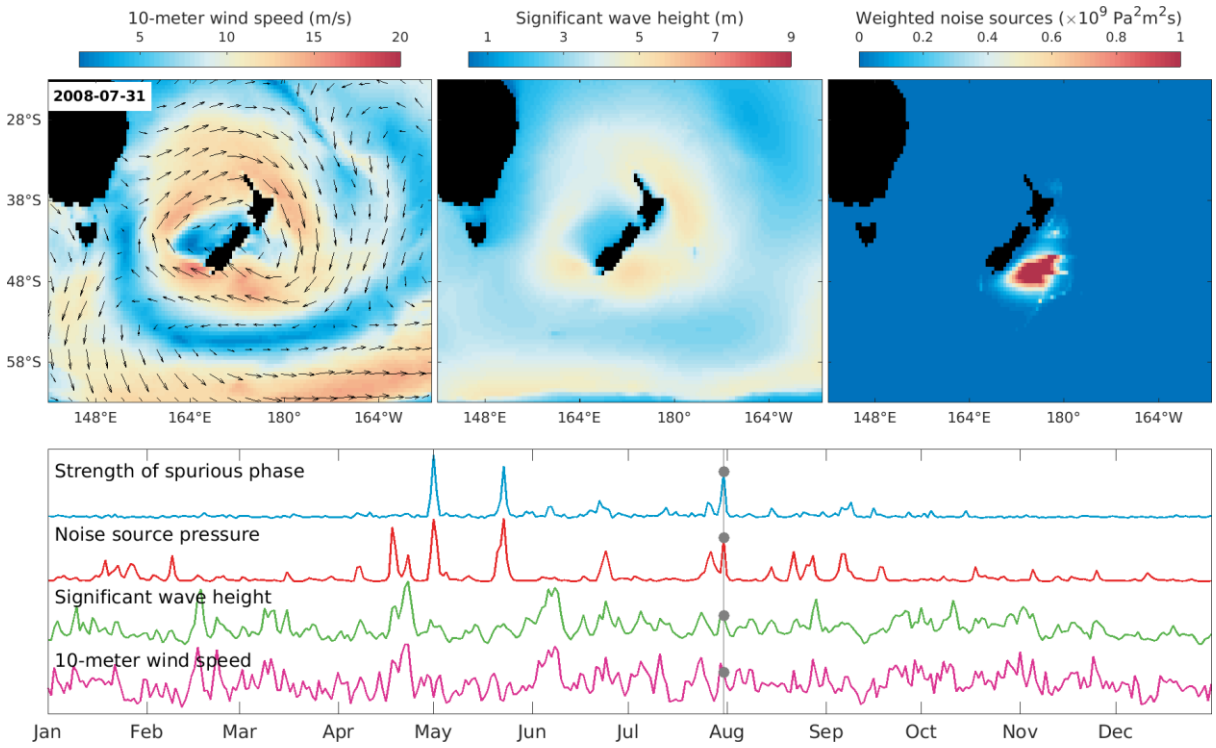
10-meter wind speed (m/s)
5 10 15 20
Significant wave height (m)
1 3 5 7 9
Weighted noise sources (×10^9 Pa^2m^2s)
0 0.2 0.4 0.6 0.8 1
2008-07-31
28°S
38°S
48°S
58°S
148°E 164°E 180° 164°W
Strength of spurious phase
Noise source pressure
Significant wave height
10-meter wind speed
Jan Feb Mar Apr May Jun Jul Aug Sep Oct Nov Dec

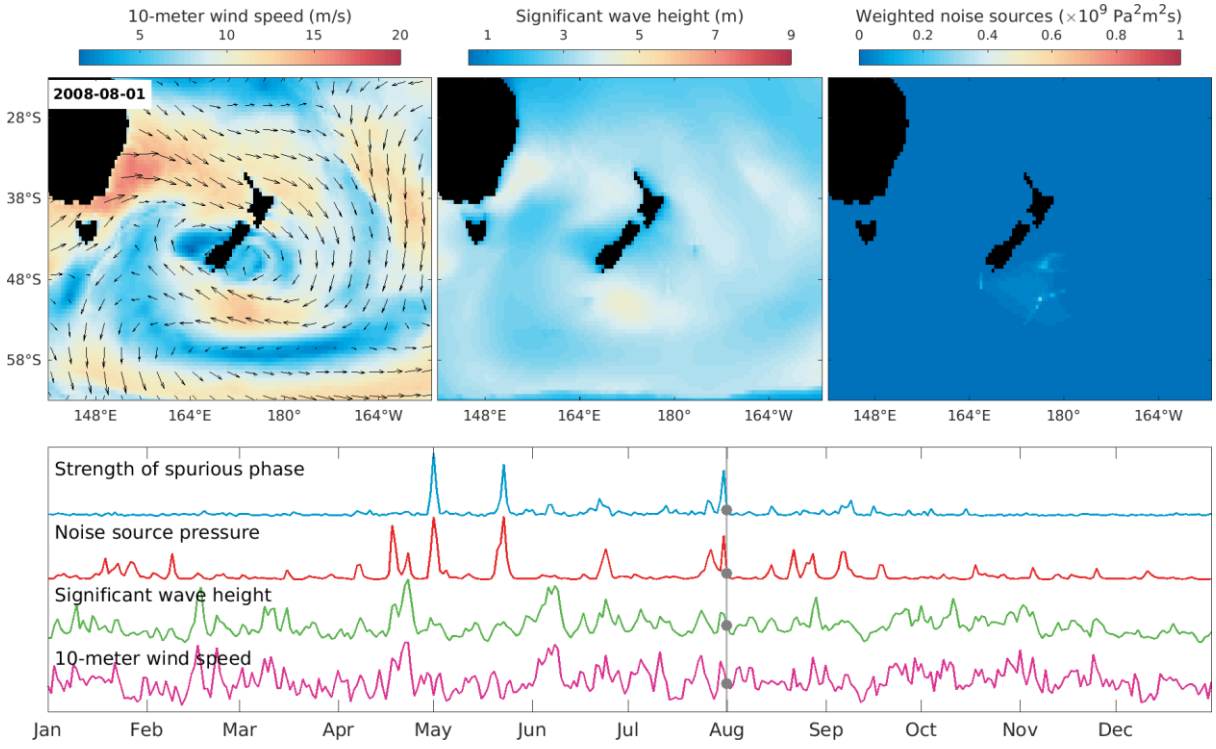
10-meter wind speed (m/s)
5 10 15 20
Significant wave height (m)
1 3 5 7 9
Weighted noise sources (×10^9 Pa^2m^2s)
0 0.2 0.4 0.6 0.8 1
2008-08-01
28°S
38°S
48°S
58°S
148°E 164°E 180° 164°W
Strength of spurious phase
Noise source pressure
Significant wave height
10-meter wind speed
Jan Feb Mar Apr May Jun Jul Aug Sep Oct Nov Dec

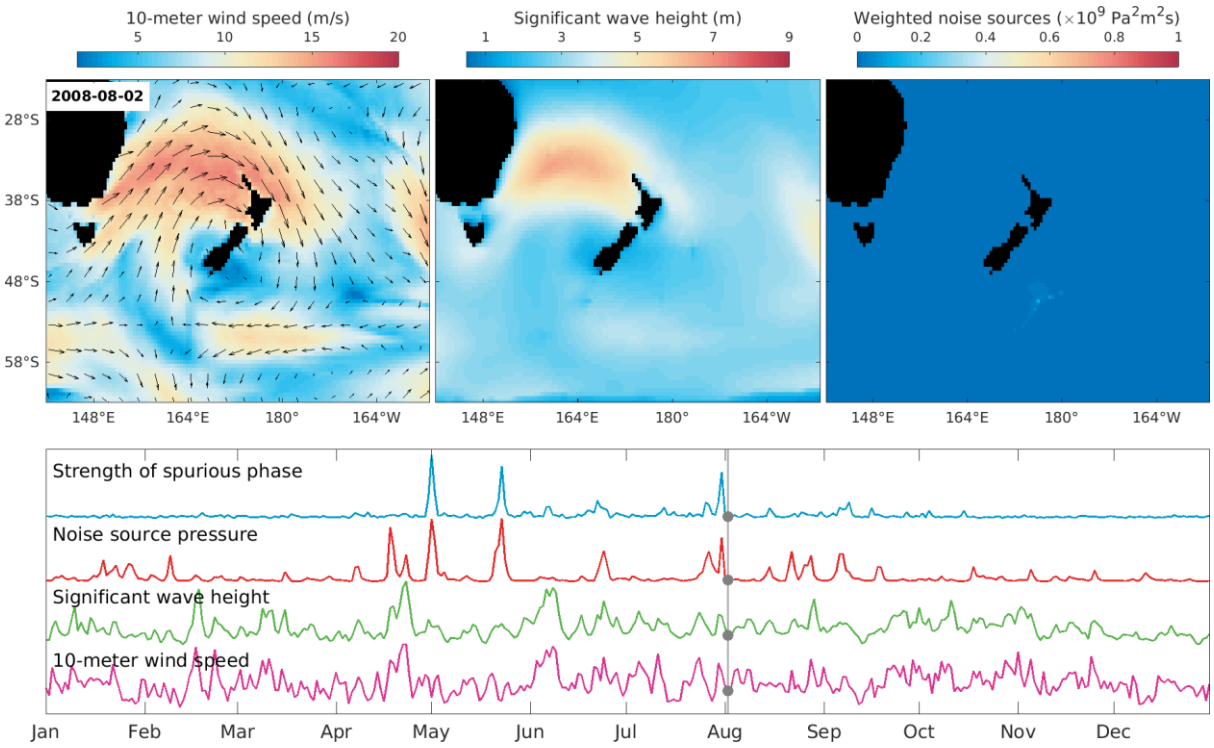

Figure 5.24. Evolution of the winds, ocean waves and microseism event around 2008-07-31. See the legend of Figure 5.22 for more details.

5.5.3. Correlating with Global Wave Heights

The global maps of average significant wave heights in the austral and northern half years of 2008 are shown in Figure 5.25. The ocean waves are most intense in mid-latitudes and are weak in low latitudes. In the northern Atlantic and Pacific oceans, the wave height exhibits quite strong seasonal variations. The northern oceans are highly active during the northern winter half year but become silent during the austral winter half year. The southern mid-latitude oceans also exhibit some degree of seasonal variations, more active during the local winter and relatively less active during the local summer. However, the seasonal variations are much weaker compared the variations in the northern Atlantic and Pacific, due to the perennially prevailing westerlies.

Recall that the spurious phase also shows similar seasonal variations. It thus behoove us to look into the links between the seasonal variations in the ocean activities and the spurious phase.

We computed the Pearson's correlation coefficients between the daily strength of the spurious phase and the daily significant wave height at each location in the oceans and thereby obtained a global map of correlation coefficients as shown in Figure 5.25c. There is no need to consider the bathymetric amplification in the calculation of correlation coefficients here, since an overall scaling of a time series does not bring any changes to the value of the normalized correlation coefficient. At a global sight, the spurious phase is positively correlated with wave heights in the southern oceans as well as the northern Indian Ocean, and is negatively correlated with wave heights in the northern oceans. The wide spreading positively / negatively correlated regions can be interpreted by the spatial connections in the time-varying activities of ocean waves (Figure 5.25d). Another reason could be that during the northern winter months, the intensive ocean activities in the northern oceans closer to FNET and LAPNET, dwarf the microseism energy coming from the distant south.

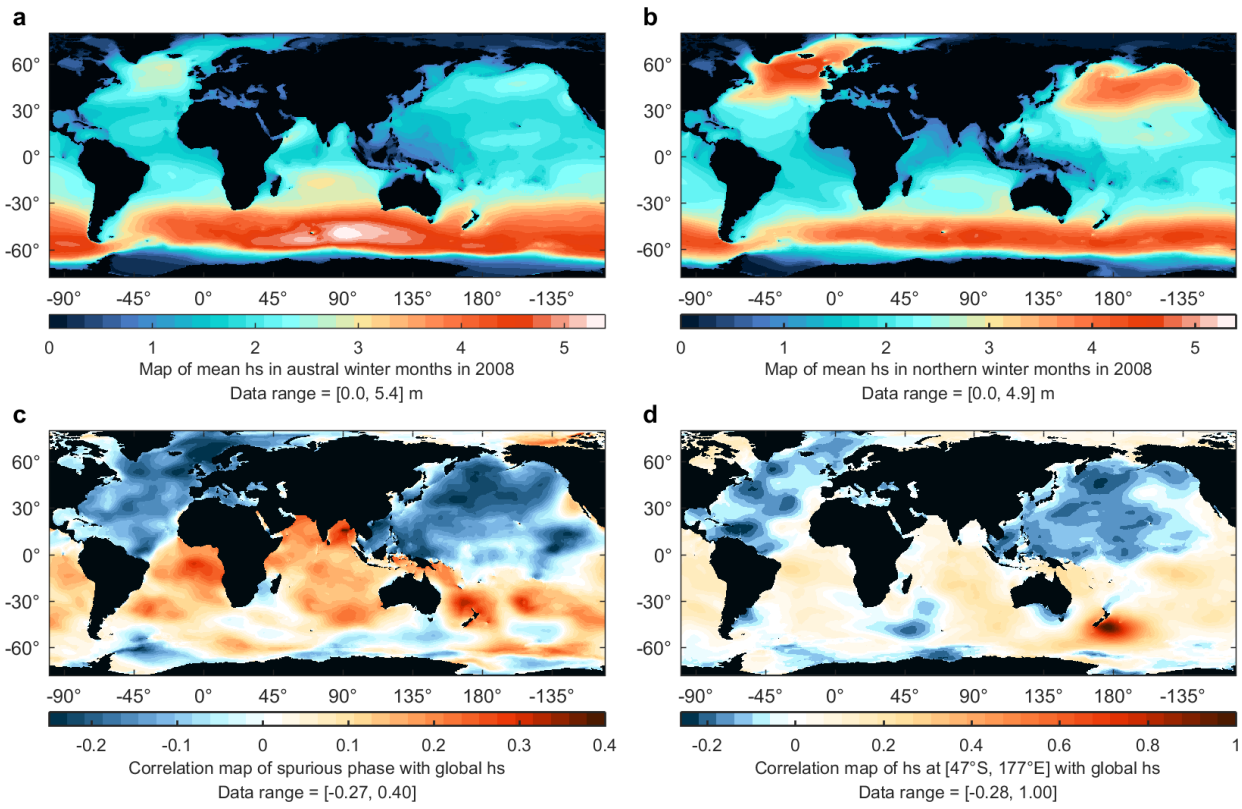

Figure 5.25. Global maps of semi-annual mean significant wave height (hs) in austral (a) and northern (b) winter months of 2008, global maps of correlation coefficients between the strength of spurious phase and hs, and between hs at [47°S, 177°E] and global hs. As for a degree of freedom of 364 for 366 samples and a p-value of 0.05 for null hypothesis, the correlation coefficients above 0.1 can be deemed to be statistically significant. Note the asymmetry of the color bar for correlation maps.

5.5.4. Correlating with Global Microseism Sources

Similar to the last subsection, we plotted in Figure 5.26 the intensity maps of microseism noise sources and the correlation map between the spurious phase and oceanic noise sources. The most energetic secondary microseism sources locate in the northern Atlantic near Greenland, the northern Pacific between Japan and Alaska, the southern Pacific and Antarctic Ocean between New Zealand and Antarctic, and between the southern Indian Ocean and Antarctic Ocean. The microseisms exhibit stronger seasonal variations compared to wave heights, especially in the southern oceans. In the northern winter months, the microseism sources in the northern Atlantic close to LAPNET and in the northern Pacific close to FNET, are so energetic that weaker microseism energy from the distant effective source region is overwhelmed. Consequently, the spurious phase is hardly constructed.

In the correlation map for the spurious phase and noise sources (Figure 5.26c), a region of high correlation coefficients can be identified in consistence with the effective source region in Figure 5.8. The maximum correlation is located at around [47°S, 177°E], coincident with the hotspot in the effective source region in Figure 5.17d where the microseism excitation for P waves is favored by the bathymetry (Figure 5.17b). The temporal variations of the wave height and microseism excitation at [47°S, 177°E] are highly similar to those of the weighted averages in the whole effective source region (Figure 5.27), signifying the dominance of the very high correlation region in the whole effective source region and the importance of the bathymetric effect on microseism excitation. Ideally, the correlation coefficients in the regions outside the effective source region should be negative or zero, since the microseism energy from these regions has adverse or neglectable effects on the construction of the spurious phase. Stronger adverse effects are expected for stronger microseism sources closer to the stations. However, due to the spatial connections in the temporal variations of microseism intensity (Figure 5.26d), a broad range of microseism sources appear positively but weakly correlated with the spurious phase. These correlations are not causal. We also noticed that there are some regions highly and positively correlated with the spurious phase, for example, at around [12°N, 88°E] in the Bay of Bengal and around [30°S, 169°E] to the northeast of New Zealand. Such high correlations cannot be rejected by null hypothesis tests and also cannot be explained by the spatial connections in Figure 5.26d. Note that the wave height (Figure 5.25a, b) and the microseism excitation (Figure 5.26a, b) in these regions are not high. Inspecting the temporal

variations of the wave height and microseism excitation in these regions and comparing with the strength of the spurious phase (Figure 5.27) reveal that even though the high correlation coefficients are statistically significant (nearly zero p-value), they are spurious. The spurious correlations stem from the coincidental simultaneous appearance of peaks in the time series dominating in the computation of correlation coefficients.

Recall that the spurious phase is conspicuous in the acausal correlations but absent from the cause correlations. We attribute the extreme asymmetry of the spurious phase to the difference in the intensity of microseism excitations in the effective noise source regions. The effective noise source for the causal spurious phase is expected to locate around [12°S, 29°W], in the low-latitude southern Atlantic Ocean east of Brazil. As can be seen from Figure 5.26, the causal source is not energetic enough to produce the causal spurious phase.

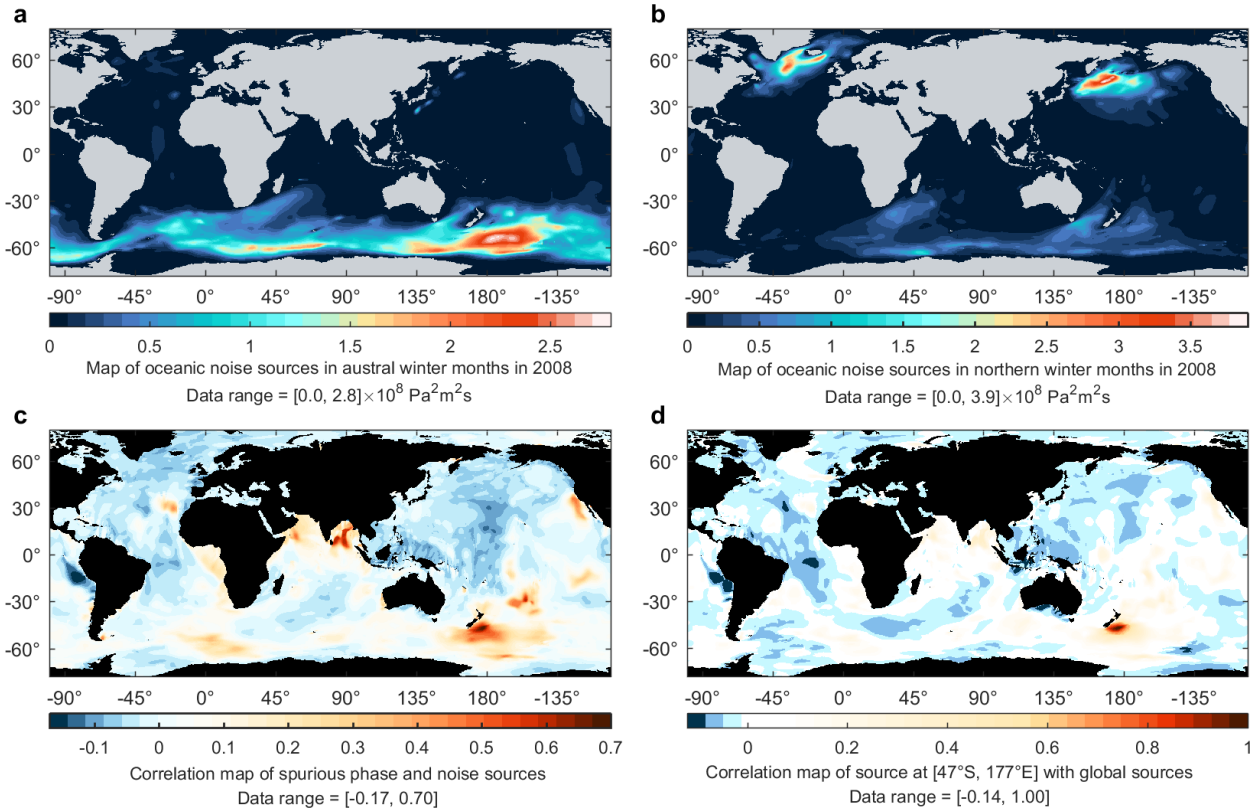

Figure 5.26. Global maps of semi-annual average PSD of 6.2 sec period oceanic microseism noise sources in austral (a) and northern (b) winter months of 2008, global maps of correlation coefficients between the strength of spurious phase and noise sources, and between the noise source at [47°S, 177°E] and global noise sources. Note the asymmetry of the color bar for correlation maps.

Figure 5.27. True correlations between the strength of spurious phase and the strength of microseism excitation in the effective source region, and spurious correlations between the strength of spurious phase and the strength of microseism noise sources at some peaks in Figure 5.26c. The equivalent surface pressures of noise sources at [12°N, 88°E] and at [30°S, 169°E] are quite low compared to the pressures at [47°S, 177°E] and thus are scaled for display. The significant wave heights are shown in the same scale.

5.6. Summary and Discussions

We observed an early spurious phase in the secondary microseism frequency band in the acausal noise correlations between FNET and LAPNET stations at teleseismic distances. The spurious phase is even directly observable in the noise correlations between a single station pair and on some single day. Through double-array slowness analysis and back-projection, we revealed that the spurious phase originates from the correlation between the microseism P and PKPab waves emanating from the oceanic noise sources south of New Zealand. Seismological observations and hindcast data in the noise source region provided independent evidences to justify our results.

The generation of the spurious phase cannot be ascribed to non-uniformity of noise source distribution, nor can be explained in the traditional way as regular seismic phases. As for the reconstruction of regular seismic phases from noise correlations in 1D model, it has been well-known that the reconstruction should be attributed to the interferometry between the wavefields at two receivers with a common slowness. The common slowness implies that, as explained in

the theory of stationary phase (Snieder 2004; Boschi and Weemstra 2015), a stationary point on the curve of inter-receiver time delay with respect to the source-receiver distance. In contrast to the reconstruction of regular seismic phases, we proved in this study that the spurious phase stems from the correlation between two wavefields with distinct slownesses. The effective noise sources responsible for the generation of the spurious phase correspond to non-stationary locations on the curve of inter-receiver time delay with respect to the source-receiver distance. We proposed a new mechanism called the interferometry of quasi-stationary phase, in contrast to the classic theory of stationary phase, to explain the emergence of stable spurious phases. A spurious phase caused by a localized strong noise source will disappear when the source distribution tends to be even. However, a spurious phase arising from the interferometry of quasi-stationary phase can still appear in the case of evenly distributed noise sources.

The spurious phase retrieved from seismic noise has no correspondence in real seismograms. However, the ray paths of the correlated P and PKPab waves yielding the spurious phase are deterministic. The interferometric waves sample specific parts of deep Earth structure and in principle, the resulting spurious phase should also be applicable in imaging and monitoring the sampled structures.

The equivalent surface pressure PSDs for secondary microseism excitation by oceanic wave-wave interaction, were synthesized based on the theory proposed by Longuet-Higgins (1950) with the hindcast directional spectra of ocean waves but without any constrains coming from seismological observations. The comparisons between the spurious phase and the synthetic noise sources, in both fine time scale and long-term scale, justified the validity of the modelling, at least in the regions concerned in this study where ocean wave heights were significant and microseism excitations were energetic. Our study also highlighted the importance of the bathymetric amplifications of microseism excitations, which has also been emphasized by many others (e.g., Kedar et al. 2008; Gualtieri et al. 2014; Hillers et al. 2015a; Nishida and Takagi 2016; Meschede et al. 2017). Considering that the strength of the spurious phase is mainly linked to the intensity of microseism noise sources confined in a specific source region, a natural application of the spurious phase is to monitor the evolution of wave-wave interactions and detect microseism events in the source region. Considering the fact that an energetic effective source is necessary but not sufficient for the reconstruction of a prominent spurious phase, it is noteworthy that the detection or monitoring is not guaranteed to be always successful. Waves from strong noise sources outside the effective source region, especially

those closer to the seismic stations, are plausible to overwhelm waves from the distant effective source region and consequently deteriorate the reconstruction of the spurious phase from noise correlations. Coming to the application of monitoring distant ocean wave height and the causal storms using microseism noise (Ebeling 2012), we do not reject the possibility since our results proved that the strength of the reconstructed spurious phase and the wave height in the effective source region are positively correlated. Nonetheless, we have to put emphasis on the point that because of the nonlinear relations between microseism excitation and ocean wave heights, together with the effect of bathymetric amplification, even strong storms or extreme wave heights are not guaranteed to be capable of inciting strong microseisms. On the contrary, moderate wave heights are sometimes possible to produce energetic microseisms (see also Ebeling, 2012; Obrebski et al., 2012).

6. Ambiguities in Noise-Derived Body Waves

Recall that in Chapter 4, we observed both regular seismic phases and spurious arrivals in the noise cross-correlations between the FNET and LAPNET station pairs. In Chapter 5, the early spurious phase in the acausal correlations was investigated elaborately. In this chapter, we analyze the noise-derived P and PcP waves and discuss situations that can cause or potentially cause ambiguities in the noise-derived seismic signals.

6.1. Effects of Noise Source Distribution

6.1.1. Near-Simultaneous P Arrivals

From the acausal vespagram (Figure 4.8) of the FNET-LAPNET correlations, one can observe a likely arrival emerging nearly simultaneous as the P arrival but with an apparently smaller slowness. Using the same way as in section 5.3.2, we split the daily correlations into the groups of LSDs, MSDs and HSDs, corresponding to relatively low, mediate and high strength of the fake P arrival. The vespagrams of the three groups were shown in Figure 6.1. The fake P arrival is quite clear in the vespagram of HSDs.

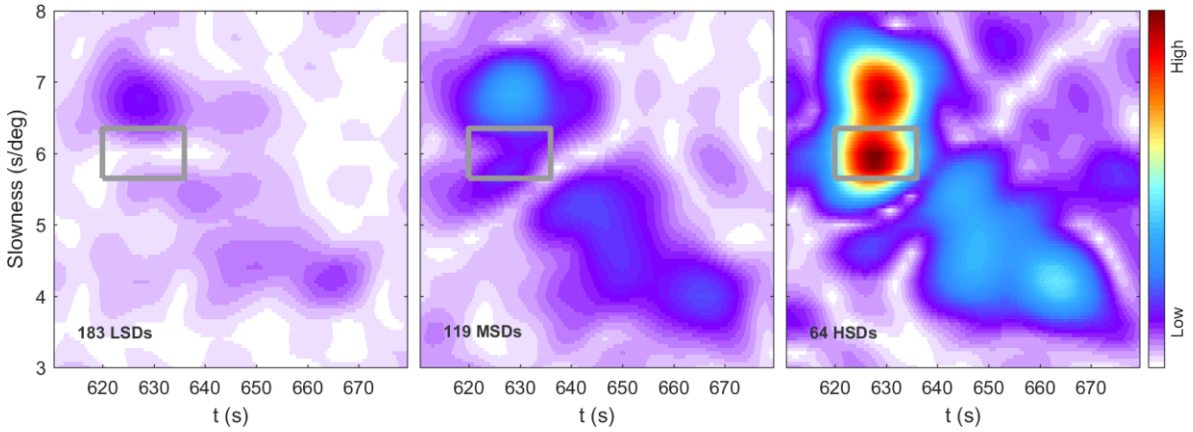

Figure 6.1. Vespagrams of the LSD, MSD and HSD groups of daily correlations. The box overlying the HSD vespagram contains an anomalous arrival emerging nearly simultaneous with the direct P wave.

6.1.2. Comparisons with Hindcast Data

6.1.2.1. Global Microseism Excitation

We plotted in in Figure 6.2 the annual average intensity of oceanic microseism noise sources at a seismic period similar to the acausal fake P arrival. The map shows that the microseism excitation is faint in the expected source region for the P-PP correlation and moderate in the expected source region for the PP-PPP correlation. Between the two expected source regions and along the great circle across FNET and LAPNET, the microseism excitation is quite energetic.

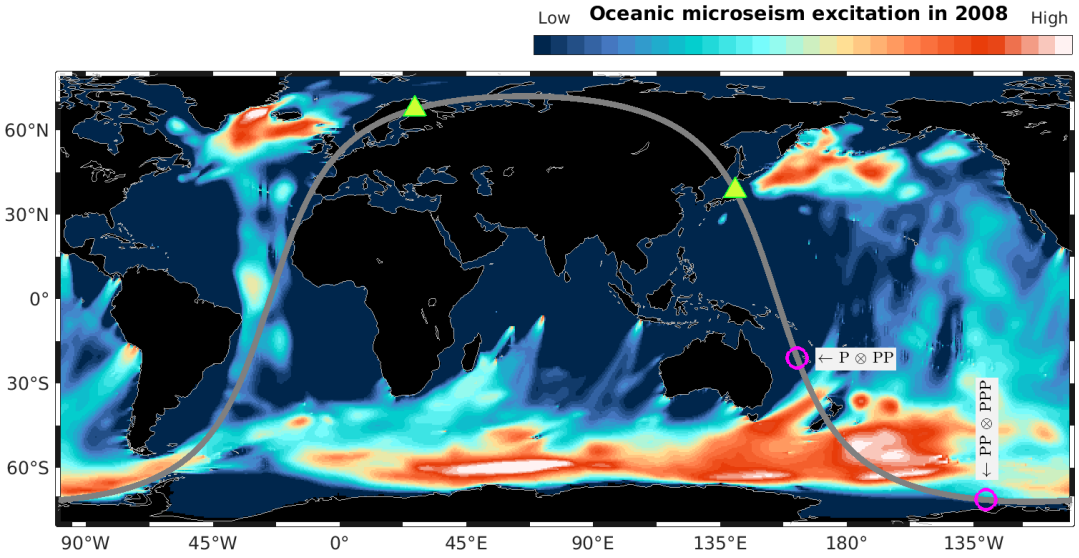

Figure 6.2. Global map of annual average PSD of oceanic secondary microseism excitation at a seismic period of 7.57 sec, which is close to the dominant period of the fake P phase. The colors are plotted in the scale of log10. Locations of FNET and LAPNET are marked by triangles. The gray line represents the great circle crossing FNET and LAPNET. The expected microseism source locations for the acausal P wave are labeled and denoted by open circles.

6.1.2.2. Global Correlation Map

Following the method of correlation map as adopted in section 5.5.4, we correlated the daily strength of the spurious P arrival with the daily microseism excitation at each point on the global ocean surface. The results were displayed in Figure 6.3. It can be seen that a spot of high correlation coefficients is present between the expected P-PP source and New Zealand, which

corresponds to a localized strong microseism noise source as displayed in Figure 6.2. The unique spot on the great circle should be the noise source responsible for the emergence of the fake P arrival.

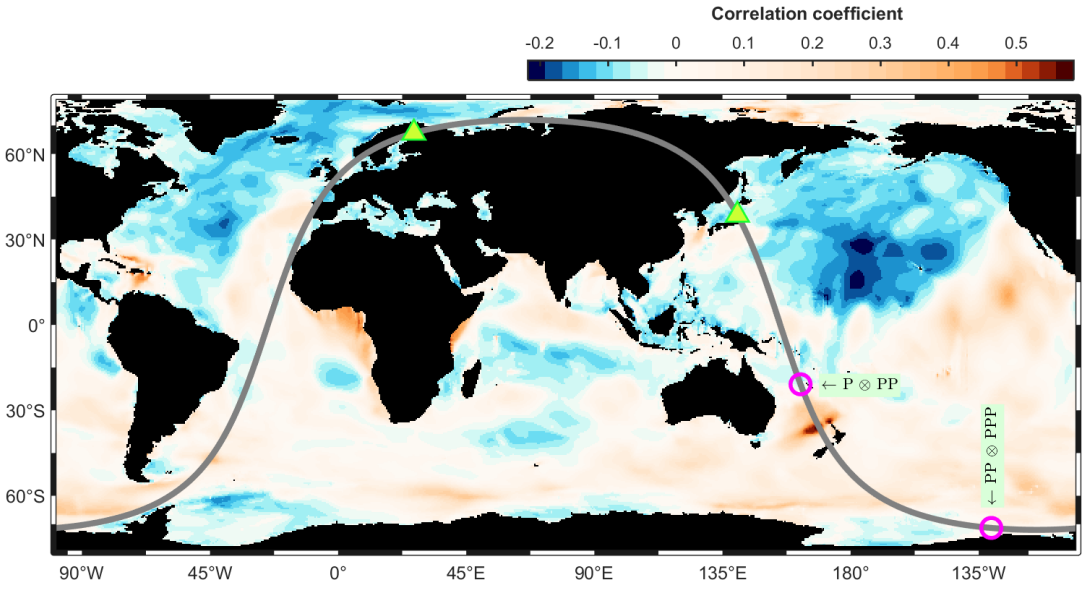

Figure 6.3. Global map of correlation coefficients bewteen daily fake P arrival and daily oceanic secondary microseism excitation in the period band of 5 to 10 sec. See legend of Figure 6.3 for descriptions on the annotations on the map.

6.1.3. Interpretations

6.1.3.1. Origins of Regular P Arrival

In section 2.2, we have discussed schematically the general cases of the reconstruction of seismic signals from correlations between coherent noise signals emanating from the effective sources and propagating along the effective ray paths. As for the specific case of teleseismic inter-receiver P arrival, referring to the prominent body phases in the global section of earthquake seismograms (Figures 3.5, 3.6 and 5.6) and considering the fact that the body waves excited by the ocean wave-wave interaction are predominantly P-type, it is likely that the reconstruction of P waves from noise correlations can be mainly ascribed to the correlations between P and PP waves and between PP and PPP waves. Considering the much lower amplitudes due to larger geometrical spreading and attenuation of longer paths, contributions from higher-order surface-reflected multiples are supposed to be minor (referring to the relative

clarity of the direct P wave and multiples in global sections of earthquake seismograms shown in Figure 3.5).

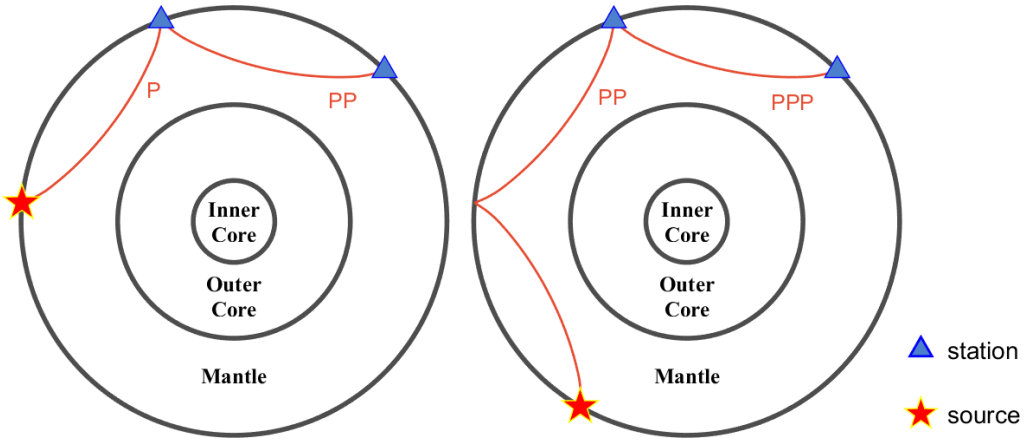

Figure 6.4. Schematic of the expected reconstruction of inter-receiver P wave from the correlation between PP and P (left), and from the correlation between PPP and PP (right).

6.1.3.2. Origins of Biased P Arrival

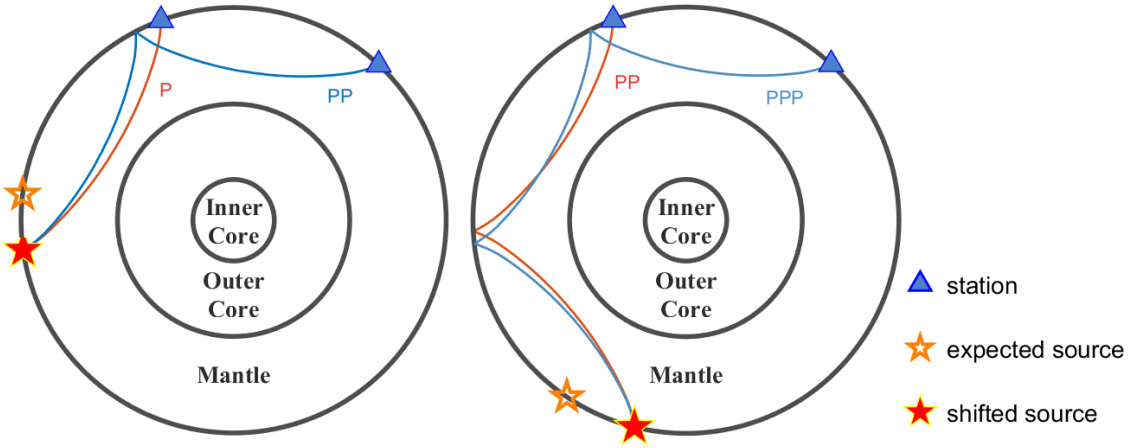

Figure 6.5. Schematic of the emergence of spurious phase close to the noise-derived P arrival due to the correlation between PP and P (left), and/or between PPP and PP (right) from localized strong sources in proximity to the expected effective sources.

Based on the smaller slowness of the fake P arrival compared to the slowness of the regular P arrival and the location of the causative noise source inferred from the correlation map in Figure 6.3, we interpret the presence of the fake P arrival as a consequence of the correlation between

the P and PP wave emanating from the localized strong microseismic source a bit farther from FNET that the expected location, which corresponds to the schema in the left panel of Figure 6.5.

6.2. Effects of Multipath Interference

In the previous section, we analyzed the generation of spurious arrival caused by localized noise source. That the causative source is localized suggests that the spurious phase disappear if the source distribution becomes uniform. In this section, we discuss some other cases that can lead to intrinsic ambiguity in the noise-derived signals. That the ambiguity is intrinsic refers to that it is inevitable and cannot be dismissed by improving the uniformity of source distribution.

6.2.1. Multipath due to Conversion

It has been mentioned in section 2.2 that, the reconstruction of an inter-receiver signal is ascribed to the correlations between waves emitted from effective sources that pass one receiver and reach the other. The correlation operation cancels the common path from source to the first receiver and reserve only the information concerning the inter-receiver path. As for the extraction of direct body waves from noise correlations, the correlated rays are a surface reflection from source *S* to receiver *B* and a direct transmission from source *S* to receiver *A* (Figure 6.6). In the first two cases in Figure 6.6, the correlation operator cancels the common path from the source *S* to receiver *A* and leads to the expected reconstruction of the inter-receiver P wave. The problem lies in the last case. In 1D depth-dependent model, the surface reflection PS in Figure 6.6c is equivalent to SP in Figure 6.6b. Thereby, the PS-S correlation in Figure 6.6c can give rise to the same signal as the SP-S correlation in Figure 6.6b. However, in the presence of lateral heterogeneity, the traveltime of PS can be different from that of SP. Consequently, the signal generated from PS-S is asynchronous with the signal generated from PP-P and SP-S. Hereafter, we call the signal stemming from the correlation between the unexpected ray paths as in Figure 6.6c **ambiguous phase** or **ambiguous signal**. The ambiguity in the noise-derived signals originates from mode conversions between P and S. The ambiguity caused by multipath can be worsen if considering conversions in higher-order multiples and/or further complicated conversions from surface waves and interface waves. The discussions

above also hold for the retrieval of inter-receiver S wave if exchanging P and S legs in Figure 6.6.

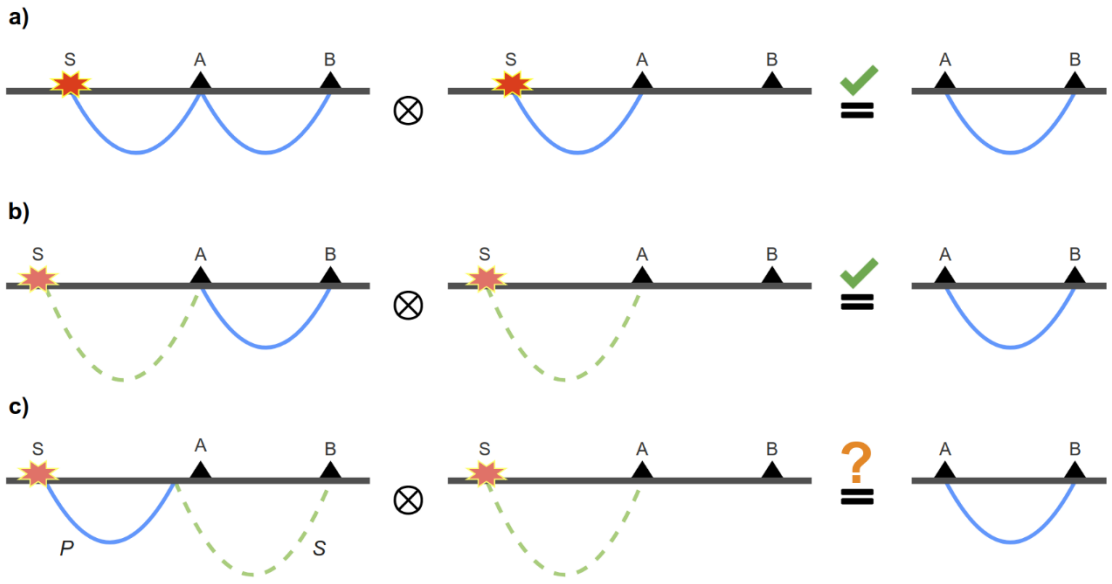

Figure 6.6. Schematic of possible interferometric ray paths giving rise to the inter-receiver P arrival: a) PP and P; b) SP and S; c) PS and S. The horizontal dark line represents the flatted Earth's surface.

6.2.2. Multipath due to Reflection

6.2.2.1. General Case

The multipath of multiples caused by mode conversions at interfaces and the consequent multipath interference can also occur in the cases of retrieving reflections from inter-receiver correlations. Here, we address another situation of multipath interference as explained in Figure 6.7, which is inevitable for the retrieval of reflections from noise correlations and cannot be eliminated by any data processing techniques.

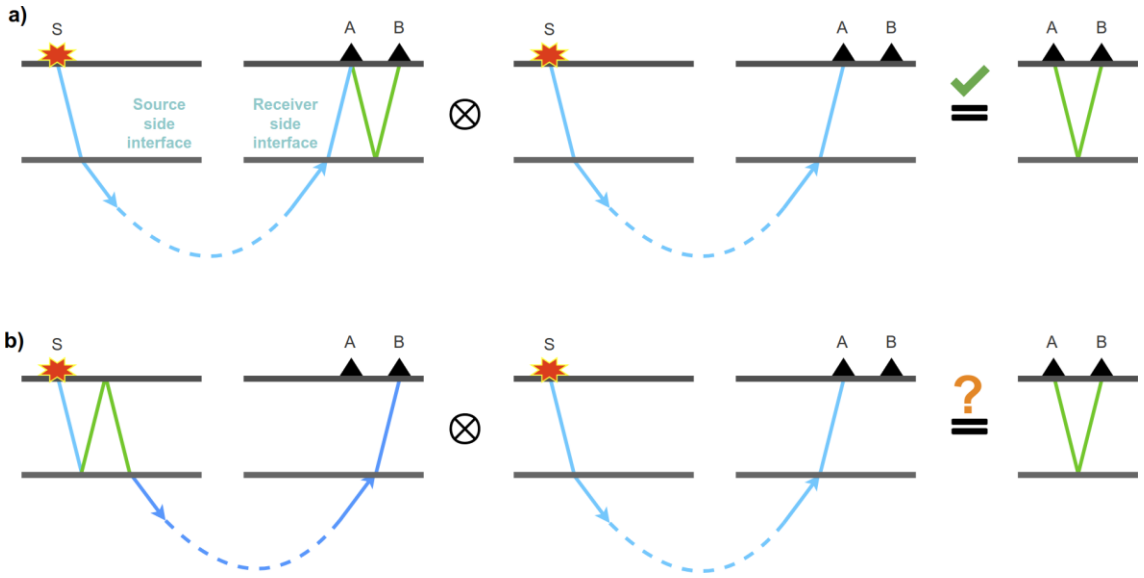

Figure 6.7. Retrieval of inter-receiver reflections from seismic interferometry. Dark lines denote the free surface and any internal interface (such as Moho, 410km, 660km, CMB, *etc*.) of the flattened Earth model. Noise source and receivers are deployed at the surface. In the case of a), the correlation operator cancels the common path from noise source *S* to receiver *A*, retaining the phase information between receivers *A* and *B*, as expected. However, in the case of b), the wave from source *S* to receiver *B* is equivalent to that in a).

6.2.2.2. Specific Case of PcP

The Earth model in Figure 6.7 is flattened. In practice, the interfaces at depth can be curved. As for the particular case of noise-based PcP-wave retrieval, we plotted the correlated ray paths in the spherical Earth model (Figure 6.8). The PKPPcP-PKP correlation cancels the common PKP path and gives rise to the expected PcP signal. However, PcPPKP has exactly the same traveltime, slowness, and amplitude as PKPPcP in 1D Earth model. Consequently, the PcPPKP-PKP correlation leads to the same signal as the PcP wave retrieved from the PKPPcP-PKP correlation. The ray paths of PcPPKP and PKPPcP are distinct from each other, but cannot be distinguished from seismological observations at surface. The PKKPPcP-PKKP correlation can also lead to the correct PcP retrieval. Note that PKKPPcP and PKPPKP share the same traveltime and slowness, suggesting that the signal derived from the PKPPKP-PKKP correlation is equivalent to the PcP wave retrieved from the PKKPPcP-PKKP correlation, except a possible difference in amplitude. Also, one can find that the differential paths between PcPPKP and PKP are the same as those between PKPPKP and PKKP.

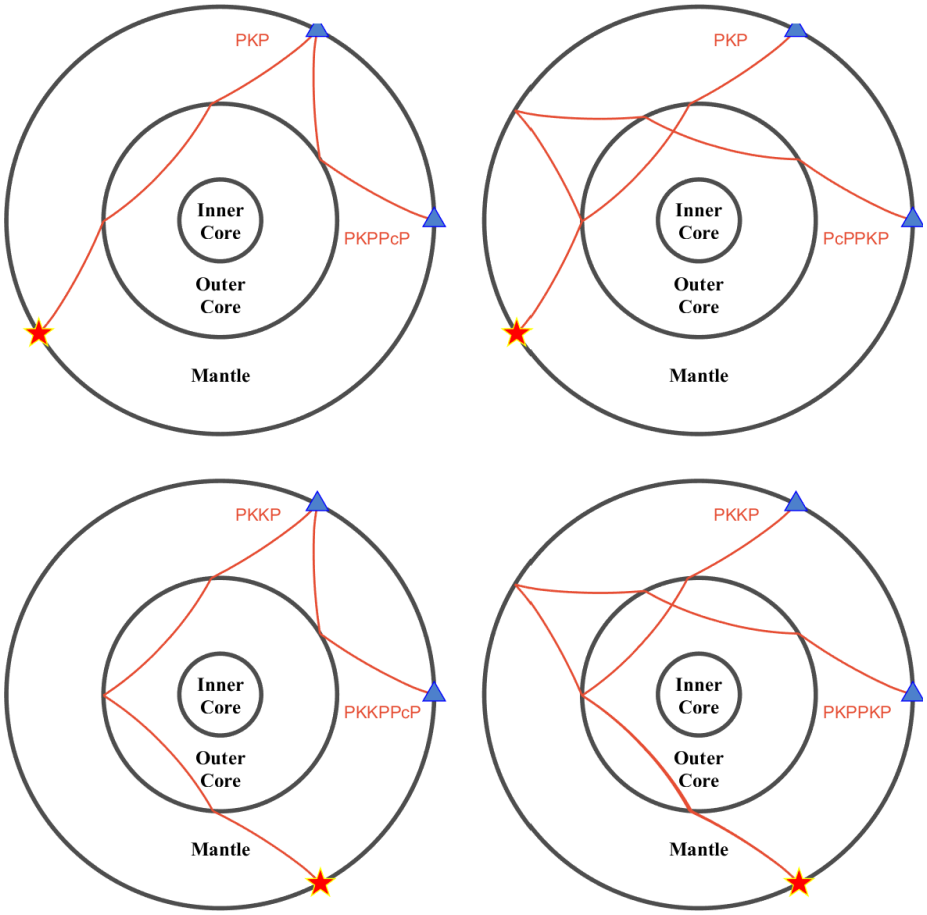

Figure 6.8. Multipath interference for the inter-station PcP wave. The last legs of the correlated ray paths are the same for all panels. There can be more combinations of correlated ray paths. The chosen phases shown here have been referred to the visible phases in the global section of earthquake seismograms.

6.2.3. Implications in Noise-Based Imaging

We expect that the noise-derived virtual seismograms converge to the Green functions of the propagation medium. The signals extracted from noise correlations are expected to be good approximate of the observed seismic phases. However, it has been shown that the multipath interference can lead to the emergence of noise-derived signals that resemble the true inter-receiver seismic phase but are totally irrelevant with the inter-receiver Green function of medium. The influence of multipath interference is two-sided. In 1D model, the ambiguous signals are perfectly in phase with the true signal in the inter-receiver seismic response. So, the only effect is to enhance the clarity of the true signal. However, in the practical Earth media, lateral heterogeneity and fluctuations in interface depth make the ambiguous signals out of

phase with the true signal. The clarity of the true signal and the resultant imaging can still be enhanced if the phase difference is sufficiently small. The imaging of interfaces is blurred if the ambiguous signals partly superpose the true signal with significant phase differences. In the presence of ambiguous signals isolated from the true signal, the noise-based imaging may be misinterpreted as multiply-layered structure. In a worse case, if the reflector on the receiver side (between receivers being correlated) is missing, the reflector on the source side (between noise sources and the first receiver) is mapped into the imaging of inter-receiver structure. The various possibilities are summarized in Figure 6.9.

We highlight that we are not refusing the feasibility of the noise-based body-wave imaging. Nevertheless, we have to appeal that special care must be taken to image the subsurface with noise-derived body waves and to interpret the results. Imaging interfaces with noise-derived reflections have been implemented by many authors (e.g., Draganov et al. 2007, 2009; Ruigrok et al. 2010; Ito et al. 2012; Poli et al. 2015; Taylor et al. 2016; Oren and Nowack 2017; Saygin et al. 2017), however, it appears that the effect of multipath interference and the potential resultant bias/error in the imaging results have always been ignored.

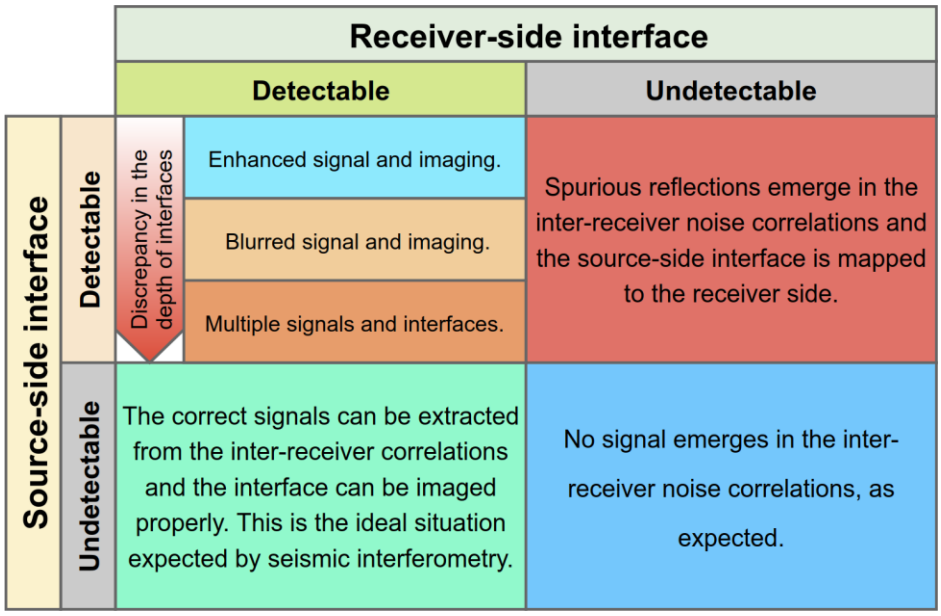

Figure 6.9. Summary over the effects of multipath interference on the imaging of interfaces on the receiver side. The detectability of an interface refers to if a corresponding body wave reflection can be reconstructed from noise correlations. If there is no interface or the contrast of the interface is too weak to give rise to a reliable reflection signal, it is regarded as undetectable.

6.3. Summary and Discussions

In this chapter, we presented real-data example of spurious phase arising from localized strong noise source, in correspondence to the synthetic example given in Figure 2.9 of section 2.2.3. In the case of FNET-LAPNET correlations, the localized microseism noise source is close to the expected source region for the P-PP correlation that can produce the regular direct P wave. The proximity in the geographic location of noise sources leads to the emergence of the spurious P arrival almost synchronous as the regular P arrival. The superposition of the spurious arrival with the regular phase unavoidably distort the waveform of the regular signal to some extent. A more risky situation should be pointed out. Imagining that the effective sources are so feeble that they fail to reconstruct the regular phase. The presence of localized strong noise source close to the effective sources gives rise to a fake phase that could be mistaken for the regular phase. Imaging with the wrong phase potentially brings significant bias/error into the results. Considering the heavy non-uniformity in the spatiotemporal distribution of noise sources, we cannot refuse the occurrences of such situations.

Regarding the retrieval of transmitted waves between receivers from ambient noise correlations, ambiguous phases can arise from the multipath interference caused by mode conversions. The amplitude of the ambiguous phases (relative to that of the true signal) is related to source mechanism, medium properties and observation geometry. In the cases that the mode conversions are weak, the effect of multipath interference can be neglected. The Noise-derived reflections are also affected by ambiguous phases resulting from multipath interference, which is inherit in seismic interferometry and less sensitive to source mechanism.

The spurious phase arising from localized noise source disappears when the source distribution tends to be uniform, or it can be reduced by techniques like the data selection filters and spatial equalization as introduced in Chapter 2. In contrast, the ambiguous phases arising from multipath interference cannot be eliminated by even distribution of noise sources, nor by elaborate signal processing. The asymmetry of PcP waves in the FNET-LAPNET correlations shown in Figure 4.6 can possibly be ascribed to the influence of multipath interference. Averaging the reflection phase in the acausal and causal inter-receiver correlations may to some extent reduce the ambiguous signals, but the effectiveness is not guaranteed. In the best case of averaging, the ambiguous phases are reduced to half strength and the true reflection is strengthened by two times. A more effective way may be the slant stack of noise correlations

for station pairs separated at varying distances and/or aligned in different azimuths, with the reflection points of the true reflection overlapped (concentrated). If the interface depth is relatively invariant, the ambiguous phases enhance the true reflection signal and improve the clarity of imaging. Providing that the interface depth fluctuates significantly at a large spatial scale, the wide spreading of source-side reflection points for the ambiguous phases is supposed to lead to unconstructive stacking of ambiguous phases, while the true noise-derived reflections share a common reflection point and can stack constructively.

7. Contributions of Thesis and Perspectives for Future Works

In Chapter 1, we reviewed the background knowledge on seismic noise. In Chapters 2 and 3, we discussed the principles and techniques of seismic interferometry. In Chapter 4, we showed that deep body waves can be extracted from noise correlations. In Chapter 5, we revealed the origin of the early spurious phase and proposed an extended version of the stationary-phase theory. In Chapter 6, we analyzed the origins of regular body phases as well as spurious phases that bring ambiguity in the noise-derived seismic signals and potentially bias the noise-based imaging. Here in the last chapter, we make a summarization over the contributions of this thesis. We also provide an outlook of ongoing works and prospect some possible works in the near future.

7.1. Contributions of Thesis

7.1.1. Contributions to Noise-Based Techniques

Toward the aspect of noise-related techniques, the contributions of this thesis include:

- ☑ Kurtosis-based selection filter for noise data pre-processing (section 2.2.4),
- ☑ Hampel filter for extracting noise level time series from continuous seismograms (section 2.3.5, section 5.4.3),
- ☑ Free scheme for computing correlation function (section 2.4.2),
- ☑ Double-array slowness analysis (section 3.2.4, section 5.2.1),
- ☑ Double-array noise source imaging (section 3.2.5, section 5.2.3),
- ☑ Slowness tracking for identifying the correlated ray paths (section 5.2.3),
- ☑ Correlation map for identifying potential noise sources (section 5.5.3, section 5.5.4).

7.1.2. Contributions to Noise-Based Theory and Observations

Toward the aspect of noise-based theory and observations, the contributions of this thesis include:

- ☑ Schematic interpretations of interferometric theory (section 2.2),

- ☑ Classification of noise sources and ambient wavefields (section 2.2.4),
- ☑ Lower and higher order descriptive statistics of continuous seismograms (section 2.3.3)
- ☑ Observation and origin of a stable early spurious phase (section 5.1, section 5.2),
- ☑ Temporal variations and classification of noise-derived body phase (section 5.3),
- ☑ Cross-validation between microseism observations and hindcast modeling (section 5.5),
- ☑ Extended interferometric theory of quasi-stationary phase (section 5.2.4),
- ☑ Spurious phase stemming from localized noise source (section 2.2.3, section 6.1),
- ☑ Ambiguity in noise-derived signals due to multipath interference (section 6.2).

7.2. Ongoing and Future Works

7.2.1. Noise-Based Deep Earth Imaging

A main aim of extracting body waves from seismic noise is towards the noise-based imaging of deep Earth structure. The work of this thesis improves the understanding about the origins of and potential biases in the noise-derived body phases penetrating into the deep Earth, which is valuable for advancing the noise-based imaging. An ongoing work is to image the lowest mantle and core-mantle boundary beneath western Asia (Kazakhstan) using the noise correlations between China Array and European networks (Figure 7.1).

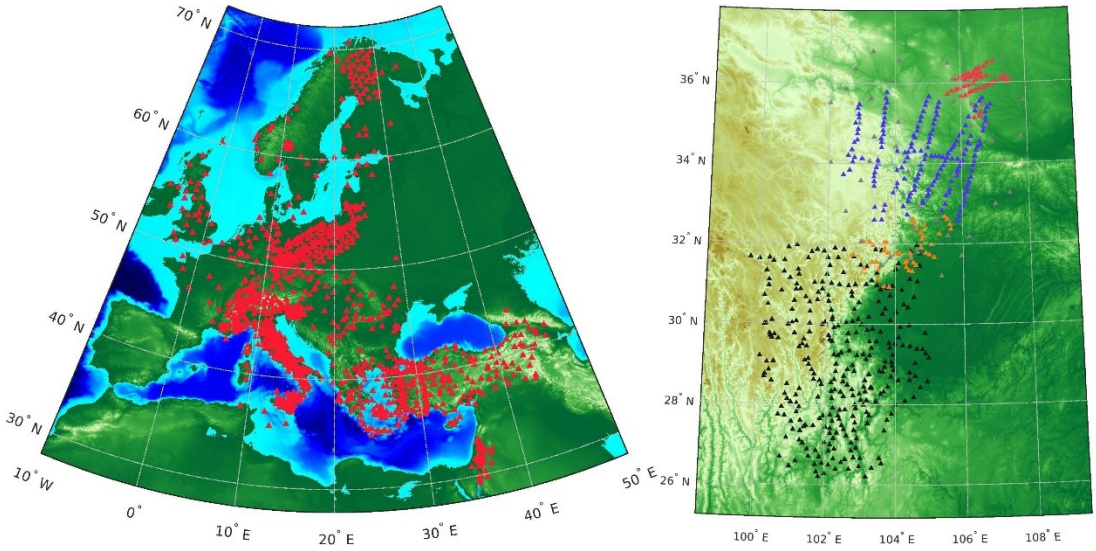

Figure 7.1. Geographic locations of about 860 broadband seismic stations in Europe (left) and about 560 stations in China (right) in operation during 2007 and 2012.

7.2.2. Compiling Catalogue of Global Microseism Events

Continuous seismic noise records and earthquake seismograms can be uniformly regarded as a convolution between the medium Green function and the source time function (STF). In principle, both can be utilized to study the Earth's structure. The occurrence of earthquakes results from the abrupt rupture of the causative faults undertaking long-term deformations and accumulated strains. Significant earthquakes are generally isolated in time. At distant receivers, an earthquake source can be deemed as a point or in a limited span, no more than several tens to hundreds km. In contrast to earthquakes, seismic noise sources are distributed in space and it is common that multiple (lots of) noise sources exist concurrently. However, there are also situations that the noise records are predominated by seismic signals from specific noise sources of high intensity, for instances, the localized strong microseism noise sources induced by large storms that have been reported by many authors (e.g., Gualtieri et al. 2014; Gerstoft and Bromirski 2016; Nishida and Takagi 2016; Farra et al. 2016; Retailleau et al. 2018).

It is unquestionable that the **earthquake catalogue** is one of the most fundamental and important database in seismology. The construction of databases for the sporadic **non-earthquake seismic sources**, such as landslides, debris flows, dam collapses, floods and avalanches, is also in progress (e.g., Allstadt et al. 2017). It is attractive and prospective if a **catalog of microseism events/noise bursts** can also be compiled and shared among the seismological community. Note that in the field of exploration seismology, microseismic event refers to tiny earthquakes, not to be confused with the microseism event mentioned here that is caused by ocean wave activities.

One should keep in mind that there are some differences in using seismic records from earthquakes and from noise sources. The main difference is that the STF of an earthquake is short in duration, generally from seconds to minutes, while the STF of a noise source is generally persistent and random in phase. The STF of earthquake is impulsive and seismic signals from earthquakes have clear jumps indicating their arrival times, at least for the direct arrivals. The origin time of earthquake and the traveltime of a seismic phase can be determined with a fair accuracy. In contrast, seismic signals from noise source superpose each other due to the long STF and generally show no discernible onsets. For instance, in the case of a stormed-induced microseismic event, the noise level at the receiver grows gradually in hours to days. There can be no clear signature indicating the exact origin time of the microseism event and

due to this obscurity, one cannot pick the absolute source-receiver traveltime of a seismic signal as from the earthquake seismogram. What we can measure is the relative time delay among stations, using the correlation technique.

7.2.3. Exploring Microseism Datasets with Machine Learning

Machine learning, a branch of artificial intelligence in computer science, has become a hot topic in recent years, boosted by the rapid improvement in computational ability and decline in costs. It is also known as **pattern recognition,** and sometimes is called **data mining**. Strictly speaking, similar to deep learning, data mining is also a subset of machine learning. The common tasks of machine learning include classification, regression and clustering.

Machine learning has been widely used in business, such as computer vision, financial market prediction, natural language processing, online fraud detection, personalized healthcare, product recommendation, search engine result refining, email spam and malware detection, speech and handwriting recognition and strategy computer games. It also has broad applications in academic community, such as astronomy and biometrics. As for earth science, the application of machine learning is extensive in a diversity of fields like climate science, environmental science, geographic information science and oceanography. In seismology, the use of machine learning is less active but there have been some applications in exploration seismology (e.g., Beckouche and Ma 2014; Chen 2018), earthquake seismology (e.g., Lekic et al. 2012; Kortström et al. 2016; Rouet-Leduc et al. 2017; Florido et al. 2018; Perol et al. 2018; Olivier et al. 2018; Kotha et al. 2018), volcano seismology (e.g., Unglert et al. 2016; Unglert and Jellinek 2017) and seismic interferometry (e.g., Paitz et al. 2018). One can expect that machine learning is a rewarding research area and will be increasingly active in seismic interferometry as well as in the whole seismology society.

7.2.4. Global Ambient Noise Correlation Wavefield

It has not been news that we know deep body waves exist in the ambient wavefields and can be extracted from noise correlations (see sections 1.3.6 and 2.1.2.2 for details). In the early works, the extraction of deep body waves generally relied on very long-term stacks (e.g.,

decade long) of ambient noise correlations (Lin and Tsai 2013; Nishida 2013) and/or under specific observation geometry, e.g., collocated stations (autocorrelation) or antipodal station pairs (Lin and Tsai 2013) that can benefit from the focusing of omnidirectional seismic waves (Rial 1978; Retailleau et al. 2014). Very sooner, authors affirmed that the reconstruction of deep phases at arbitrary distances can be facilitated by binning or beamforming (Boué et al. 2013a, 2014a; Xia et al. 2016) noise correlations of one year or several months. With the aid of spatial stacking, the very-long-term observation is not necessary. In this thesis, we showed that it is even feasible to extract clear body-wave signals from noise correlations on single day and between single station pair.

Ruigrok et al. (2008) simulated the propagation of 6.4 sec period P waves in a modified lossless PREM Earth model (Dziewonski and Anderson 1981) with an acoustic finite difference (AFD) modelling program (Figure 7.2). They synthesized global sections of inter-receiver correlation functions from the elastodynamic representation integrals (see their Equations 20 and 21). Both regular and spurious arrivals are visible in the synthetic correlation sections (Figure 7.3). The model used by Ruigrok et al. (2008) was over simplified and their results were purely based on numerical modelling, which likely led them to attributing the presence of spurious phases in the synthetic section to numerical errors and sparse noise source distribution.

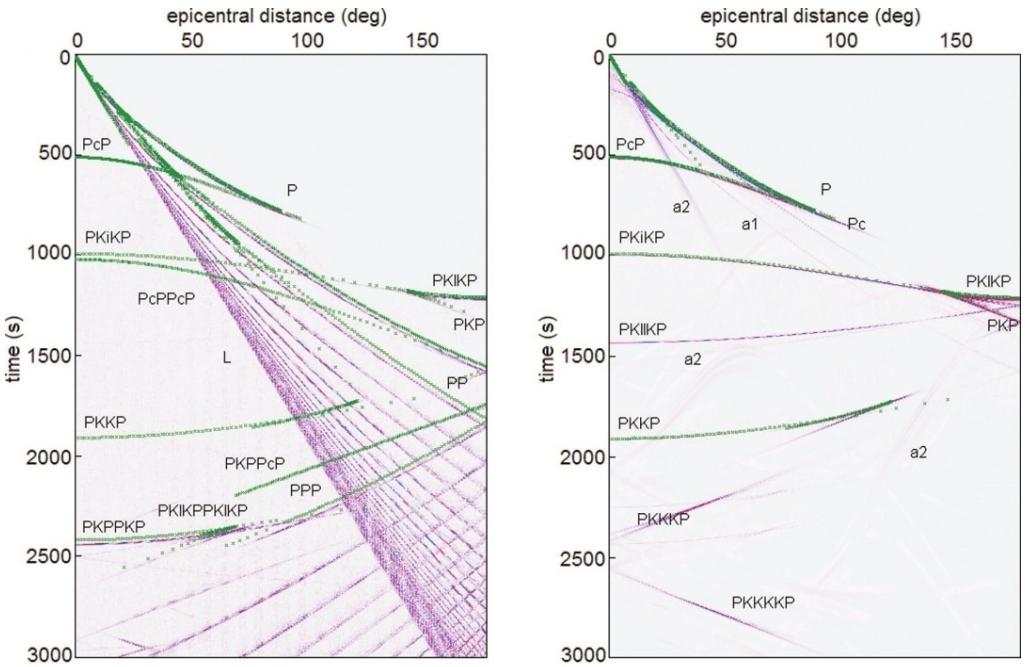

Figure 7.2. AFD-modeled global sections for a 1D lossless Earth model with (left) and without (right) free surface multiples. Reproduced from Figure 6 of Ruigrok et al. (2008).

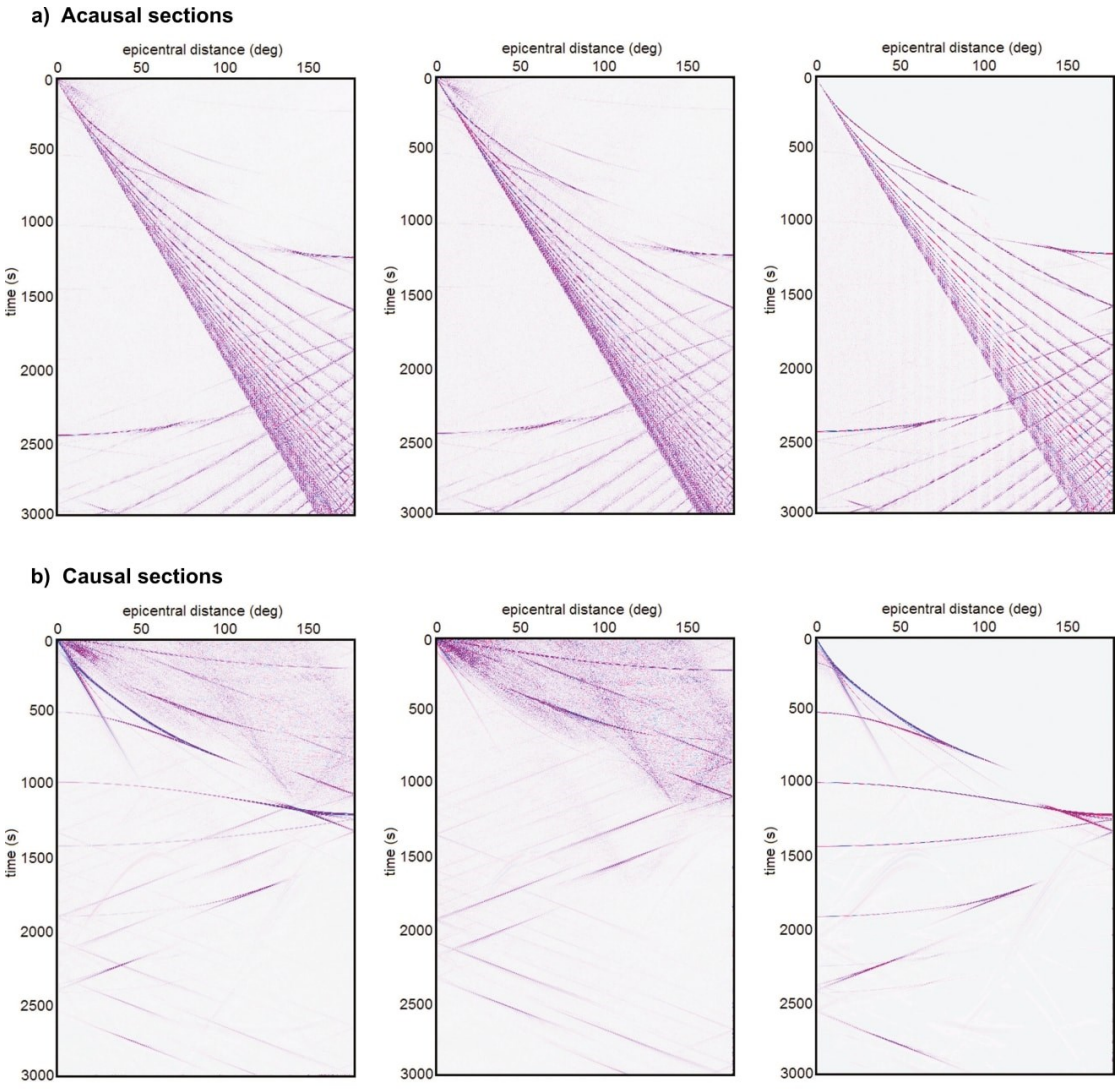

Figure 7.3. Global sections of acausal (a) and causal (b) noise correlations with (left) and without (middle) the contributions from near-offset sources, in comparisons with the AFD-derived sections (right). Reproduced from Figures 10 and 11 of Ruigrok et al. (2008).

The global correlation section were created from real seismograms five year later (Boué et al. 2013a; Nishida 2013). Boué et al. (2013a) calculated the correlation functions of the vertical components of continuous seismograms from 339 global broadband stations (Figure 7.4a), in the period band of 5 to 100 sec. They constructed a global section of ZZ correlation functions and compared it with a synthetic section simulated using the spectral element code AxiSEM (Nissen-Meyer et al. 2014) and the PREM Earth model (Figure 7.4). In the particular frequency band of seismic hum, Nishida (2013) created the global sections of ZZ, RR and TT noise

correlations (Figure 7.5a), using 9 years' three-component seismograms recorded by 658 broadband stations. Several seismic phases can be identified by comparing with the sections of corresponding Green functions.

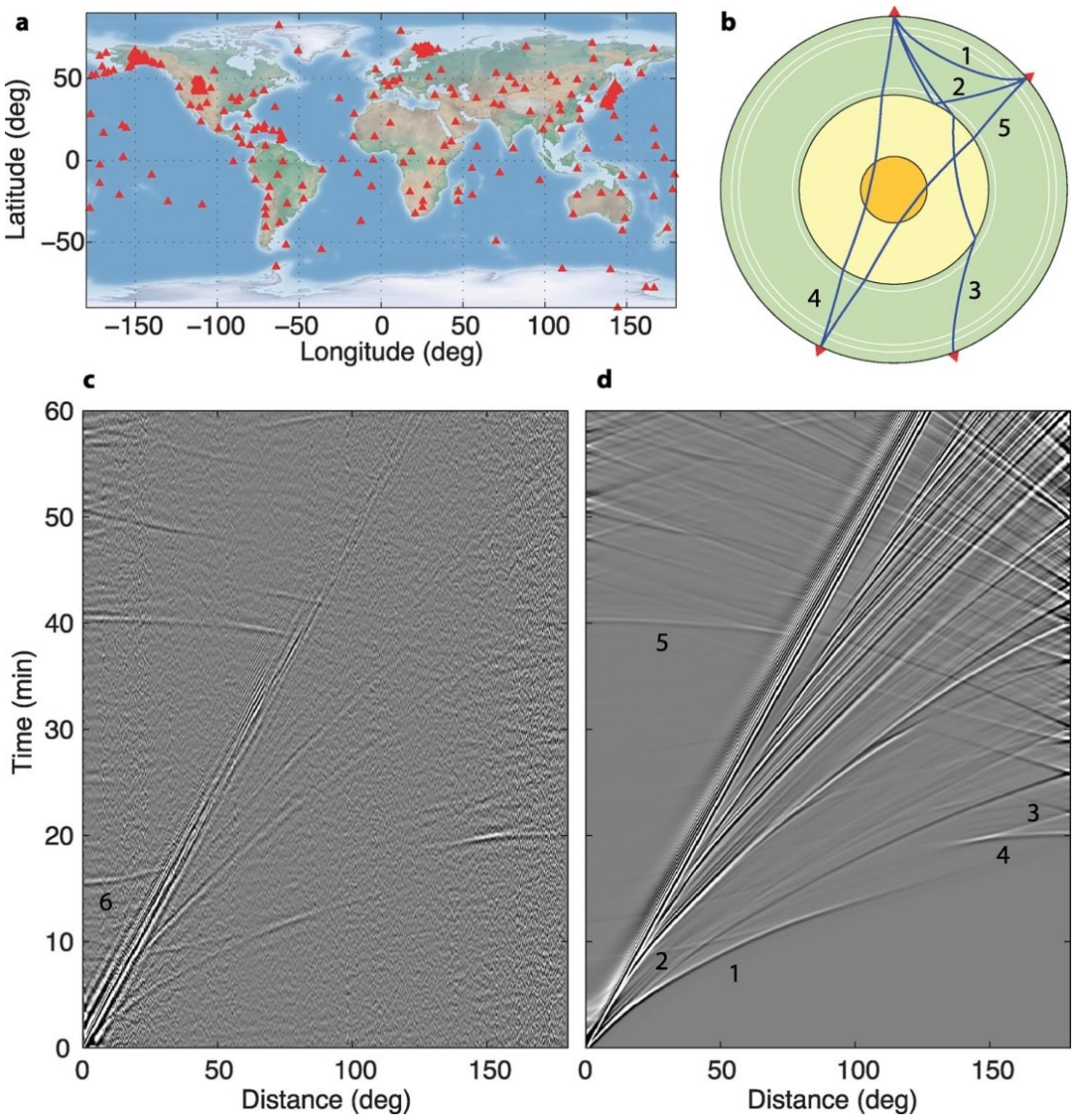

Figure 7.4. (a) The geographic locations of seismic stations being correlated. (b) The paths of mantle and core phases labeled in the global sections. (c) Global section of virtual seismograms retrieved from noise correlations, filtered in the period band of 25 to 100 sec. The ScS phase is labeled as 6, with the path indicated by 2 in (b). (d) Global section of synthetic seismograms modeled using the AxiSEM program and the PREM Earth model including attenuation, with a 40 sec dominant period vertical force source applied to the surface (1, P; 2, PcP; 3, PKP; 4, PKIKP; 5, PKIKPPKIKP). Reproduced from Figure 1 of Boué et al. (2013a).

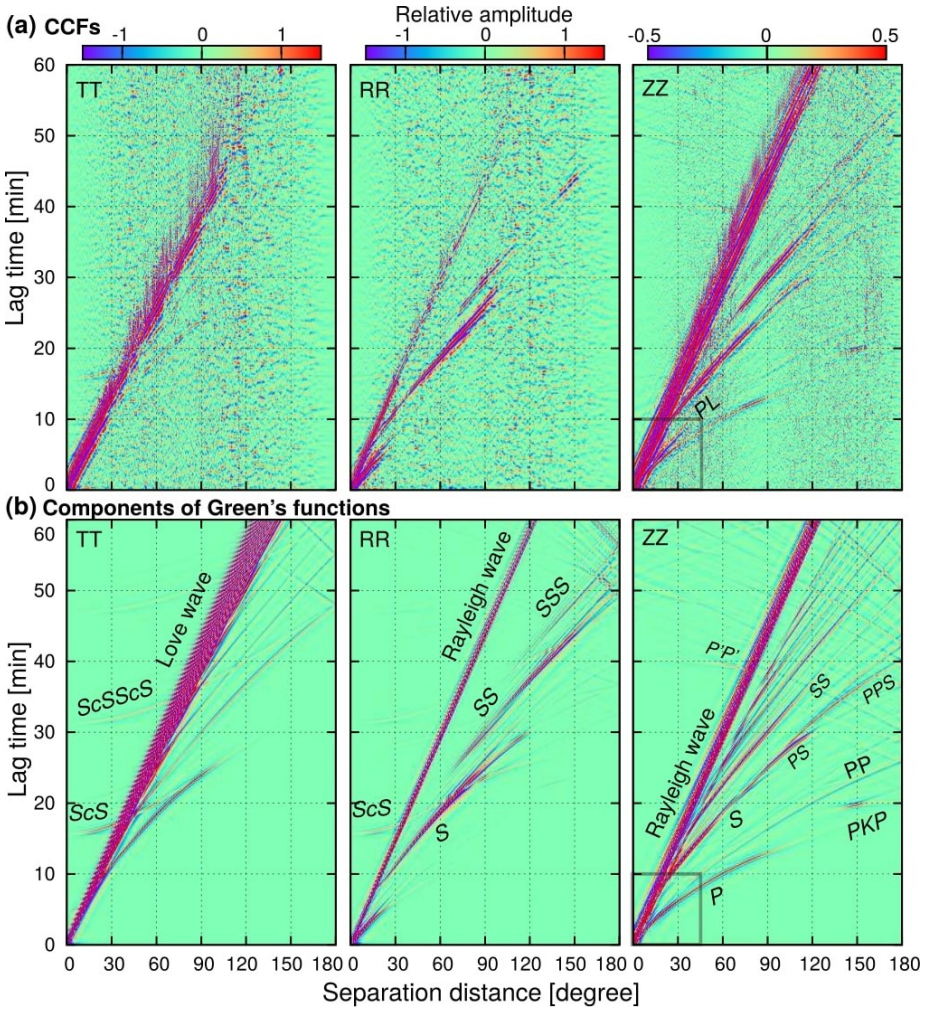

Figure 7.5. Global sections of TT, RR, and ZZ components of cross-correlation functions (a) and of theoretical Green functions (b). Reproduced from Figure 3 of Nishida (2013).

The construction and analysis of global correlation sections are also one of our ongoing works. The approach to construct the correlation sections can be regarded as a mix of that of Ruigrok et al. (2008) and that of Boué et al. (2013a). The techniques proposed in chapter 2 and 3 of this thesis are useful in the analysis of the noise-derived signals.

7.2.5. Global Coda Correlation Wavefield

In recent years, correlations of coda waves from large earthquakes are attracting increasing interests (Huang et al. 2015; Xia et al. 2015; Poli et al. 2017; Phạm et al. 2018; Wu et al. 2018; Kennett and Pham 2018). The interpretations and potential applications of seismic signals derived from coda correlations are also our ongoing work.

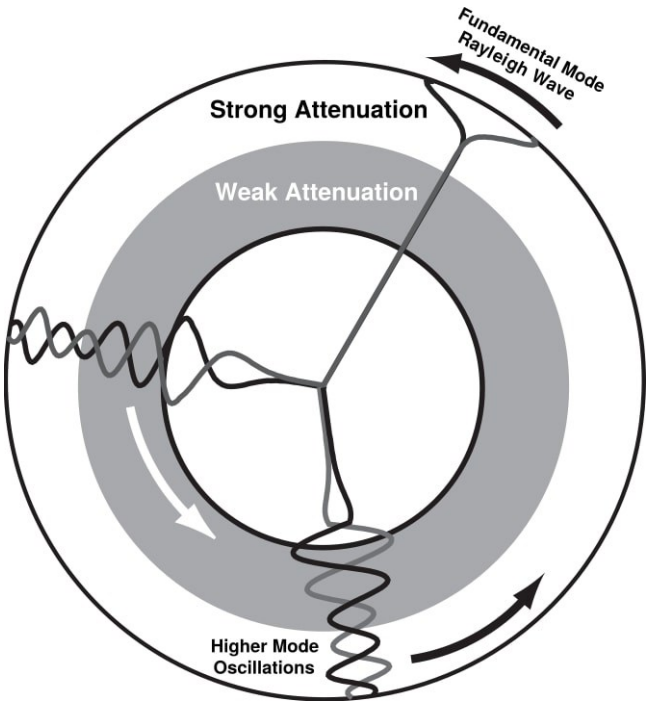

Figure 7.6. Cartoon illustration of the depth-dependent attenuation structure of Earth and the propagation of fundamental-mode and higher-mode oscillations. The mantle is characterized by strong attenuations in the upper parts and weak attenuations in the lower parts. Reproduced from Figure 9 of Maeda et al. (2006).

Coda waves from large earthquakes can last for several tens hours [see Figures 7 and 10 of Maeda et al. (2006), Figure 1 of Sens-Schönfelder et al. (2015) and Figure 1 of Poli et al. (2017) for examples]. The coda wavefield is not equipartitioned but exhibit clear directivity characterized by dominant energy flux along the great circles across the epicenter of large earthquake [see Figures 4 and 5 of Sens-Schönfelder et al. (2015) and Figure 1d of Poli et al. (2017) for examples]. FK analysis and vespagrams of late codas have revealed that the dominant periods of late codas (free oscillations of Earth excited by large earthquakes) are in the period band of seismic hum (free oscillations of Earth excited by ocean infragravity waves) and the main constituents of late codas are steeply-travelling deep body phases with small slownesses [see Figures 4 to 6 of Maeda et al. (2006), Figures 2 and 3 of Sens-Schönfelder et al. (2015) and Figure 1d of Poli et al. (2017) for examples]. Maeda et al. (2006) interpreted the late coda waves as higher modes resulting from the weak attenuation in the lower mantle (Figure 7.6). Boué et al. (2014a) found a connection between global seismicity and the presence of noise-derived body waves in the period band of seismic hum (Figure 7.7).

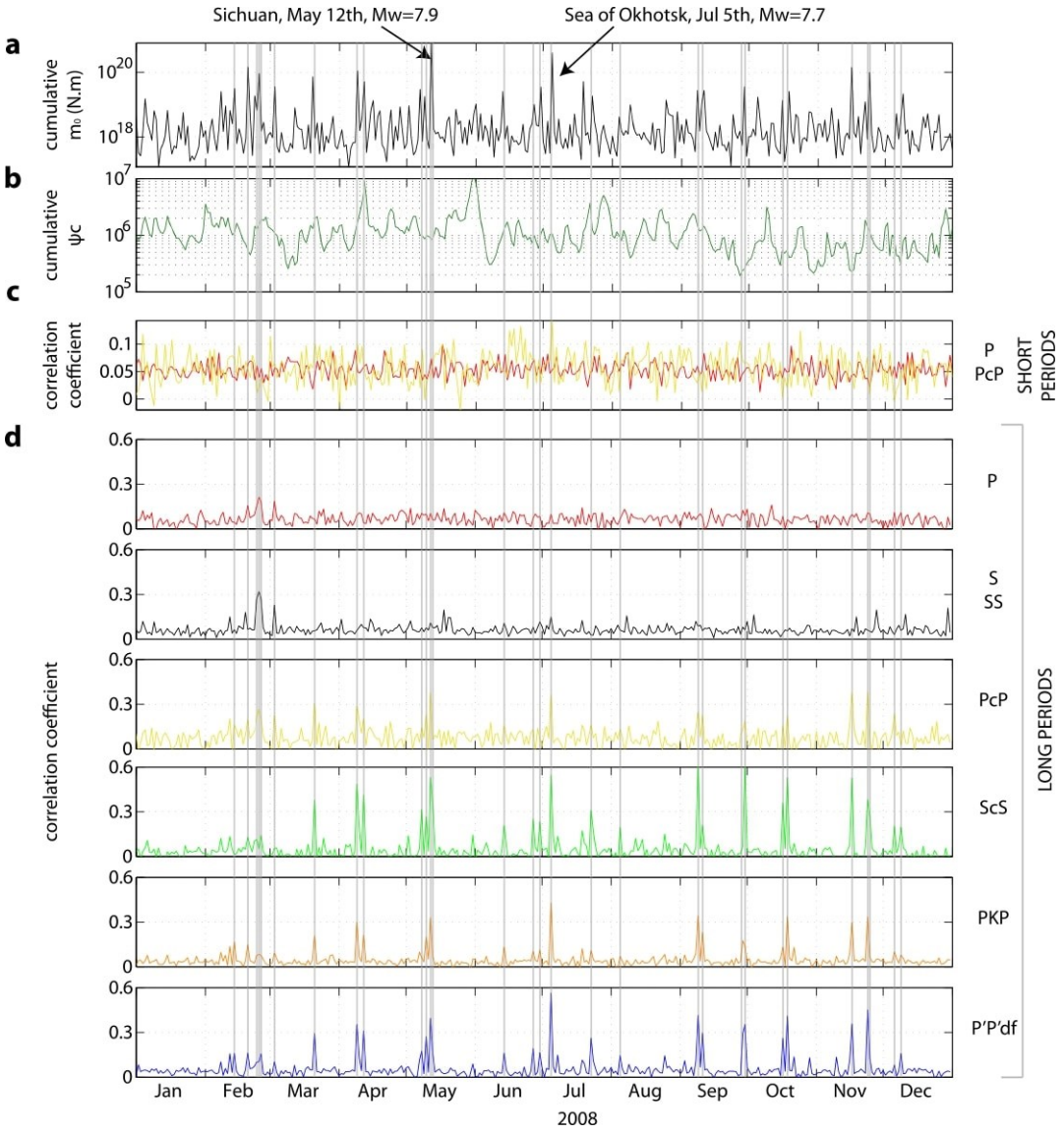

Figure 7.7. a) Daily cumulative global seismic moments. b) Daily secondary microseism excitation at a seismic period of 7 sec. c) Correlation coefficients of global seismicity with noise-derived P and PcP waves in the period band of secondary microseisms. (d) Correlation coefficients of global seismicity with different phases in the period band of seismic hum. Reproduced from Figure 3 of Boué et al. (2014a).

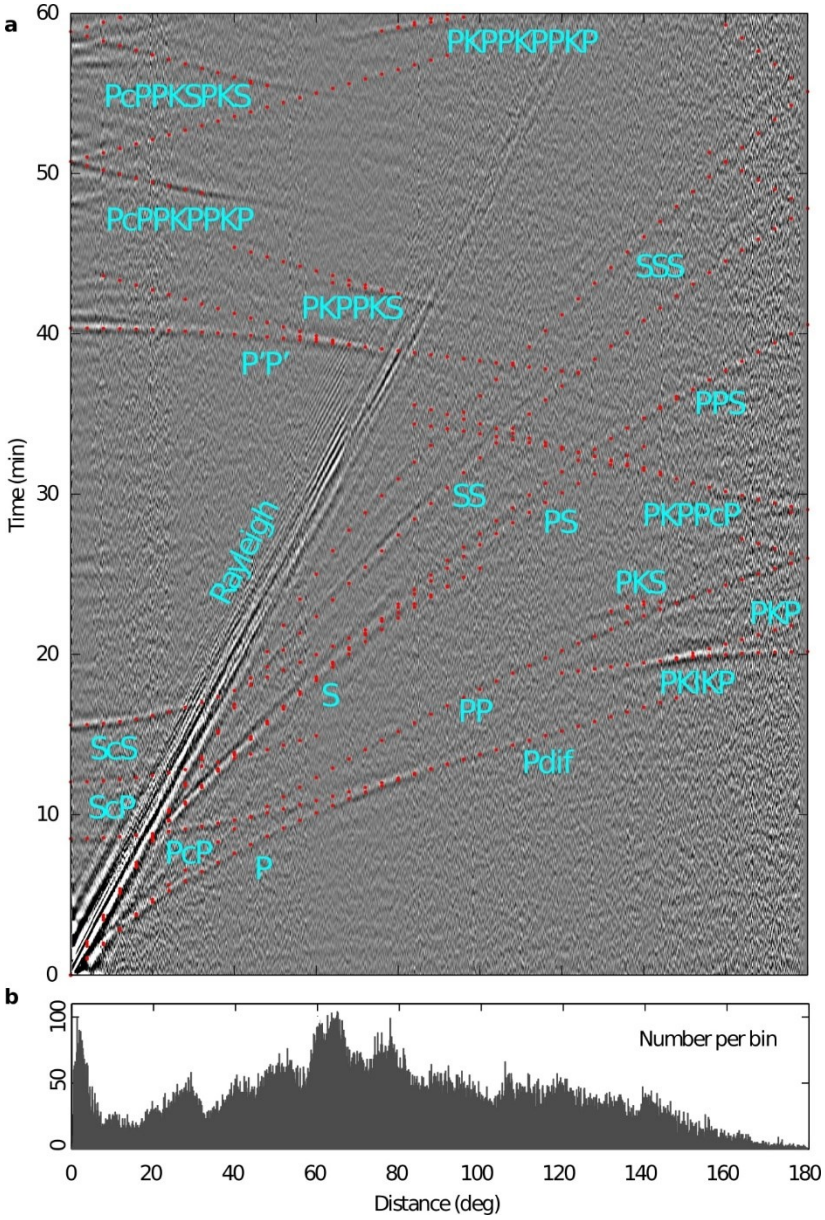

Figure 7.8. (a) Global section of virtual seismograms reconstructed from correlations of Z components of continuous seismograms, with major seismic phases labeled. (b) Number of station pairs per inter-station distance bin. Reproduced from Figure 1S of Boué et al. (2013a).

In the data processing of Boué et al. (2013a, 2014a), the coda waves from large earthquakes were retained. Therefore, the global correlation section in Figure 7.4c is a mix of ambient noise correlations and coda correlations. The global ZZ correlation section with seismic phase names labeled is shown in Figure 7.8. Besides the regular seismic phases, some spurious phases that have no correspondence in the observed earthquake seismograms can also be observed. Some spurious features can find correspondence in the synthetic global section of coda correlations [see Figure 4 of Boué et al. (2014a)]. One of the strangest feature observed from the global ZZ

correlation section is the presence of nearly vertically traveling ScS waves at short distance, even in the autocorrelations (Figure 7.8). Poli et al. (2017) interpreted the nearly vertically traveling ScS-like signal appearing in the ZZ coda correlations in terms of modal analysis (Figure 7.9) and generalized rays (Figure 7.10). The same methods were used by Kennett and Pham (2018) to discuss the global section of coda correlations created from observed and synthetic earthquake seismograms by Phạm et al. (2018).

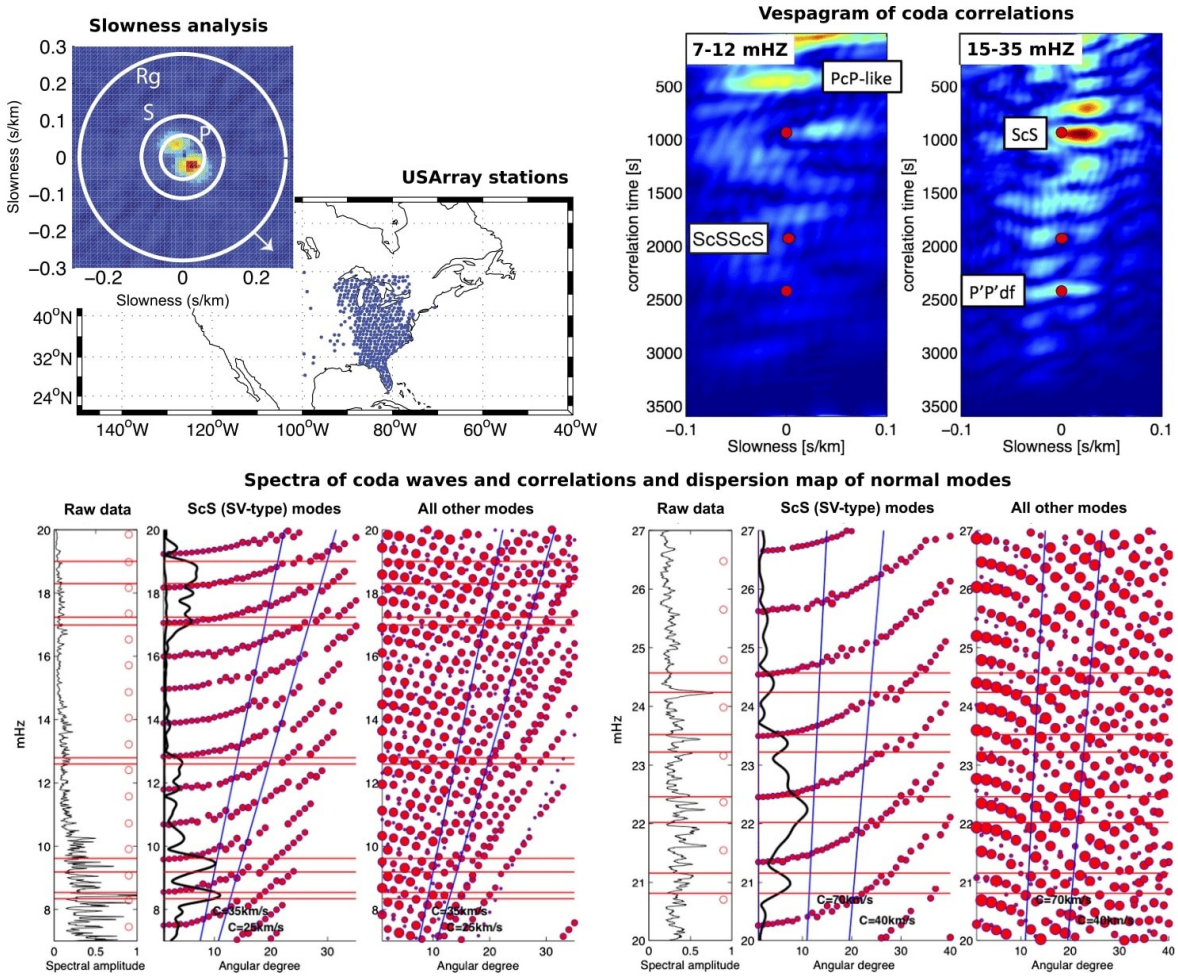

Figure 7.9. Modal interpretation for the ScS-like arrival observed from the vespagram of coda correlations, reproduced from Figures 1 and 3 to 5 of Poli et al. (2017). The vertical components of seismic recordings of the 2013 Okhotsk Sea earthquake from about 400 USArray stations were used in the computation of the coda correlations. The panels are explained by the labels and titles. See the original reference for more instructions.

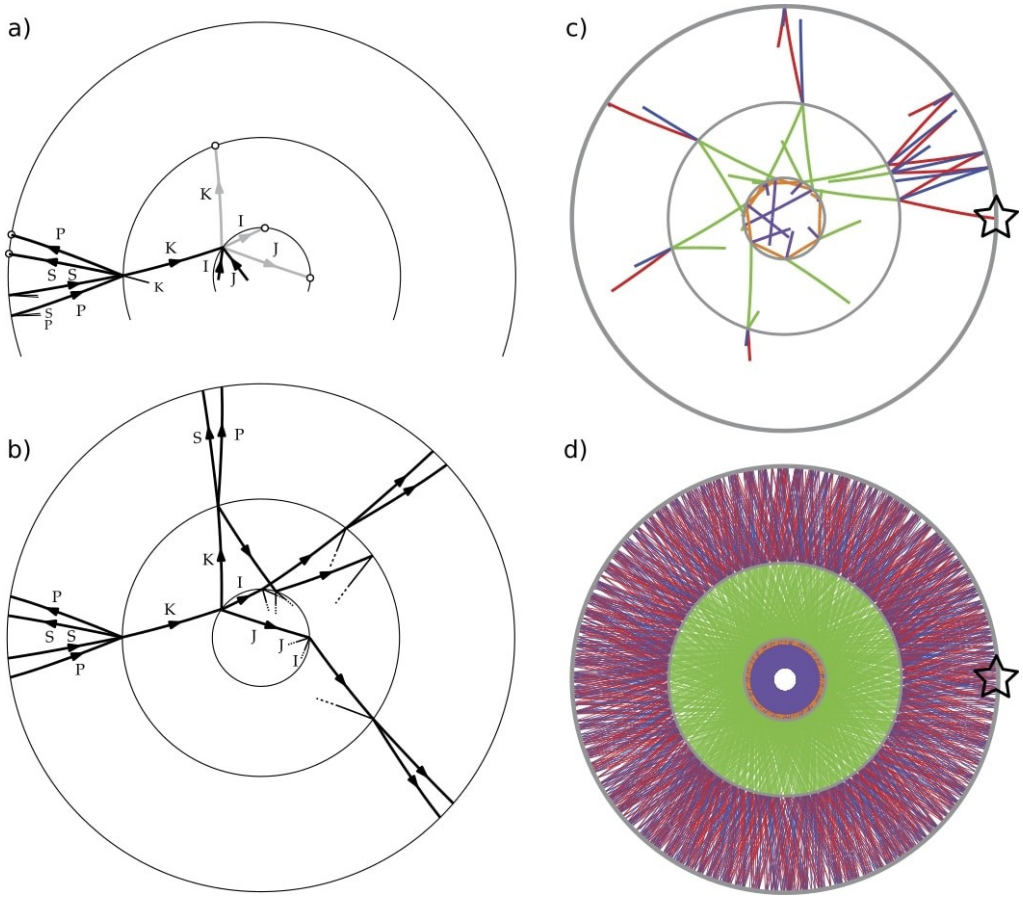

Figure 7.10. Ray representation of spherical mode $_{52}S_{13}$ (a, b) and time evolution of the associated rays (c, d). Reproduced from Figure 8 of Poli et al. (2017).

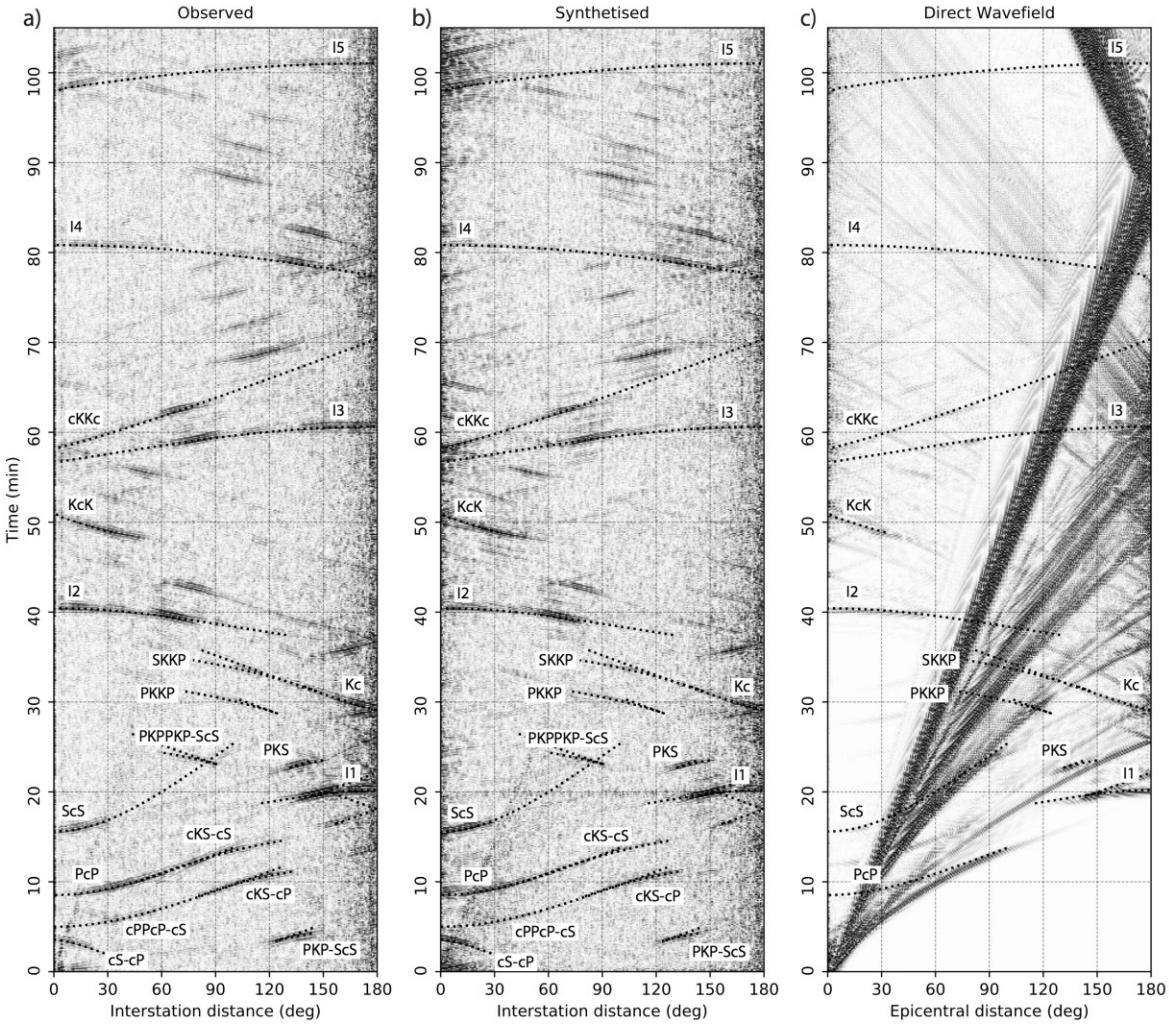

Figure 7.11. Global sections of 2-hr coda correlations created from observed (a) and synthetic (b) seismograms. All sections are filtered in the period band of 15 to 50 sec. The global section of directly modelled seismograms is plotted in (c) for comparisons. Reproduced from Figure 1 of Kennett and Pham (2018). See the reference for instructions on the conventions of labeled phase names.

References

Abbott BP, Abbott R, Abbott TD, et al (2016) Observation of Gravitational Waves from a Binary Black Hole Merger. Phys Rev Lett 116:061102. doi: 10.1103/PhysRevLett.116.061102

Aki K (1965) A note on the use of microseisms in determining the shallow structure of the Earth's crust. Geophysics 30:665–666. doi: 10.1190/1.1439640

Aki K (1957) Space and time spectra of stationary stochastic waves, with special reference to microtremors. Bull. Earthq. Res. Inst. 35:415–457.

Aki K, Richards PG (2002) Quantitative seismology, 2nd edn. University Science Books

Albert DG, Decato SN (2017) Acoustic and seismic ambient noise measurements in urban and rural areas. Appl Acoust 119:135–143. doi: 10.1016/j.apacoust.2016.12.015

Allen R (1982) Automatic phase pickers: Their present use and future prospects. Bull Seismol Soc Am 72:S225-242.

Allstadt KE, McVey BG, Malone SD (2017) Seismogenic landslides, debris flows, and outburst floods in the western United States and Canada from 1977 to 2017.

Alsop L, Sutton G, Ewing M, et al (1961) Free Oscillations of the Earth Observed on Strain and Pendulum Seismographs. J Geophys Res 66:631--641. doi: 10.1029/JZ066i002p00631

Amante C, Eakins BW (2009) ETOPO1 1 Arc-Minute Global Relief Model: Procedures, Data Sources and Analysis. NOAA Technical Memorandum NESDIS NGDC-24.

Ardhuin F (2018) Large scale forces under surface gravity waves at a wavy bottom: a mechanism for the generation of primary microseisms. Geophys Res Lett 45:8173-8181. doi: 10.1029/2018GL078855

Ardhuin F, Balanche A, Stutzmann E, Obrebski M (2012) From seismic noise to ocean wave parameters: General methods and validation. J Geophys Res 117:1–19. doi: 10.1029/2011JC007449

Ardhuin F, Chapron B, Collard F (2009) Observation of swell dissipation across oceans. Geophys Res Lett 36:L06607. doi: 10.1029/2008GL037030

Ardhuin F, Gualtieri L, Stutzmann E (2015) How ocean waves rock the Earth: Two mechanisms explain microseisms with periods 3 to 300s. Geophys Res Lett 42:765–772. doi: 10.1002/2014GL062782

Ardhuin F, Herbers THC (2013) Noise generation in the solid Earth, oceans and atmosphere, from nonlinear interacting surface gravity waves in finite depth. J Fluid Mech 716:316–348.

Ardhuin F, Rawat A, Aucan J (2014) A numerical model for free infragravity waves: Definition and validation at regional and global scales. Ocean Model 77:20–32. doi: 10.1016/j.ocemod.2014.02.006

Ardhuin F, Roland A (2012) Coastal wave reflection, directional spread, and seismoacoustic noise sources. J Geophys Res Ocean 117. doi: 10.1029/2011JC007832

Ardhuin F, Stutzmann E (2012) On the Longuet-Higgins--Hasselmann theory for double-frequency microseisms, and practical estimation of seismic noise from ocean wave model results. Technical Report.

Ardhuin F, Stutzmann E, Schimmel M, Mangeney A (2011) Ocean wave sources of seismic noise. J Geophys Res Ocean 116:1–21. doi: 10.1029/2011JC006952

Aster RC, McNamara DE, Bromirski PD (2010) Global trends in extremal microseism intensity. Geophys Res Lett 37:1–5. doi: 10.1029/2010GL043472

Aster RC, McNamara DE, Bromirski PD (2008) Multidecadal Climate-induced Variability in Microseisms. Seismol Res Lett 79:194–202. doi: 10.1785/gssrl.79.2.194

Astola J, Kuosmanen P (1997) Fundamentals of nonlinear digital filtering. CRC Press

Backus M, Burg J, Baldwin D, Bryan E (1964) Wide-band extraction of mantle P waves from ambient noise. Geophysics 29:672–692. doi: 10.1190/1.1439404

Baig AM, Campillo M, Brenguier F (2009) Denoising Seismic noise cross correlations. J Geophys Res Solid Earth 114:1–12. doi: 10.1029/2008JB006085

Baillard C, Crawford WC, Ballu V, et al (2014) An automatic kurtosis-based P-and S-phase picker designed for local seismic networks. Bull Seismol Soc Am 104:394–409. doi: 10.1785/0120120347

Bakulin A, Calvert R (2004) Virtual source: new method for imaging below complex overburden and 4D. In: 2004 SEG Annual Meeting.

Bakulin A, Calvert R (2006) The virtual source method: Theory and case study. Geophysics 71:SI139-SI150. doi: 10.1190/1.2216190

Barmin MP, Levshin AL, Yang Y, Ritzwoller MH (2011) Epicentral location based on Rayleigh wave Empirical Green's Functions from ambient seismic noise. Geophys J Int 184:869–884.

Baskir E, Weller C (1975) Sourceless Reflection Seismic Exploration. Geophysics 40:158–159.

Beckouche S, Ma J (2014) Simultaneous dictionary learning and denoising for seismic data. Geophysics 79:A27–A31. doi: 10.1190/geo2013-0382.1

Behm M, Leahy GM, Snieder R (2014) Retrieval of local surface wave velocities from traffic noise - an example from the La Barge basin (Wyoming). Geophys Prospect 62:223–243. doi: 10.1111/1365-2478.12080

Behm M, Snieder R (2013) Love waves from local traffic noise interferometry. Lead Edge 32:628–632. doi: 10.1190/tle32060628.1

Behr Y, Townend J, Bowen M, et al (2013) Source directionality of ambient seismic noise inferred from three-component beamforming. J Geophys Res Solid Earth 118:240–248. doi: 10.1029/2012JB009382

Ben-Menahem A (1995) A Concise History of Mainstream Seismology: Origins, Legacy, and Perspectives. Bull Seismol Soc Am 85:1202–1225.

Benioff H, Press F, Smith S (1961) Excitation of the free oscillations of the Earth by earthquakes. J Geophys Res 66:605. doi: 10.1029/JZ066i002p00605

Bensen GD, Ritzwoller MH, Barmin MP, et al (2007) Processing seismic ambient noise data to obtain reliable broad-band surface wave dispersion measurements. Geophys J Int 169:1239–1260.

Bensen GD, Ritzwoller MH, Shapiro NM (2008) Broadband ambient noise surface wave tomography across the United States. J Geophys Res Solid Earth 113:B05306. doi: 10.1029/2007JB005248

Berger J, Davis P, Ekström G (2004) Ambient Earth noise: A survey of the Global Seismographic Network.

J Geophys Res B Solid Earth 109:1–10. doi: 10.1029/2004JB003408

Bernard P (1941) Sur certaines propriétés de la boule étudiées à l'aide des enregistrements seismographiques. Bull Inst Ocean Monaco 800:1–19.

Bernard P (1990) Historical sketch of microseisms from past to future. Phys Earth Planet Inter 63:145–150. doi: 10.1016/0031-9201(90)90013-N

Bernard P, Martel L (1990) A possible origin of 26 s microseisms. Phys Earth Planet Inter 63:229–231. doi: 10.1016/0031-9201(90)90022-P

Bertin X, Bakker A de, Dongeren A van, et al (2018) Infragravity waves: from driving mechanisms to impacts. Earth-Science Rev 177:774–799. doi: 10.1016/j.earscirev.2018.01.002

Bettig B, Bard PY, Scherbaum F, et al (2001) Analysis of dense array noise measurements using the modified spatial auto-correlation method (SPAC): Application to the Grenoble area. Boll di Geofis Teor ed Appl 42:281–304.

Beucler É, Mocquet A, Schimmel M, et al (2015) Observation of deep water microseisms in the North Atlantic Ocean using tide modulations. Geophys Res Lett 42:316–322. doi: 10.1002/2014GL062347

Bogiatzis P, Ishii M (2016) DigitSeis: A New Digitization Software for Analog Seismograms. Seismol Res Lett 87:726–736. doi: 10.1785/0220150246

Bokelmann GHR, Baisch S (1999) Nature of narrow-band signals at 2.083 Hz. Bull Seismol Soc Am 89:156–164.

Bonnefoy-Claudet S, Cotton F, Bard PY (2006) The nature of noise wavefield and its applications for site effects studies. A literature review. Earth-Science Rev 79:205–227.

Bormann P (1998) Conversion and comparability of data presentations on seismic background noise. J Seismol 2:37–45. doi: 10.1023/A:1009780205669

Bormann P, Wielandt E (2013) Seismic signals and noise. In: Bormann P (ed) New Manual of Seismological Observatory Practice 2 (NMSOP2), 2nd edn. GFZ, Potsdam, pp 1–62

Boschi L, Weemstra C (2015) Stationary-phase integrals in the cross correlation of ambient noise. Rev Geophys 53:411–451. doi: 10.1002/2014RG000455

Boué P, Denolle M, Hirata N, et al (2016) Beyond basin resonance: characterizing wave propagation using a dense array and the ambient seismic field. Geophys J Int 206:1261–1272. doi: 10.1093/gji/ggw205

Boué P, Poli P, Campillo M, et al (2013a) Teleseismic correlations of ambient seismic noise for deep global imaging of the Earth. Geophys J Int 194:844–848. doi: 10.1093/gji/ggt160

Boué P, Poli P, Campillo M, Roux P (2014a) Reverberations, coda waves and ambient noise: Correlations at the global scale and retrieval of the deep phases. Earth Planet Sci Lett 391:137–145.

Boué P, Roux P, Campillo M, Briand X (2014b) Phase velocity tomography of surface waves using ambient noise cross correlation and array processing. J Geophys Res Solid Earth 119:519–529.

Boué P, Roux P, Campillo M, de Cacqueray B (2013b) Double beamforming processing in a seismic prospecting context. Geophysics 78:V101–V108. doi: 10.1190/geo2012-0364.1

Bowden DC, Tsai VC, Lin FC (2015) Site amplification, attenuation, and scattering from noise correlation amplitudes across a dense array in Long Beach, CA. Geophys Res Lett 42:1360–1367.

Bowden DC, Tsai VC, Lin FC (2017) Amplification and attenuation across USArray using ambient noise wavefront tracking. J Geophys Res Solid Earth 122:10,086-10,101. doi: 10.1002/2017JB014804

Brenguier F, Campillo M, Hadziioannou C, et al (2008a) Postseismic relaxation along the san andreas fault at Parkfield from continuous seismological observations. Science 321:1478–1481.

Brenguier F, Clarke D, Aoki Y, et al (2011) Monitoring volcanoes using seismic noise correlations. Comptes Rendus - Geosci 343:633–638. doi: 10.1016/j.crte.2010.12.010

Brenguier F, Kowalski P, Ackerley N, et al (2016) Toward 4D Noise-Based Seismic Probing of Volcanoes: Perspectives from a Large-N Experiment on Piton de la Fournaise Volcano. Seismol Res Lett 87:15–25. doi: 10.1785/0220150173

Brenguier F, Shapiro NM, Campillo M, et al (2007) 3-D surface wave tomography of the Piton de la Fournaise volcano using seismic noise correlations. Geophys Res Lett 34:L02305.

Brenguier F, Shapiro NM, Campillo M, et al (2008b) Towards forecasting volcanic eruptions using seismic noise. Nat Geosci 1:126–130. doi: 10.1038/ngeo104

Bromirski PD (2002) The near-coastal microseism spectrum: Spatial and temporal wave climate relationships. J Geophys Res 107:1–20. doi: 10.1029/2001JB000265

Bromirski PD (2001) Vibrations from the “Perfect Storm”. Geochemistry, Geophysics, Geosystems 2: 2000GC000119. doi: 10.1029/2000GC000119

Bromirski PD, Duennebier FK, Stephen RA (2005) Mid-ocean microseisms. Geochemistry, Geophysics, Geosystems 6:1–19. doi: 10.1029/2004GC000768

Bromirski PD, Flick RE, Graham N (1999) Ocean wave height determined from inland seismometer data: Implications for investigating wave climate changes in the NE Pacific. J Geophys Res 104:20753–20766. doi: 10.1029/1999JC900156

Bromirski PD, Gerstoft P (2009) Dominant source regions of the Earth’s “hum” are coastal. Geophys Res Lett 36:L13303. doi: 10.1029/2009GL038903

Bromirski PD, Stephen RA, Gerstoft P (2013) Are deep-ocean-generated surface-wave microseisms observed on land? J Geophys Res Solid Earth 118:3610–3629. doi: 10.1002/jgrb.50268

Brune JN, Oliver J (1959) The seismic noise of the earth’s surface. Bull Seismol Soc Am 49:349–353.

Brzak K, Gu YJ, Ökeler A, et al (2009) Migration imaging and forward modeling of microseismic noise sources near southern Italy. Geochemistry, Geophysics, Geosystems 10:Q01012.

Burtin A, Hovius N, Turowski JM (2016) Seismic monitoring of torrential and fluvial processes. Earth Surf Dyn 4:285–307. doi: 10.5194/esurf-4-285-2016

Campillo M (2006) Phase and correlation in “random” seismic fields and the reconstruction of the green function. Pure Appl Geophys 163:475–502. doi: 10.1007/s00024-005-0032-8

Campillo M, Paul A (2003) Long-Range Correlations in the Diffuse Seismic Coda. Science 299:547–549. doi: 10.1126/science.1078551

Campillo M, Roux P (2015) Crust and Lithospheric Structure - Seismic Imaging and Monitoring with Ambient Noise Correlations. In: Treatise on Geophysics. pp 391–417

Capon J (1969) High-resolution frequency-wavenumber spectrum analysis. Proc IEEE 57:1408–1418. doi:

10.1109/PROC.1969.7278

Cara F, Di Giulio G, Milana G, et al (2010) On the stability and reproducibility of the horizontal-to-vertical spectral ratios on ambient noise: Case study of Cavola, Northern Italy. Bull Seismol Soc Am 100:1263–1275. doi: 10.1785/0120090086

Carter JA, Barstow N, Pomeroy PW, et al (1991) High-frequency seismic noise as a function of depth. Bull Seism Soc Am 81:1101–1114.

Cessaro RK (1994) Sources of Primary and Secondary Microseisms. Bull Seismol Soc Am 84:142–148.

Chaput J, Campillo M, Aster RC, et al (2015) Multiple scattering from icequakes at Erebus volcano, Antarctica: Implications for imaging at glaciated volcanoes. J Geophys Res B Solid Earth 120:1129–1141. doi: 10.1002/2014JB011278

Chaput J, Clerc V, Campillo M, et al (2016) On the practical convergence of coda-based correlations: A window optimization approach. Geophys J Int 204:736–747. doi: 10.1093/gji/ggv476

Chaves EJ, Schwartz SY (2016) Monitoring transient changes within overpressured regions of subduction zones using ambient seismic noise. Sci Adv. doi: 10.1126/sciadv.1501289

Chen JH, Froment B, Liu QY, Campillo M (2010) Distribution of seismic wave speed changes associated with the 12 May 2008 Mw 7.9 Wenchuan earthquake. Geophys Res Lett 37:L18302.

Chen L-W, Chen Y-N, Gung Y, et al (2017) Strong near-surface seismic anisotropy of Taiwan revealed by coda interferometry. Earth Planet Sci Lett 475:224–230. doi: 10.1016/J.EPSL.2017.07.016

Chen T, Wu HR (2001) Adaptive impulse detection using center-weighted median filters. IEEE Signal Process Lett 8:1–3. doi: 10.1109/97.889633

Chen X, Tian D, Wen L (2015) Microseismic sources during Hurricane Sandy. J Geophys Res Solid Earth 120:6386–6403. doi: 10.1002/2015JB012282

Chen Y (2018) Automatic microseismic event picking via unsupervised machine learning. Geophys J Int 212:88–102. doi: 10.1093/gji/ggx420

Chen Z, Gerstoft P, Bromirski PD (2016) Microseism source direction from noise cross-correlation. Geophys J Int 205:810–818. doi: 10.1093/gji/ggw055

Claerbout JF (1968) Synthesis of a Layered Medium From Its Acoustic Transmission Response. Geophysics 33:264–269. doi: 10.1190/1.1439927

Clarke D, Zaccarelli L, Shapiro NM, Brenguier F (2011) Assessment of resolution and accuracy of the Moving Window Cross Spectral technique for monitoring crustal temporal variations using ambient seismic noise. Geophys J Int 186:867–882. doi: 10.1111/j.1365-246X.2011.05074.x

Colombi A, Boschi L, Roux P, Campillo M (2014a) Green's function retrieval through cross-correlations in a two-dimensional complex reverberating medium. J Acoust Soc Am 135:1034–1043.

Colombi A, Chaput J, Brenguier F, et al (2014b) On the temporal stability of the coda of ambient noise correlations. Comptes Rendus - Geosci 346:307–316. doi: 10.1016/j.crte.2014.10.002

Cooper RI., Longuet-Higgins MS (1951) An experimental study of the pressure variations in standing water waves. Proc R Soc London, A 206:424–435. doi: 10.1098/rspa.1951.0079

Cornou C, Guéguen P, Bard PY, Haghshenas E (2004) Ambient noise energy bursts observation and

modeling: Trapping of harmonic structure-soil induced-waves in a topmost sedimentary layer. J Seismol 8:507–524. doi: 10.1007/s10950-004-1980-7

Coughlin M, Harms J (2014a) Constraining the gravitational wave energy density of the Universe using Earth's ring. Phys Rev D 90:042005. doi: 10.1103/PhysRevD.90.042005

Coughlin M, Harms J (2014b) Upper limit on a stochastic background of gravitational waves from seismic measurements in the range 0.05-1 Hz. Phys Rev Lett 112:101102.

Coughlin M, Harms J (2014c) Constraining the gravitational-wave energy density of the Universe in the range 0.1 Hz to 1 Hz using the Apollo Seismic Array. Phys Rev D 90:102001.

Cox H (1973) Spatial correlation in arbitrary noise fields with application to ambient sea noise. J Acoust Soc Am 54:1289–1301. doi: 10.1121/1.1914426

Crotwell HP, Owens TJ, Ritsema J (1999) The TauP Toolkit: Flexible Seismic Travel-time and Ray-path Utilities. Seismol Res Lett 70:154–160. doi: 10.1785/gssrl.70.2.154

Cupillard P, Capdeville Y (2010) On the amplitude of surface waves obtained by noise correlation and the capability to recover the attenuation: A numerical approach. Geophys J Int 181:1687–1700.

Cupillard P, Stehly L, Romanowicz B (2011) The one-bit noise correlation: A theory based on the concepts of coherent and incoherent noise. Geophys J Int 184:1397–1414.

Curtis A, Gerstoft P, Sato H, et al (2006) Seismic interferometry—turning noise into signal. Lead Edge 25:1082–1092. doi: 10.1190/1.2349814

Curtis A, Halliday D (2010) Directional balancing for seismic and general wavefield interferometry. Geophysics 75:SA1. doi: 10.1190/1.3298736

Daneshvar MR, Clay CS, Savage MK (1995) Passive Seismic imaging using microearthquakes. Geophysics 60:1178–1186. doi: 10.1190/1.1443846

Davies D, Kelly EJ, Filson JR (1971) Vespa Process for Analysis of Seismic Signals. Nat Phys Sci 232:8–13. doi: 10.1038/physci232008a0

Davy C, Barruol G, Fontaine FR, et al (2014) Tracking major storms from microseismic and hydroacoustic observations on the seafloor. Geophys Res Lett. doi: 10.1002/2014GL062319

Davy C, Stutzmann E, Barruol G, et al (2015) Sources of secondary microseisms in the Indian Ocean. Geophys J Int. doi: 10.1093/gji/ggv221

De Plaen RSM, Lecocq T, Caudron C, et al (2016) Single-station monitoring of volcanoes using seismic ambient noise. Geophys Res Lett 43:8511–8518. doi: 10.1002/2016GL070078

de Verdiere YC (2006) Mathematical models for passive imaging I: General background. ArXiv ID: math-ph/0610043

Deen M, Wielandt E, Stutzmann E, et al (2017) First Observation of the Earth's Permanent Free Oscillations on Ocean Bottom Seismometers. Geophys Res Lett 44:10,988-10,996. doi: 10.1002/2017GL074892

Denolle MA, Boué P, Hirata N, Beroza GC (2018) Strong Shaking Predicted in Tokyo From an Expected M7+ Itoigawa-Shizuoka Earthquake. J Geophys Res Solid Earth. doi: 10.1029/2017JB015184

Denolle MA, Dunham EM, Prieto GA, Beroza GC (2014) Strong ground motion prediction using virtual earthquakes. Science 343:399–403. doi: 10.1126/science.1245678

Denolle MA, Dunham EM, Prieto GA, Beroza GC (2013) Ground motion prediction of realistic earthquake sources using the ambient seismic field. J Geophys Res 118:2102–2118. doi: 10.1029/2012JB009603

Derode A, Larose E, Campillo M, Fink M (2003a) How to estimate the Green's function of a heterogeneous medium between two passive sensors? Application to acoustic waves. Appl Phys Lett 83:3054–3056. doi: 10.1063/1.1617373

Derode A, Larose E, Tanter M, et al (2003b) Recovering the Green's function from field-field correlations in an open scattering medium (L). J Acoust Soc Am 113:2973. doi: 10.1121/1.1570436

Dewey J, Byerly P (1969) The early history of Seismometry (to 1900). Bull Seismol Soc Am 59:183–227.

Díaz J (2016) On the origin of the signals observed across the seismic spectrum. Earth-Science Rev 161:224–232. doi: 10.1016/j.earscirev.2016.07.006

Douma H, Snieder R (2006) Correcting for bias due to noise in coda wave interferometry. Geophys J Int 164:99–108. doi: 10.1111/j.1365-246X.2005.02807.x

Douze E (1967) Short-period seismic noise. Bull Seismol Soc Am 57:55.

Draganov D, Campman X, Thorbecke J, et al (2009) Reflection images from ambient seismic noise. Geophysics 74:A63–A67. doi: 10.1190/1.3193529

Draganov D, Wapenaar K, Mulder W, et al (2007) Retrieval of reflections from seismic background-noise measurements. Geophys Res Lett 34:0–3. doi: 10.1029/2006GL028735

Draganov D, Wapenaar K, Thorbecke J (2006) Seismic interferometry: Reconstructing the earth's reflection response. Geophysics 71:SI61-SI70. doi: 10.1190/1.2209947

Duputel Z, Ferrazzini V, Brenguier F, et al (2009) Real time monitoring of relative velocity changes using ambient seismic noise at the Piton de la Fournaise volcano (La Réunion) from January 2006 to June 2007. J Volcanol Geotherm Res 184:164–173. doi: 10.1016/j.jvolgeores.2008.11.024

Durand S, Montagner JP, Roux P, et al (2011) Passive monitoring of anisotropy change associated with the Parkfield 2004 earthquake. Geophys Res Lett 38. doi: 10.1029/2011GL047875

Duvall TL, Jefferies SM, Harvey JW, Pomerantz MA (1993) Time-distance helioseismology. Nature 362:430–432. doi: 10.1038/362430a0

Dylan Mikesell T, van Wijk K, Blum TE, et al (2012) Analyzing the coda from correlating scattered surface waves. J Acoust Soc Am 131:EL275-EL281. doi: 10.1121/1.3687427

Dyson FJ (1969) Seismic Response of the Earth to a Gravitational Wave in the 1-Hz Band. Astrophys J 156:529–540. doi: 10.1086/149986

Dziewonski A, Landisman M (1970) Great Circle Rayleigh and Love Wave Dispersion from 100 to 900 Seconds. Geophys J Int 19:37–91. doi: 10.1111/j.1365-246X.1970.tb06739.x

Dziewonski AM, Anderson DL (1981) Preliminary reference Earth model. Phys Earth Planet Inter 25:297–356. doi: 10.1016/0031-9201(81)90046-7

Ebeling CW (2012) Inferring Ocean Storm Characteristics from Ambient Seismic Noise. In: Dmowska R (ed) Advances in Geophysics. Elsevier, pp 1–33

Ebeling CW, Stein S (2011) Seismological identification and characterization of a large hurricane. Bull Seismol Soc Am 101:399–403. doi: 10.1785/0120100175

Eibl EPS, Lokmer I, Bean CJ, Akerlie E (2017) Helicopter location and tracking using seismometer recordings. Geophys J Int 209:901–908. doi: 10.1093/gji/ggx048

Ekström G (2017) Short-period surface-wave phase velocities across the conterminous United States. Phys Earth Planet Inter 270:168–175. doi: 10.1016/j.pepi.2017.07.010

Ekström G (2001) Time domain analysis of Earth's long-period background seismic radiation. J Geophys Res Solid Earth 106:26483–26493. doi: 10.1029/2000JB000086

Ekström G, Abers GA, Webb SC (2009) Determination of surface-wave phase velocities across USArray from noise and Aki's spectral formulation. Geophys Res Lett 36:L18301. doi: 10.1029/2009GL039131

Eric L, Stephen H (2009) Monitoring stress related velocity variation in concrete with a 2x10(-5) relative resolution using diffuse ultrasound. J Acoust Soc Am 125:1853–1856. doi: 10.1121/1.3079771

Ermert L, Sager K, Afanasiev M, et al (2017) Ambient Seismic Source Inversion in a Heterogeneous Earth: Theory and Application to the Earth's Hum. J Geophys Res Solid Earth 122:9184–9207. doi: 10.1002/2017JB014738

Ermert L, Villaseñor A, Fichtner A (2016) Cross-correlation imaging of ambient noise sources. Geophys J Int 204:347–364. doi: 10.1093/gji/ggv460

Essen H-H, Krüger F, Dahm T, Grevemeyer I (2003) On the generation of secondary microseisms observed in northern and central Europe. J Geophys Res 108:2506–2520. doi: 10.1029/2002JB002338

Euler GGG, Wiens DDA, Nyblade AA (2014) Evidence for bathymetric control on the distribution of body wave microseism sources from temporary seismic arrays in Africa. Geophys J Int 197:1869–1883. doi: 10.1093/gji/ggu105

Evangelidis CP, Melis NS (2012) Ambient noise levels in greece as recorded at the hellenic unified seismic network. Bull Seismol Soc Am 102:2507–2517. doi: 10.1785/0120110319

Farra V, Stutzmann E, Gualtieri L, et al (2016) Ray-theoretical modeling of secondary microseism P waves. Geophys J Int 206:1730–1739. doi: 10.1093/gji/ggw242

Feng J, Yao H, Poli P, et al (2017) Depth variations of 410 km and 660 km discontinuities in eastern North China Craton revealed by ambient noise interferometry. Geophys Res Lett 44:8328–8335.

Ferretti G, Zunino A, Scafidi D, et al (2013) On microseisms recorded near the Ligurian coast (Italy) and their relationship with sea wave height. Geophys J Int 194:524–533. doi: 10.1093/gji/ggt114

Fichtner A (2014) Source and processing effects on noise correlations. Geophys. J. Int. 197:1527–1531.

Fichtner A (2015) Source-structure trade-offs in ambient noise correlations. Geophys J Int 202:678–694. doi: 10.1093/gji/ggv182

Fichtner A, Stehly L, Ermert L, Boehm C (2017) Generalized interferometry - I: Theory for interstation correlations. Geophys J Int 208:603–638. doi: 10.1093/gji/ggw420

Fix JE (1972) Ambient earth motion in the period range from 0.1 to 2560 sec. Bull Seismol Soc Am 62:1753–1760.

Florido E, Asencio-Cortés G, Aznarte JL, et al (2018) A novel tree-based algorithm to discover seismic patterns in earthquake catalogs. Comput Geosci 115:96–104. doi: 10.1016/j.cageo.2018.03.005

Friedrich A, Krüger F, Klinge K (1998) Ocean-generated microseismic noise located with the Gräfenberg

array. J Seismol 2:47–64. doi: 10.1023/A:1009788904007

Froment B, Campillo M, Chen JHH, Liu QYY (2013) Deformation at depth associated with the 12 May 2008 MW 7.9 Wenchuan earthquake from seismic ambient noise monitoring. Geophys Res Lett 40:78–82. doi: 10.1029/2012GL053995

Froment B, Campillo M, Roux P, et al (2010) Estimation of the effect of nonisotropically distributed energy on the apparent arrival time in correlations. Geophysics 75:SA85-SA93. doi: 10.1190/1.3483102

Froment B, Campillo M, Roux P (2011) Reconstructing the Green's function through iteration of correlations. Comptes Rendus - Geosci 343:623–632. doi: 10.1016/j.crte.2011.03.001

Fukao Y, Nishida K, Suda N, et al (2002) A theory of the Earth's background free oscillations. J Geophys Res Solid Earth 107:ESE 11-1-ESE 11-10. doi: 10.1029/2001JB000153

Gal M, Reading AM, Ellingsen SP, et al (2014) Improved implementation of the fk and Capon methods for array analysis of seismic noise. Geophys J Int 198:1045–1054. doi: 10.1093/gji/ggu183

Gallot T, Catheline S, Roux P, Campillo M (2012) A passive inverse filter for Green's function retrieval. J Acoust Soc Am 131:EL21-EL27. doi: 10.1121/1.3665397

García-Jerez A, Piña-Flores J, Sánchez-Sesma FJ, et al (2016) A computer code for forward calculation and inversion of the H/V spectral ratio under the diffuse field assumption. Comput Geosci 97:67–78. doi: 10.1016/j.cageo.2016.06.016

Garnier J, Papanicolaou G (2009) Passive Sensor Imaging Using Cross Correlations of Noisy Signals in a Scattering Medium. SIAM J Imaging Sci 2:396–437. doi: doi:10.1137/080723454

Garrison T (2008) Essentials of oceanography, 5th edn. Brooks/Cole

Gentili S, Michelini A (2006) Automatic picking of P and S phases using a neural tree. J Seismol 10:39–63. doi: 10.1007/s10950-006-2296-6

Gerstoft P, Bromirski PD (2016) "Weather bomb" induced seismic signals. Science 353:869–870. doi: 10.1126/science.aag1616

Gerstoft P, Fehler MC, Sabra KG (2006a) When Katrina hit California. Geophys Res Lett 33:L17308. doi: 10.1029/2006GL027270

Gerstoft P, Sabra KG, Roux P, et al (2006b) Green's functions extraction and surface-wave tomography from microseisms in southern California. Geophysics 71:SI23. doi: 10.1190/1.2210607

Gerstoft P, Shearer PM, Harmon N, Zhang J (2008) Global P, PP, and PKP wave microseisms observed from distant storms. Geophys Res Lett 35:4–9. doi: 10.1029/2008GL036111

Gerstoft P, Tanimoto T (2007) A year of microseisms in southern California. Geophys Res Lett 34:2–7. doi: 10.1029/2007GL031091

Godin OA (2007) Emergence of the acoustic Green's function from thermal noise. J Acoust Soc Am 121:EL96-EL102. doi: 10.1121/1.2430764

Godin OA (2006) Recovering the acoustic green's function from ambient noise cross correlation in an inhomogeneous moving medium. Phys Rev Lett 97:054301. doi: 10.1103/PhysRevLett.97.054301

Godin OA (2009) Emergence of deterministic Green's functions from noise generated by finite random sources. Phys Rev E 80:066605. doi: 10.1103/PhysRevE.80.066605

Gorbatov A, Saygin E, Kennett B (2013) Crustal properties from seismic station autocorrelograms. Geophys J Int 192:861–870. doi: 10.1093/gji/ggs064

Gouédard P, Cornou C, Roux P (2008a) Phase-velocity dispersion curves and small-scale geophysics using noise correlation slantstack technique. Geophys J Int 172:971–981.

Gouédard P, Roux P, Campillo M, Verdel A (2008b) Convergence of the two-point correlation function toward the Green's function in the context of a seismic-prospecting data set. Geophysics 73:V47–V53. doi: 10.1190/1.2985822

Gouédard P, Stehly L, Brenguier F, et al (2008c) Cross-correlation of random fields: Mathematical approach and applications. In: Geophysical Prospecting. Blackwell Publishing Ltd, pp 375–393

Green DN, Bastow ID, Dashwood B, Nippress SEJ (2017) Characterizing Broadband Seismic Noise in Central London. Seismol Res Lett 88:113–124. doi: 10.1785/0220160128

Grêt A, Snieder R, Aster RC, Kyle PR (2005) Monitoring rapid temporal change in a volcano with coda wave interferometry. Geophys Res Lett 32:1–4. doi: 10.1029/2004GL021143

Grevemeyer I, Herber R, Essen H-H (2000) Microseismological evidence for a changing wave climate in the northeast Atlantic Ocean. Nature 408:349–352. doi: 10.1038/35042558

Groos JC, Bussat S, Ritter JRR (2012) Performance of different processing schemes in seismic noise cross-correlations. Geophys J Int 188:498–512. doi: 10.1111/j.1365-246X.2011.05288.x

Groos JC, Ritter JRR (2009) Time domain classification and quantification of seismic noise in an urban environment. Geophys J Int 179:1213–1231. doi: 10.1111/j.1365-246X.2009.04343.x

Gu YJ, Dublanko C, Lerner-Lam A, et al (2007) Probing the sources of ambient seismic noise near the coasts of southern Italy. Geophys Res Lett 34:L22315. doi: 10.1029/2007GL031967

Gu YJ, Sacchi M (2009) Radon transform methods and their applications in mapping mantle reflectivity structure. Surv Geophys 30:327–354. doi: 10.1007/s10712-009-9076-0

Gualtieri L, Stutzmann E, Capdeville Y, et al (2015) On the shaping factors of the secondary microseismic wavefield. J Geophys Res B Solid Earth 120:6241–6262. doi: 10.1002/2015JB012157

Gualtieri L, Stutzmann E, Capdeville Y, et al (2013) Modelling secondary microseismic noise by normal mode summation. Geophys J Int 193:1732–1745. doi: 10.1093/gji/ggt090

Gualtieri L, Stutzmann E, Farra V, et al (2014) Modelling the ocean site effect on seismic noise body waves. Geophys J Int 197:1096–1106. doi: 10.1093/gji/ggu042

Guéguen P, Langlais M, Garambois S, et al (2017) How sensitive are site effects and building response to extreme cold temperature? The case of the Grenoble's (France) City Hall building. Bull Earthq Eng 15:889–906. doi: 10.1007/s10518-016-9995-3

Gusev A V., Kravchuk VK, Rudenko VN (1990) Arguments in favour of a program of seismic detection of gravity wave bursts. Nuovo Cim C 13:847–854. doi: 10.1007/BF02512001

Gutenberg B (1947) Microseisms and Weather Forecasting. J Meteorol 4:21–28.

Gutenberg B (1958) Microseisms. In: Advances in Geophysics. pp 53–92

Hadziioannou C, Larose E, Baig A, et al (2011) Improving temporal resolution in ambient noise monitoring of seismic wave speed. J Geophys Res Solid Earth 116:B07304. doi: 10.1029/2011JB008200

Hadziioannou C, Larose E, Coutant O, et al (2009) Stability of monitoring weak changes in multiply scattering media with ambient noise correlation: laboratory experiments. J Acoust Soc Am 125:3688–3695. doi: 10.1121/1.3125345

Haendel A, Ohrnberger M, Krüger F (2016) Extracting near-surface QL between 1–4 Hz from higher-order noise correlations in the Euroseistest area, Greece. Geophys J Int 207:655–666.

Halliday D, Curtis A (2008) Seismic interferometry, surface waves and source distribution. Geophys J Int 175:1067–1087. doi: 10.1111/j.1365-246X.2008.03918.x

Hanasoge SM (2013) Measurements and kernels for source-structure inversions in noise tomography. Geophys J Int 196:971–985. doi: 10.1093/gji/ggt411

Hanasoge SM, Branicki M (2013) Interpreting cross-correlations of one-bit filtered seismic noise. Geophys J Int 195:1811–1830. doi: 10.1093/gji/ggt337

Haned A, Stutzmann E, Schimmel M, et al (2016) Global tomography using seismic hum. Geophys J Int 204:1222–1236. doi: 10.1093/gji/ggv516

Harmon N, Gerstoft P, Rychert CA, et al (2008) Phase velocities from seismic noise using beamforming and cross correlation in Costa Rica and Nicaragua. Geophys Res Lett 35:L19303.

Harrison EP (1924) Microseisms and Storm Forecasts. Nature 114:645–645. doi: 10.1038/114645b0

Hasselmann K (1963) A statistical analysis of the generation of microseisms. Rev Geophys 1:177–210. doi: 10.1029/RG001i002p00177

Hasselmann K (1966) Feynman diagrams and interaction rules of wave-wave scattering processes. Rev. Geophys. 4:1–32.

Haubrich RA (1965) Earth noise, 5 to 500 millicycles per second: 1. Spectral stationarity, normality, and nonlinearity. J Geophys Res 70:1415–1427. doi: 10.1029/JZ070i006p01415

Haubrich RA, McCamy K (1969) Microseisms: Coastal and pelagic sources. Rev Geophys 7:539–571. doi: 10.1029/RG007i003p00539

Haubrich RA, Munk WH, Snodgrass FE (1963) Comparative spectra of microseisms and swell. Bull Seismol Soc Am 53:27–37.

Hejazi Nooghabi A, Boschi L, Roux P, de Rosny J (2017) Coda reconstruction from cross-correlation of a diffuse field on thin elastic plates. Phys Rev E 96:032137. doi: 10.1103/PhysRevE.96.032137

Hillers G, Ben-Zion Y (2011) Seasonal variations of observed noise amplitudes at 2-18 Hz in southern California. Geophys J Int 184:860–868. doi: 10.1111/j.1365-246X.2010.04886.x

Hillers G, Ben-Zion Y, Campillo M, Zigone D (2015a) Seasonal variations of seismic velocities in the San Jacinto fault area observed with ambient seismic noise. Geophys J Int 202:920–932.

Hillers G, Campillo M, Ma KF (2014) Seismic velocity variations at TCDP are controlled by MJO driven precipitation pattern and high fluid discharge properties. Earth Planet Sci Lett 391:121–127. doi: 10.1016/j.epsl.2014.01.040

Hillers G, Graham N, Campillo M, et al (2012) Global oceanic microseism sources as seen by seismic arrays and predicted by wave action models. Geochemistry, Geophysics, Geosystems 13: Q01021. doi: 10.1029/2011GC003875

Hillers G, Retailleau L, Campillo M, et al (2015b) In situ observations of velocity changes in response to tidal deformation from analysis of the high-frequency ambient wavefield. J Geophys Res B Solid Earth 120:210–225. doi: 10.1002/2014JB011318

Hobiger M, Wegler U, Shiomi K, Nakahara H (2016) Coseismic and post-seismic velocity changes detected by Passive Image Interferometry: comparison of one great and five strong earthquakes in Japan. Geophys J Int 205:1053–1073. doi: 10.1093/gji/ggw066

Holcomb LG (1998) Spectral structure in the earth's microseismic background between 20 and 40 seconds. Bull Seismol Soc Am 88:744–757.

Holcomb LG (1980) Microseisms: A twenty-six-second spectral line in long-period earth motion. Bull Seismol Soc Am 70:1055–1070.

Hsu L, Finnegan NJ, Brodsky EE (2011) A seismic signature of river bedload transport during storm events. Geophys Res Lett 38. doi: 10.1029/2011GL047759

Hu W, Pryor SC, Letson F, et al (2017) Investigation of gust-seismic relationships and applications to gust detection. J Geophys Res Atmos 122:140–151. doi: 10.1002/2016JD025858

Huang H, Yao H, Van Der Hilst RD (2010) Radial anisotropy in the crust of SE Tibet and SW China from ambient noise interferometry. Geophys Res Lett 37. doi: 10.1029/2010GL044981

Huang HH, Lin FC, Tsai VC, Koper KD (2015) High-resolution probing of inner core structure with seismic interferometry. Geophys Res Lett 42:10622–10630. doi: 10.1002/2015GL066390

Hutt CR, Ringler AT, Gee LS (2017) Broadband seismic noise attenuation versus depth at the albuquerque seismological laboratory. Bull Seismol Soc Am 107:1402–1412. doi: 10.1785/0120160187

Hwang H, Haddad RA (1995) Adaptive Median Filters: New Algorithms and Results. IEEE Trans Image Process 4:499–502. doi: 10.1109/83.370679

Ishii M, Ishii H, Bernier B, Bulat E (2015) Efforts to Recover and Digitize Analog Seismograms from Harvard-Adam Dziewo ski Observatory. Seismol Res Lett 86:255–261. doi: 10.1785/0220140165

Ito Y, Shiomi K (2012) Seismic scatterers within subducting slab revealed from ambient noise autocorrelation. Geophys Res Lett 39:12–17. doi: 10.1029/2012GL053321

Ito Y, Shiomi K, Nakajima J, Hino R (2012) Autocorrelation analysis of ambient noise in northeastern Japan subduction zone. Tectonophysics 572–573:38–46. doi: 10.1016/j.tecto.2011.09.019

Jacques AA, Horel JD, Crosman ET, et al (2017) Tracking Mesoscale Pressure Perturbations Using the USArray Transportable Array. Mon Weather Rev 145:3119–3142. doi: 10.1175/MWR-D-16-0450.1

Jurkevics A (1988) Polarization Analysis of Three-Component Array Data. Bull Seismol Soc Am 78:1725–1743.

Kedar S, Longuet-Higgins M, Webb F, et al (2008) The origin of deep ocean microseisms in the North Atlantic Ocean. Proc R Soc A Math Phys Eng Sci 464:777–793. doi: 10.1098/rspa.2007.0277

Kennett B, Engdahl ER (1991) Traveltimes for global earthquake location and phase identification. Geophys J Int 105:429–465. doi: 10.1111/j.1365-246X.1991.tb06724.x

Kennett B, Saygin E, Salmon M (2015) Stacking autocorrelograms to map Moho depth with high spatial resolution in southeastern Australia. Geophys Res Lett 42:7490–7497. doi: 10.1002/2015GL065345

Kennett BLN, Engdahl ER, Buland R (1995) Constraints on seismic velocities in the Earth from traveltimes. Geophys J Int 122:108–124. doi: 10.1111/j.1365-246X.1995.tb03540.x

Kennett BLN, Pham T-S (2018) The nature of Earth's correlation wavefield: late coda of large earthquakes. Proc R Soc A Math Phys Eng Sci 474:20180082. doi: 10.1098/rspa.2018.0082

Kimman WP, Campman X, Trampert J (2012) Characteristics of seismic noise: Fundamental and higher mode energy observed in the northeast of the Netherlands. Bull Seismol Soc Am 102:1388–1399. doi: 10.1785/0120110069

Kiser E, Ishii M (2017) Back-Projection Imaging of Earthquakes. Annu Rev Earth Planet Sci 45:271–299. doi: 10.1146/annurev-earth-063016-015801

Kobayashi N, Nishida K (1998) Continuous excitation of planetary free oscillations by atmospheric disturbances. Nature 395:357–360. doi: 10.1038/26427

Koper KD, Burlacu R (2015) The fine structure of double-frequency microseisms recorded by seismometers in North America. J Geophys Res B Solid Earth 120:1677–1691. doi: 10.1002/2014JB011820

Koper KD, de Foy B (2008) Seasonal anisotropy in short-period seismic noise recorded in South Asia. Bull Seismol Soc Am 98:3033–3045. doi: 10.1785/0120080082

Koper KD, De Foy B, Benz H (2009) Composition and variation of noise recorded at the Yellowknife Seismic Array, 1991-2007. J Geophys Res Solid Earth 114:B10310. doi: 10.1029/2009JB006307

Koper KD, Seats K, Benz H (2010) On the composition of earth's short-period seismic noise field. Bull Seismol Soc Am 100:606–617. doi: 10.1785/0120090120

Kortström J, Uski M, Tiira T (2016) Automatic classification of seismic events within a regional seismograph network. Comput Geosci 87:22–30. doi: 10.1016/j.cageo.2015.11.006

Kosovichev AG, Duvall TL, Scherrer PH (2000) Time-Distance Inversion Methods and Results. In: Helioseismic Diagnostics of Solar Convection and Activity. Springer Netherlands, Dordrecht, pp 159–176

Kotha SR, Cotton F, Bindi D (2018) A new approach to site classification: Mixed-effects Ground Motion Prediction Equation with spectral clustering of site amplification functions. Soil Dyn Earthq Eng 110:318–329. doi: 10.1016/j.soildyn.2018.01.051

Krüger F, Weber M, Scherbaum F, Schlittenhardt J (1993) Double beam analysis of anomalies in the core-mantle boundary region. Geophys Res Lett 20:1475–1478. doi: 10.1029/93GL01311

Kulhánek O (2002) The structure and interpretation of seismograms. In: International Geophysics. Elsevier B.V., pp 333–348

Küperkoch L, Meier T, Lee J, Friederich W (2010) Automated determination of P-phase arrival times at regional and local distances using higher order statistics. Geophys J Int 181:1159–1170. doi: 10.1111/j.1365-246X.2010.04570.x

Lacoss RT, Kelly EJ, Toksöz MN (1969) Estimation of Seismic Noise Structure Using Arrays. Geophysics 34:21–38. doi: 10.1190/1.1439995

Landès M, Hubans F, Shapiro NM, et al (2010) Origin of deep ocean microseisms by using teleseismic body waves. J Geophys Res Solid Earth 115:1–14. doi: 10.1029/2009JB006918

Langet N, Maggi A, Michelini A, Brenguier F (2014) Continuous kurtosis-based migration for seismic event detection and location, with application to Piton de la Fournaise volcano, La Réunion. Bull Seismol Soc Am 104:229–246. doi: 10.1785/0120130107

Langston CA, Chi Chiu SC, Lawrence Z, et al (2009) Array observations of microseismic noise and the nature of H/V in the mississippi embayment. Bull Seismol Soc Am 99:2893–2911.

Larose E (2006) Mesoscopics of ultrasound and seismic waves: application to passive imaging. Ann Phys (Paris) 31:1–126. doi: 10.1051/anphys:2007001

Larose E, Carrière S, Voisin C, et al (2015) Environmental seismology: What can we learn on earth surface processes with ambient noise? J. Appl. Geophys. 116:62–74.

Larose E, de Rosny J, Margerin L, et al (2006a) Observation of multiple scattering of kHz vibrations in a concrete structure and application to monitoring weak changes. Phys Rev E 73:1–7.

Larose E, Derode A, Campillo M, Fink M (2004) Imaging from one-bit correlations of wideband diffuse wave fields. J Appl Phys 95:8393–8399. doi: 10.1063/1.1739529

Larose E, Khan A, Nakamura Y, Campillo M (2005) Lunar subsurface investigated from correlation of seismic noise. Geophys Res Lett 32:1–4. doi: 10.1029/2005GL023518

Larose E, Margerin L, Derode A, et al (2006b) Correlation of random wavefields: An interdisciplinary review. Geophysics 71:SI11-SI21. doi: 10.1190/1.2213356

Larose E, Montaldo G, Derode A, Campillo M (2006c) Passive imaging of localized reflectors and interfaces in open media. Appl Phys Lett 88:8–10. doi: 10.1063/1.2186112

Larose E, Roux P, Campillo M (2007) Reconstruction of Rayleigh-Lamb dispersion spectrum based on noise obtained from an air-jet forcing. J Acoust Soc Am 122:3437–3444. doi: 10.1121/1.2799913

Larose E, Roux P, Campillo M, Derode A (2008) Fluctuations of correlations and Green's function reconstruction: Role of scattering. J Appl Phys 103:1–10. doi: 10.1063/1.2939267

Lawrence JF, Prieto GA (2011) Attenuation tomography of the western United States from ambient seismic noise. J Geophys Res Solid Earth 116:B06302. doi: 10.1029/2010JB007836

Lecocq T, Longuevergne L, Pedersen HA, et al (2017) Monitoring ground water storage at mesoscale using seismic noise: 30 years of continuous observation and thermo-elastic and hydrological modeling. Sci Rep 7:14241. doi: 10.1038/s41598-017-14468-9

Lehujeur M, Vergne J, Maggi A, Schmittbuhl J (2017) Ambient noise tomography with non-uniform noise sources and low aperture networks: case study of deep geothermal reservoirs in northern Alsace, France. Geophys J Int 208:193–210. doi: 10.1093/gji/ggw373

Lekic V, Cottaar S, Dziewonski A, Romanowicz B (2012) Cluster analysis of global lower mantle tomography: A new class of structure and implications for chemical heterogeneity. Earth Planet Sci Lett 357–358:68–77. doi: 10.1016/j.epsl.2012.09.014

Leroy C, Lani S, Sabra KG, et al (2012) Enhancing the emergence rate of coherent wavefronts from ocean ambient noise correlations using spatio-temporal filters. J Acoust Soc Am 132:883–893.

Lewis MA, Gerstoft P (2012) Shear wave anisotropy from cross-correlation of seismic noise in the Parkfield pilot hole. Geophys J Int 188:626–630. doi: 10.1111/j.1365-246X.2011.05285.x

Lin F-C, Ritzwoller MH, Shen W (2011) On the reliability of attenuation measurements from ambient noise cross-correlations. Geophys Res Lett 38. doi: 10.1029/2011GL047366

Lin F-C, Ritzwoller MH, Townend J, et al (2007) Ambient noise Rayleigh wave tomography of New Zealand. Geophys J Int 170:649–666. doi: 10.1111/j.1365-246X.2007.03414.x

Lin FC, Moschetti MP, Ritzwoller MH (2008) Surface wave tomography of the western United States from ambient seismic noise: Rayleigh and Love wave phase velocity maps. Geophys J Int 173:281–298. doi: 10.1111/j.1365-246X.2008.03720.x

Lin FC, Tsai VC (2013) Seismic interferometry with antipodal station pairs. Geophys Res Lett 40:4609–4613. doi: 10.1002/grl.50907

Lin FC, Tsai VC, Schmandt B, et al (2013) Extracting seismic core phases with array interferometry. Geophys Res Lett 40:1049–1053. doi: 10.1002/grl.50237

Lin J-Y, Lee T-C, Hsieh H-S, et al (2014) A Study of Microseisms Induced by Typhoon Nanmadol Using Ocean-Bottom Seismometers. Bull Seismol Soc Am 104:2412–2421. doi: 10.1785/0120130237

Lin T-L, Langston CA (2007) Infrasound from thunder: A natural seismic source. Geophys Res Lett 34:L14304. doi: 10.1029/2007GL030404

Lin T, Langston CA (2009) Thunder-induced ground motions: 1. Observations. J Geophys Res 114:B04303. doi: 10.1029/2008JB005769

Liu Q, Koper KD, Burlacu R, et al (2016a) Source locations of teleseismic P, SV, and SH waves observed in microseisms recorded by a large aperture seismic array in China. Earth Planet Sci Lett 449:39–47. doi: 10.1016/j.epsl.2016.05.035

Liu QY, van der Hilst RD, Li Y, et al (2014a) Eastward expansion of the Tibetan Plateau by crustal flow and strain partitioning across faults. Nat Geosci 7:361–365. doi: 10.1038/ngeo2130

Liu X, Ben-Zion Y (2016) Estimating correlations of neighbouring frequencies in ambient seismic noise. Geophys J Int 206:1065–1075. doi: 10.1093/gji/ggw196

Liu X, Ben-Zion Y, Zigone D (2015) Extracting seismic attenuation coefficients from cross-correlations of ambient noise at linear triplets of stations. Geophys J Int 203:1149–1163. doi: 10.1093/gji/ggv357

Liu X, Ben-Zion Y, Zigone D (2016b) Frequency domain analysis of errors in cross-correlations of ambient seismic noise. Geophys J Int 207:1630–1652. doi: 10.1093/gji/ggw361

Liu Z, Huang J, Peng Z, Su J (2014b) Seismic velocity changes in the epicentral region of the 2008 Wenchuan earthquake measured from three-component ambient noise correlation techniques. Geophys Res Lett 41:37–42. doi: 10.1002/2013GL058682

Lobkis OI, Weaver RL (2001) On the emergence of the Green's function in the correlations of a diffuse field. J Acoust Soc Am 110:3011–3017. doi: 10.1121/1.1417528

Lobkis OI, Weaver RL (2003) Coda-Wave Interferometry in Finite Solids: Recovery of P-to-S Conversion Rates in an Elastodynamic Billiard. Phys Rev Lett 90:254302. doi: 10.1103/PhysRevLett.90.254302

Longuet-Higgins MS (1950) A Theory of the Origin of Microseisms. Philos Trans R Soc A Math Phys Eng Sci 243:1–35. doi: 10.1098/rsta.1950.0012

Longuet-Higgins MS, Ursell F (1948) Sea waves and microseisms. Nature 162:700. doi: 10.1038/162700a0

Louie JN (2001) Faster, better: Shear-wave velocity to 100 meters depth from refraction microtremor arrays. Bull Seismol Soc Am 91:347–364. doi: 10.1785/0120000098

Lunedei E, Malischewsky P (2015) A Review and Some New Issues on the Theory of the H/V Technique for Ambient Vibrations. In: Geotechnical, Geological and Earthquake Engineering. Springer, pp 371–394

Ma S, Beroza GC (2012) Ambient-field Green's functions from asynchronous seismic observations. Geophys Res Lett 39: L06301. doi: 10.1029/2011GL050755

Ma S, Prieto GA, Beroza GC (2008) Testing community velocity models for southern California using the ambient seismic field. Bull Seismol Soc Am 98:2694–2714. doi: 10.1785/0120080947

Macquet M, Paul A, Pedersen HA, et al (2014) Ambient noise tomography of the Pyrenees and the surrounding regions: Inversion for a 3-D Vs model in the presence of a very heterogeneous crust. Geophys J Int 199:402–415. doi: 10.1093/gji/ggu270

Maeda T, Obara K, Yukutake Y (2010) Seismic velocity decrease and recovery related to earthquake swarms in a geothermal area. Earth, Planets and Space 62:685–691. doi: 10.5047/eps.2010.08.006

Maeda T, Sato H, Ohtake M (2006) Constituents of Vertical-component Coda Waves at Long Periods. Pure Appl Geophys 163:549–566. doi: 10.1007/s00024-005-0031-9

Mainsant G, Larose E, Brnnimann C, et al (2012) Ambient seismic noise monitoring of a clay landslide: Toward failure prediction. J Geophys Res Earth Surf 117. doi: 10.1029/2011JF002159

Manuel K, Sundararajan R, Williams J (2008) Hurricanes and global warming: Results from downscaling IPCC AR4 simulations. Bull Am Meteorol Soc 89:347–367. doi: 10.1175/BAMS-89-3-347

Margerin L, Sato H (2011) Generalized optical theorems for the reconstruction of Green's function of an inhomogeneous elastic medium. J Acoust Soc Am 130:3674–3690. doi: 10.1121/1.3652856

McNamara DE DE, Buland RPR (2004) Ambient Noise Levels in the Continental United States. Bull Seismol Soc Am 94:1517–1527. doi: 10.1785/012003001

Medeiros WE, Schimmel M, do Nascimento AF (2015) How much averaging is necessary to cancel out cross-terms in noise correlation studies? Geophys J Int 203:1096–1100. doi: 10.1093/gji/ggv336

Mehta K, Bakulin A, Sheiman J, et al (2007) Improving the virtual source method by wavefield separation. Geophysics 72:V79. doi: 10.1190/1.2733020

Meier U, Shapiro NM, Brenguier F (2010) Detecting seasonal variations in seismic velocities within Los Angeles basin from correlations of ambient seismic noise. Geophys J Int 181:985–996.

Melo G, Malcolm A (2011) Microquake seismic interferometry with SVD-enhanced Green's function recovery. Lead Edge 30:556. doi: 10.1190/1.3589114

Melo G, Malcolm A, Mikesell D, van Wijk K (2013) Using SVD for improved interferometric green's function retrieval. Geophys J Int. doi: 10.1093/gji/ggt172

Meschede M, Stutzmann É, Farra V, et al (2017) The Effect of Water Column Resonance on the Spectra of Secondary Microseism P Waves. J Geophys Res Solid Earth 122:8121–8142.

Miche A (1944) Mouvements ondulatoire de la mer en profondeur croissante ou décroissante. Première partie. Mouvements ondulatoires périodiques et cylindriques en profondeur constante. Ann des Ponts

Chaussés 114:42–78.

Minato S, Tsuji T, Ohmi S, Matsuoka T (2012) Monitoring seismic velocity change caused by the 2011 Tohoku-oki earthquake using ambient noise records. Geophys Res Lett 39: L09309.

Miyazawa M, Snieder R, Venkataraman A (2008) Application of seismic interferometry to extract P- and S-wave propagation and observation of shear-wave splitting from noise data at Cold Lake, Alberta, Canada. Geophysics 73:D35. doi: 10.1190/1.2937172

Möllhoff M, Bean CJ (2016) Seismic Noise Characterization in Proximity to Strong Microseism Sources in the Northeast Atlantic. Bull Seismol Soc Am 106:464–477. doi: 10.1785/0120150204

Mordret A, Jolly AD, Duputel Z, Fournier N (2010) Monitoring of phreatic eruptions using Interferometry on Retrieved Cross-Correlation Function from Ambient Seismic Noise: Results from Mt. Ruapehu, New Zealand. J Volcanol Geotherm Res 191:46–59. doi: 10.1016/j.jvolgeores.2010.01.010

Mordret A, Mikesell TD, Harig C, et al (2016) Monitoring southwest Greenland's ice sheet melt with ambient seismic noise. Sci Adv 2:e1501538. doi: 10.1126/sciadv.1501538

Mordret A, Rivet D, Landès M, Shapiro NM (2015) Three-dimensional shear velocity anisotropic model of Piton de la Fournaise Volcano (La Réunion Island) from ambient seismic noise. J Geophys Res Solid Earth 120: 406-427. doi: 10.1002/2014JB011654

Mordret A, Sun H, Prieto GA, et al (2017) Continuous monitoring of high-rise buildings using seismic interferometry. Bull Seismol Soc Am 107:2759–2773. doi: 10.1785/0120160282

Moreau L, Stehly L, Boué P, et al (2017) Improving ambient noise correlation functions with an SVD-based Wiener filter. Geophys J Int 211:418–426. doi: 10.1093/gji/ggx306

Moschetti MP, Ritzwoller MH, Shapiro NM (2007) Surface wave tomography of the western United States from ambient seismic noise: Rayleigh wave group velocity maps. Geochemistry, Geophysics, Geosystems 8: Q08010. doi: 10.1029/2007GC001655

Mulargia F (2017) Cosmic signatures in earth's seismic tremor? Mon Not R Astron Soc Lett 464:L11–L15. doi: 10.1093/mnrasl/slw180

Mulargia F, Kamenshchik A (2016) The gravitational resolving power of global seismic networks in the 0.1-10 Hz band. Phys Lett A 380:1503–1507. doi: 10.1016/j.physleta.2016.02.032

Munk WH (1950) Proceedings 1st International Conference on Coastal Engineering. ASCE, Long Beach, California, pp 1–4

Nakahara H (2006a) Theoretical background of retrieving Green's function by cross-correlation: One-dimensional case. Geophys J Int 165:719–728. doi: 10.1111/j.1365-246X.2006.02916.x

Nakahara H (2006b) A systematic study of theoretical relations between spatial correlation and Green's function in one-, two- and three-dimensional random scalar wavefields. Geophys J Int 167:1097–1105. doi: 10.1111/j.1365-246X.2006.03170.x

Nakamura Y (1989) A method for dynamic characteristics estimation of subsurface using microtremor on the ground surface. Quarterly Report of the Railway Technical Reasearch Institute 30: 25–33.

Nakata N, Boué P, Brenguier F, et al (2016) Body and surface wave reconstruction from seismic noise correlations between arrays at Piton de la Fournaise volcano. Geophys Res Lett 43:1047–1054. doi:

10.1002/2015GL066997

Nakata N, Chang JP, Lawrence JF, Boué P (2015) Body wave extraction and tomography at Long Beach, California, with ambient-noise interferometry. J Geophys Res B Solid Earth 120:1159–1173. doi: 10.1002/2015JB011870

Nakata N, Snieder R (2014) Monitoring a building using deconvolution interferometry. II: Ambient-vibration analysis. Bull Seismol Soc Am. doi: 10.1785/0120130050

Nakata N, Snieder R, Tsuji T, et al (2011) Shear wave imaging from traffic noise using seismic interferometry by cross-coherence. Geophysics 76:SA97-SA106. doi: 10.1190/geo2010-0188.1

Neale J, Harmon N, Srokosz M (2017a) Monitoring remote ocean waves using P-wave microseisms. J Geophys Res Ocean 122:470–483. doi: 10.1002/2016JC012183

Neale JW, Harmon N, Srokosz M (2017b) Improving microseismic P-wave source location with multiple seismic arrays. J Geophys Res Solid Earth 123: 476–492. doi: 10.1002/2017JB015015

Ness N, Harrison J, Slichiter L, Angeles L (1961) Observations of the free oscillations of the earth. J Geophys Res 2:621–629. doi: 10.1029/JZ066i002p00621

Nishida K (2013) Global propagation of body waves revealed by cross-correlation analysis of seismic hum. Geophys Res Lett 40:1691–1696. doi: 10.1002/grl.50269

Nishida K (2017) Ambient seismic wave field. Proc Japan Acad Ser B 93:423–448. doi: 10.2183/pjab.93.026

Nishida K (2014) Source spectra of seismic hum. Geophys J Int 199: 416–429. doi: 10.1093/gji/ggu272

Nishida K, Kawakatsu H, Obara K (2008) Three-dimensional crustal S wave velocity structure in Japan using microseismic data recorded by Hi-net tiltmeters. J Geophys Res Solid Earth 113:1–22. doi: 10.1029/2007JB005395

Nishida K, Kobayashi N, Fukao Y (2000) Resonant oscillations between the solid earth and the atmosphere. Science 287:2244–2246. doi: 10.1126/science.287.5461.2244

Nishida K, Kobayashi N, Fukao Y (2002) Origin of Earth's ground noise from 2 to 20 mHz. Geophys Res Lett 29:52-1-52–4. doi: 10.1029/2001GL013862

Nishida K, Montagner J-PJ-P, Kawakatsu H (2009) Global Surface Wave Tomography Using Seismic Hum. Science 326:112–112. doi: 10.1126/science.1176389

Nishida K, Takagi R (2016) Teleseismic S wave microseisms. Science 353:919–921.

Nissen-Meyer T, van Driel M, Stähler SC, et al (2014) AxiSEM: broadband 3-D seismic wavefields in axisymmetric media. Solid Earth 5:425–445. doi: 10.5194/se-5-425-2014

Niu F, Silver PG, Daley TM, et al (2008) Preseismic velocity changes observed from active source monitoring at the Parkfield SAFOD drill site. Nature 454:204–208. doi: 10.1038/nature07111

Obermann A, Froment B, Campillo M, et al (2014) Seismic noise correlations to image structural and mechanical changes associated with the Mw 7.9 2008 Wenchuan earthquake. J Geophys Res Solid Earth 119:3155–3168. doi: 10.1002/2013JB010932

Obrebski M, Ardhuin F, Stutzmann E, Schimmel M (2013) Detection of microseismic compressional (P) body waves aided by numerical modeling of oceanic noise sources. J Geophys Res Solid Earth 118:4312–4324. doi: 10.1002/jgrb.50233

Obrebski MJ, Ardhuin F, Stutzmann E, Schimmel M (2012) How moderate sea states can generate loud seismic noise in the deep ocean. Geophys Res Lett 39:1–6. doi: 10.1029/2012GL051896

Okada H (2003) The Microtremor Survey Method. SEG

Oliver J (1962) A worldwide storm of microseisms with periods of about 27 seconds. Bull Seism Soc Am 52:507–517.

Olivier G, Brenguier F, Campillo M, et al (2015) Body-wave reconstruction from ambient seismic noise correlations in an underground mine. Geophysics 80:KS11-KS25. doi: 10.1190/geo2014-0299.1

Olivier G, Chaput J, Borchers B (2018) Using Supervised Machine Learning to Improve Active Source Signal Retrieval. Seismol Res Lett 89:1023–1029. doi: 10.1785/0220170239

Oren C, Nowack RL (2017) Seismic body-wave interferometry using noise autocorrelations for crustal structure. Geophys J Int 208:321–332. doi: 10.1093/gji/ggw394

Paitz P, Gokhberg A, Fichtner A (2018) A neural network for noise correlation classification. Geophys J Int 212:1468–1474. doi: 10.1093/gji/ggx495

Paul A, Campillo M, Margerin L, et al (2005) Empirical synthesis of time-asymmetrical Green functions from the correlation of coda waves. J Geophys Res Solid Earth 110:1–13. doi: 10.1029/2004JB003521

Peck L (2008) Overview of Seismic Noise and its Relevance to Personnel Detection. Technical Report ERDC/CRREL TR-08-5.

Pedersen HA, Krüger F, Achauer U, et al (2007) Influence of the seismic noise characteristics on noise correlations in the Baltic shield. Geophys J Int 168:197–210. doi: 10.1111/j.1365-246X.2006.03177.x

Perol T, Gharbi M, Denolle M (2018) Convolutional neural network for earthquake detection and location. Sci Adv 4:e1700578. doi: 10.1126/sciadv.1700578

Peterson J (1993) Observations and Modeling of Seismic Background Noise. U.S. Geol. Surv. Open File Report 93-322.

Peterson J (1980) Preliminary observations of noise spectra at the SRO and ASRO stations. USGS Open-File Report 80-992.

Phạm T-S, Tkalčić H, Sambridge M, Kennett B (2018) Earth's Correlation Wavefield: Late Coda Correlation. Geophys Res Lett 45:3035–3042. doi: 10.1002/2018GL077244

Phạm TS, Tkalčić H (2017) On the feasibility and use of teleseismic P wave coda autocorrelation for mapping shallow seismic discontinuities. J Geophys Res 122:3776–3791. doi: 10.1002/2017JB013975

Picozzi M (2005) Joint inversion of H/V ratios and dispersion curves from seismic noise: Estimating the S-wave velocity of bedrock. Geophys Res Lett 32:L11308. doi: 10.1029/2005GL022878

Planès T, Mooney MA, Rittgers JBR, et al (2016) Time-lapse monitoring of internal erosion in earthen dams and levees using ambient seismic noise. Géotechnique 66:301–312. doi: 10.1680/jgeot.14.P.268

Planès T, Rittgers JB, Mooney MA, et al (2017) Monitoring the tidal response of a sea levee with ambient seismic noise. J Appl Geophys 138:255–263. doi: 10.1016/j.jappgeo.2017.01.025

Poli P, Campillo M, de Hoop M (2017) Analysis of intermediate period correlations of coda from deep earthquakes. Earth Planet Sci Lett 477:147–155. doi: 10.1016/j.epsl.2017.08.026

Poli P, Campillo M, Pedersen H (2012a) Body-Wave Imaging of Earth's Mantle Discontinuities from

Ambient Seismic Noise. Science 338:1063–1065. doi: 10.1126/science.1228194

Poli P, Pedersen HA, Campillo M (2012b) Emergence of body waves from cross-correlation of short period seismic noise. Geophys J Int 188:549–558. doi: 10.1111/j.1365-246X.2011.05271.x

Poli P, Pedersen HA, Campillo M (2013) Noise directivity and group velocity tomography in a region with small velocity contrasts: The northern Baltic shield. Geophys J Int 192:413–424.

Poli P, Thomas C, Campillo M, Pedersen HA (2015) Imaging the D″ reflector with noise correlations. Geophys Res Lett 42:60–65. doi: 10.1002/2014GL062198

Poppeliers C, Mallinson D (2015) High-frequency seismic noise generated from breaking shallow water ocean waves and the link to time-variable sea states. Geophys Res Lett 42:8563–8569

Poupinet G, Ellsworth WL, Frechet J (1984) Monitoring velocity variations in the crust using earthquake doublets: An application to the Calaveras Fault, California. J Geophys Res Solid Earth 89:5719–5731.

Prieto GA, Beroza GC (2008) Earthquake ground motion prediction using the ambient seismic field. Geophys Res Lett 35:L14304. doi: 10.1029/2008GL034428

Prieto GA, Denolle M, Lawrence JF, Beroza GC (2011) On amplitude information carried by the ambient seismic field. Comptes Rendus - Geosci 343:600–614. doi: 10.1016/j.crte.2011.03.006

Prieto GA, Lawrence JF, Beroza GC (2009) Anelastic Earth structure from the coherency of the ambient seismic field. J Geophys Res Solid Earth 114:B07303. doi: 10.1029/2008JB006067

Prieto GA, Lawrence JF, Chung AI, Kohler MD (2010) Impulse response of civil structures from ambient noise analysis. Bull Seismol Soc Am 100:2322–2328. doi: 10.1785/0120090285

Pyle ML, Koper KD, Euler GG, Burlacu R (2015) Location of high-frequency P wave microseismic noise in the Pacific Ocean using multiple small aperture arrays. Geophys Res Lett 42:2700–2708.

Quiros DA, Brown LD, Kim D (2016) Seismic interferometry of railroad induced ground motions: body and surface wave imaging. Geophys J Int 205:301–313. doi: 10.1093/gji/ggw033

Rascle N, Ardhuin F, Queffeulou P, Croizé-Fillon D (2008) A global wave parameter database for geophysical applications. Part 1: Wave-current-turbulence interaction parameters for the open ocean based on traditional parameterizations. Ocean Model 25:154–171. doi: 10.1016/j.ocemod.2008.07.006

Renalier F, Jongmans D, Campillo M, Bard P-Y (2010) Shear wave velocity imaging of the Avignonet landslide (France) using ambient noise cross correlation. J Geophys Res 115:1–14.

Resio DT, Swail VR, Jensen RE, Cardone VJ (1999) Wind speed scaling in fully developed seas. J Phys Oceanogr 29:1801–1811. doi: 10.1175/1520-0485(1999)029<1801:WSSIFD>2.0.CO;2

Retailleau L, Boué P, Stehly L, Campillo M (2017) Locating Microseism Sources Using Spurious Arrivals in Intercontinental Noise Correlations. J Geophys Res 122:8107–8120. doi: 10.1002/2017JB014593

Retailleau L, Landès M, Gualtieri L, et al (2018) Detection and analysis of a transient energy burst with beamforming of multiple teleseismic phases. Geophys J Int 212:14–24. doi: 10.1093/gji/ggx410

Retailleau L, Shapiro NM, Guilbert J, et al (2014) Antipodal focusing of seismic waves observed with the USArray. Geophys J Int 199:1030–1042. doi: 10.1093/gji/ggu309

Rhie J, Romanowicz B (2004) Excitation of Earth's continuous free oscillations by atmosphere–ocean–seafloor coupling. Nature 431:552–556. doi: 10.1038/nature02942

Rhie J, Romanowicz B (2006) A study of the relation between ocean storms and the Earth's hum. Geochemistry, Geophysics, Geosystems 7. doi: 10.1029/2006GC001274

Riahi N, Bokelmann G, Sala P, Saenger EH (2013) Time-lapse analysis of ambient surface wave anisotropy: A three-component array study above an underground gas storage. J Geophys Res 118:5339–5351. doi: 10.1002/jgrb.50375

Riahi N, Gerstoft P (2015) The seismic traffic footprint: Tracking trains, aircraft, and cars seismically. Geophys Res Lett 42: 2674–2681. doi: 10.1002/2015GL063558

Rial JA (1978) On the focusing of seismic body waves at the epicentre's antipode. Geophys J Int 55:737–743. doi: 10.1111/j.1365-246X.1978.tb05940.x

Richter T, Sens-Schönfelder C, Kind R, Asch G (2014) Comprehensive observation and modeling of earthquake and temperature-related seismic velocity changes in northern Chile with passive image interferometry. J Geophys Res Solid Earth 119:4747–4765. doi: 10.1002/2013JB010695

Rickett J, Claerbout J (1996) Passive seismic imaging applied to synthetic data. In: SEP-Report. pp 83–90

Rickett J, Claerbout J (1999) Acoustic daylight imaging via spectral factorization: Helioseismology and reservoir monitoring. Lead Edge 18:957–960. doi: 10.1190/1.1438420

Rickett JE, Claerbout JF (2000) Calculation of the sun's acoustic impulse response by multi-dimensional spectral factorization. Solar Physics 192:203–210. doi: 10.1023/A:1005205406377

Ritzwoller MH, Lin FC, Shen W (2011) Ambient noise tomography with a large seismic array. Comptes Rendus - Geosci 343:558–570. doi: 10.1016/j.crte.2011.03.007

Rodgers PW (1968) The response of the horizontal pendulum seismometer to Rayleigh and Love waves, tilt, and free oscillations of the earth. Bull Seismol Soc Am 58:1385–1406.

Rohde MD, Ringler AT, Hutt CR, et al (2017) Characterizing Local Variability in Long-Period Horizontal Tilt Noise. Seismol Res Lett 88:822–830. doi: 10.1785/0220160193

Ross ZE, Ben-Zion Y (2014) Automatic picking of direct P, S seismic phases and fault zone head waves. Geophys J Int 199:368–381. doi: 10.1093/gji/ggu267

Rost S, Thomas C (2002) Array seismology: Methods and applications. Rev Geophys 40:1008.

Rost S, Thomas C (2009) Improving seismic resolution through array processing techniques. Surv Geophys 30:271–299. doi: 10.1007/s10712-009-9070-6

Roth DL, Finnegan NJ, Brodsky EE, et al (2017) Bed load transport and boundary roughness changes as competing causes of hysteresis in the relationship between river discharge and seismic amplitude recorded near a steep mountain stream. J Geophys Res 122:1182–1200. doi: 10.1002/2016JF004062

Rouet-Leduc B, Hulbert C, Lubbers N, et al (2017) Machine Learning Predicts Laboratory Earthquakes. Geophys Res Lett 44:9276–9282. doi: 10.1002/2017GL074677

Roux P (2009) Passive seismic imaging with directive ambient noise: Application to surface waves and the San Andreas fault in Parkfield, CA. Geophys J Int 179:367–373.

Roux P, Cornuelle BD, Kuperman W a, Hodgkiss WS (2008) The structure of raylike arrivals in a shallow-water waveguide. J Acoust Soc Am 124:3430–3439. doi: 10.1121/1.2996330

Roux P, Fink M (2003) Green's function estimation using secondary sources in a shallow water environment.

J Acoust Soc Am 113:1406–1416. doi: 10.1121/1.1542645

Roux P, Kuperman WA (2004) Extracting coherent wave fronts from acoustic ambient noise in the ocean. J Acoust Soc Am 116:1995–2003. doi: 10.1121/1.1797754

Roux P, Moreau L, Lecointre A, et al (2016) A methodological approach towards high-resolution surface wave imaging of the San Jacinto Fault Zone using ambient-noise recordings at a spatially dense array. Geophys J Int 206:980–992. doi: 10.1093/gji/ggw193

Roux P, Sabra KG, Gerstoft P, et al (2005a) P-waves from cross-correlation of seismic noise. Geophys Res Lett 32:1–4. doi: 10.1029/2005GL023803

Roux P, Sabra KG, Kuperman WA, Roux A (2005b) Ambient noise cross correlation in free space: Theoretical approach. J Acoust Soc Am 117:79–84. doi: 10.1121/1.1830673

Ruigrok E, Campman X, Draganov D, Wapenaar K (2010) High-resolution lithospheric imaging with seismic interferometry. Geophys J Int 183:339–357. doi: 10.1111/j.1365-246X.2010.04724.x

Ruigrok E, Draganov D, Wapenaar K (2008) Global-scale seismic interferometry: Theory and numerical examples. Geophys Prospect 56:395–417. doi: 10.1111/j.1365-2478.2008.00697.x

Ruigrok E, Gibbons S, Wapenaar K (2017) Cross-correlation beamforming. J Seismol 21:495–508. doi: 10.1007/s10950-016-9612-6

Saade M, Montagner JP, Roux P, et al (2017) Monitoring of seismic anisotropy at the time of the 2008 Iwate-Miyagi (Japan) earthquake. Geophys J Int 211:483–497. doi: 10.1093/gji/ggx321

Sabra KG, Gerstoft P, Roux P, et al (2005a) Extracting time-domain Green's function estimates from ambient seismic noise. Geophys Res Lett 32:1–5. doi: 10.1029/2004GL021862

Sabra KG, Gerstoft P, Roux P, et al (2005b) Surface wave tomography from microseisms in Southern California. Geophys Res Lett 32:1–4. doi: 10.1029/2005GL023155

Sabra KG, Roux P, Kuperman WA (2005c) Emergence rate of the time-domain Green's function from the ambient noise cross-correlation function. J Acoust Soc Am 118:3524–3531. doi: 10.1121/1.2109059

Sadeghisorkhani H, Gudmundsson O, Roberts R, et al (2016) Mapping the source distribution of microseisms using noise covariogram envelopes. Geophys J Int 205:1473–1491.

Sadeghisorkhani H, Gudmundsson Ó, Roberts R, Tryggvason A (2017) Velocity-measurement bias of the ambient noise method due to source directivity: a case study for the Swedish National Seismic Network. Geophys J Int 209:1648–1659. doi: 10.1093/gji/ggx115

Saito T (2010) Love-wave excitation due to the interaction between a propagating ocean wave and the sea-bottom topography. Geophys J Int 182:1515–1523. doi: 10.1111/j.1365-246X.2010.04695.x

Salvermoser J, Hadziioannou C, Stähler SC (2015) Structural monitoring of a highway bridge using passive noise recordings from street traffic. J Acoust Soc Am 138:3864–3872. doi: 10.1121/1.4937765

Sánchez-Sesma FJ, Campillo MM (2006) Retrieval of the Green's function from cross correlation: The canonical elastic problem. Bull Seismol Soc Am 96:1182–1191. doi: 10.1785/0120050181

Sánchez-Sesma FJ, Pérez-Ruiz JA, Campillo M, Luzón F (2006) Elastodynamic 2D Green function retrieval from cross-correlation: Canonical inclusion problem. Geophys Res Lett 33:L13305.

Saragiotis CD, Hadjileontiadis LJ, Panas SM (2002) PAI-S/K: A robust automatic seismic P phase arrival

identification scheme. IEEE Trans Geosci Remote Sens 40:1395–1404.

Sato H (2010) Retrieval of Green's function having coda waves from the cross-correlation function in a scattering medium illuminated by a randomly homogeneous distribution of noise sources on the basis of the first-order Born approximation. Geophys J Int 180:759–764.

Sato H (2009) Green's function retrieval from the CCF of coda waves in a scattering medium. Geophys J Int 179:1580–1583. doi: 10.1111/j.1365-246X.2009.04398.x

Sato H, Fehler MC, Maeda T (2012) Seismic Wave Propagation and Scattering in the Heterogeneous Earth : Second Edition. Springer Berlin Heidelberg, Berlin, Heidelberg

Saygin E, Cummins PR, Lumley D (2017) Retrieval of the P wave reflectivity response from autocorrelation of seismic noise: Jakarta Basin, Indonesia. Geophys Res Lett 44:792–799.

Scherbaum F (1987a) Seismic Imaging of the Site Response Using Microearthquake Recordings. Part I. Method. In: Bulletin of the Seismological Society of America. pp 1905–1923

Scherbaum F (1987b) Seismic Imaging of the Site response Using Microearthquake Recordings. Part II. Application to the Swabian Jua, Southwest Germany, Seismic Network. Bull Seismol Soc Am 77:1924–1944.

Schimmel M, Stutzmann E, Ardhuin F, Gallart J (2011) Polarized Earth's ambient microseismic noise. Geochemistry, Geophysics, Geosystems 12:1–14. doi: 10.1029/2011GC003661

Schulte-Pelkum V, Earle PS, Vernon FL (2004) Strong directivity of ocean-generated seismic noise. Geochemistry, Geophysics, Geosystems 5:1–13. doi: 10.1029/2003GC000520

Schultz R, Jeffrey Gu Y (2013) Flexible, inversion-based Matlab implementation of the Radon transform. Comput Geosci 52:437–442. doi: 10.1016/j.cageo.2012.08.013

Schuster GT (2001) Theory of Daylight/Interferometric Imaging - Tutorial. In: 63rd EAGE Conference & Exhibition.

Schuster GT, Yu J, Sheng J, Rickett J (2004) Interferometric/daylight seismic imaging. Geophys J Int 157:838–852. doi: 10.1111/j.1365-246X.2004.02251.x

Seats K ~J., Lawrence J ~E., Prieto G ~A. (2012) Improved ambient noise correlation functions using Welch's method. Geophys J Int 188:513–523. doi: 10.1111/ j.1365- 246X.2011.05263.x

Sens-Schönfelder C (2008) Synchronizing seismic networks with ambient noise. Geophys J Int 174:966–970. doi: 10.1111/j.1365-246X.2008.03842.x

Sens-Schönfelder C, Larose E (2008) Temporal changes in the lunar soil from correlation of diffuse vibrations. Phys Rev E 78:045601. doi: 10.1103/PhysRevE.78.045601

Sens-Schönfelder C, Snieder R, Stähler SC (2015) The lack of equipartitioning in global body wave coda. Geophys Res Lett 42:7483–7489. doi: 10.1002/2015GL065108

Sens-Schönfelder C, Wegler U (2006) Passive image interferemetry and seasonal variations of seismic velocities at Merapi Volcano, Indonesia. Geophys Res Lett 33:1–5. doi: 10.1029/2006GL027797

Seydoux L, de Rosny J, Shapiro NM (2017) Pre-processing ambient noise cross-correlations with equalizing the covariance matrix eigenspectrum. Geophys J Int 210:1432–1449. doi: 10.1093/gji/ggx250

Seydoux L, Shapiro NM, de Rosny J, Landès M (2016) Spatial coherence of the seismic wavefield

continuously recorded by the USArray. Geophys Res Lett 43:9644–9652.

Shapiro NM, Campillo M (2004) Emergence of broadband Rayleigh waves from correlations of the ambient seismic noise. Geophys Res Lett 31:8–11. doi: 10.1029/2004GL019491

Shapiro NM, Ritzwoller MH, Bensen GD (2006) Source location of the 26 sec microseism from cross-correlations of ambient seismic noise. Geophys Res Lett 33: L18310. doi: 10.1029/2006GL027010

Shapiro NMN, Campillo M, Stehly L (2005) High-Resolution Surface-Wave Tomography from Ambient Seismic Noise. Science 307:1615–1618. doi: 10.1126/science.1108339

Sheen DH, Shin JS, Kang TS, Baag CE (2009) Low frequency cultural noise. Geophys Res Lett 36:1–5. doi: 10.1029/2009GL039625

Shen Y, Ren Y, Gao H, Savage B (2012) An Improved Method to Extract Very-Broadband Empirical Green's Functions from Ambient Seismic Noise. Bull Seismol Soc Am 102:1872–1877.

Sheng Y, Denolle MA, Beroza GC (2017) Multicomponent C3 green's functions for improved long-period ground-motion prediction. Bull Seismol Soc Am 107:2836–2845. doi: 10.1785/0120170053

Snieder R (2004) Extracting the Green's function from the correlation of coda waves: A derivation based on stationary phase. Phys Rev E 69:046610. doi: 10.1103/PhysRevE.69.046610

Snieder R (2006) The theory of coda wave interferometry. PAGEOPH 163:455–473. doi: 10.1007/s00024-005-0026-6

Snieder R (2007) Extracting the Green's function of attenuating heterogeneous acoustic media from uncorrelated waves. J Acoust Soc Am 121:2637–2643. doi: 10.1121/1.2713673

Snieder R, Miyazawa M, Slob E, et al (2009) A comparison of strategies for seismic interferometry. Surv Geophys 30:503–523. doi: 10.1007/s10712-009-9069-z

Snieder R, Şafak E (2006) Extracting the building response using seismic interferometry: Theory and application to the Millikan Library in Pasadena, California. Bull Seismol Soc Am 96:586–598. doi: 10.1785/0120050109

Snieder R, Sens-Schönfelder C (2015) Seismic interferometry and stationary phase at caustics. J Geophys Res B Solid Earth 120:4333–4343. doi: 10.1002/2014JB011792

Snieder R, Sheiman J, Calvert R (2006a) Equivalence of the virtual-source method and wave-field deconvolution in seismic interferometry. Phys Rev E 73:066620. doi: 10.1103/PhysRevE.73.066620

Snieder R, Wapenaar K, Larner K (2006b) Spurious multiples in seismic interferometry of primaries. Geophysics 71:SI111-SI124. doi: 10.1190/1.2211507

Soldati G, Zaccarelli L, Faenza L, Michelini A (2015) Monitoring of crustal seismic velocity variations in the L'Aquila fault zone inferred from noise cross-correlation. Geophys J Int 202:604–611. doi: 10.1093/gji/ggv172

Spica Z, Perton M, Beroza GC (2017) Lateral heterogeneity imaged by small-aperture ScS retrieval from the ambient seismic field. Geophys Res Lett 44:8276–8284. doi: 10.1002/2017GL073230

Stehly L, Boué P (2017) On the interpretation of the amplitude decay of noise correlations computed along a line of receivers. Geophys J Int 118:ggx021. doi: 10.1093/gji/ggx021

Stehly L, Campillo M, Froment B, Weaver RL (2008) Reconstructing Green's function by correlation of the

coda of the correlation (C3) of ambient seismic noise. J Geophys Res Solid Earth 113:B11306. doi: 10.1029/2008JB005693

Stehly L, Campillo M, Shapiro NM (2007) Traveltime measurements from noise correlation: Stability and detection of instrumental time-shifts. Geophys J Int 171:223–230.

Stehly L, Campillo M, Shapiro NM (2006) A study of the seismic noise from its long-range correlation properties. J Geophys Res 111:B10306. doi: 10.1029/2005JB004237

Stehly L, Cupillard P, Romanowicz B (2011) Towards improving ambient noise tomography using simultaneously curvelet denoising filters and SEM simulations of seismic ambient noise. Comptes Rendus - Geosci 343:591–599. doi: 10.1016/j.crte.2011.03.005

Stehly L, Froment B, Campillo M, et al (2015) Monitoring seismic wave velocity changes associated with the Mw 7.9 Wenchuan earthquake: Increasing the temporal resolution using curvelet filters. Geophys J Int 201:1939–1949. doi: 10.1093/gji/ggv110

Steim JM (2015) Theory and Observations - Instrumentation for Global and Regional Seismology. In: Treatise on Geophysics. Elsevier, pp 29–78

Stutzmann E, Ardhuin F, Schimmel M, et al (2012) Modelling long-term seismic noise in various environments. Geophys J Int 191:707–722. doi: 10.1111/j.1365-246X.2012.05638.x

Stutzmann E, Schimmel M, Patau G, Maggi A (2009) Global climate imprint on seismic noise. Geochemistry, Geophysics, Geosystems 10:Q11004. doi: 10.1029/2009GC002619

Suda N, Nawa K, Fukao Y (1998) Earth's background free oscillations. Science 279:2089–2091. doi: 10.1126/science.279.5359.2089

Sufri O, Koper KD, Burlacu R, de Foy B (2014) Microseisms from Superstorm Sandy. Earth Planet Sci Lett 402:324–336. doi: 10.1016/j.epsl.2013.10.015

Sun W, Kennett B (2017) Mid-lithosphere discontinuities beneath the western and central North China Craton. Geophys Res Lett 44:1302–1310. doi: 10.1002/2016GL071840

Suomela J (2014) Median Filtering is Equivalent to Sorting. http://arxiv.org/abs/1406.1717

Sutton GH, Barstow N (1996) Ocean bottom microseisms from a distant supertyphoon. Geophys Res Lett 23:499–502. doi: 10.1029/96GL00419

Taira T, Brenguier F, Kong Q (2015) Ambient noise-based monitoring of seismic velocity changes associated with the 2014 Mw 6.0 South Napa earthquake. Geophys Res Lett 42:6997–7004. doi: 10.1002/2015GL065308

Takano T, Nishimura T, Nakahara H, et al (2014) Seismic velocity changes caused by the Earth tide: Ambient noise correlation analyses of small-array data. Geophys Res Lett 41:6131–6136. doi: 10.1002/2014GL060690

Tanimoto T (1999) Excitation of normal modes by atmospheric turbulence: Source of long-period seismic noise. Geophys J Int 136:395–402. doi: 10.1046/j.1365-246X.1999.00763.x

Tanimoto T (2005) The oceanic excitation hypothesis for the continuous oscillations of the Earth. Geophys J Int 160:276–288. doi: 10.1111/j.1365-246X.2004.02484.x

Tanimoto T (2007a) Excitation of normal modes by non-linear interaction of ocean waves. Geophys J Int

168:571–582. doi: 10.1111/j.1365-246X.2006.03240.x

Tanimoto T (2007b) Excitation of microseisms. Geophys Res Lett. doi: 10.1029/2006GL029046

Tanimoto T, Alvizuri C (2006) Inversion of the HZ ratio of microseisms for S-wave velocity in the crust. Geophys J Int 165:323–335. doi: 10.1111/j.1365-246X.2006.02905.x

Tanimoto T, Eitzel M, Yano T (2008) The noise cross-correlation approach for Apollo 17 LSPE data: Diurnal change in seismic parameters in shallow lunar crust. J Geophys Res Solid Earth 113:E08011. doi: 10.1029/2007JE003016

Tanimoto T, Hadziioannou C, Igel H, et al (2016a) Seasonal variations in the Rayleigh-to-Love wave ratio in the secondary microseism from colocated ring laser and seismograph. J Geophys Res Solid Earth 121:2447–2459. doi: 10.1002/2016JB012885

Tanimoto T, Heki K, Artru-Lambin J (2015) Interaction of Solid Earth, Atmosphere, and Ionosphere. In: Treatise on Geophysics, 2nd editio. Elsevier, pp 421–443

Tanimoto T, Lin CJ, Hadziioannou C, et al (2016b) Estimate of Rayleigh-to-Love wave ratio in the secondary microseism by a small array at Piñon Flat observatory, California. Geophys Res Lett 43:11,173–11,181. doi: 10.1002/2016GL071133

Tanimoto T, Rivera L (2008) The ZH ratio method for long-period seismic data: Sensitivity kernels and observational techniques. Geophys J Int 172:187–198. doi: 10.1111/j.1365-246X.2007.03609.x

Tanimoto T, Um J (1999) Cause of continuous oscillations of the Earth. J Geophys Res 104:28723–28739. doi: 10.1029/1999JB900252

Tanimoto T, Um J, Nishida K, Kobayashi N (1998) Earth's continuous oscillations observed on seismically quiet days. Geophys Res Lett 25:1553–1556. doi: 10.1029/98GL01223

Tatom FB, Vitton SJ (2001) The Transfer of Energy from a Tornado into the Ground. Seismol Res Lett 72:12–21. doi: 10.1785/gssrl.72.1.12

Tayfun MA (1980) Narrow-band nonlinear sea waves. J Geophys Res 85:1548.

Taylor G, Rost S, Houseman G (2016) Crustal imaging across the North Anatolian Fault Zone from the autocorrelation of ambient seismic noise. Geophys Res Lett 43:2502–2509.

Tian Y, Ritzwoller MH (2015) Directionality of ambient noise on the Juan de Fuca plate: Implications for source locations of the primary and secondary microseisms. Geophys J Int 201:429–443.

Tibuleac IM, von Seggern D (2012) Crust-mantle boundary reflectors in Nevada from ambient seismic noise autocorrelations. Geophys J Int 189:493–500. doi: 10.1111/j.1365-246X.2011.05336.x

Tillotson K, Komar PD (1997) The Wave Climate of the Pacific Northwest (Oregon and Washington): A Comparison of Data Sources. J Coast Res 13:440–452. doi: 10.2307/4298639

Tomar G, Shapiro NM, Mordret A, et al (2017) Radial anisotropy in Valhall: Ambient noise-based studies of Scholte and Love waves. Geophys J Int 208:1524–1539. doi: 10.1093/gji/ggw480

Tonegawa T, Fukao Y, Nishida K, et al (2013) A temporal change of shear wave anisotropy within the marine sedimentary layer associated with the 2011 Tohoku-Oki earthquake. J Geophys Res Solid Earth 118:607–615. doi: 10.1002/jgrb.50074

Traer J, Gerstoft P (2014) A unified theory of microseisms and hum. J Geophys Res 119:3317–3339. doi:

10.1002/2013JB010504

Traer J, Gerstoft P, Bromirski PD, Shearer PM (2012) Microseisms and hum from ocean surface gravity waves. J Geophys Res 117:1–16. doi: 10.1029/2012JB009550

Trnkoczy A (2012) Understanding and parameter setting of STA/LTA trigger algorithm. In: Bormann P (ed) New Manual of Seismological Observatory Practice 2 (NMSOP-2). GFZ, Potsdam, pp 1–20

Trujillo AP, Thurman H V. (2008) Essentials of oceanography, 5th edn. Pearson Education

Tsai VC (2009) On establishing the accuracy of noise tomography travel-time measurements in a realistic medium. Geophys J Int 178:1555–1564. doi: 10.1111/j.1365-246X.2009.04239.x

Tsai VC (2010) The relationship between noise correlation and the Green's function in the presence of degeneracy and the absence of equipartition. Geophys J Int 182:1509–1514. doi: 10.1111/j.1365-246X.2010.04693.x

Tsai VC, Moschetti MP (2010) An explicit relationship between time-domain noise correlation and spatial autocorrelation (SPAC) results. Geophys J Int 182:454–460. doi: 10.1111/j.1365-246X.2010.04633.x

Tsutsui T (1992) Pseudoreflection Profiling Method: an Efficient Complement To CDP Method. Geophys Prospect 40:15–30. doi: 10.1111/j.1365-2478.1992.tb00362.x

Tytell J, Vernon F, Hedlin M, et al (2016) The USArray Transportable Array as a Platform for Weather Observation and Research. Bull Am Meteorol Soc 97:603–619. doi: 10.1175/BAMS-D-14-00204.1

Ugalde A, Gaite B, Villaseñor A (2014) Temporal variations of seismic velocity at Paradox Valley, Colorado, using passive image interferometry. Bull Seismol Soc Am. doi: 10.1785/0120130133

Unglert K, Jellinek AM (2017) Feasibility study of spectral pattern recognition reveals distinct classes of volcanic tremor. J Volcanol Geotherm Res 336:219–244. doi: 10.1016/j.jvolgeores.2017.03.006

Unglert K, Radić V, Jellinek AM (2016) Principal component analysis vs. self-organizing maps combined with hierarchical clustering for pattern recognition in volcano seismic spectra. J Volcanol Geotherm Res 320:58–74. doi: 10.1016/j.jvolgeores.2016.04.014

Valovcin A, Tanimoto T (2017) Modeling the Excitation of Seismic Waves by the Joplin Tornado. Geophys Res Lett 44:10,256-10,261. doi: 10.1002/2017GL074185

Vassallo M, Bobbio A, Iannaccone G (2008) A Comparison of Sea-Floor and On-Land Seismic Ambient Noise in the Campi Flegrei Caldera, Southern Italy. Bull Seismol Soc Am 98:2962–2974. doi: 10.1785/0120070152

Vassallo M, Festa G, Bobbio A (2012) Seismic Ambient Noise Analysis in Southern Italy. Bull Seismol Soc Am 102:574–586. doi: 10.1785/0120110018

Ventosa S, Schimmel M, Stutzmann E (2017) Extracting surface waves, hum and normal modes: time-scale phase-weighted stack and beyond. Geophys J Int 211:30–44. doi: 10.1093/gji/ggx284

Verbeke J, Boschi L, Stehly L, et al (2012) High-resolution Rayleigh-wave velocity maps of central Europe from a dense ambient-noise data set. Geophys J Int 188:1173–1187.

Vinnik LP (1973) Sources of microseismic P waves. PAGEOPH 103:282–289. doi: 10.1007/BF00876404

Wang T, Song X (2017) Support for equatorial anisotropy of Earth's inner-inner core from seismic interferometry at low latitudes. Phys Earth Planet Inter. doi: 10.1016/j.pepi.2017.03.004

Wang T, Song X, Xia HH (2015) Equatorial anisotropy in the inner part of Earth's inner core from autocorrelation of earthquake coda. Nat Geosci 8:1–4. doi: 10.1038/NGEO2354

Wapenaar K (2004) Retrieving the elastodynamic Green's function of an arbitrary inhomogeneous medium by cross correlation. Phys Rev Lett 93:254301. doi: 10.1103/PhysRevLett.93.254301

Wapenaar K (2003) Synthesis of an inhomogeneous medium from its acoustic transmission response. Geophysics 68:1756–1759. doi: 10.1190/1.1620649

Wapenaar K (2006) Green's function retrieval by cross-correlation in case of one-sided illumination. Geophys Res Lett 33:L19304. doi: 10.1029/2006GL027747

Wapenaar K, Broggini F, Snieder R (2012) Creating a virtual source inside a medium from reflection data: Heuristic derivation and stationary-phase analysis. Geophys J Int 190:1020–1024. doi: 10.1111/j.1365-246X.2012.05551.x

Wapenaar K, Draganov D, Snieder R, et al (2010a) Tutorial on seismic interferometry: Part 1 — Basic principles and applications. Geophysics 75:75A195-75A209. doi: 10.1190/1.3457445

Wapenaar K, Fokkema J (2006) Green's function representations for seismic interferometry. Geophysics 71:SI33-SI46. doi: 10.1190/1.2213955

Wapenaar K, Fokkema J, Snieder R (2005) Retrieving the Green's function in an open system by cross correlation: A comparison of approaches (L). J Acoust Soc Am 118:2783–2786.

Wapenaar K, Ruigrok E, van der Neut J, Draganov D (2011a) Improved surface-wave retrieval from ambient seismic noise by multi-dimensional deconvolution. Geophys Res Lett 38:L01313.

Wapenaar K, Slob E, Snieder R (2006) Unified Green's Function Retrieval by Cross Correlation. Phys Rev Lett 97:234301. doi: 10.1103/PhysRevLett.97.234301

Wapenaar K, Slob E, Snieder R (2010b) On seismic interferometry, the generalized optical theorem, and the scattering matrix of a point scatterer. Geophysics 75:SA27. doi: 10.1190/1.3374359

Wapenaar K, Slob E, Snieder R, Curtis A (2010c) Tutorial on seismic interferometry: Part 2 — Underlying theory and new advances. Geophysics 75:75A211–75A227. doi: 10.1190/1.3463440

Wapenaar K, Thorbecke J (2017) Virtual sources and their responses, Part I: time-reversal acoustics and seismic interferometry. Geophys Prospect 65:1411–1429. doi: 10.1111/1365-2478.12496

Wapenaar K, Thorbecke J, van der Neut J, et al (2017) Virtual sources and their responses, Part II: data-driven single-sided focusing. Geophys Prospect 65:1430–1451. doi: 10.1111/1365-2478.12495

Wapenaar K, van der Neut J, Ruigrok E, et al (2011b) Seismic interferometry by crosscorrelation and by multidimensional deconvolution: A systematic comparison. Geophys J Int 185:1335–1364. doi: 10.1111/j.1365-246X.2011.05007.x

Weaver R, Froment B, Campillo M (2009) On the correlation of non-isotropically distributed ballistic scalar diffuse waves. J Acoust Soc Am 126:1817. doi: 10.1121/1.3203359

Weaver RL (2013) Retrieval of Green's function in the radiative transfer regime. J Acoust Soc Am 133:792–798. doi: 10.1121/1.4774370

Weaver RL (2011) On the amplitudes of correlations and the inference of attenuations, specific intensities and site factors from ambient noise. Comptes Rendus - Geosci 343:615–622.

Weaver RL, Hadziioannou C, Larose E, Campillo M (2011) On the precision of noise correlation interferometry. Geophys J Int 185:1384–1392. doi: 10.1111/j.1365-246X.2011.05015.x

Weaver RL, Lobkis OI (2001) Ultrasonics without a Source: Thermal Fluctuation Correlations at MHz Frequencies. Phys Rev Lett 87:134301. doi: 10.1103/PhysRevLett.87.134301

Weaver RL, Lobkis OI (2004) Diffuse fields in open systems and the emergence of the Green's function (L). J Acoust Soc Am 116:2731–2734. doi: 10.1121/1.1810232

Weaver RL, Lobkis OI (2005) Fluctuations in diffuse field–field correlations and the emergence of the Green's function in open systems. J Acoust Soc Am 117:3432–3439. doi: 10.1121/1.1898683

Weaver RL, Lobkis OI (2006) Diffuse fields in ultrasonics and seismology. Geophysics 71:SI5–SI9. doi: 10.1190/1.2212247

Webb SC (2007) The Earth's "hum" is driven by ocean waves over the continental shelves. Nature 445:754–756. doi: 10.1038/nature05536

Webb SC (2008) The earth's hum: The excitation of earth normal modes by ocean waves. Geophys J Int 174:542–566. doi: 10.1111/j.1365-246X.2008.03801.x

Weemstra C, Boschi L, Goertz A, Artman B (2013) Seismic attenuation from recordings of ambient noise. Geophysics 78:Q1–Q14. doi: 10.1190/geo2012-0132.1

Weemstra C, Westra W, Snieder R, Boschi L (2014) On estimating attenuation from the amplitude of the spectrally whitened ambient seismic field. Geophys J Int 197:1770–1788. doi: 10.1093/gji/ggu088

Wegler U, Lühr B-G, Snieder R, Ratdomopurbo A (2006) Increase of shear wave velocity before the 1998 eruption of Merapi volcano (Indonesia). Geophys Res Lett 33:L09303. doi: 10.1029/2006GL025928

Wegler U, Nakahara H, Sens-Schönfelder C, et al (2009) Sudden drop of seismic velocity after the 2004 Mw6.6 mid-Niigata earthquake, Japan, observed with Passive Image Interferometry B06305. J Geophys Res Solid Earth 114:B06305. doi: 10.1029/2008JB005869

Wegler U, Sens-Schönfelder C (2007) Fault zone monitoring with passive image interferometry. Geophys J Int 168:1029–1033. doi: 10.1111/j.1365-246X.2006.03284.x

Westfall PH (2014) Kurtosis as Peakedness, 1905–2014. R.I.P. The American Statistician 68:191–195. doi: 10.1080/00031305.2014.917055

Withers M, Aster R, Young C, et al (1998) A Comparison of Select Trigger Algorithms for Automated Global Seismic Phase and Event Detection. Bull Seismol Soc Am 88:95–106.

Woodard MF (1997) Implications of Localized, Acoustic Absorption for Heliotomographic Analysis of Sunspots. Astrophys J 485:890–894. doi: 10.1086/304468

Wu B, Xia H, Wang T, Shi X (2018) Simulation of core phases from coda interferometry. J Geophys Res Solid Earth. doi: 10.1029/2017JB015405

Xia HH, Song X, Wang T (2016) Extraction of triplicated PKP phases from noise correlations. Geophys J Int 205:499–508. doi: 10.1093/gji/ggw015

Xia Y, Ni S, Zeng X (2013) Twin enigmatic microseismic sources in the Gulf of Guinea observed on intercontinental seismic stations. Geophys J Int 194:362–366. doi: 10.1093/gji/ggt076

Xia Y, Ni S, Zeng X, et al (2015) Synchronizing intercontinental seismic networks using the 26 s persistent

localized microseismic source. Bull Seismol Soc Am 105:2101–2108. doi: 10.1785/0120140252

Xie J, Ni S, Chu R, Xia Y (2018) Assessing the short-term clock drift of early broadband stations with burst events of the 26 s persistent and localized microseism. Geophys J Int 212:324–332.

Xu Y, Koper KD, Burlacu R (2017) Lakes as a Source of Short-Period (0.5-2 s) Microseisms. J Geophys Res Solid Earth 122:8241–8256. doi: 10.1002/2017JB014808

Yang Y, Ritzwoller MH (2008) Characteristics of ambient seismic noise as a source for surface wave tomography. Geochemistry, Geophysics, Geosystems 9. doi: 10.1029/2007GC001814

Yang Y, Ritzwoller MH, Levshin AL, Shapiro NM (2007) Ambient noise Rayleigh wave tomography across Europe. Geophys J Int 168:259–274. doi: 10.1111/j.1365-246X.2006.03203.x

Yao H, Beghein C, Van Der Hilst RD (2008) Surface wave array tomography in SE Tibet from ambient seismic noise and two-station analysis - II. Crustal and upper-mantle structure. Geophys J Int 173:205–219. doi: 10.1111/j.1365-246X.2007.03696.x

Yao H, van der Hilst RD (2009) Analysis of ambient noise energy distribution and phase velocity bias in ambient noise tomography, with application to SE Tibet. Geophys J Int 179:1113–1132. doi: 10.1111/j.1365-246X.2009.04329.x

Yao H, van der Hilst RD, de Hoop M V (2006) Surface-wave array tomography in SE Tibet from ambient seismic noise and two-station analysis - I. Phase velocity maps. Geophys J Int 166:732–744. doi: 10.1111/j.1365-246X.2006.03028.x

Yao H, Van Der Hilst RD, Montagner JP (2010) Heterogeneity and anisotropy of the lithosphere of SE Tibet from surface wave array tomography. J Geophys Res Solid Earth 115:B12307. doi: 10.1029/2009JB007142

Ying Y, Bean CJ, Bromirski PD (2014) Propagation of microseisms from the deep ocean to land. Geophys Res Lett 41:6374–6379. doi: 10.1002/2014GL060979

Yoritomo JY, Weaver RL (2016) Fluctuations in the cross-correlation for fields lacking full diffusivity: The statistics of spurious features. J Acoust Soc Am 140:702–713. doi: 10.1121/1.4959002

Young IR (1999a) Wind Generated Ocean Waves. Elsevier

Young IR (1999b) Seasonal variability of the global ocean wind and wave climate. Int J Climatol 19:931–950. doi: 10.1002/(SICI)1097-0088(199907)19:9<931::AID-JOC412>3.0.CO;2-O

Zeng X, Ni S (2010) A persistent localized microseismic source near the Kyushu Island, Japan. Geophys Res Lett 37:L24307. doi: 10.1029/2010GL045774

Zeng X, Ni S (2014) Evidence for an Independent 26-s Microseismic Source near the Vanuatu Islands. Pure Appl Geophys 171:2155–2163. doi: 10.1007/s00024-014-0811-1

Zhan Z, Ni S, Helmberger D V., Clayton RW (2010) Retrieval of Moho-reflected shear wave arrivals from ambient seismic noise. Geophys J Int 182:408–420. doi: 10.1111/j.1365-246X.2010.04625.x

Zhan Z, Tsai VC, Clayton RW (2013) Spurious velocity changes caused by temporal variations in ambient noise frequency content. Geophys J Int. doi: 10.1093/gji/ggt170

Zhang J, Gerstoft P, Bromirski PD (2010a) Pelagic and coastal sources of P-wave microseisms: Generation under tropical cyclones. Geophys Res Lett. doi: 10.1029/2010GL044288

Zhang J, Gerstoft P, Shearer PM (2010b) Resolving P-wave travel-time anomalies using seismic array observations of oceanic storms. Earth Planet Sci Lett 292:419–427. doi: 10.1016/j.epsl.2010.02.014

Zhang J, Yang X (2013) Extracting surface wave attenuation from seismic noise using correlation of the coda of correlation. J Geophys Res Solid Earth 118:2191–2205. doi: 10.1002/jgrb.50186

Zhao P-P, Chen J-H, Liu Q-Y, et al (2015) Fine structure of middle and upper crust of the Longmenshan Fault zone from short period seismic ambient noise. Chinese J Geophys 58:4018–4030.

Zheng S, Sun X, Song X, et al (2008) Surface wave tomography of China from ambient seismic noise correlation. Geochemistry, Geophysics, Geosystems 9. doi: 10.1029/2008GC001981

Zopf DO, Creech H, Quinn WH (1976) Wavemeter: A land-based system for measuring nearshore ocean waves. Marine Technology Society Journal 10: 19-25.

Zürn W, Exß J, Steffen H, et al (2007) On reduction of long-period horizontal seismic noise using local barometric pressure. Geophys J Int 171:780–796. doi: 10.1111/j.1365-246X.2007.03553.x